

**POLITECNICO DI MILANO**

Facoltà di Ingegneria Industriale

Corso di Laurea Magistrale in  
Ingegneria Energetica



**AN INTEGRATED THERMODYNAMIC/CFD APPROACH  
TO EJECTOR MODELING**

Relatore: Prof. Paolo Chiesa

Co-relatore: Ing. Riccardo Mereu

Tesi di Laurea di:

Giorgio Besagni

Matricola 759956

Anno Accademico 2011 - 2012



This work is dedicated to

my father

my mother

my sister

in memory of

my grandfather Ennio

my grandmother Maria

*“Voici mon secret. Il est très simple:*

*on ne voit bien qu'avec le cœur.*

*L'essentiel est invisible pour les yeux.”*



# Acknowledgments

Il ringraziamento più grande lo devo alla mia famiglia, perché se sono arrivato fino a questo giorno lo devo a loro, ai loro sorrisi, al loro sostegno e affetto.

Ringrazio il mio relatore, il Professor Paolo Chiesa, per il tempo che mi ha dedicato, per la pazienza e l'umanità. Ringrazio molto anche la Professoressa Emanuela Colombo per i consigli e la gentilezza. A loro va il merito del dottorato che inizierò.

Doveroso il ringraziamento a Riccardo, per come mi ha seguito in questi mesi, per i consigli, le osservazioni, la pazienza e l'immaneabile buon umore.

Ringrazio il Professor Fabio Inzoli e tutti i miei futuri colleghi di dottorato, per come mi hanno accolto nell'ambiente del gruppo di ricerca.

Grazie a Marco, per l'amicizia di questi anni, per essermi sempre stato a ascoltare, per le camminate e i consigli.

Grazie a Matteo, compagno di corso e amico in questi anni di università, lo ringrazio per l'immensa pazienza, i consigli, i discorsi. Cinque anni di corsi, con un amico così, sono pesati meno.

Grazie alla mia squadra di Croce Rossa, il Mercoledì notte, perché se ogni volta che mi metto la divisa sono sempre di buon umore, lo devo in buona parte a voi. Grazie Adriano, Daniele, Laura, Rosy, Paola, Claudia Z. e Claudia L.L. Siete grandi.

Grazie a Enzo, per il continuo sostegno e perché molto di quello che ho imparato come volontario, soccorritore e persona lo devo in buona parte a te.

Grazie a Piero perché mi ha insegnato che il vero cammino comincia quando finisce la strada.

Grazie ai compagni di viaggio, per i chilometri percorsi insieme. In particolare a Giorgio, Riccardo, Roberto, Sergio ed Elisa.

Grazie agli amici di lunga data Lorenzo, Riccardo e Giulia, perché non mi serve vedervi spesso per sapere che posso contare su di voi.

Grazie a tutte le persone che in questi anni mi hanno accompagnato e che ora hanno presto strade diverse. Molto devo anche a loro.

A handwritten signature in black ink, appearing to read 'Giorgio', written in a cursive style.



# Abstract

Ejectors are widely used in energy engineering and, from the first half of the twentieth century, a large amount of studies have been conducted on modeling and analyzing ejectors by using thermodynamic and Computational Fluid-Dynamics(CFD) approaches. Both modeling techniques have advantages and limits: the former ensures limited computational time and less cost than experimental method for predicting ejector performance, but it is unable to describe internal flow behavior; the latter is able to provide deep understanding of local phenomena, but it requires a higher computational cost and specific competencies in numerical methods. The integrated thermodynamic/CFD approach, proposed in this thesis, defines guidelines and proposes a novel ejectors model that, combining advantages of both described techniques, has potentiality of predicting ejectors performance, accounting local flow behavior. This approach will be applied to the case of a single phase subsonic ejector, providing a model with a structure ready to be implemented in energy power plant simulation codes. In order to achieve this result the thesis is structured as follow: in the first chapters, a description of ejector technology and a review of its modeling state-of-the-art will be provided. In the second part the structure of the novel thermodynamic model and the CFD approach will be outlined. The section related with the computational model validation is composed by a comparison of different turbulence models for subsonic ejector and by the description of a qualified approach for numerical investigation requiring application of best practices and software recommendations (the  $Q^3$  approach is used, which include the three interdependent, but related, dimensions: software reliability, user knowledge and process control). At the end, the integration of these two modeling approaches will be described and commented.

**Keywords:** ejector technology; ejector modeling; convergent nozzle; under-expanded jets; CFD; RANS turbulence models;





## Italian abstract

Gli eiettori trovano largo impiego nell'ingegneria energetica e, dalla prima metà del ventesimo secolo, sono stati presentati molti lavori sulla loro modellazione e analisi, usando sia un approccio termodinamico che uno basato sulla termo fluidodinamica computazionale (CFD). Entrambe queste tecniche hanno vantaggi e limiti: la prima assicura tempi di calcolo e costi minori rispetto a analisi sperimentali, a fronte di un'incapacità nel descrivere il campo di moto interno; la seconda è idonea alla descrizione di fenomeni locali, ma richiede maggiori oneri computazionali e specifiche competenze nell'ambito dei metodi numerici. L'approccio integrato termodinamico/CFD, proposto in questa tesi, definisce linee guida e propone un nuovo modello per eiettori che, riunendo i vantaggi di entrambe queste tecniche, ha la potenzialità di predire le prestazioni di eiettori tenendo in considerazione i fenomeni fluidodinamici locali. Questo approccio sarà applicato a un eiettore subsonico con flusso monofase, presentando un modello con una struttura facilmente implementabile in codici per la simulazione di impianti di potenza. Per arrivare a questo risultato la tesi è strutturata come segue: nei primi capitoli è presentata una descrizione della tecnologia degli eiettori e una presentazione sullo stato dell'arte della loro modellazione. Nella seconda parte è presentata la struttura del nuovo modello termodinamico e dell'approccio CFD. La sezione relativa alla validazione del modello numerico è costituita dal confronto delle prestazioni di modelli di turbolenza RANS per eiettori subsonici e dalla descrizione di un approccio qualificato che richiede l'applicazione delle migliori pratiche e competenze sull'utilizzo del software (è utilizzato l'approccio  $Q^3$ , che include tre dimensioni indipendenti ma collegate: l'affidabilità del software, la competenza dell'utente e il controllo del processo). In conclusione sarà descritta e commentata l'integrazione di questo due approcci modellistici.

**Italian keywords:** tecnologia degli eiettori; modellazione degli eiettori; ugello convergente; getti sotto-espansi; CFD; modelli di turbolenza RANS.



# Contents

<b>ACKNOWLEDGMENTS</b> .....	<b>I</b>
<b>ABSTRACT</b> .....	<b>III</b>
<b>ITALIAN ABSTRACT</b> .....	<b>V</b>
<b>CONTENTS</b> .....	<b>VII</b>
<b>LIST OF FIGURES</b> .....	<b>X</b>
<b>LIST OF TABLES</b> .....	<b>XIII</b>
<b>INTRODUCTION</b> .....	<b>1</b>
<b>CHAPTER 1 EJECTOR TECHNOLOGY</b> .....	<b>3</b>
1.1 CLASSIFICATION .....	3
1.2 OPERATING CONDITIONS.....	4
1.2.1 <i>Supersonic ejectors</i> .....	4
1.2.2 <i>Subsonic ejectors</i> .....	4
1.3 APPLICATIONS IN ENERGY FIELD.....	5
1.3.1 <i>Supersonic ejector applications in energy field</i> .....	5
1.3.1.1 Refrigeration .....	6
1.3.1.2 SOFC and MCFC power plants .....	7
1.3.2 <i>Subsonic ejector applications in energy field</i> .....	8
1.3.2.1 PEMFC .....	8
1.3.2.2 CLC.....	10
<b>CHAPTER 2 EJECTOR MODELING</b> .....	<b>11</b>
2.1 INTRODUCTION TO EJECTOR MODELING: MODELS STRUCTURE.....	11
2.1.1 <i>Approach</i> .....	11
2.1.2 <i>Fundamental hypothesis of thermodynamic models</i> .....	11
2.1.3 <i>Equations to be solved</i> .....	12
2.1.4 <i>Boundary conditions</i> .....	13
2.1.5 <i>Initial conditions</i> .....	13
2.1.6 <i>Turbulence modeling</i> .....	13
2.1.7 <i>Auxiliary relations</i> .....	14
2.2 THERMODYNAMIC EJECTOR MODELING: STORY AND CURRENT STATE-OF-THE-ART .....	15
2.2.1 <i>A brief story on thermodynamic ejector modeling</i> .....	15
2.2.2 <i>Subsonic ejector modeling: a recent theme of research</i> .....	22
2.2.3 <i>Limitations of thermodynamic models</i> .....	30
2.3 EJECTOR EFFICIENCIES AND THEIR ROLE IN THERMODYNAMIC MODELING.....	31
2.3.1 <i>Ejector global efficiency</i> .....	31
2.3.2 <i>Ejector efficiencies</i> .....	32
2.3.2.1 Primary Nozzle .....	33
2.3.2.2 Suction nozzle .....	33
2.3.2.3 Aerodynamic throat.....	34
2.3.2.4 Mixing chamber .....	35

2.3.2.5 Diffuser .....	37
2.3.2.6 Ejector efficiencies used in literature .....	37
2.3.3 Role of the integrated thermodynamic/CFD model .....	39
2.4 CFD EJECTOR MODELING: STORY AND CURRENT STATE-OF-THE-ART .....	39
2.4.1 A brief story on CFD ejector modeling .....	39
2.4.2 Guidelines in CFD ejector modeling .....	41
<b>CHAPTER 3 THERMODYNAMIC MODEL.....</b>	<b>47</b>
3.1 BASIS OF THE NOVEL THERMODYNAMIC MODEL .....	47
3.1.1 Power plant simulation codes constrains and modification over the typical 1D approach.....	47
3.1.2 CFD contributions.....	48
3.2 DESCRIPTION OF THE NOVEL THERMODYNAMIC MODEL .....	49
3.2.1 Hypothesis .....	49
3.2.2 Input.....	49
3.2.3 Preliminary calculations: flow compositions .....	50
3.2.4 Primary nozzle.....	51
3.2.5 Exit suction zone.....	53
3.2.6 Mixing.....	54
3.2.7 Diffuser.....	56
3.3 BASIS OF INTEGRATION.....	56
<b>CHAPTER 4 CFD MODEL .....</b>	<b>57</b>
4.1 Q <sup>3</sup> APPROACH.....	57
4.1.1 Introduction.....	57
4.2.2 Protocol structure.....	57
4.2 CFD CYCLE PHASE 1 - PROBLEM ANALYSIS .....	58
4.2.1 Frame of action and general purposes.....	58
4.2.2 Problem identification.....	58
4.3 CFD CYCLE PHASE 2 - CONCEPTUAL MODEL SETTING: RESULTS AND APPROACH.....	59
4.3.1 Specific goals of the CFD analysis.....	59
4.3.2 State-of-the-art of CFD in the field .....	59
4.3.3 Expected results and benchmark used.....	59
4.3.4 General approach: main assumption and working hypothesis.....	60
4.3.5 Activities and plan .....	60
4.4 CFD CYCLE PHASE 3 – MODEL BUILDING AND SOLVING: DEPLOYMENT .....	61
4.4.1 Pre-processing.....	61
4.4.1.1 Domain identification and Geometry setting.....	61
4.4.1.2 Mesh strategy and generation.....	62
4.4.2 Model setting .....	66
4.4.2.1 Solver .....	66
4.4.2.2 Turbulence approach .....	66
4.4.2.3 Physical properties .....	67
4.4.2.4 Operating conditions .....	67
4.4.2.5 Boundary conditions .....	67
4.4.3 Numerical setting.....	69
4.4.3.1 Numerical strategy .....	69
4.4.3.2 Convergence control .....	70
4.5 CFD CYCLE PHASE 4 – PROBLEM EVALUATION, ASSESSMENT AND REVIEW.....	70

4.5.1 Calculation verification.....	71
4.5.1.1 Run 6: velocity .....	73
4.5.1.2 Run 7: velocity .....	78
4.5.1.3 Run 9: Velocity .....	83
4.5.1.4 Run 9: Total Temperature .....	89
4.5.1.5 Run 10: velocity .....	92
4.5.2 Calculation validation and critical review of the model .....	96
4.5.3 Strategy improvement.....	96
4.6 IMPORTANT REMARKS .....	96
4.6.1 Turbulence models performance comparison .....	96
4.6.1.1 Convergence behavior.....	97
4.6.1.3 Flow field (comparison with velocity data).....	97
4.6.1.2 Thermal field (comparison with temperature data) .....	98
4.6.1.4 Results.....	99
4.6.2 Approach and guidelines for CFD ejector modeling.....	99
4.6.3 Applications.....	100
<b>CHAPTER 5 INTEGRATION.....</b>	<b>101</b>
5.1 PART 1: APPLICATION OF THE CFD APPROACH .....	101
5.1.1 Range of analysis.....	101
5.1.1.1 Primary range of analysis: primary mass flow rate variation .....	101
5.1.1.2 Secondary range of analysis: secondary mass flow rate variation.....	102
5.2.2 Results .....	104
5.2.2.1 Efficiencies .....	104
5.2.2.2 Flow behavior .....	106
5.2 PART 2: THE RELATIONSHIP BETWEEN INTERNAL FLOW AND EFFICIENCIES. ....	116
5.2.1 Nozzle .....	116
5.2.2 Suction.....	121
5.2.3 Mixing.....	125
5.3 PART 3: THE INTEGRATED THERMODYNAMIC/CFD MODEL FOR SINGLE PHASE SUBSONIC EJECTOR .....	135
5.3.1 Initialization .....	135
5.3.2 Thermodynamic model code.....	135
5.3.3 CFD efficiency LOOPS.....	135
5.3.4 Model structure .....	135
<b>CONCLUSIONS .....</b>	<b>137</b>
<b>REFERENCES.....</b>	<b>139</b>

# List of figures

Figure 1-1 Ejector layout; taken from [27] .....	3
Figure 1-2 Operation modes of supersonic ejector; taken from [30] .....	4
Figure 1-3 Operation modes of subsonic ejector; modified from [25] .....	5
Figure 1-4 JRC layout; taken from [41] .....	6
Figure 1-5 Rolls-Royce fuel cell system .....	7
Figure 1-6 PEM based system studied by [25] .....	9
Figure 1-7 PEM based system studied by [54] .....	9
Figure 1-8 (a) ejectors used on both Air Reactor and Fuel Reactor lines [56] and (b) ejector used on Fuel Reactor line only.....	10
Figure 2-1 Density contour on nozzle outlet (Simulation run 9, section 4.5.1.3).....	12
Figure 2-2 (a) Velocity distribution and (b) mixing section; taken from [75] .....	17
Figure 2-3 Ejector studied by Zhu et al. [25] .....	25
Figure 2-4 Radial velocity distribution in zone 2; taken from [25] .....	27
Figure 2-5 Subsonic ejector operating condition; taken from [55] .....	29
Figure 2-6 Ejector flow field; taken from [130] .....	43
Figure 2-7 Effects of a mesh improvement; modified from [24] .....	44
Figure 2-8 Turbulence modeling results comparison: (a) $k - \epsilon$ and (b) $k - \omega$ model .....	44
Figure 3-1 Ejector studied .....	47
Figure 4-1 Protocol structure; modified from [118].....	58
Figure 4-2 Activities and plan.....	61
Figure 4-3 Ejector geometry; taken from [137].....	62
Figure 4-4 Benchmark ejector; taken from [119].....	62
Figure 4-5 2D Mesh used in previous work; taken from [119].....	63
Figure 4-6 Comparison between mesh (Figure 4-5) used and geometry in [137].....	63
Figure 4-7 Mesh developed with GAMBIT .....	64
Figure 4-8 Mesh developed with GAMBIT with details .....	64
Figure 4-9 Aspect ratio comparison .....	65
Figure 4-10 Cell surface comparison .....	65
Figure 4-11 Element skewness comparison .....	66
Figure 4-12 Boundary conditions used .....	68
Figure 4-13 Mixing sections traverse locations; taken from [137] .....	72
Figure 4-14 Velocity contours (run 6) .....	73
Figure 4-15 Velocity profiles at $x = 2.54\text{cm}$ (run 6).....	74
Figure 4-16 Velocity profiles at $x = 7.62\text{cm}$ (run 6).....	74
Figure 4-17 Velocity profiles at $x = 17.78\text{cm}$ (run 6).....	75
Figure 4-18 Velocity profiles at $x = 26.67\text{cm}$ (run 6).....	75
Figure 4-19 Considerations about velocity profiles at $x = 2.54\text{cm}$ (run 6).....	76
Figure 4-20 Considerations about velocity profiles at $x = 7.62\text{cm}$ (run 6).....	77
Figure 4-21 Velocity contours (run 7) .....	78
Figure 4-22 Velocity profiles at $x = 2.54\text{cm}$ (run 7).....	79
Figure 4-23 Velocity profiles at $x = 7.62\text{cm}$ (run 7).....	79
Figure 4-24 Velocity profiles at $x = 17.78\text{cm}$ (run 7).....	80
Figure 4-25 Velocity profiles at $x = 26.67\text{cm}$ (run 7).....	80
Figure 4-26 Considerations about velocity profiles at $x = 2.54\text{cm}$ (run 6).....	81

Figure 4-27 Run 7 nozzle exit velocity contours for (a) $k - \varepsilon$ Standard and (b) $k - \varepsilon$ Realizable.....	82
Figure 4-28 Velocity contours (run 9).....	83
Figure 4-29 Velocity profiles at $x = 2.54\text{cm}$ (run 9).....	84
Figure 4-30 Velocity profiles at $x = 5.08\text{cm}$ (run 9).....	84
Figure 4-31 Velocity profiles at $x = 7.62\text{cm}$ (run 9).....	85
Figure 4-32 Velocity profiles at $x = 12.7\text{cm}$ (run 9).....	85
Figure 4-33 Velocity profiles at $x = 17.78\text{cm}$ (run 9).....	86
Figure 4-34 Velocity profiles at $x = 26.67\text{cm}$ (run 9).....	86
Figure 4-35 Considerations about velocity profiles at $x = 5.08\text{cm}$ (run 9).....	87
Figure 4-36 Total temperature contours (run 9).....	89
Figure 4-37 Total temperature profiles at $x = 7.62\text{cm}$ (run 9).....	90
Figure 4-38 Total temperature profiles at $x = 26.67\text{cm}$ (run 9).....	90
Figure 4-39 Run 9 nozzle exit total temperature contours for (a) $k - \varepsilon$ Standard and (b) $k - \varepsilon$ Realizable.....	91
Figure 4-40 Velocity contours (run 10).....	92
Figure 4-41 Velocity profiles at $x = 2.54\text{cm}$ (run 10).....	93
Figure 4-42 Velocity profiles at $x = 7.62\text{cm}$ (run 10).....	93
Figure 4-43 Velocity profiles at $x = 17.78\text{cm}$ (run 10).....	94
Figure 4-44 Velocity profiles at $x = 26.67\text{cm}$ (run 10).....	94
Figure 4-45 CFD cyclic process.....	96
Figure 4-46 Total temperature profiles at $x = 7.62\text{cm}$ (run 9).....	98
Figure 4-47 Total temperature profiles at $x = 26.67\text{cm}$ (run 9).....	99
Figure 5-1 Relations between primary mass flow rate variations, primary inlet pressure and primary inlet velocity.....	107
Figure 5-2 Simulation results: Mach contours.....	108
Figure 5-3 Subsonic jet flow from a sonic nozzle; taken from [143].....	109
Figure 5-4 Moderately under-expanded jet flow from a sonic nozzle; taken from [143].....	110
Figure 5-5 Highly under-expanded jet flow from a sonic nozzle; taken from [143].....	110
Figure 5-6 NPR=1.893; taken from [136].....	111
Figure 5-7 NPR=2.50; taken from [136].....	111
Figure 5-8 NPR=2.75; taken from [136].....	111
Figure 5-9 NPR=3.00; taken from [136].....	111
Figure 5-10 NPR=3.10; taken from [136].....	112
Figure 5-11 NPR=4.00; taken from [136].....	112
Figure 5-12 Relations between primary mass flow rate variations, secondary inlet pressure, secondary inlet velocity.....	113
Figure 5-13 Simulation results: Effects of improving $m_s$ (CASE11) - Mach contours.....	114
Figure 5-14 Simulation results: Effects of improving $m_s$ (run9) - Mach contours.....	115
Figure 5-15 Simulation results: Effects of improving $m_s$ (CASE2) - Mach contours.....	115
Figure 5-16 Nozzle efficiencies 3D plot.....	116
Figure 5-17 Nozzle efficiencies 2D plot.....	117
Figure 5-18 Nozzle efficiencies relationship with flow fields (part a).....	118
Figure 5-19 Nozzle efficiencies relationship with flow fields (part b).....	119
Figure 5-20 Error between CFD nozzle efficiencies and interpolating function proposed.....	120
Figure 5-21 Suction efficiencies 3D plot.....	121
Figure 5-22 Suction efficiencies 2D plot with considerations.....	122
Figure 5-23 Suction efficiencies relationship with flow fields.....	123

<i>Figure 5-24 Error between CFD suction efficiencies and interpolating function proposed</i> .....	124
<i>Figure 5-25 Mixing efficiencies</i> .....	125
<i>Figure 5-26 Mixing efficiencies 2D plot with considerations</i> .....	126
<i>Figure 5-27 Mixing efficiencies relationship with flow fields (part a)</i> .....	127
<i>Figure 5-28 Mixing efficiencies relationship with flow fields (part b)</i> .....	128
<i>Figure 5-29 Mixing efficiencies relationship with flow fields (part c)</i> .....	129
<i>Figure 5-30 Mixing efficiencies relationship with flow fields (part d)</i> .....	130
<i>Figure 5-31 Mixing efficiencies relationship with flow fields (part e)</i> .....	131
<i>Figure 5-32 Interpolating surface</i> .....	132
<i>Figure 5-33 Mixing efficiencies relationship with flow fields (with interpolating surface)</i> .....	133
<i>Figure 5-34 Error between CFD mixing efficiencies and interpolating function proposed</i> .....	134
<i>Figure 5-35 The integrated thermodynamic/CFD model</i> .....	136



# List of tables

<i>Table 2-1 Relevant studies about thermodynamic model for supersonic single phase ejectors...</i>	22
<i>Table 2-2 Relevant studies about thermodynamic model for subsonic single phase ejectors .....</i>	30
<i>Table 2-3 Value of parameters for <math>\eta_{exp}</math> [77].....</i>	34
<i>Table 2-4 Value of parameters for <math>\eta_{exp}</math> [71].....</i>	35
<i>Table 2-5 Mixing efficiencies; taken from [63].....</i>	36
<i>Table 2-6 Ejector efficiencies: a brief overview.....</i>	38
<i>Table 2-7 Experimental flow visualization studies.....</i>	43
<i>Table 4-1 Operating conditions of tests performed by Gilbert and Hill [137] .....</i>	60
<i>Table 4-2 Solver settings.....</i>	66
<i>Table 4-3 Working fluid properties.....</i>	67
<i>Table 4-4 Operating conditions taken from [137] .....</i>	67
<i>Table 4-5 Boundary condition for temperature, mass flow rate and pressure.....</i>	68
<i>Table 4-6 Boundary conditions for turbulence .....</i>	69
<i>Table 4-7 Numerical setting used.....</i>	70
<i>Table 4-8 Control parameter used.....</i>	70
<i>Table 4-9 Comparison between experimental data and simulation results for data point <math>y^* = 0.0056</math>, <math>x = 2.54\text{cm}</math> and <math>v_{exp} = 377.93\text{ ms}</math> .....</i>	76
<i>Table 4-10 Comparison between experimental data and simulation results for data point, <math>x = 7.62\text{cm}</math>, <math>y^* = 0.0048</math> and <math>v_{exp} = 275.41\text{ ms}</math> .....</i>	77
<i>Table 4-11 Comparison between experimental data and simulation results .....</i>	77
<i>Table 4-12 Comparison between experimental data and simulation results for data point <math>x = 2.54\text{cm}</math>, <math>y^* = 0.0115</math> and <math>v_{exp} = 377.74\text{ ms}</math> .....</i>	82
<i>Table 4-13 Comparison between experimental data and simulation results for data point <math>y^* = 0.00679</math>, <math>x = 7.62\text{cm}</math> and <math>v_{exp} = 283.66\text{ ms}</math> .....</i>	82
<i>Table 4-14 Comparison between experimental data and simulation results .....</i>	82
<i>Table 4-15 Comparison between experimental data and simulation results for data point <math>x = 2.54\text{cm}</math>, <math>y^* = 0</math> and <math>v_{exp} = 386.13\text{ ms}</math>.....</i>	87
<i>Table 4-16 Comparison between experimental data and simulation results .....</i>	88
<i>Table 4-17 Comparison between experimental data and simulation results .....</i>	88
<i>Table 4-18 Comparison between experimental data and simulation results for data point <math>x = 7.62\text{cm}</math>, <math>y^* = 0</math> and <math>T_0, exp = 337.06\text{ K}</math> .....</i>	91
<i>Table 4-19 Comparison between experimental data and simulation results for data point <math>x = 26.67\text{cm}</math>, <math>y^* = -0.01</math> and <math>T_0, exp = 322.17\text{ K}</math> .....</i>	91
<i>Table 4-20 Comparison between experimental data and simulation results .....</i>	95
<i>Table 5-1 Primary range of analysis.....</i>	102
<i>Table 5-2 Secondary range of analysis .....</i>	103
<i>Table 5-3 Efficiency results.....</i>	106
<i>Table 5-4 Coefficients of nozzle efficiency interpolating function .....</i>	120
<i>Table 5-5 Coefficients of suction efficiency interpolating function.....</i>	124
<i>Table 5-6 Coefficients of mixing efficiency interpolating function .....</i>	132



# Introduction

---

Ejectors are widely used in energy engineering for: (i) refrigeration applications [1], [2], (ii) fuel cells based systems [3], and (iii) advanced energy conversion power plants [4], [5], [6]. So, from the first half of the 20<sup>th</sup> century, beside experimental investigations [7], [8], [9], [10], [11], [12], [13], [14], [15], [16], [17], [18], [19], [20], [21] a large amount of works has been conducted on modeling and analyzing ejectors by using thermodynamic and Computational Fluid-Dynamics (CFD) approaches [22].

Both modeling techniques have advantages and limits: the former ensures limited computational time and less cost than experimental method for predicting ejector performance, but it is unable to describe internal flow behavior; the latter is able to provide deep understanding of local phenomena, but it requires a higher computational cost and specific competencies in numerical methods [23].

However, He et al. [23], after studying progress of mathematical modeling on ejectors, concluded that, though a large amount of studies have been presented on ejector modeling, further efforts are still needed:

1. to study the influence of variable isentropic coefficients, which are taken as constant in almost all existing thermodynamic models;
2. to improve the accuracy of the models based on turbulence modeling;
3. to build a simulation package of the whole ejector-based system by combining the model of the ejector and other components in the system.

This thesis starts from above remarks and proposes an ejector integrated thermodynamic/CFD modeling approach which will be applied to a single phase subsonic ejector.

The goals of this integrated approach are:

1. giving guidelines on CFD ejectors modeling;
2. providing efficiencies maps using a validated CFD approach;
3. proposing a novel thermodynamic model that uses efficiencies maps given by CFD simulations: this model will provide global parameters by considering local flow behavior;
4. developing a thermodynamic model ready to be integrated in energy power plant simulation codes;

Moreover, the application of the integrated approach to a single phase subsonic ejector will provide:

1. the first study focused on comparison of different turbulence models for the case of a convergent nozzle-ejector (in literature there are only studies about comparison of turbulence models for supersonic ejectors [24]);
2. further development for subsonic ejector modeling, which is an uncharted field of study [25].

In the next chapters a description of ejector technology (Chapter 1) and a review of ejector modeling state-of-the-art (Chapter 2) will be provided. In the second part the structure of the novel thermodynamic model (Chapter 3) and the CFD model (Chapter 4) will be discussed. In the third part of the thesis the integration of these two modeling approaches will be described and commented (Chapter 5). At the end, conclusions and future developments will be outlined.

# Chapter 1 Ejector technology

Ejector, also known as injector or jet pump is a device constituted by a primary nozzle, a suction chamber, a mixing chamber and a diffuser (Figure 1-1) [26].

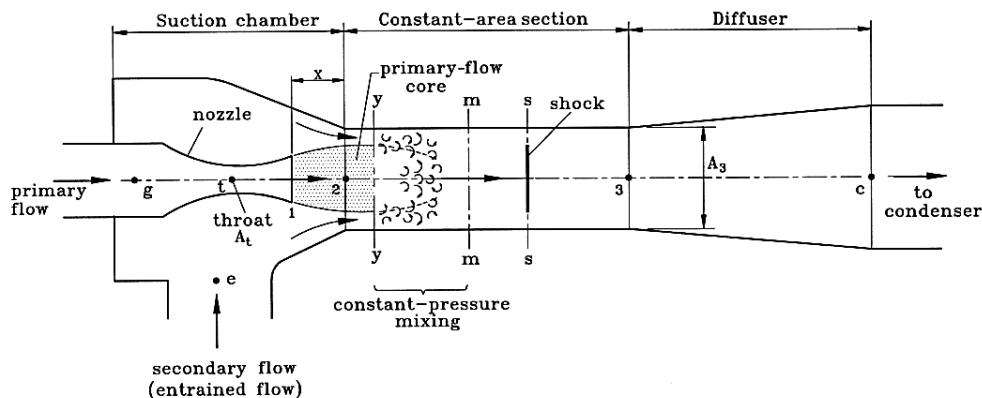


Figure 1-1 Ejector layout; taken from [27]

A high total energy “primary fluid” or “motive fluid”, expands and accelerates through the primary nozzle, flows out and creates a low pressure region at the nozzle exit plane and, subsequently, in the suction/mixing chamber. Hence, a “secondary fluid” or “entrained fluid” is drawn by both the entrainment effect (due to pressure reduction around nozzle exit) and the shear action between the primary and secondary fluids. By the end of the mixing chamber the two streams are completely mixed and a compression of the flow is achieved through a subsonic diffuser.

## 1.1 Classification

There are three ways of classifying ejectors:

1. supersonic and subsonic ejectors, according to the design of the nozzle:
  - *subsonic ejectors*: if nozzle is a converged;
  - *supersonic ejectors*: if nozzle is a converged-divergent;
2. CAM and CPM ejectors [28], according to the position of the nozzle:
  - *Constant Area Mixing (CAM) ejectors*: if nozzle exit is located within constant-area section;

- *Constant Pressure Mixing (CPM) ejectors*: if nozzle exit is located within suction chamber;
3. single phase and two phase ejectors [23], according to the number of flow phases:
    - *single phase ejectors*: if there is a single phase flow inside ejector;
    - *two phase ejectors*: if there is a two phase flow inside ejector.

## 1.2 Operating conditions

### 1.2.1 Supersonic ejectors

In supersonic ejectors two choking phenomena exist [29]: in addition to the one in the nozzle, the second results from the acceleration of the entrained flow from a stagnant state, at the suction port, to a supersonic flow, in the constant-area section. Figure 1-2 shows the variation of entrainment ratio  $\omega = \dot{m}_s/\dot{m}_p$  with the discharge pressure, at fixed inlet conditions:

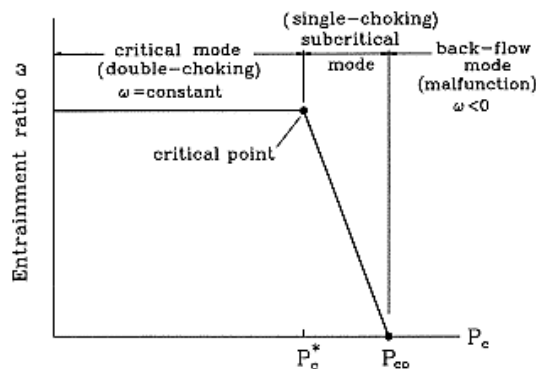


Figure 1-2 Operation modes of supersonic ejector; taken from [30]

Ejector performance can then be divided into three operational modes, according to the back pressure (Figure 1-2):

1. double-chocking or critical mode: both primary and secondary flows are choked;
2. single-chocking or subcritical mode: only primary flow is choked;
3. back-flow or malfunction mode: primary flow does not entrain secondary flow and suction chamber is filled by primary flow.

### 1.2.2 Subsonic ejectors

The flow in the convergent nozzle can be either subsonic or sonic (Figure 1-3a) by pressure ratio critical value  $v_{cr} = (p_{0,s}/p_{0,p})_{cr} = [2/(\gamma + 1)]^{\gamma/(\gamma+1)}$ :

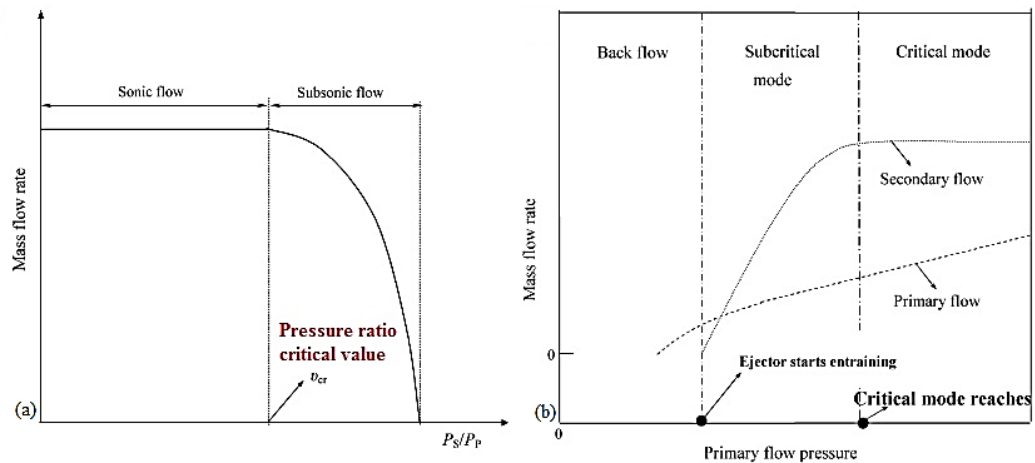


Figure 1-3 Operation modes of subsonic ejector; modified from [25]

According to the conditions of the primary and secondary flows, ejector performance is divided into three operational modes (Figure 1-3b):

1. critical: primary flow is choked ( $p_{p,0} \geq p_{s,0}/v_{cr}$ ) and secondary mass flow rate keeps near constant;
2. sub-critical: primary flow is not choked ( $p_{p,0} < p_{s,0}/v_{cr}$ ) and secondary mass flow rate is very sensitive to the operating conditions;
3. back-flow: primary flow does not entertain secondary flow and suction chamber is filled by primary flow.

Ejector may work in the subcritical mode or even in back flow mode during start up, load changes and shut down [25].

## 1.3 Applications in energy field

### 1.3.1 Supersonic ejector applications in energy field

Ejectors upon which studies focused their attention are supersonic ones and found their applications in:

1. refrigeration;
2. Solid Oxide Fuel Cell (SOFC) and Molten Carbonate Fuel Cell (MCFC) power plants.

### 1.3.1.1 Refrigeration

Jet refrigeration is a present field of study [31] because of applications in processes where heat is available in large quantities at low enthalpy [19], [32], such as thermal energy provided by solar collector [33] or waste heat [34], [35], [36] coming from power plants [37], [38], [39] or industrial processes [40]; in Figure 1-4 a Jet Refrigeration Cycle (JRC) is represented:

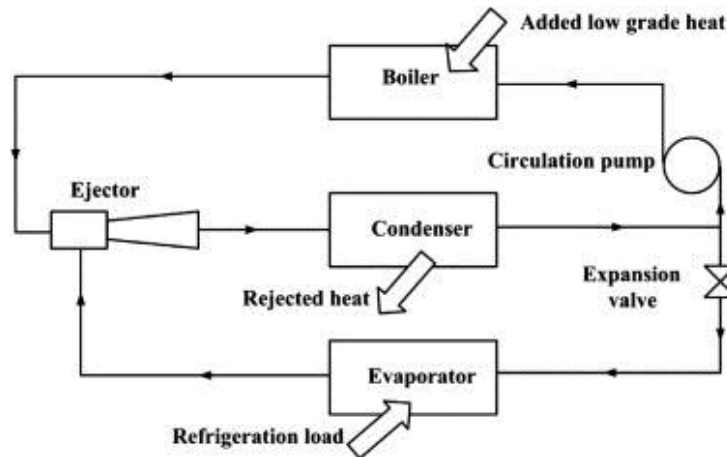


Figure 1-4 JRC layout; taken from [41]

Comparing to the typical refrigeration cycle (vapor compression cycle), in jet refrigeration the ejector, the boiler and the circulating pump are used to replace the compressor: boiler uses low grade heat to generate high pressure and high temperature vapor, which is the primary flow that enters the ejector and entertain secondary fluid from the evaporator. Then the pressure of the mixed stream rises to the condenser pressure in the diffuser and the flow is discharged from the ejector to the condenser where it change phase from vapor to liquid rejecting heat. One part of the liquid leaving the condenser enters the evaporator after passing through the expansion valve, and the other part increases its pressure using pump before flowing to the generator to be vaporized again. Meantime, the low pressure and low temperature refrigerant is vaporized in evaporator by absorbing heat from the cooled media.

Among the very large amount of works in literature, following reviews are able to give current state-of-the-art in jet refrigeration:

1. **2012.** Bravo et al. [1] described the latest developments of jet refrigeration and hybrid jet refrigeration systems are presented; the importance of working fluid in the performance of the system is emphasized;
2. **2012.** Sarkar [42] provided a literature review on two-phase ejectors and their applications in vapor compression refrigeration and heat pump systems;
3. **2012.** Sumeru et al. [43] presented a review on two-phase ejector as an expansion device in vapor compression refrigeration cycle;



4. **2011.** Elbel [31] gave an overview of historical and present developments on ejectors utilized to improve the performance of air-conditioning and refrigeration systems;
5. **2009.** Abdulateef et al. [33] focused on Solar jet refrigeration system (SJRS);
6. **2004.** Chunnanond and Aphornratana [2] presented a review on ejector applications in refrigeration technology, providing detailed description of possible cycle configurations beside JRC: (i) Booster assisted ejector cycle, (ii) Hybrid vapor compression-jet cycle, (iii) Hybrid ejector-absorption refrigeration cycle and (iv) Solar jet refrigeration system (SJRS);

Jet refrigeration system is an interesting technology because of its advantages [23]:

1. it can alleviate environment problems by using low grade thermal energy sources to drive the system instead of high grade electric energy, hence it can reduce  $CO_2$  emissions resulting from the combustion of fossil fuels;
2. it is simple and with no-moving parts, noise-free, reliable, long lifetime, low initial and running cost;
3. natural substances, such as water, can be utilized as working fluids, which have zero ozone depletion potential.

Despite advantages, standard vapor compression systems still dominate, due to low jet refrigeration systems efficiency ( $COP_{JRC} \approx 0.1 \div 0.6$  [1]): further development is required to improve their performance.

### 1.3.1.2 SOFC and MCFC power plants

Supersonic ejectors can be used in SOFC [44], [45], [46] or MCFC [47], [48] cathodic and/or anodic recirculation lines (Figure 1-5) instead of fans or blowers (increasing system reliability) [3].

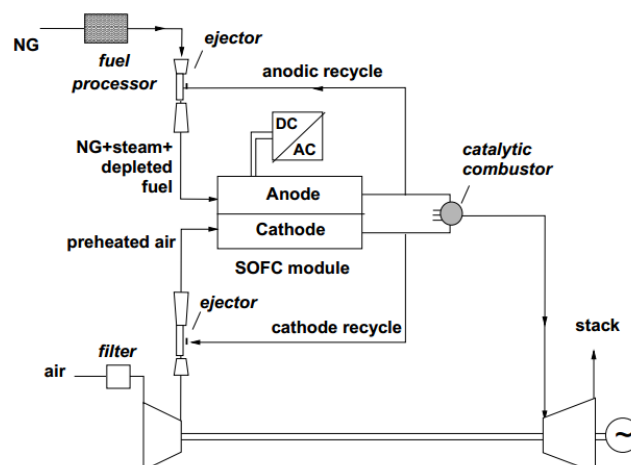


Figure 1-5 Rolls-Royce fuel cell system

**Anodic recirculation.** High pressure fuel (primary flow) flows through the ejector, where the low pressure anodic exhaust (secondary flow) is entrained and mixes with the primary flow. The resulting mixed stream flows out the diffuser to at a higher pressure and then enters into the connected reformer [45].

According to Marsano et al [44], the functions of the ejector is recirculating the anodic gas to:

1. raise the secondary flow pressure to meet the FC pressure at the required level;
2. supply sufficient heat required for the reforming reactions in the reformer;
3. provide enough secondary flow rate to maintain a proper “Steam to Carbon Ratio” (STCR) avoiding carbon deposition in the reformer and FC stacks.

**Cathodic recirculation.** This ejector is used as an heat exchanger to pre-heat gas at cathode inlet [45].

**A remark on SOFC/MCFC modeling.** Since the cost of energy for fuel compression is remarkable [49], an extreme care should be taken in ejector design and an accurate model for evaluating both on-design and off-design ejector performances is required, but most of ejector existing models are developed for refrigeration applications.

These modeling approaches will cause large errors if used to model ejectors in SOFC systems due to the differences in geometries, working fluids properties and operating conditions [50]:

1. the diameter ratio of mixing chamber to nozzle throat is much bigger, due to the requirement of larger entrainment ratio;
2. primary and secondary flows are overheated gases instead of saturated vapors;
3. primary and secondary flows temperature and composition are different from refrigeration ones;
4. pressure raise of the secondary flow is smaller than in refrigeration application.

### 1.3.2 Subsonic ejector applications in energy field

Subsonic ejectors are used in:

1. Proton Exchange Membrane Fuel Cell (PEMFC) based systems;
2. Chemical Looping Combustion (CLC) power plants.

#### 1.3.2.1 PEMFC

PEM fuel cell is a subject of great interest because of its (i) high power density, (ii) low operating temperature and (iii) short start-up time [51].

The fuel, hydrogen, is usually stored highly pressurized, while the pressure of the fuel cell stack is relatively low; this high-pressure difference can be exploited by an ejector

that uses the high-pressure hydrogen as the primary fluid to entertain the anodic exhaust (Figure 1-6).

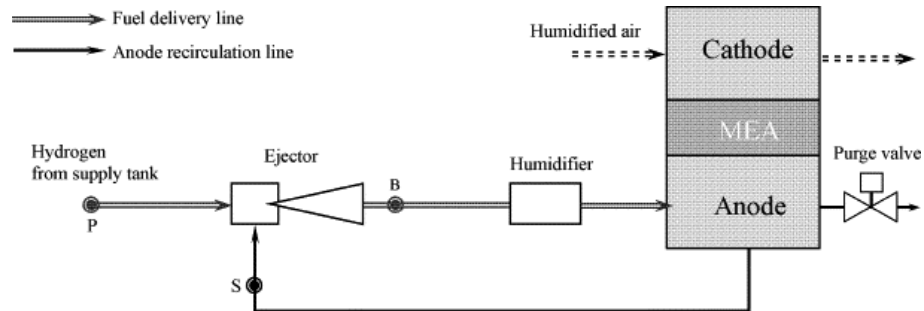


Figure 1-6 PEM based system studied by [25]

In PEMFC based systems, ejector is used to [25]:

1. utilize the pressure potential energy of hydrogen otherwise wasted;
2. recycle the unconsumed hydrogen to increase the fuel usage efficiency;
3. regulate the anode humidity with the recycle gas;
4. raise the secondary flow pressure to the level required by the cell.

PEM fuel cell must have a strictly control of water on electrodes [51]: in order to avoid condensation of water vapor (due to the low temperature of the primary and secondary flows) ejector has a convergent nozzle instead of a convergent–divergent one [25]: this is the main difference between ejectors used in PEM or in SOFC systems.

PEMFC based system (similar to the one in Figure 1-6) with an ejector on anodic recirculation line have been studied by [25], [52] and [53], whereas He et al. [54], [55] studied an hybrid fuel delivery system that consists of two supply and two recirculation lines (Figure 1-7).

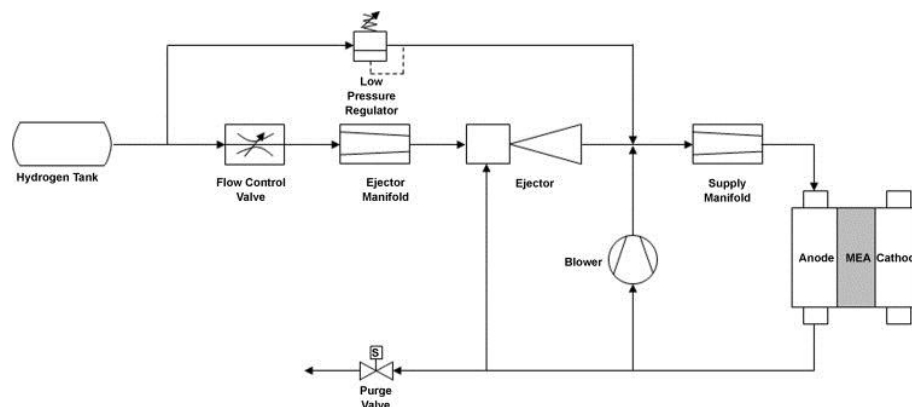


Figure 1-7 PEM based system studied by [54]

The supply lines operate basing on the load demand: at low load demand, the supply line with a low pressure regulator mainly accounts for the supply of fuel, while at a high load demand the other line with a flow control valve is used to supply additional flow. An ejector and a blower is used to mix the exiting unconsumed fuel with the supplying flow through two recirculation lines.

### 1.3.2.2 CLC

Subsonic ejector are used in fixed bed CLC power plants [56] (Figure 1-8):

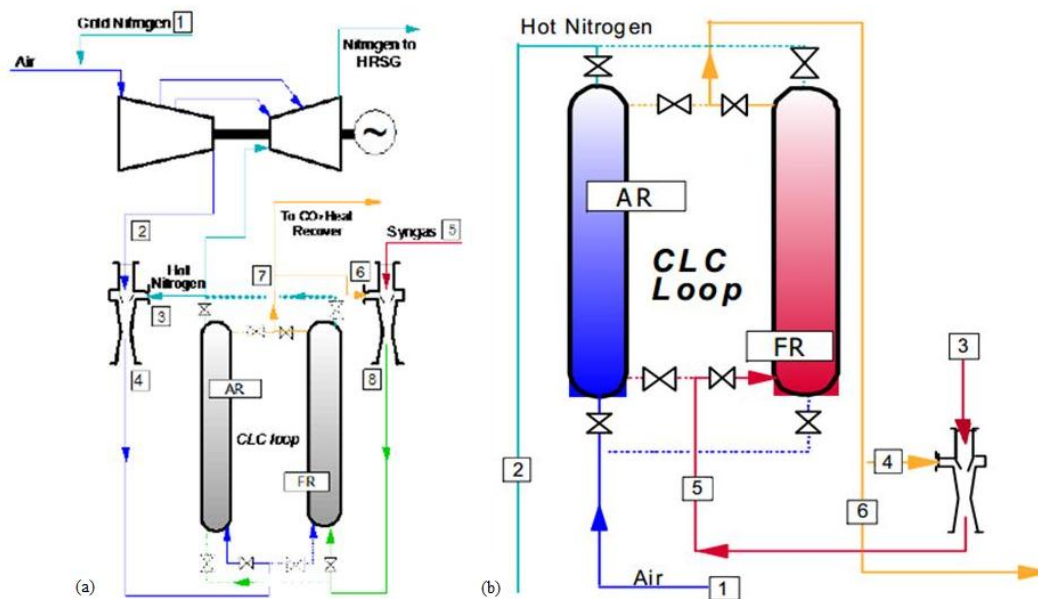


Figure 1-8 (a) ejectors used on both Air Reactor and Fuel Reactor lines [56] and (b) ejector used on Fuel Reactor line only.

Penati [56] used ejectors on both Air Reactor and Fuel Reactor (Figure 1-8a) recirculation lines. Ejectors function is recirculating Nitrogen and exhausts, providing enough  $\Delta p$  to win reactors pressure loss (due to high temperature<sup>1</sup>, a compressor cannot be used).

However due to high mass flow rate on Air Reactor, power plant efficiency gets worse if ejector performance is low: to overcome this problem ejector can be used only on Fuel Reactor recirculation line (Figure 1-8b).

<sup>1</sup>  $T_{exhaust} \approx 1200^{\circ}C$  and  $T_{Nitrogen} \approx 900^{\circ}C$  [56]

## Chapter 2 Ejector modeling

---

On the basis of governing equations, coupled with appropriate assumptions, it's possible to build up models for studying ejector performance. In this this chapter is presented a review about **single-phase** ejector modeling, because this is by far the case where there is higher experience in modeling techniques: for this reason is possible to give guidelines for future studies. **Two-phase flow** ejector modeling is an interesting new field of study, but there is obviously less experience [22], [23]: a multi-phase approach requires, beyond competences in ejector modeling, not only a complete knowledge of two-phase flow behaviors but also a remarkable experience in Multiphase Computational Fluid Dynamics, which is a present field of study [57], [58].

### 2.1 Introduction to ejector modeling: models structure

Main steps in building a model are:

1. choosing approach;
2. choosing fundamental hypothesis;
3. defining governing equation to be solved;
4. choosing auxiliary relations needed to close the governing equations.

In following sections each of these points will be deeply examined.

#### 2.1.1 Approach

There are two main ways of approaching ejector modeling [22], [23]:

1. *thermodynamic modes*. One-dimensional steady-state explicit equations are used to obtain state and parameters along the ejector. Detailed information such as shock interactions or turbulent mixing of two streams cannot be obtained by these models;
2. *CFD models*. Numerical methods are applied to solve the partial implicit differential governing equations, after being discretized using control volume techniques [59], [60].

#### 2.1.2 Fundamental hypothesis of thermodynamic models

Due to the complexity of flow behavior (choking, shock and mixing of the two streams are too complicated to be modeled in a thermodynamic approach), some ideal assumptions are needed. On the other hand, some factors that do not influence the flow significantly can be neglected, reducing problem complexity.

Here is presented the list of basic assumptions common to every thermodynamic model:

- I. *inner wall of the ejector is adiabatic*: neglecting heat transfer between the ejector and the environment, allows using isentropic relations;
- II. *flow inside the ejector is steady and isentropic*: this hypothesis is based on assumption [I];
- III. *primary and secondary fluid are supplied to the ejector at zero velocity*: inlet pressure and temperature are also equal to the total pressure and temperature;
- IV. *velocity at the ejector outlet is neglected*;
- V. *two fluids begin to mix with a uniform pressure at the mixing section*.

### 2.1.3 Equations to be solved

Thermodynamic models are based on the following equations:

1. conservation of mass:

$$\sum \rho_{in} u_{in} A_{in} = \sum \rho_{out} u_{out} A_{out} \quad (3.1)$$

2. conservation of momentum:

$$p_{in} A_{in} + \sum \dot{m}_{in} u_{in} = p_{out} A_{out} + \sum \dot{m}_{out} u_{out} \quad (3.2)$$

3. conservation of energy;

$$\sum \left[ \dot{m}_{in} \left( h_{in} + \frac{u_{in}^2}{2} \right) \right] = \sum \left[ \dot{m}_{out} \left( h_{out} + \frac{u_{out}^2}{2} \right) \right] \quad (3.3)$$

CFD models are based on Navier-Stoker equations coupled with a turbulence modeling approach; due to the presence of a transonic flow, equations to be solved have to take into consideration both turbulence and compressibility (Figure 2-1 represents density contours at nozzle exit of a subsonic ejector: there is a remarkable density variation).

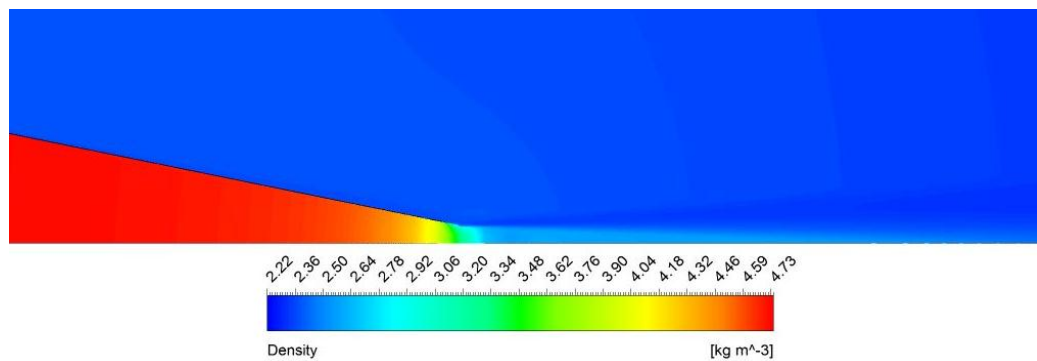


Figure 2-1 Density contour on nozzle outlet (Simulation run 9, section 4.5.1.3)

In a Reynolds-Averaged-Navier–Stokes (RANS) approach, the solver has to deal with Favre averaged Navier-Stokes equations [59] coupled with a RANS turbulence models:

$$\left\{ \begin{array}{l} \frac{\partial \bar{\rho}}{\partial t} + \text{div}(\bar{\rho} \tilde{\mathbf{v}}) = 0 \\ \frac{\partial(\bar{\rho} \tilde{v}_x)}{\partial t} + \text{div}(\bar{\rho} \tilde{v}_x \tilde{\mathbf{v}}) = -\frac{\partial \bar{p}}{\partial x} + \text{div}[\mu \text{grad}(\tilde{v}_x)] - \left[ \frac{\partial(\bar{\rho} v_x'^2)}{\partial x} + \frac{\partial(\bar{\rho} v_y'^2)}{\partial y} + \frac{\partial(\bar{\rho} v_z'^2)}{\partial z} \right] + S_{Mx} \\ \frac{\partial(\bar{\rho} \tilde{v}_y)}{\partial t} + \text{div}(\bar{\rho} \tilde{v}_y \tilde{\mathbf{v}}) = -\frac{\partial \bar{p}}{\partial y} + \text{div}[\mu \text{grad}(\tilde{v}_y)] - \left[ \frac{\partial(\bar{\rho} v_x'^2)}{\partial x} + \frac{\partial(\bar{\rho} v_y'^2)}{\partial y} + \frac{\partial(\bar{\rho} v_z'^2)}{\partial z} \right] + S_{My} \\ \frac{\partial(\bar{\rho} \tilde{v}_z)}{\partial t} + \text{div}(\bar{\rho} \tilde{v}_z \tilde{\mathbf{v}}) = -\frac{\partial \bar{p}}{\partial z} + \text{div}[\mu \text{grad}(\tilde{v}_z)] - \left[ \frac{\partial(\bar{\rho} v_x'^2)}{\partial x} + \frac{\partial(\bar{\rho} v_y'^2)}{\partial y} + \frac{\partial(\bar{\rho} v_z'^2)}{\partial z} \right] + S_{Mz} \\ \frac{\partial(\bar{\rho} \tilde{\phi})}{\partial t} + \text{div}(\bar{\rho} \tilde{\phi} \tilde{\mathbf{v}}) = -\frac{\partial \bar{p}}{\partial z} + \text{div}[\mu \text{grad}(\tilde{\phi})] - \left[ \frac{\partial(\bar{\rho} v_x' \phi)}{\partial x} + \frac{\partial(\bar{\rho} v_y' \phi)}{\partial y} + \frac{\partial(\bar{\rho} v_z' \phi)}{\partial z} \right] + S_{Mz} \end{array} \right.$$

*Turbulence model equations*

#### 2.1.4 Boundary conditions

Boundary conditions describe the behavior of the simulation at the edges of the control volume:

- thermodynamic models common [23] use pressures at inlets and exit of the ejector. Also the mass flow rates [61] or the velocities of the primary and secondary fluids have been used as boundary conditions in some literatures;
- CFD models common [23] use thermodynamics conditions at inlets (pressures and temperatures), pressure outlet [60] and no slip condition at walls.

#### 2.1.5 Initial conditions

Some thermodynamic models need initial condition to start simulation, such as expansion ratio  $D_t/D_{mix}$  [61], entrainment ratio  $\omega = \dot{m}_s/\dot{m}_p$  [62] or cross-section area of the constant-area throat tube  $D_{mix}$  [27]; CFD model need to be initialized and, due to the presence of multiple inlets (primary and secondary flow), it's suggested an hybrid initialization [60].

#### 2.1.6 Turbulence modeling

Turbulence has strong effect on the flowing process; CFD models use Boussinesq hypothesis [59], which brings to turbulence models based on an eddy viscosity assumption (Reynolds stress tensor is proportional to the mean deformation rate tensor):

$$-\overline{u_i' u_j'} = \mu_t \left( \frac{\partial u_i}{\partial x_j} + \frac{\partial u_j}{\partial x_i} \right) - \frac{2}{3} \rho k \delta_{ij} \quad (3.4)$$

Thermodynamic models cannot model turbulence phenomena in detail: dissipation term is implemented by frictional and mixing losses, which are accounted by applying coefficients introduced in the governing equations [63] (section 2.3 for further details).

### 2.1.7 Auxiliary relations

Auxiliary relations involve state equation, and variable relations; first of all it's important to define the kind of approach toward fluid, giving state equation:

$$h = h(p, \rho) \quad (3.5)$$

For an ideal gas it becomes:

$$pv = nR^*T \quad (3.6)$$

Mach number is defined as:

$$M = v/c \quad (3.7)$$

Where  $c$  is the sonic velocity:  $c = \sqrt{\left(\frac{\partial p}{\partial \rho}\right)_{is}}$ ; for an ideal gas it becomes:

$$c = \sqrt{\gamma R^* T} \quad (3.8)$$

A typical approach to thermodynamic ejector modeling uses the hypothesis of isentropic transformation [III], which gives the following equations (where  $-i$  is a generic ejector section):

1. mass flow rate per area unit:

$$\frac{\dot{m}}{A_i} = p_0 M_i \sqrt{\frac{\gamma_i}{R^* T_0}} \sqrt{\left(\frac{1}{1 + \frac{\gamma_i - 1}{2} M_i^2}\right)^{(\gamma_i + 1)/(\gamma_i - 1)}} \quad (3.9)$$

2. area ratio between two sections:

$$\frac{A_{i+1}}{A_i} = \frac{M_i}{M_{i+1}} \left(\frac{1 + \frac{\gamma - 1}{2} M_{i+1}^2}{1 + \frac{\gamma - 1}{2} M_i^2}\right)^{\frac{\gamma + 1}{2(\gamma - 1)}} \quad (3.10)$$

3. pressure ration between two section:

$$\frac{p_i}{p_{i+1}} = \left(\frac{1 + \frac{\gamma - 1}{2} M_{i+1}^2}{1 + \frac{\gamma - 1}{2} M_i^2}\right)^{\frac{\gamma}{\gamma - 1}} \quad (3.11)$$

Remembering the relations between static and total variables:



$$\left(\frac{p_{0,i}}{p_i}\right)^{\frac{\gamma-1}{\gamma}} = \frac{T_{0,i}}{T_i} = 1 + \frac{\gamma-1}{2}M_i^2 \quad (3.12)$$

and the following relation:

$$\frac{p}{\rho^\gamma} = \text{constant} \quad (3.13)$$

## 2.2 Thermodynamic ejector modeling: story and current state-of-the-art

Thermodynamic models deal with global parameters: starting from a set of hypothesis (section 2.1.2), equations (section 2.1.3) and boundary conditions (section 2.1.4), they are able to provide global information on ejector, such as outlet conditions or the entertainment ratio  $\omega = \dot{m}_s/\dot{m}_p$ ; one of best examples of this global approach is given by Yu and Li works [64], [65] that are able to provide a very synthetic formulation for  $\omega$  starting from assumptions, balance equations and boundary conditions:

$$\omega = \sqrt{\eta_p \eta_{mix} \eta_{diff} \frac{(h_{p,in} - h_{p,nozzle,exit})}{(h_{mixing\ chambre\ inlet} - h_{in,diff})}} - 1 \quad (3.14)$$

In this section a review on thermodynamic modeling is provided, remarking the approach used in each study and advancement achieved from first works till nowadays.

### 2.2.1 A brief story on thermodynamic ejector modeling

Ejector modeling has been developed since first half of the 20<sup>th</sup> century with reference to supersonic ejector, due to an increasing interest in steam jet refrigeration. In 1942 Keenan and Neumann [66] applied a one-dimensional analysis based on continuity, momentum and energy equations to predict ejectors performance under ideal gas assumption, but the difficulty in offering an analytical solution for the momentum equation, forced to use some experimental coefficients.

Later, in 1950 Keenan et al. presented a work [28] where two theoretical methods to approach ejector modeling were introduced, laying the fundamental models of one-dimensional ejectors design theory:

- Constant Pressure Mixing (CPM) model: during mixing is supposed  $dp = 0$ ;
- Constant Area Mixing (CAM) model: during mixing is supposed  $dA = 0$ .

Keenan et al. [28] also demonstrated that the former ejector technology (CPM) has better performance, but the latter model (CAM) offers better agreement with

experimental results: for this reason, most of the mathematical models that followed are based on CPM ejectors.

Beside fundamental hypothesis pointed out in section 2.1.2, in [28] (i) were supposed that primary and secondary streams start mixing immediately after discharging from nozzles and (ii) no efficiencies were used to correct isentropic process:

1. the former assumption was overcome in 1977 by Munday and Bagster [29] who further developed the CPM model by assuming that (i) primary and secondary fluid start mixing in a section in suction/mixing chamber and that (ii) primary flow creates a converging duct for secondary flow;
2. the latter assumption was overtaken later in 1995 by Eames et al. [61] that modified Keenan's model [28] to include irreversibility associated with the primary nozzle, mixing chamber and diffuser. This work is based on CPM theory but without considering Munday and Bagster [29] theory (in [61] it's supposed that two streams mixed at the primary nozzle exit plane).

It's important to remark that the works of Munday and Bagster [29] and Eames et al. [61] have given in the past and they give nowadays the basis of the approach in ejector modeling theory: a coupling between the theory proposed by Munday and Bagster [29] and the model proposed by Eames et al. [61] is presented in 1999 by Aly et al. [62].

However none of above models took in account secondary fluid choking: to overcome this lack in 1999 Huang et al. [27] presented a double choking model based on Munday and Bagster's [29] theory. Obviously, a double choking model have an increasing number of equations to consider secondary fluid choking.

All of the models considered above are based on ideal gas assumption: an improvement was given in 2000 by the work of Rodgaris and Alexis [67] who improved Munday and Bagster's [29] model by using thermodynamic and transportation properties of real gas (using R717 as media); later, in 2001, Cizungu et al. [15] proposed one of the first studies to compare system performance with different working fluids. Others studies concerning real gas effects were published back till now:

- **2004.** Selvaraju and Mani [68] used R134a, R152a, R290, R600a, R717;
- **2005.** Yapici and Ersoy [69] used R123;
- **2006.** Yu et al. [65] used R134a, R152a and R142b;
- **2007.** Yu et al. [70] used R142b;
- **2012.** Cardemil and Colle [71] used R141b, Steam, Carbon dioxide.

Once basis theory of ejector modeling was settled, the use of non-constant ejector efficiencies values was pointed out as main way to improve the accuracy of thermodynamic ejector models: their importance was already discussed in 1999 by Aly et al. [62], who found that efficiencies have a remarkable influence on system performance. In 2004 Selvaraju and Mani [68] proposed a model that uses an expression to describe the frictional loss in the constant area section (relating loss to

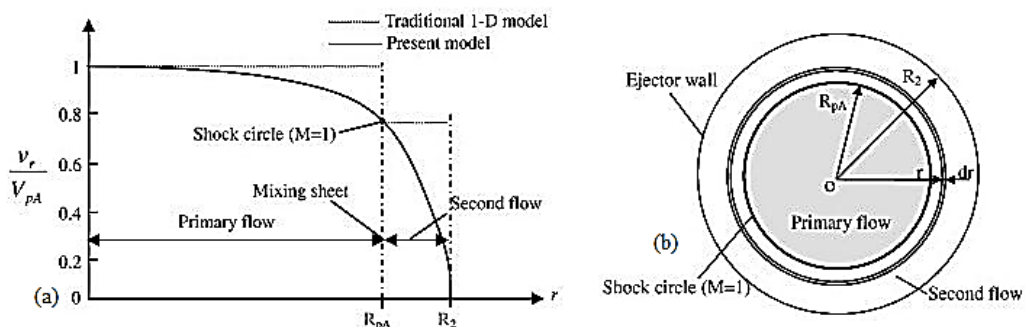
Reynolds number through friction factor in the form of the Darcy-Weisbach equation). Recently, in 2012, Liu et al. [72] proposed the first model using variable ejector efficiencies (estimated using empirical correlations retrieved from [73]). Further information on ejector efficiencies can be found in section 2.3.

General structure of approach presented in above studies (resulting from the coupling between the theory proposed by Munday and Bagster [29] and the model proposed by Eames et al. [61]) uses relations described in section 2.1.7 and models are organized in the following parts: (1) determining velocity and thermodynamic properties in the inlet of mixing section for both primary and secondary fluid; (2) using momentum equation to obtain condition of the outlet of mixing section; (3) using gas dynamics relations to study shock wave effects over Mach number and pressure; (6) determining velocity and thermodynamic conditions at diffuser outlet.

All of the models mentioned above gave only quantitative information, so Ouzanne e Aidoun in 2003 [74] proposed a local mathematical model based on Munday and Bagster's [29] theory, isentropic flow and real gas (R142b): ejector is divided in control volumes and, for each of it, balance equations are solved; this model gives both qualitative and quantitative information on operation and performance of ejector.

All works that have been presented above are based on the approach proposed in [29]; in 2007, Zhu et al. [75] developed a new approach to ejector modeling, proposing a model, called "Shock Circle Model" (SCM), which have been applied to an ejector operating in double-choking condition. Main features of this model are (i) the introduction of the "shock cycle" at the entrance of the mixing chamber (defined as the section where secondary fluid chokes) together with (ii) a 2D expression for velocity distribution to approximate the viscosity flow near the ejector inner wall:

1. shock circle (Figure 2-2): it's assumed that for double-choking operating condition only the layer between primary and secondary flow is in the choking condition and, being the layer very thin, it's assumed that the layer sheet is a circle with zero thickness (which is defined as "shock circle");



2. 2D velocity function (nomenclature from Figure 2-2) proposed in [75]:

$$v_r = \begin{cases} v_{p,2}, & \text{se } 0 \leq r \leq r_{p,2} \\ v_{p,2} \left(1 - \frac{r}{r_2}\right)^{\frac{1}{n_v}}, & \text{se } r_{p,2} < r \leq r_2 \end{cases} \quad (3.15)$$

Using logarithms,  $n_v$  can be defined as:

$$n_v = \frac{\ln\left(1 - \frac{r}{r_2}\right)}{\ln\left(\frac{v_r}{v_{p,2}}\right)} \quad (3.16)$$

In order to calculate  $n_v$ , conditions at the “shock circle” are used: (i) the radius of the circle and (ii) the speed of sound at the shock circle:

$$\begin{cases} r_{p,2} = \frac{D_{p,2}}{2} \\ M_{mixing,2} = 1 = \sqrt{\gamma RT_{s,2}} \end{cases} \quad (3.17)$$

Hence:

$$n_v = \frac{\ln\left(1 - \frac{D_{p,2}}{D_2}\right)}{\ln\left(\frac{\sqrt{T_{p,2}/T_{s,2}}}{M_{p,2}}\right)} \quad (3.18)$$

Once  $n_v$  is known, secondary flow mean velocity and mass flow rate can be defined:

$$\bar{v}_{s,2} = \frac{\int_{r_{p,2}}^{r_2} 2\pi v_r dr}{\pi(r_2^2 - r_{p,2}^2)} \quad (3.19)$$

$$\dot{m}_s = \int_{r_{p,2}}^{r_2} \bar{\rho}_s v_r dA \quad (3.20)$$

Beside above consideration, general structure of this approach uses typical relations presented in section 2.1.7 and model is organized in the following parts: (1) determining the primary mass flow rate using isentropic flow relations; (2) determining velocity and thermodynamic properties in nozzle throat; (3) determining velocity and thermodynamic properties in the aerodynamic throat (4) approximating the velocity distribution of secondary flow by a 2D function; (5) deriving a simple formula for secondary mass flow rate; (5) establishing the energy conservation equation for primary and secondary flow.

Above model structure has been used for studying:

- refrigeration cycle with supersonic ejector operating in double-choking condition [75];
- SOFC anodic recirculation with supersonic ejector operating in double-choking condition [50];
- SOFC anodic recirculation, with supersonic ejector operating in: (i) back-flow, (ii) choking and (iii) double-choking condition [76];

Similar approaches, based on SCM, were developed for studying:

- refrigeration cycle with or without steam condensation during flow expansion, with supersonic ejector operating in double-choking condition [77]<sup>2</sup>;
- PEMFC anodic recirculation, with subsonic ejector [25], [55]<sup>3</sup>;

Moreover SCM has been the basis for other models, such as the simplified ejector model for control and optimization presented in Zhu et al. [78].

Compared with a typical 1D model (such as the one proposed by Huang et. al. [27]) SMC model offers several advantages:

1. SCM is easy to run (there are less equation than standard 1D models in the solution procedure);
2. SCM can better predict ejector performance;
3. modeling of the mixing process in the constant area chamber is avoided;
4. only two basis coefficients ( $\eta_p$  and  $\eta_s$ ) are used in SCM compared with 4 in the classical 1D models ( $\eta_p$ ,  $\eta_s$ ,  $\eta_{mix}$  and  $\eta_{diff}$ ).

Last improvement in thermodynamic ejector modeling, as already remarked, is given by the proposal of a new approach (applied to a two-phase ejector) proposed in 2012 by the work Liu et al. [72], which is the first that develop a model using variable ejector efficiencies (estimated using empirical correlations retrieved from [73]).

In Table 2-1 a brief overview of relevant studies on thermodynamic modeling of single phase supersonic ejectors is presented.

Reference	Working fluid	Year, authors, work contributions and eventual presence of experimental data
[66]	Air	<b>1942.</b> <i>Keenan and Neumann.</i> First paper to develop analytical model of ejectors. <b>Experimental.</b>

<sup>2</sup> In this case there is not  $n_v$ , in fact it's used a linear function for secondary flow velocity.

<sup>3</sup> Further details on this model can be found in section 3.2.2.3

- [28] Air **1950.** *Keenan et al.* Fundamental work that laid the basis of CPM and CAM ejector modeling. **Experimental.**
- [79] Air **1958.** *Fabri and Siestrunck.* Fundamental study of ejector flow phenomena; it introduced the idea of aerodynamic throat. **Experimental.**
- [29] Water **1977.** *Munday and Bagster.* Fundamental work that further developed Keenan theory [28] by considering that (i) primary and secondary fluid start mixing in a section in suction/mixing chamber and that (ii) primary flow creates a converging duct for secondary flow. **Experimental.**
- [80] Air **1982.** *Dutton et al.* They considered ejectors where secondary stream enters at a supersonic velocity; mention of the effect of boundary layers on ejector operation. **Experimental.**
- [81] Diatomic gas with  $\gamma = 1/4$  **1986.** *Dutton and Carroll.* Molecular weight was included as optimization parameter; distinction between different operating regimes. **Experimental.**
- [82] Ideal gas **1990.** *Sokolov and Hershgal.* One of the first studies to consider working fluids other than air or water vapor. **Experimental.**
- [61] Water **1995.** *Eames et al.* One of the first works that used isentropic efficiency coefficients in order to take in account losses.
- [62] Steam **1999.** *Aly et al.* Coupling between the theory proposed by Munday and Bagster [29] and the model proposed by Eames et al. [61] with considerations about ejectors efficiencies influences over system performance.
- [27] R141b **1999.** *Huang et al.* 1D model that supposed a constant-pressure mixing occurring inside the constant-area section; experiments are used to calculate isentropic efficiency coefficients that include friction and mixing losses; coefficients used in many subsequent studies. **Experimental.**
- [67] R717 **2000.** *Rodgaris and Alexis.* Improved Munday and Bagster's [29] model by using real gas properties.
- [15] R123, 134a, R152a, R717 **2001.** *Cizungu et al.* One of the first studies to compare performance with different working fluids
- [74] R141b **2003.** Ouzanne and Aidoun. Local mathematical model to give

- both qualitative and quantitative information on operation and performance of ejectors (use NIST database for R141b) .
- [68] R134a, R152a, R290, R600, R717 **2004.** *Selvaraju, and. Mani.* First work to propose a non-constant formulation of  $\eta_{mix}$ , related to friction loss in the constant area section.
- [69] R123 **2005.** *Yapici and Ersoy,* Local model for optimization of CAM ejector.
- [65] R134a, 152a, R142b **2006.** *Yu et al.* Best examples of global approach: provide a very syntactical formulation for  $\omega$  starting from balance equations, boundary conditions and assumptions (see equation 3.14).
- [70] R142b **2007.** *Yu et al.* Along with [65] is an important example of global approach: provide a very syntactical formulation for  $\omega$  starting from balance equations, boundary conditions and assumptions (see equation 3.14)
- [75] R141b, R11 **2007.** *Zhu et al.* Develops model that is simpler than most 1D models; takes into account radial velocity variation within mixing chamber from oblique shock
- [50] Methane, Air **2007.** *Zhu et al.* Uses model from Zhu et al. [75]; application in SOFC anodic recirculation with ejector operating in double-choking condition.
- [76] Methane, Air **2008.** *Zhu et al.* Uses model from Zhu et al. [75]; SOFC application in anodic recirculation, with ejector operating in: (i) back-flow, (ii) choking and (iii) double-choking condition [76]
- [78]. Validated with R141b **2008.** *Zhu et al.* Simplified ejector model for control and optimization.
- [83] R134a **2009.** *Guo and Shen.* Model similar to Huang et al. [27]; gas property derived from NIST REFPROP.
- [77] R141b, R11, steam **2009.** *Zhu et al.* Uses model from Zhu et al. [75]; application in refrigeration cycle with or without steam condensation during flow expansion, with ejector operating in double-choking condition
- [71] R141b, Steam,  $CO_2$  **2012.** *Cardemil and Colle,* The real gas equations of state are used to consider either dry or wet vapor working fluids

[72]	$CO_2$	<b>2012.</b> <i>Liu et al.</i> First model that <u>uses variable efficiencies</u> estimated using empirical correlations, instead of being assumed to be constant value (two-phase flow ejector). <b>Experimental.</b>
------	--------	--

Table 2-1 Relevant studies about thermodynamic model for supersonic single phase ejectors

### 2.2.2 Subsonic ejector modeling: a recent theme of research

Subsonic ejector modeling is a recent theme of research and is linked to the growing interest in PEM fuel cell (section 1.3.2.2): the task of these models is to provide global parameters, such as outlet conditions or mass flow rate ( $\dot{m}_p$ ,  $\dot{m}_s$ ) flowing through the ejectors, for a given set of boundary conditions.

In this section, the models referring to literature presented in section 1.3.2.2 will be described; they all use different sets of equations to calculate  $\dot{m}_p$  and  $\dot{m}_s$  considering as working fluid  $H_2$  and  $H_2O$  (PEM anode recirculating stream):

- first models proposed in literature ( [52], [53] and [54]) used convergent nozzle equations;
- Zhu and Li [25] proposed a model based on the same approach of Zhu et al [75], providing a more advanced model, which can simulate both a sub-critical and a critical ejector operating condition. This model has some constants that were calibrated using a CFD model;
- He et al. [55] proposed an improvement of [25], providing a model that is able to simulate every operating condition of the ejector (back-flow, sub-critical and critical).

**2006: 1D model proposed by Bao et al.** [52]. Bao et al. in [52] used nozzle flow equations to calculate  $\dot{m}_p$ ; naming upstream pressure  $p_{p,0}$  and downstream pressure  $p_{s,0}$ , flow characteristic is divided into two regions by the critical pressure ratio: sonic ( $p_{p,0} \geq \frac{p_{s,0}}{\nu_{cr}}$ ) and subsonic flow ( $p_{p,0} < \frac{p_{s,0}}{\nu_{cr}}$ ). Using isentropic flow relations and energy equation we can obtain:

- for sonic flow:

$$\dot{m}_p = \sqrt{\eta_p} \frac{p_p A_t}{\sqrt{R_p T_p}} \sqrt{\gamma \left( \frac{2}{\gamma + 1} \right)^{\frac{\gamma+1}{\gamma-1}}} \quad (3.21)$$

- for subsonic flow



$$\dot{m}_p = \frac{p_p A_t}{\sqrt{R_p T_p}} \sqrt{2 \left[ \frac{\left(\frac{p_s}{p_p}\right)^{\frac{2}{\gamma}} - \left(\frac{p_s}{p_p}\right)^{\frac{1+\gamma}{\gamma}}}{(\gamma-1)} \right]} \sqrt{\eta_p} \quad (3.22)$$

This model is able to take in consideration both critical and subcritical ejector operating condition (section 1.2.2).

**2006: 1D model proposed by Karnik et Al [53].** Karnik et al. [53] studied a subsonic ejector using a 1D-CAM model:

- primary flow  $\dot{m}_p$  through the ejector is obtained using the equation for choked flow through a nozzle:

$$\dot{m}_p = \frac{p_p A_t}{\sqrt{R_p T_p}} \sqrt{\gamma \left(\frac{2}{\gamma+1}\right)^{\frac{\gamma+1}{\gamma-1}}} \sqrt{\eta_p} \quad (3.23)$$

- secondary flow  $\dot{m}_s$  depends upon the primary and secondary pressures :

$$\dot{m}_s = \begin{cases} \frac{p_s (A_{mix} - A_{py})}{\sqrt{R_s T_s}} \sqrt{\gamma \left(\frac{2}{\gamma+1}\right)^{\frac{\gamma+1}{\gamma-1}}} \sqrt{\eta_s}, & A_{py} > A_{mix} \\ 0 & \text{otherwise} \end{cases} \quad (3.24)$$

In these relations:

1.  $A_t$ : nozzle throat;
2.  $\eta_p$ : efficiency of the primary nozzle;
3.  $\eta_s$ : efficiency for the secondary flow path (suction chamber);
4.  $A_{mix}$ : area of mixing tube;
5.  $A_{py}$ : primary flow aerodynamic section determined supposing isentropic flow:

$$A_{py} = \frac{A_t}{\eta_{exp} M_{py}} \left[ \frac{2}{\gamma-1} \left(1 + \frac{\gamma-1}{2}\right) M_{py}^2 \right]^{\frac{\gamma+1}{2(\gamma-1)}} \quad (3.25)$$

Where  $\eta_{exp}$ : is the coefficient that accounts for loss of primary flow affected at the boundary and  $M_{py}$  is the Mach number of primary flow at the section where the secondary flow is choked:

$$M_{py}^2 = \left[ \left(\frac{p_p}{p_s}\right)^{\frac{\gamma-1}{\gamma}} \left(\frac{\gamma+1}{2}\right) - 1 \right] \frac{2}{\gamma-1} \quad (3.26)$$

Obviously this model is unable to take in consideration subcritical ejector operating condition (section 1.2.2).

**2008: 1D model proposed by He et al.** [54]. He et al. in [54] used a 1D-CAP to build a model for a subsonic ejector with both primary and secondary streams operating in choking condition:

- mass flow rate of the primary steam  $\dot{m}_p$  :

$$\dot{m}_p = \frac{p_p A_t}{\sqrt{R_p T_p}} \sqrt{\gamma \left( \frac{2}{\gamma + 1} \right)^{\frac{\gamma+1}{\gamma-1}}} \sqrt{\eta_p} \quad (3.27)$$

- mass flow rate of the secondary steam  $\dot{m}_s$ :

$$\dot{m}_s = \frac{p_s A_{sy}}{\sqrt{R_s T_s}} \sqrt{\gamma \left( \frac{2}{\gamma + 1} \right)^{\frac{\gamma+1}{\gamma-1}}} \sqrt{\eta_s} \quad (3.28)$$

In these relations:

1.  $A_t$ : nozzle throat;
2.  $\eta_p$ : efficiency of the primary nozzle;
6.  $\eta_s$ : efficiency for the secondary flow path (suction chamber);
3.  $A_{mix}$ : area of mixing tube;
4.  $A_{sy}$ : the hypothetical throat area equal to the secondary flow section area where the flow is choked:

$$A_{sy} = \begin{cases} A_{mix} - A_{py}, & \text{if } A_{py} < A_{mix} \\ 0, & \text{if } A_{py} \geq A_{mix} \end{cases} \quad (3.29)$$

Where  $A_{py}$  is the primary flow section area determined by:

$$A_{py} = \frac{A_t}{\eta_{exp} M_{py}} \left[ \frac{2}{\gamma - 1} \left( 1 + \frac{\gamma - 1}{2} \right) M_{py}^2 \right]^{\frac{\gamma+1}{2(\gamma-1)}} \quad (3.30)$$

Where  $\eta_{exp}$ : is the coefficient that accounts for loss of primary flow affected at the boundary and  $M_{py}$  is the Mach number of primary flow at the section where the secondary flow is choked:

$$M_{py}^2 = \left[ \left( \frac{p_p}{p_s} \right)^{\frac{\gamma-1}{\gamma}} \left( \frac{\gamma + 1}{2} \right) - 1 \right] \frac{2}{\gamma - 1} \quad (3.31)$$

Obviously this model is unable to take in consideration subcritical ejector operating condition (section 1.2.2).

**2009: 1D\2D model proposed by Zhu and Li et al.** [25]. Li and Zhu in [25] presented a 1D\2D model that can simulate both a sub-critical (primary flow is subsonic) and a critical (primary flow is choked) operating condition; due to the importance of this model, a detailed description has to be provided.

The following assumptions are made in developing the model:

1. the primary flow is treated as the ideal gas;
2. the primary and secondary flow velocity is uniform in the radial direction inside the ejector;
3. the velocity of the secondary flow inside the ejector is non-uniformly distributed in the radial direction;
4. pressure and temperature of both the primary and the secondary flows are uniformly distributed in the radial direction of ejector;
5. the isentropic relations hold in calculating friction losses using isentropic efficiencies.

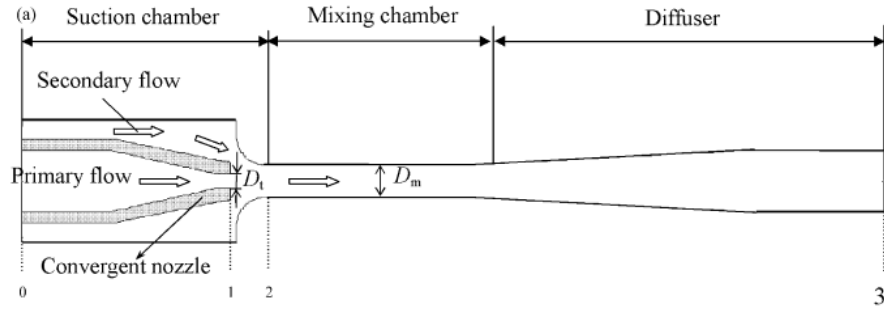


Figure 2-3 Ejector studied by Zhu et al. [25]

#### Primary flow.

The flow through the convergent nozzle (between inlet and throat) is divided into two different regions: subsonic and sonic flow: due to the absence of a divergent part, the flow can only reach sonic flow condition when the pressure ratio is greater than the critical value  $v_{cr} = \left(\frac{2}{\gamma+1}\right)^{\frac{\gamma}{\gamma-1}}$ .

Using isentropic flow relations and energy equation we can obtain (i) Mach number of nozzle throat  $M_t$  of the primary flow and (ii) nozzle geometry  $A_t$ :

- sonic flow ( $p_{p,0} \geq \frac{p_{s,0}}{v_{cr}}$ ):

$$\begin{cases} \dot{m}_p = \frac{p_p A_t}{\sqrt{R_p T_p}} \sqrt{\gamma \left(\frac{2}{\gamma+1}\right)^{\frac{\gamma+1}{\gamma-1}}} \sqrt{\eta_p} \\ M_t = 1 \end{cases} \quad (3.32)$$

- subsonic flow ( $p_{p,0} < \frac{p_{s,0}}{v_{cr}}$ ):

$$\left\{ \begin{array}{l} \dot{m}_p = \frac{p_p A_t}{\sqrt{R_p T_p}} \sqrt{2 \frac{\left[ \left( \frac{p_s}{p_p} \right)^{\frac{2}{\gamma}} - \left( \frac{p_s}{p_p} \right)^{\frac{1+\gamma}{\gamma}} \right]}{(\gamma - 1)}} \sqrt{\eta_p} \\ M_t = \sqrt{2 \frac{\left[ 1 - \left( \frac{p_s}{p_p} \right)^{\frac{\gamma-1}{\gamma}} \right]}{(\gamma - 1)}} \end{array} \right. \quad (3.33)$$

Where  $\eta_p$  is the isentropic coefficient taking into account the flow friction loss.

Primary flow expands fully in the suction chamber: the pressure of the expansion flow can be represented by the secondary flow pressure  $p_s$ . Using isentropic flow and energy balance laws for the primary flow from zone 1 to zone 2 can be determined:

1. Mach number:

$$\frac{p_p}{p_s} = \left[ 1 + \frac{1}{2}(\gamma - 1)M_{p,2}^2 \right]^{\frac{\gamma}{\gamma-1}} \quad (3.29)$$

2. temperature:

$$\frac{T_p}{T_{p,2}} = 1 + \frac{1}{2}(\gamma - 1)M_{p,2}^2 \quad (3.30)$$

3. velocity:

$$v_{p,2} = M_{p,2} \sqrt{\gamma R_p T_{p,2}} \quad (3.31)$$

4. aerodynamic throat:

$$\frac{\xi_{exp} D_{p,2}}{D_t} = \left[ \frac{2 + (\gamma - 1)M_{p,2}^2}{2 + (\gamma - 1)M_t^2} \right]^{\frac{\gamma+1}{4(\gamma-1)}} \left( \frac{M_t}{M_{p,2}} \right)^{0.5} \quad (3.32)$$

Where  $\xi_{exp}$  is a coefficient accounting for the frictional loss due to the mixing process.

#### *Secondary flow.*

Ejector performance is significantly affected by the flow characteristics in zone 2, where a mixing layer separates primary and secondary flows (which has a non-linear velocity distribution due to the turbulent flow and fluid viscosity as shown in Figure 2-4).

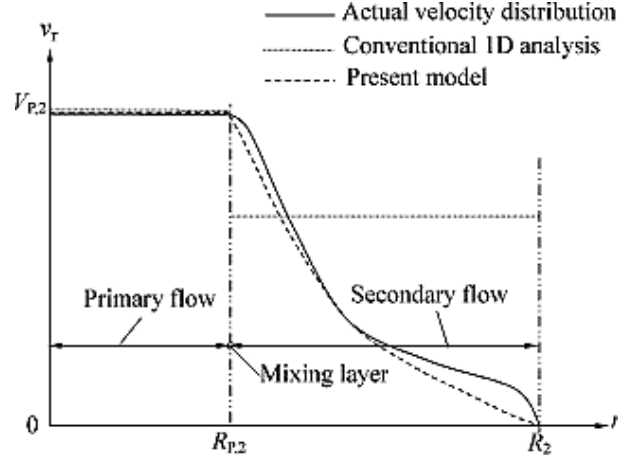


Figure 2-4 Radial velocity distribution in zone 2; taken from [25]

While in conventional 1D analysis, both velocities of the primary flow and secondary flow are treated uniform in the radial direction in [25] is proposed a 2D function:

$$v_r = \begin{cases} v_{p,2}, & \text{se } 0 \leq r \leq r_{p,2} \\ v_{p,2} \left( \frac{r_2 - r}{r_2 - r_{p,2}} \right)^{n_v}, & \text{se } r_{p,2} < r \leq r_2 \end{cases} \quad (3.33)$$

Based on this 2D velocity function and defining  $\bar{\rho}_s = p_s/R_s T_s$  the average density of the secondary, mean mass flow rate of secondary flow at Section 2 is:

$$\begin{aligned} \dot{m}_s &= \int_{r_{p,2}}^{r_2} \bar{\rho}_s v_r dA = \frac{2\pi v_{p,2} \bar{\rho}_s}{(r_2 - r_{p,2})^{n_v}} \int_{r_{p,2}}^{r_2} (r_2 - r)^{n_v} r dr = \\ &= \frac{2\pi \bar{\rho}_s v_{p,2} (r_2 - r_{p,2}) (r_2 + r_{p,2} + n_v r_{p,2})}{(n_v + 1)(n_v + 2)} \end{aligned} \quad (3.34)$$

Remembering that  $v_{p,2} = \dot{m}_s / \rho_s A_{s,2}$  and  $A_{s,2} = \pi(r_2^2 - r_{p,2}^2)$ , mean velocity of secondary flow can be evaluated as:

$$v_{s,2} = \frac{2v_{p,2}(r_2 + r_{p,2} + n_v r_{p,2})}{A_{s,2}(n_v + 1)(n_v + 2)(r_2 + r_{p,2})} \quad (3.35)$$

The velocity of the secondary flow is modeled by a 2D exponential function: this improvement led to a model which is capable of predicting the ejector performance within less uncertainties compared to the conventional 1D analysis [53], [52], [54]. Moreover, this treatment of the secondary flow velocity makes this model simpler than the conventional CAM or CAP theory: the model need only one algebraic equation for calculating  $\dot{m}_s$ .

At last an energy balance is written, under the hypothesis of ideal gas:

$$\begin{aligned} \sum_i \dot{m}_p c_{p,p} T_p + \sum_i \dot{m}_s c_{p,s} T_s \\ = \sum_i (\dot{m}_s + \dot{m}_p) c_{p,3} T_3 + E_{loss} \end{aligned} \quad (3.36)$$

Where  $E_{loss} \approx \frac{1}{2}(1 - \eta_p)\dot{m}_p v_{p,2}^2 + \frac{1}{2}(1 - \eta_s)\dot{m}_s v_{s,2}^2$ .

$n_v$

$n_v$  is the exponent of the velocity function and is very important, because it involves the pattern of the concave velocity distribution curve. Its value is not a constant, but is influenced by the ejector geometries and working conditions; in order to determine its value [25] propose a numerical method based on CFD technique and on regression, which bring to the following expression:

$$n_v = A_1 e^{(\beta_p/0.05)} + A_2 \beta_D + A_3 \quad (3.37)$$

Where  $\beta_p = p_s^{0.8}/p_p^{1.1}$  e  $\beta_D = D_m/D_t$  e  $A_1, A_2$  e  $A_3$  are 3 parameters which can be evaluated by CFD analysis ; in fact above expression can be re-written as:

$$\psi \chi = \Gamma + \Delta \quad (3.38)$$

Where:

$$\chi = \begin{bmatrix} A_1 \\ A_2 \\ A_3 \end{bmatrix}; \Gamma = \begin{bmatrix} n_v^1 \\ n_v^2 \\ \cdot \\ \cdot \\ n_v^n \end{bmatrix}; \psi = \begin{bmatrix} e^{(\beta_p^1/0.05)} & \beta_D^1 & 1 \\ e^{(\beta_p^2/0.05)} & \beta_D^2 & 1 \\ \cdot & \cdot & \cdot \\ \cdot & \cdot & \cdot \\ e^{(\beta_p^n/0.05)} & \beta_D^n & 1 \end{bmatrix}$$

Best evaluation  $X^*$  of  $X$  can be obtained using least square method:

$$X^* = (\psi^T \psi)^{-1} \psi^T \Gamma \quad (3.39)$$

**2011: 1D model proposed by He et al. [55].** Also in this study the flow through the convergent nozzle is divided into two different regions: subsonic and sonic flow: due to the absence of a divergent part, the flow can only reach sonic flow condition when the pressure ratio is greater than the critical value  $v_{cr} = \left(\frac{2}{\gamma+1}\right)^{\frac{\gamma}{\gamma-1}}$ .

$$\begin{cases} \dot{m}_p = \frac{p_p A_t}{\sqrt{R_p T_p}} \sqrt{\gamma \left(\frac{2}{\gamma+1}\right)^{\frac{\gamma+1}{\gamma-1}}} \sqrt{\eta_p}, & \text{if } p_{p,0} \geq \frac{p_{s,0}}{v_{cr}} \\ \dot{m}_p = \frac{p_p A_t}{\sqrt{R_p T_p}} \sqrt{2 \frac{\left[\left(\frac{p_s}{p_p}\right)^{\frac{2}{\gamma}} - \left(\frac{p_s}{p_p}\right)^{\frac{1+\gamma}{\gamma}}\right]}{(\gamma-1)}} \sqrt{\eta_p}, & \text{if } p_{p,0} < \frac{p_{s,0}}{v_{cr}} \end{cases} \quad (3.40)$$

An exponential function along the direction of the radius is used to describe the velocity distribution at mixing section (zone 2-2, Figure 2-3), using the same approach proposed by Zhu and Li et al. [25] and described in section 2.2.2.5.

Hence,  $\dot{m}_s$  in critical mode ( $\dot{m}_s^{critical}$ ) is:

$$\dot{m}_s^{critical} = \frac{2\pi \bar{\rho}_s v_{p,2} (r_2 - r_{p,2}) (r_2 + r_{p,2} + n_v r_{p,2})}{(n_v + 1)(n_v + 2)} \quad (3.41)$$

Remembering subsonic ejectors operating conditions (Figure 2-5):

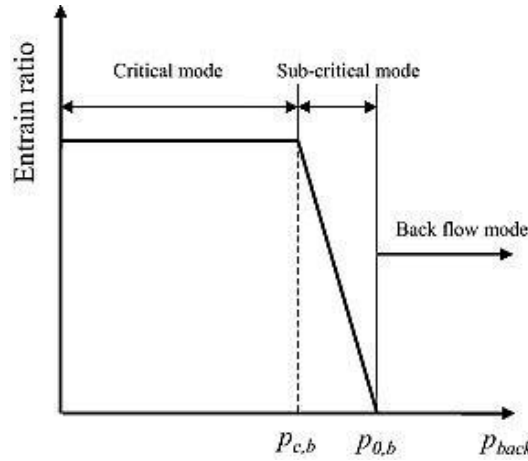


Figure 2-5 Subsonic ejector operating condition; taken from [55]

When the backpressure becomes  $p_{o,b}$ ,  $\dot{m}_s = 0$  (Figure 2-5), hence, the real mass flow rate of the secondary flow depending on the working modes or back pressure is derived from a linear interpolation:

$$\dot{m}_s = \begin{cases} 0, & \text{if } p \geq p_{o,b} \\ \dot{m}_s^{critical} \frac{p_{o,b} - p}{p_{o,b} - p_{c,b}}, & \text{if } p_{c,b} < p < p_{o,b} \\ \dot{m}_s^{critical}, & \text{if } p_{p,0} \leq p_{c,b} \end{cases} \quad (3.42)$$

This model is able to take in consideration every operating condition: back-flow, sub-critical or critical (section 1.2.2).

**Overview of existing models for subsonic ejectors.** Table 2-2 provides an overview of studies presented above.

Reference	Working fluid	Year, authors and work contributions
[52]	$H_2, H_2O$	<b>2006.</b> <i>Bao et al.</i> Used nozzle flow equations to calculate primary and secondary mass flow rate. This model that can simulate both a sub-critical and a critical operating condition
[53]	$H_2, H_2O$	<b>2006.</b> <i>Karnik et al.</i> 1D-CAM model for subsonic ejector. This model can simulate only critical operating condition.
[54]	$H_2, H_2O$	<b>2008.</b> <i>He et al.</i> 1D-CAP model for a subsonic ejector with both primary and secondary streams operating in choking condition. This model can simulate only critical operating condition.
[25]	$H_2, H_2O$	<b>2009.</b> <i>Zhu and Li.</i> 1D\2D model that can simulate both a sub-critical and a critical operating condition. CFD analysis to calibrate model constants.
[55]	$H_2, H_2O$	<b>2011.</b> <i>He et al.</i> Improvement of the model proposed by Zhu and Li [25]: this model that can simulate every operating condition (back-flow, sub-critical or critical)

Table 2-2 Relevant studies about thermodynamic model for subsonic single phase ejectors

### 2.2.3 Limitations of thermodynamic models

Section 2.2.1 and 2.2.2 presented progression in the development of thermodynamic models, but, although remarkable advancement in analytical modeling, that approach has some limitations [23], [22]:

1. model structure;
2. global approach;
3. local flow behavior;
4. coefficients used.

**Model structure.** Classical models structure is based on Keenan model [28]: ejector is divided in component (motive nozzle, suction nozzle, mixing section, and diffuser) and mass, energy, and momentum balances are solved on each section taking into account assumption (such as Bagster and Munday theory [29]). Although this approach is a good start, all assumptions (ideal gas, normal shock and isentropic flow) make it



inaccurate for a wide variety of applications. As a result, following studies (Table 2-1) have worked to improve this approach in three ways:

1. including loss coefficients to account for frictional and mixing losses;
2. removing the ideal gas assumption;
3. considering other fluids than air.

Despite efforts to improve upon the Keenan model, a large degree of uncertainty and error in results still remains: recently Zhu et al. [75] attempted to change classical approach with SCM and Liu et al. [72] proposed a model with variable isentropic efficiencies.

**Global approach.** Thermodynamic models are typically focused on global, rather than local, ejector performance: the majority of the analytical studies are concerned with the ability to predict global performance and they validate their results based on overall external aspects (such as  $\omega$  or ejector inlet/outlet conditions). Only the works of Zhu et al. [75], [50], [76], [77] attempted to predict local quantities (assuming radial velocity profile inside the mixing section).

**Local flow behavior.** Part of degree of uncertainty and error in thermodynamic model results is due to lack of understanding of the underlying flow phenomena: ejector performance is highly influenced by local phenomena and flow behavior (shock waves, interactions between shock waves and boundary layers, adverse pressure gradients, flow recirculation and flow separations). Thermodynamic models are unable to considerate those effects.

**Coefficients used.** Most sources of losses have been aggregated into empirical coefficients that are specific to the fluid and geometry. Some studies have calculated a few of these losses directly, but it appears that the complexity of flow, especially inside the mixing section, is too complex to be modeled completely and accurately with thermodynamic models using constant efficiencies (see section 2.3 for further details on efficiencies).

## 2.3 Ejector efficiencies and their role in thermodynamic modeling

In this sections is provided a review on ejector local and global efficiency.

### 2.3.1 Ejector global efficiency.

Mitchel and London defined a global parameter to describe ejectors [84], defined as the ratio between recovery of secondary flow pressure and primary flow kinetic energy:

$$\eta_{eject} = \frac{\dot{m}_s(p_{exit} - p_s)/\rho_s}{\dot{m}_p(v_{p,2}^2/2)} = \omega \frac{(p_{exit} - p_s)/\rho_s}{(v_{p,2}^2/2)} \quad (3.43)$$

Taking into account that part of the kinetic energy of the primary flow is recovered in diffuser:

$$\eta_{eject} = \omega \frac{(p_{exit} - p_s)/\rho_s}{[(v_{p,2}^2/2) - (p_{exit} - p_p)/\rho_p]} \quad (3.44)$$

### 2.3.2 Ejector efficiencies

In 1D thermodynamic models friction losses and irreversibility associated with the primary nozzle, suction, mixing and diffuser, are accounted by using efficiencies; typical approach is to use constant efficiencies (one of the few exception is given by Liu et al. [72] that use empirical correlation for efficiencies<sup>4</sup>); that may be (Table 2-6):

- selected arbitrarily;
- taken from literature;
- selected such that the experimentally measured performance data would fit best to the predicted model values;
- determined using a CFD model [73], [63].

It's important to remark that the validity of thermodynamic models is highly dependent on the value of efficiency constants [62]; in the following part are discussed how efficiencies are defined and evaluated in literature.

**A remark on efficiencies calculation.** Nozzles and diffuser efficiencies are typically evaluated using isentropic relations. In order to calculate the nozzle/suction/diffuser outlet isentropic enthalpy, the entropy at the nozzle inlet must be known. Assuming an ideal gas, the entropy can be easily determined from the inlet pressure and temperature: if the pressure at the nozzle exit is known, the isentropic enthalpy is obtained.

---

<sup>4</sup> Liu et al. [72] determined efficiencies using a numerical ejector model and external ejector measurements of mass flow rates, pressures and temperatures in the test runs of a controllable ejector [73]: those correlations are to be used in following boundaries:  $8.0 \text{ MPa} < P_p < 14.0 \text{ MPa}$  ;  $2.5 \text{ MPa} < P_s < 5.0 \text{ MPa}$  ;  $1.8 \text{ mm} < D_t < 2.7 \text{ mm}$ ;  $D_{mix} = 4 \text{ mm}$ . It's important to remark that Liu et al. [72] efficiencies are related to a two phase flow ejector.

### 2.3.2.1 Primary Nozzle

$\eta_p$  is determined by comparing simulated enthalpies to an isentropic process:

$$\eta_p = \frac{h_{p,in} - h_{p,nozzle,exit}}{h_{p,in} - h_{p,nozzle,exit,is}} \quad (3.45)$$

Liu et al. [72] uses an empirical correlation developed based Liu and Groll work [73]:

$$\begin{aligned} \eta_p = & -36.137 - 4.160(p_p/p_s) + 1.161(p_p/p_s)^2 \\ & - 0.106(p_p/p_s)^3 + 212.320(D_{mix}/D_t) \\ & - 355.359(D_{mix}/D_t)^2 + 196.035(D_{mix}/D_t)^3 \end{aligned} \quad (3.46)$$

Liu et al. [73] found that  $\eta_p$  decreases as the ejector throat diameter decreases, which is also remarked by Varga et al. [85] that, using CFD, obtained ejector downstream conditions have almost no effect on primary nozzle efficiency and there was only a small increase in  $\eta_p$  with increasing nozzle diameter (0.92 ÷ 0.95).

Aly et al. [62], pointed out that a 20% change in the nozzle efficiency (from 100% to 80%) affects the entertainment ratio  $\omega$  by 25%.

### 2.3.2.2 Suction nozzle

$\eta_s$  is determined by comparing simulated enthalpies to an isentropic process:

$$\eta_s = \frac{h_{s,in} - h_{s,nozzle,exit}}{h_{s,in} - h_{s,nozzle,exit,is}} \quad (3.47)$$

Liu et al. [72] uses an empirical correlation developed based Liu and Groll work [73]:

$$\begin{aligned} \eta_s = & -3173.171 - 934.12(p_p/p_s) + 314.471(p_p/p_s)^2 \\ & + 79.521(p_p/p_s)^3 - 12.222(p_p/p_s)^4 \\ & + 0.814(p_p/p_s)^5 + 694222.1\omega \\ & - 2956145\omega^2 + 7950453\omega^3 \\ & - 114327270\omega^4 + 6689155\omega^5 \\ & - 649905.1Z + 2647000Z^2 - 6885025Z^3 \\ & + 9627131Z^4 - 5490126Z^5 \end{aligned} \quad (3.48)$$

Where  $Z = (p_p/p_s)^{0.02}$ .

Varga et al. [85], using CFD, found  $\eta_s$  to be constant ( $\approx 0.9$ ) when the ejector was operating in critical mode. However, when operating in subcritical mode, there was a sudden drop in its value due to separation of the fluid flow from the ejector wall near

the primary nozzle exit plane. This suction efficiency trend was also found by Liu et al. [73], who concluded that the suction nozzle efficiency is affected by the suction nozzle inlet pressure, ejector throat area, and motive nozzle exit position.

### 2.3.2.3 Aerodynamic throat

Munday and Bagster [29] modified the CPM model [28] using the assumption that primary flow creates a converging duct for secondary flow, creating an aerodynamic throat; this is the typical approach at the basis of ejector modeling, but there is some diversity in the literature on how aerodynamic throat is taken into account:

- Zhu et al. [75] defined an isentropic expansion efficiency due to frictional losses in the mixing chamber as:

$$\eta_{exp} = \left[ \frac{d'_{p,chocking}}{d_{p,chocking}} \right]^2 \quad (3.49)$$

Where  $d_{p,chocking}$  is the diameter of the primary flow at the cross section where the secondary fluid gets choaked and  $d'_{p,chocking}$  is the value considering an ideal case:

$$d'_{p,chocking} = \left[ \frac{2 + (\gamma - 1)M_{p,chocking}^2}{2 + (\gamma - 1)M_{nozzl\ exit}^2} \right]^{\frac{\gamma+1}{4(\gamma-1)}} \sqrt{\frac{M_{nozzle,exit}}{M_{p,chocking}} d_{nozzle,exit}} \quad (3.50)$$

Similar approach is used for a subsonic ejector too in Zhu and Li [25].

In [75]  $\eta_{exp} = \eta_p \eta_s$ , whereas, Zhu et al [77] demonstrated that and is  $\eta_{exp}$  is independent of the ejector geometries proposed a relation, by comparing experimental data with model results:

$$\eta_{exp} = A + Bp_r \quad (3.51)$$

Where  $p_r = p_{s,0}/p_{p,0}$  and A, B depends on working fluid:

Coefficient	R141b	R11	Steam
A	0.87	0.67	0.77
B	0.6	0.9	0.1

Table 2-3 Value of parameters for  $\eta_{exp}$  [77]

- Cardemil and Colle [71], proposed following relations for  $\eta_{exp}$ :

$$\eta_{exp} = \sqrt{\frac{A_{p,ideal}}{A_{p,real}}} \quad (3.52)$$

Cardemil and Colle [71] also provided a relation for  $\psi_{exp}$ , by comparing experimental data with model results:

$$\eta_{exp} = \frac{A}{p_r A_r} + B \quad (3.53)$$

Where  $p_r = p_{s,0}/p_{p,0}$ ,  $A_r = D_{mix}/D_t$  and A, B depends on working fluid:

Coefficient	R141b	Steam	CO <sub>2</sub>
A	0.046	0.0265	0.374
B	0.764	0.847	0.5209

Table 2-4 Value of parameters for  $\eta_{exp}$  [71]

### 2.3.2.4 Mixing chamber

In mixing chamber primary and secondary streams mix and the complexity of this phenomena is taken into account by using efficiencies; there is some diversity in the literature on how losses in the mixing chamber are taken into account:

- Tyagi and Murty [86] defined a mixing efficiency as an entrainment efficiency (the fraction of the kinetic energy in the motive fluid transmitted to the mixture):

$$\eta_{entr} = \frac{(\dot{m}_s + \dot{m}_p)(h_{out,diff} + h_{out,mix})}{\dot{m}_p(h_p + h_{p,in,mix})} \quad (3.54)$$

- many works (such as [30], [61], [27], [62] and [71]) defined mixing efficiency as a momentum transfer efficiency:

$$\eta_{mix} = \frac{(\dot{m}_s + \dot{m}_p)v_{mix,out}}{\dot{m}_p v_{p,in,mix} + \dot{m}_s v_{s,in,mix}} \quad (3.55)$$

- Aly et al. [62] and Korres et al. [87] defined mixing efficiency as a momentum transfer efficiency, assuming negligible velocity of secondary stream at suction nozzle exit:

$$\eta_{mix} = \frac{(\dot{m}_s + \dot{m}_p)v_{mix,out}}{\dot{m}_p v_{p,in,mix}} \quad (3.56)$$

- Yu et al. [65] considered that losses in the mixing chamber can be written as:

$$\eta_{mix} = \left[ \frac{(1 + \omega)v_{mix,out}}{v_{in,mixing}} \right]^2 \quad (3.57)$$

- Ciguzu et al. [15] and Selvaraju et al. [68] defined mixing losses as a friction factor  $f_{mix}$  in the form of the Darcy–Weisbach equation: the former considered  $f_{mix}$  a constant value taken from the literature (Table 2-6) and the latter calculated its value according to an empirical correlation for smooth walls:

$$f_{mix} = 2 \frac{d_m}{L_m} \left[ \frac{v_{p,in,mix} + \omega v_{s,in,mix}}{(1 + \omega)v_{mix,out}} - (p_{p,in,mix} - p_{mix}) \frac{A_{mix}}{(\dot{m}_s + \dot{m}_p)v_{mix,out}} - 1 \right] \quad (3.58)$$

Is important remarking that “*this approach is inherently incorrect, since most irreversible losses along the mixing process are due to the viscous shear layer between primary and secondary flow and not to wall friction*” (cit. [63]).

- Liu et al. [72] uses an empirical correlation based on Liu and Groll work [73]:

$$\eta_{mix} = -6869.077 + 19308.18Z - 18089.31Z^2 + 5649.417Z^3 \quad (3.59)$$

Where  $Z = \left(\frac{D_t}{D_{mix}}\right)^{0.1} (1 + \omega)^{0.35}$ .

Liu et al. [72] pointed out that  $\eta_{mix}$  (defined as a momentum transfer efficiency) is not a constant and Varga et al. [63] demonstrate how mixing efficiencies are strictly related to geometry and operating conditions (Table 2-5: please note that outlet condition refers to a saturate condition, so imposing  $T_{out}$  is the same of imposing  $p_{out}$ ).

$\frac{D_{mix}}{D_t}$	$T_{out}$	$\omega$	$\eta_{entr}$ Eq. (3.54)	$\eta_{mix}$ Eq. (3.55)	$\eta_{mix}$ Eq. (3.56)	$\eta_{mix}$ Eq. (3.57)	$f_{mix}$ Eq. (3.58)	$\eta_{exp}$ Eq. (3.49)
13.5	30.0	0.23	0.70	0.90	0.93	0.87	0.05	0.82
	35.0	0.23	0.71	0.90	0.93	0.87	0.05	0.83
	36.0	0.23	0.73	0.91	0.94	0.89	0.04	0.85
	37.0	0.23	0.73	0.92	0.95	0.89	0.04	0.89
	39.0	0.23	0.77	0.93	0.96	0.92	0.04	0.87
	39.5	0.23	0.77	0.93	0.96	0.93	0.03	0.87
16.3	30.0	0.28	0.67	0.88	0.91	0.83	0.06	0.91
	35.0	0.28	0.70	0.90	0.93	0.87	0.05	0.90
20.9	30.0	0.36	0.66	0.89	0.93	0.86	0.06	0.88
	32.0	0.35	0.72	0.90	0.94	0.89	0.05	0.87
	33.0	0.07	0.83	0.87	0.87	0.75	0.07	0.86
26.4	25.0	0.46	0.65	0.90	0.95	0.91	0.05	0.93
	28.0	0.46	0.70	0.92	0.98	0.96	0.04	0.94
	30.0	0.05	0.77	0.82	0.82	0.67	0.10	0.66

Table 2-5 Mixing efficiencies; taken from [63]

Also Huang et al. [30] found that  $\eta_{mix}$  (equation 3.55) cannot be taken as constant; in their study they found out that it varies slightly with the ejector area ratio  $D_{mix}/D_t$  and, in order to fit the test results, an empirical relation is found:

$$\eta_{mix} \left( \frac{D_{mix}}{D_t} \right) = \begin{cases} 0.80, D_{mix}/D_t \geq 8.3 \\ 0.82, 6.9 < D_{mix}/D_t < 8.3 \\ 0.84, D_{mix}/D_t \leq 6.9 \end{cases} \quad (3.60)$$

In [30] is also proposed a relation for  $\eta_{mix}$  (equation 3.47):

$$\eta_{mix} = 1.087 - 0.02857 \frac{D_{mix}}{D_t} \quad (3.61)$$

At last Cardemil and Colle [71], proposed another relation for  $\eta_{mix}$  (equation 3.47), using as benchmark experimental data provided by Huang et al. [30]:

$$\eta_{mix} = 0.9788 - 0.0073 \frac{D_{mix}}{D_t} \quad (3.62)$$

### 2.3.2.5 Diffuser

$\eta_{diff}$  is determined by comparing simulated enthalpies to an isentropic process:

$$\eta_{diff} = \frac{h_{diff,out,is} - h_{diff,in}}{h_{diff,out} - h_{diff,in}} \quad (3.63)$$

Varga et al. [85] found that  $\eta_{diff}$  ranges from very low values ( $\sim 0.5$ ) to high values ( $\sim 0.89$ ): at low back pressures, the final shock wave happens in the diffuser (higher losses) and at higher back pressure, the shock wave moves back into the constant area chamber (the entire flow in the diffuser becomes subsonic and consequently losses are much smaller). It was also found that the  $\eta_{diff}$  increases with area ratio  $D_{mix}/D_t$ : at higher values (smaller  $D_t$ ) the kinetic energy of the primary stream is smaller and consequently the final shock wave occurs further upstream and also the mixed flow had smaller momentum (lower loss through the shock wave). Anyway, Aly et al. [62] found that a change in the nozzle efficiency slightly affects the entertainment ratio.

### 2.3.2.6 Ejector efficiencies used in literature

Table 2-6 lists ejector efficiencies used in thermodynamic model found in literature and previously examined; in Table 2-6 are also listed two-phase ejector (green ones) that encounter ejector efficiencies using same relationships seen above for single phase ejector (often single phase efficiency are used in two phase ejectors model [88]).

Year	Ref.	Evaluation modality	$\eta_p$	$\eta_s$	$\eta_{mix}$	$f_{mix}$	$\eta_{exp}$	$\eta_d$	
1985	[86]	Assumption	0.90		0.8			0.9	
1994	[89]	Assumed	0.90					0.75	
1995	[61]	Exp. data fit	0.85		0.95			0.85	
1995	[88]	Assumed	0.85	0.85				0.70	
1996	[90]	Assumption	0.85					0.85	
1998	[91]	Literature	0.90		1			0.85	
1999	[27]	Exp. data fit	0.95	0.85	0.8- 0.84				
1999	[30]	Assumption		0.85					
1999	[62]	Assumption	0.90		0.95			0.90	
1999	[17]	Literature	0.85					0.85	
2000	[67]	Assumption	0.80		0.80			0.80	
2001	[15]	Literature	0.95	0.95		0.03		0.85	
2002	[92]	Assumption	1		1			1	
2003	[93]	Assumed	0.70		0.80			0.80	
2004	[68]	Literature	0.95	0.95		f(Re)		0.85	
2004	[94]	Assumed	0.90	0.90				0.90	
2005	[69]	Assumption	0.85					0.85	
2005	[95]	Assumed	0.90	0.90				0.80	
2006	[65]	Assumption	0.85		0.95			0.85	
2006	[96]	Assumed	0.85	0.85				0.75	
2007	[75]	Literature	0.95 ÷ 0.9				0.765 ÷ 0.8075		
2007	[16]	Assumption	0.80	0.95	0.935			0.8	
2007	[50]	No info available on $\eta_p$ and $\eta_{exp}$ numerical value; ref. to [75]							
2007	[64]	Assumed	0.90		0.85			0.85	
2007	[97]	Literature	0.70					0.80	
2008	[98]	Literature	0.90		0.85			0.85	
2008	[73]	CFD	<i>Trend</i>	<i>Trend</i>	<i>Trend</i>				
2008	[76]	No info available on $\eta_p$ , $\eta_{mix}$ and $\eta_{exp}$ numerical value; ref. to [75]							
2009	[63]	CFD	<i>Trend</i>	<i>Trend</i>	<i>Trend</i>	<i>Trend</i>	<i>Trend</i>	<i>Trend</i>	
2009	[77]	Mixed	0.72 ÷ 0.9 (Assumed)				Exp. Data fit Eq. (3.51)		
2012	[72]	Literature	<b>First work to use correlation for <math>\eta_p</math>, <math>\eta_s</math> and <math>\eta_{mix}</math></b>						
			0.85		Assumed 0.77				
2012	[71]	Mixed	0.85 ÷ 0.95 (Literature)	0.95 (Lit.)	0.77 or data fit Eq (3.56)		Exp. Data fit. Eq (3.53)	0.95 (Lit.)	

Table 2-6 Ejector efficiencies: a brief overview



### 2.3.3 Role of the integrated thermodynamic/CFD model

The complexity of flow behavior, especially inside the mixing section, is too complex to be modeled completely and accurately using constant efficiencies in thermodynamic models: an integrated thermodynamic/CFD approach may solve this problem, using computational-fluid-dynamic to provide efficiency function with relate local phenomena to global parameters. Further details on CFD ejector modeling will be provided in next section.

## 2.4 CFD ejector modeling: story and current state-of-the-art

Ejector performance is highly influenced by local phenomena and flow behavior: shock waves, interactions between shock waves and boundary layers, adverse pressure gradients, flow recirculation and flow separations: the understanding of these phenomena and the consequences of them over performance will improve design in term of: (i) geometry, (ii) working fluid and (iii) operating condition [23].

Despite the progress of thermodynamic models [23], they only provide global information and are unable to correctly reproduce the flow physics locally along the ejector [99]: so if the purpose is to optimize ejector performance the main way is to change approach and to use a different tool, such CFD modeling: literature review will point out how Computational Fluid-Dynamics is becoming the usual tool to analyze and improve ejector performance by predicting both global operation and local flow structure.

### 2.4.1 A brief story on CFD ejector modeling

Early numerical simulations gave poor results due to problems in (i) numerical model and in (ii) mesh used.

In fact, first CFD simulations did not consider compressibility<sup>5</sup> [100] or turbulence [101], [102]; where turbulence was taken into account, only  $k - \varepsilon$  based models were used without experimental validations and no justification on the use of a particular model, except CPU cost, were carried out [100], [103], [104]. Moreover because of poor mesh resolution, early CFD models [100], [103], [104] failed in tracking shock wave and gave poor agreement with experimental results. Furthermore, even if some experimental comparison were performed they just dealt with global parameters and no

---

<sup>5</sup> Which is a severe error, because ejector operating conditions involve transonic flow.

local validations were performed (also today there is only limited information available on comparing models results to experimental data [105]).

In order to overcome these problems Bartosiewicz et al. [24] presented an important study about the importance of turbulence models validation and to the need of adopting a mesh suitable for the purposes: they both compare six different turbulence models performance and different kind of mesh. This validated model was used by Bartosiewicz et al in [106] to reproduce different operation modes of a supersonic ejector, ranging from on-design point to off design in order to capture the shock-boundary layer interaction, flow separation and recirculation at the primary flow nozzle exit and the diffuser.

The importance of validation pointed out by Bartosiewicz's et al. in [24] is so important that later studies devoted the larger part of their work to validation process, such as Sriveerakul et al. [106] , Hemid et al. [107] and Scott et al. [20]

After turbulence modeling and mesh suitability issues were handled, were presented studies aimed to take out another source of error: ideal gas hypothesis. Passage toward real gas have been presented with different work, such as the ones of Rusly et al. [108] and Bartosiewicz's et al. [106], [106]

When main problems of numerical models were solved, CFD has become more and more important in analyzing and improving ejector performance both:

1. linking global operation to local flow structure [109]
2. studying the influence of parameters on ejector performance; here are presented some among the most recent studies:
  - **2007.** Sriveerakul et al. in [110] investigated the influence of operating pressures, primary nozzle size, inlet diameter of the constant area section and throat length;
  - **2009.** Varga et al. in [85] investigated the influence of the area ratio between the nozzle and the constant area section, nozzle exit position and constant area length;
  - **2010.** Zhu et al. in [111] investigated the effects of primary nozzle exit position and mixing section converging angle;
  - **2010.** Ji et al in [112] investigated the effects of operating pressure and mixing section converging angle;
  - **2012.** Ogenortha et al. [113] investigated the possibility of using lobed nozzle in order to enhance pressure recovery;
  - **2012.** Yang et al. in [114] investigated the effects of different nozzle structure (conical, elliptical, square, rectangular and cross-shaped).
  - **2012.** Ruangtrakoon in [115] investigated the effect of the primary nozzle geometries;
  - **2012.** Varga et al [116] investigate the possibility of increasing ejector performance using a spindle to provide variable area ratio.

We conclude that if CFD model is validated [20], [24], [106], [107], [117] if a protocol for quality insurance [118] is used and if proper guidelines are followed both in building up mesh, and in setting up numerical and turbulence models (section 2.4.2) Computational Fluid-Dynamics can:

1. give a complete and correct view of the flow field [110];
2. investigate operating conditions [105], [106], [108], [110], [112];
3. be used as an efficient diagnosis tool of ejector analysis [99], [106]
4. investigate performance parameters closer to reality than thermodynamic models can predict [108], [106];
5. provide information for design and performance optimization [85], [106], [110], [111], [112], [113], [114], [115], [116].

Not only CFD has been proposed as concurrency to thermodynamic approach for evaluating ejector performance, but recently, in 2009, Varga et al. [63] proposed a study where CFD was used as a supporting tool for thermodynamic analysis by investigating ejector efficiencies; however up to nowadays no integrated thermodynamic/CFD model has been proposed

It's also important to underline that all of these studies were based on supersonic ejector and up to nowadays there are very few works on subsonic ejector and there is no work on turbulence models validation for that technology.

#### 2.4.2 Guidelines in CFD ejector modeling

From the above bibliographical review, guidelines in CFD ejector modeling comes out:

1. protocol to insure quality;
2. knowledge of flow phenomena;
3. mesh must be able to capture every phenomena;
4. knowledge of equations to be solved;
5. knowledge of phenomena complexity;
6. numerical methods must be suitable;
7. RANS turbulence models must be suitable;
8. provide CFD model validation.

**Protocol.** Computational Fluid-dynamics analysis has become a useful research and design instrument albeit with errors and uncertainties. Appropriate standards and protocols for increasing confidence and reliability need to be identified and applied, such as the one proposed by Colombo et al. [118] who proposed a methodological approach to qualify CFD, named  $Q^3$ , which is based on three interdependent, but related, dimensions: software reliability, user knowledge and process control.

**Knowledge of flow behavior.** Before starting a CFD study is very important to have a clear idea of flow fields to be simulated; this goal can be achieved by:

1. consulting previous study (see for example section 2.4.1 for state-of-the-art in single phase ejector modeling);
2. analyzing benchmark from literature for model validation:
  - *subsonic ejector*. NASA benchmark can be used [119];
  - *supersonic ejector*. Standard approach is to validate CFD model over global parameters obtained through experimental investigation during validation of thermodynamic models (Table 2-1). Some works along with CFD model presented an experimental facility used to validate their results [20], [105], [106], [107], [111], [112], [117] meanwhile other works used previous experimental data, such as measurement [120], [121] or flow visualization (see next point).
3. experimental flow visualization (Table 2-7): is very helpful for both the comprehension of complex flow phenomena and the validation of CFD models.
  - *diffraction methods (shadowgraph, schlieren methods)*. These techniques proved to be very effective to visualize the shock structures occurring in ejectors, but do not allow the visual distinction between two interacting flows;
  - *light scattering by small particles (Rayleigh and Mie scatterings)*. These methods use laser light sheet techniques and allow the visualization of a precise section of the flow (tomographic investigation).

Year	Ref.	Visualization method	Contribution
1958	[79]	Schlieren	Visualize the different flow patterns that occur in supersonic air ejectors and to propose a classification of the flow regimes in ejectors.
1976	[122]	Laser	Visualization of shock waves.
1991	[123]	Laser	Visualization of fluid mixing in supersonic flows.
1991	[124]	Schlieren	Investigation of performance characteristics of an under expanded multiple jet ejector.
1994	[125]	Laser	Investigation of two stream mixing.
1995	[126]	Laser	Visualization of interaction of two streams inside an air ejector operating in a mixed flow condition.
2001	[127]	Schlieren	Investigate the transient behavior of the startup of a supersonic flow from rest.
2001	[128]	Laser	Visualization of the mixing zone between two high-speed flows inside an ejector.
2001	[129]	Laser	Visualization of the processes of formation of drops .
2002	[121]	Laser	Evaluate and validate computational models.

2002	[120]	Laser	visualizing the mixing flow between.
2003	[130]	Schlieren	Study of flow field at the entrance of the mixing chamber .
2004	[131]	Laser	Visualization of choking phenomena of secondary flow and validation of CFD model.
2005	[132]	Schlieren	Study the transonic instability in the entrance part of the mixing chamber of an high-speed ejector.
2008	[133]	Schlieren	Investigation of structure and characteristics of the pseudo-shock waves.
2008	[134]	Laser	Evaluate and validate computational models.
2009	[135]	Laser	Visualization of the droplet condensation phenomenon and validation of a computational model.
2009	[136]	Shadowgraph and schlieren	Visualization of ejector flow behavior dependence from pressure boundary conditions.
2011	[21]	Laser	Presents flow imaging techniques based on laser sheet methods developed for investigating flow in ejectors remarking how these methods enables the visualization of specific phenomena (shock structure, flow instabilities, mixing process).

Table 2-7 Experimental flow visualization studies

**Mesh must be able to capture every phenomena.** After phenomena to be simulated have been understood, a mesh able to correctly represent the physics of the problem must be built up. This phase is very important and it can be achieved only through awareness of flow behavior: for the sake of clearness here is reported an example using an image, taken from Dvorak and Safarik's works [130], [132], representing a visualizations of shock wave phenomena at the exit of the nozzle in a supersonic ejector.

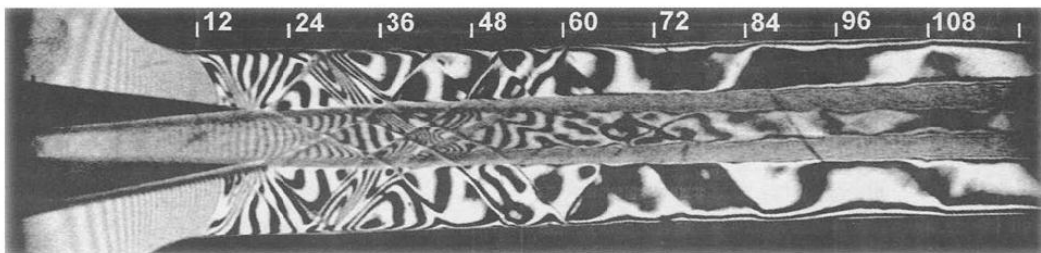


Figure 2-6 Ejector flow field; taken from [130]

These phenomena are characterized by strong gradient and an adequate mesh is to be used to correctly represent them (using higher cells density near shock wave or mesh adaptation algorithm based on gradient).

An improvement of mesh can provide an improvement in results accuracy: Bartosiewicz et al. [24] compared resulting axis static pressure along the ejector using 3 different mesh: (i) a MESH without adaptation and probe to obtain pressure data along

the axis is not modeled, (ii) a MESH without adaptation, but probe is modeled and (iii) a MESH with adaptation and probe is modeled: a mesh closer to reality and able to represent the physics of the problem gives better results.

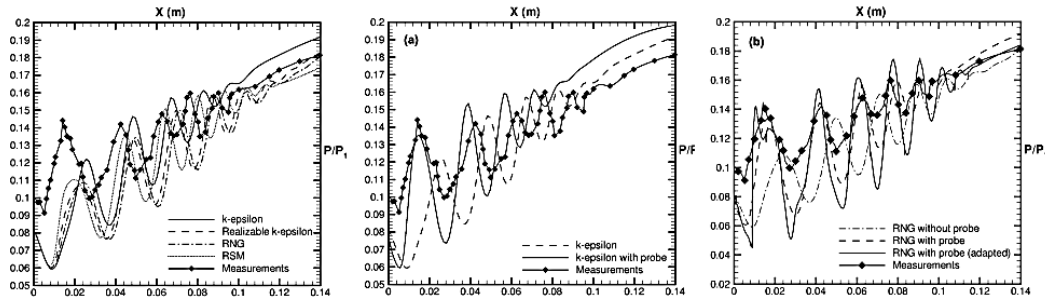


Figure 2-7 Effects of a mesh improvement; modified from [24]

**Knowledge of equations to be solved.** As stated in section 2.1.3 the solver have to deal with PDEs that take into consideration both compressibility and turbulence.

**Knowledge of phenomena complexity.** Flow field is characterized by shock-boundary layer interaction, flow separation, recirculation and adverse pressure gradient: those phenomena affects ejector performance. For example, back-flow condition is due to shock-boundary layer interaction [106]. These phenomena are also very difficult to simulate and numerical approaches are to be carefully chosen: for example [106] studied flow separation with different turbulence models:

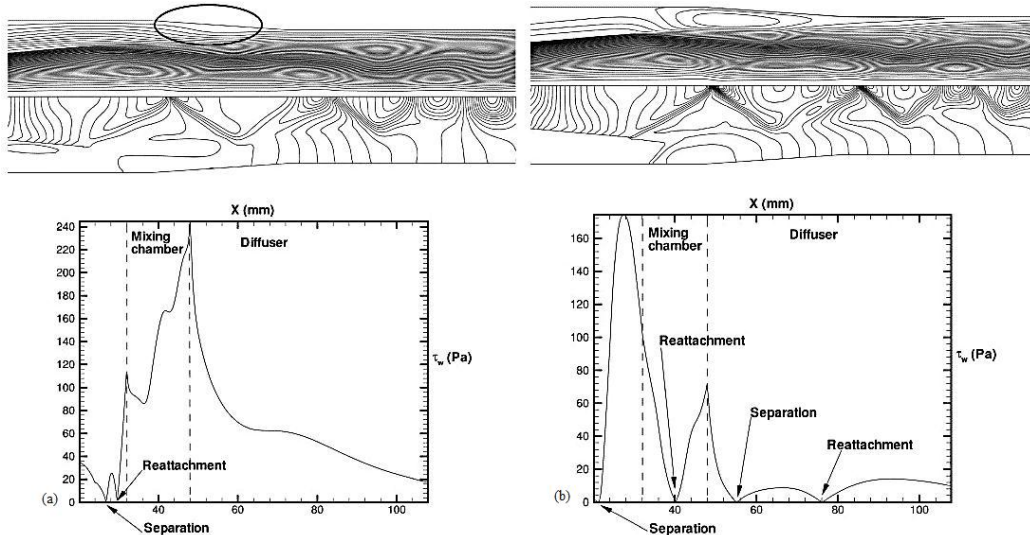


Figure 2-8 Turbulence modeling results comparison: (a)  $k - \epsilon$  and (b)  $k - \omega$  model

With reference to Figure 2-8, can be easily remarked out how different turbulence models give very different results:

- $k - \varepsilon$  model: predict a weak oblique shocks that appear from the primary nozzle lip, involving a slight flow separation and reattachment before the flow reaches constant area section of the mixing chamber;
- $k - \omega$  model: predict strong oblique shocks that induce an intense recirculation zone in the secondary stream; the flow undergoes another separation and reattachment farther downstream in the diffuser.

At this point is clear the importance of awareness flow field behavior both for comprehending phenomena inside ejector and use the correct numerical model.

**Numerical methods should be suitable.** Due to the presence of shock waves are to be chosen suitable numerical methods not affected by an excessive numerical diffusion must be chosen: second order schemes have to be used instead of first order ones [59] (which can be used in order to obtain preliminary flow fields).

**RANS turbulence models should be suitable.** In order to correctly represent every operating condition a suitable turbulence model is to be chosen. Bartosiewicz et al. in [24] and [106], tested and compared six RANS turbulence models<sup>6</sup> performance using as reference data the measurement of Desevaux e Aeschbacher [120] and Desevaux et al. [121] over a supersonic ejector.

This investigation has shown that the  $k - \varepsilon$  *RNG* and the  $k - \omega$  *SST* models were the best suited to predict the shock phase, strength, and the mean line of pressure recovery with the  $k - \omega$  *SST* model shown better performance in term of stream mixing,

However up to nowadays there is no validation over RANS turbulence models for the case of a subsonic ejector.

**Provide CFD model validation.** The whole CFD approach must be validated and not only turbulence model: is suggested to perform validation on local measurement (local flow behavior) instead of comparing global parameters.

---

<sup>6</sup> RANS turbulence models tested were:  $k - \varepsilon$ ,  $k - \varepsilon$  *RNG*,  $k - \varepsilon$  *Realizable*,  $k - \omega$ ,  $k - \omega$  *SST* and *RSM*





## Chapter 3 Thermodynamic model

---

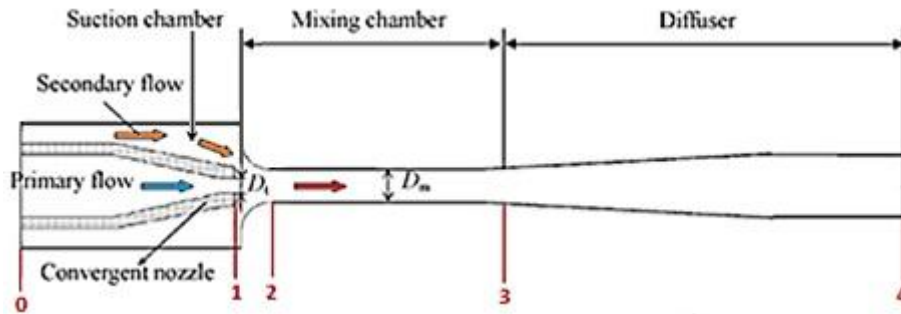


Figure 3-1 Ejector studied

In this chapter the structure of the novel thermodynamic model is developed and the basis of the integrated thermodynamic/CFD approach are built.

### 3.1 Basis of the novel thermodynamic model

Here the fundamentals of a novel 1D thermodynamic model are presented. The literature review presented in the previous paragraph, the conclusions of He et al. [23], the want of integrating an ejector model in a power plant simulation code, pointed out the following features:

1. ejector model must have a structure compatible with power plant simulation codes;
2. CFD study will provide information on flow behavior that will be implemented in the thermodynamic model using variable isentropic efficiencies;
3. the model should be able to take in account both off-design and on-design operating condition (section 1.2).

This new model will be designed for a single phase subsonic ejector, but the structure is generalizable and, changing primary nozzle equations, it may be easily used for single phase supersonic ejectors too. Anyway a supersonic ejector has different flow behavior, so another CFD study has to be conducted in order to have information on efficiencies.

#### 3.1.1 Power plant simulation codes constrains and modification over the typical 1D approach

The novel model has to be ready to be integrated in power plants simulation codes, so its input and output parameters must be suitable; this forces to modify the structure of traditional thermodynamic models, which requires in input is the following parameters:

- $D_t$ : diameter of nozzle throat;
- $D_{mix}$ : diameter of mixing section;
- $p_p$ : pressure of primary flow;
- $T_p$ : temperature of primary flow;
- $p_s$ : pressure of secondary flow
- $T_s$ : of secondary flow;
- $p_{exit}$ : outlet pressure.

Traditional thermodynamic models are built to provide, as output, the entertainment ratio  $\omega$  (which is the most important performance parameter in an ejector working in a refrigeration cycle).

Our task is to implement ejector in a code which is able to simulate generic power plants, so it's by far more interesting fixing the recovery of static secondary flow pressure  $\Delta p_s/p_s = (p_s - p_e)/p_s$  and search for  $p_{0,p}$ <sup>7</sup> which satisfies that constrain. Moreover an energy system code solves balance equations (mass, moment and energy): as consequence, primary/secondary mass flow rate and thermodynamic properties have to be provided as input.

For those reasons a deep redesign of the classical thermodynamic models approach is necessary. Our novel model has to be structured to receive as input: (i) primary and secondary mass flow rate, (ii) compositions and (iii) thermodynamic properties; the outputs will be  $p_{0,p}$  and thermodynamic conditions of the mixed flow.

### 3.1.2 CFD contributions

CFD analysis, beside important contribution in literature over validation of RANS turbulence models for a subsonic ejector, will provide a contribution to the thermodynamic model by producing ejector efficiency maps: this will allow to relate

---

<sup>7</sup> The interest in  $p_{0,p}$  is given to the importance and value of pressure in a power plants: in fact pressure has to be given by compressor spending work (a fluid with higher pressure has a higher exergy).

global operation with local flow features. Obviously, this numerical assessment of efficiencies, will introduce iterative LOOPS in 1D model.

## 3.2 Description of the novel thermodynamic model

Following equations refer to the ejector represented in Figure 3-1.

### 3.2.1 Hypothesis

This model hypothesis are the following:

- I. *inner wall of the ejector is adiabatic*: neglecting heat transfer between the ejector and the environment, isentropic relations can be used;
- II. *flow inside the ejector is steady and isentropic*: this hypothesis is based on assumption [I];
- III. *primary and secondary fluid are supplied to the ejector at zero velocity*: inlet pressure and temperature are also equal to the total pressure and temperature;
- IV. *velocity at the ejector outlet is neglected*;
- V. *primary and secondary flow are treated as ideal gas*;
- VI. *primary and secondary velocity are uniform in each sections*;
- VII. *primary and secondary thermodynamic conditions are uniform in each sections*;
- VIII. *isentropic relations consider friction losses using isentropic efficiencies*.

### 3.2.2 Input

Remembering previous considerations (section 3.1.1), this model requires the following input parameters:

- $\dot{m}_p$ : primary mass flow rate;
- $\dot{m}_s$ : secondary mass flow rate;
- $p_p$ : primary flow pressure;
- $T_p$ : primary flow temperature;
- $p_s$ : secondary flow pressure;
- $T_s$ : secondary flow temperature;
- ejector geometry is a CFD constrain: CFD approach fixes  $D_{mix}/D_t$  and  $D_{suction}/D_t$ ;
- $\eta_{diff}$ : diffuser isentropic efficiency (this is due to CFD model that will be developed in Chapter 4, which will not consider a diffuser: a further development of this thesis may propose a CFD model that consider a diffuser too).

Moreover, first attempt isentropic efficiencies ( $\eta_p^I, \eta_s^I, \eta_{mix}^I$ ) are required in order to initialize efficiencies LOOPS: values reported in Table 2-6 can be used.

### 3.2.3 Preliminary calculations: flow compositions

**Primary flow composition.** From primary mass flow rate  $\dot{m}_p$  and primary flow composition it's possible to calculate molecular mass:

$$MM_p = \sum_{i=1}^n x_{p,i} MM_i \quad (4.1)$$

Molar flow rate:

$$\dot{N}_p = \frac{\dot{m}_p}{MM_p} \quad (4.2)$$

Molar flow rate of the i-element:

$$\dot{N}_{p,i} = x_i \dot{N}_p \quad (4.3)$$

It's also possible to calculate  $c_{p,p}$  and  $R_p$ :

$$c_{p,p} = \sum_{i=1}^n x_{p,i} c_{p,i} \quad (4.4)$$

$$R_p^* = \frac{R}{MM_p} \quad (4.5)$$

**Secondary flow composition.** From secondary mass flow rate  $\dot{m}_s$  and secondary flow composition it's possible to calculate molecular mass:

$$MM_s = \sum_{i=1}^n x_{s,i} MM_i \quad (4.6)$$

Molar flow rate:

$$\dot{N}_s = \frac{\dot{m}_s}{MM_s} \quad (4.7)$$

Molar flow rate of the i-element:

$$\dot{N}_{s,i} = x_i \dot{N}_s \quad (4.8)$$

It's also possible to calculate  $c_{p,p}$  and  $R_s$ :

$$c_{p,s} = \sum_{i=1}^{n \text{ speci}} x_{s,i} c_{p,i} \quad (4.9)$$

$$R_s^* = \frac{R}{MM_s} \quad (4.10)$$

**Mixed flow composition.** Molar mass flow rate of the i-element:

$$\dot{N}_{3,i} = \dot{N}_{p,i} + \dot{N}_{s,i} \quad (4.11)$$

Molar flow rate:

$$\dot{N}_3 = \sum_{i=1}^n \dot{N}_{3,i} \quad (4.12)$$

Mixed flow composition:

$$x_{3,i} = \frac{\dot{N}_{3,i}}{\dot{N}_3} \quad (4.13)$$

It's also possible to calculate  $c_{p,p}$  and  $R_{mix}$ :

$$c_{p,3} = \sum_{i=1}^n x_{3,i} c_{p,i} \quad (4.14)$$

$$R_3^* = \frac{R}{MM_3} \quad (4.15)$$

### 3.2.4 Primary nozzle

The flow through the convergent nozzle (between inlet and throat) is divided into two different regions (subsonic and sonic flow): in fact, due the absence of a divergent part, the flow can only reach sonic flow condition when the pressure ratio is equal or greater

than the critical value  $\left(\frac{p_s}{p_p}\right)_{cr} = v_{cr} = \left(\frac{2}{\gamma+1}\right)^{\frac{\gamma}{\gamma-1}}$ .

Using isentropic flow relations and energy equation we can obtain (i) primary flow Mach number in nozzle throat  $M_t$  and (ii) nozzle geometry  $A_t$ :

- for sonic flow ( $p_{p,0} \geq \frac{p_{s,0}}{v_{cr}}$ ):

$$\begin{cases} A_t = \dot{m}_p \sqrt{\frac{R_p T_p}{\eta_p \gamma}} \frac{1}{p_p} \sqrt{\left(\frac{2}{\gamma+1}\right)^{\frac{\gamma+1}{\gamma-1}}} \\ M_t = 1 \end{cases} \quad (4.16)$$

- for subsonic flow ( $p_{p,0} < \frac{p_{s,0}}{v_{cr}}$ ):

$$\begin{cases} A_t = \dot{m}_p \sqrt{\frac{R_p T_p}{\eta_p \gamma}} \frac{1}{p_p} \sqrt{\frac{(\gamma-1)}{2 \left[ \left(\frac{p_{s,2}}{p_p}\right)^{\frac{2}{\gamma}} - \left(\frac{p_{s,2}}{p_p}\right)^{\frac{1+\gamma}{\gamma}} \right]}} \\ M_t = \sqrt{\frac{2 \left[ 1 - \left(\frac{p_{s,2}}{p_p}\right)^{\frac{\gamma-1}{\gamma}} \right]}{(\gamma-1)}} \end{cases} \quad (4.17)$$

Where  $\eta_p$  is the isentropic efficiency accounting for friction loss. CFD study will provide information about the relationship of  $\eta_p$  with operating conditions and with flow fields. Through a variable  $\eta_p$  function, this novel thermodynamic model will be able to link global operation of the nozzle with local flow behavior.

Known  $A_t$ , nozzle geometry can be determined by:

$$d_t = \sqrt{\frac{4A_t}{\pi}} \quad (4.18)$$

Constant area mixing section and suction exit geometry is defined by the CFD study that will be presented in Chapter 5 (due to the fact that CFD model will be validated on a non-axisymmetric geometry, constants  $k_1$  and  $k_2$  will be given by hydraulic diameter ratio):

$$d_{mix} = d_t * k_1 \quad (4.19)$$

$$d_s = d_t * k_2 \quad (4.20)$$

Hence:

$$A_{mix} = \frac{d_{mix}^2 \pi}{4} \quad (4.21)$$

$$A_{s,exit} = \pi(r_{suction}^2 - r_t^2) \quad (4.22)$$

We can also calculate nozzle exit conditions remembering that, due to hypothesis [III], inlet thermodynamic conditions can be referred as total conditions: in a one-dimensional isentropic flow the expression that link static to total condition is (using  $i$  is a generic ejector section):

$$\left(\frac{p_{0,i}}{p_i}\right)^{\frac{\gamma-1}{\gamma}} = \frac{T_{0,i}}{T_i} = 1 + \frac{\gamma-1}{2}M_i^2 \quad (4.23)$$

Remembering that  $p_{0,i} = \text{constant}$  and  $T_{0,i} = \text{constant}$  in a isentropic flow and using  $\eta_p$ ; nozzle primary flow temperature is:

$$T_t = \frac{T_{0,p}}{1 + \frac{\gamma-1}{2}\eta_p M_t^2} = \frac{T_p}{1 + \frac{\gamma-1}{2}\eta_p M_t^2} \quad (4.24)$$

Velocity on nozzle exit can be calculated using:

$$v_t = M_t \sqrt{\gamma R_p^* T_t} \quad (4.25)$$

From continuity equation  $(p_t v_t A_t)/(R_p^* T_t) = \dot{m}_p$ , nozzle pressure is determined:

$$p_t = \frac{R_p^* T_t}{v_t A_t} \dot{m}_p \quad (4.26)$$

### 3.2.5 Exit suction zone

Remembering that  $A_{s,exit} = \pi(r_{suction}^2 - r_t^2)$ , secondary flow velocity at the exit of suction chamber, is determined using mass flow information:

$$v_{s,exit} = \frac{\dot{m}_s}{\bar{\rho}_s A_{s,exit}} \quad (4.27)$$

Where  $\bar{\rho}_s = p_s/R_s^* T_s$  is density of secondary flow; as will be clear with CFD simulations Mach number of secondary flow does not change very much in suction chamber, so  $\bar{\rho}_s$  can be considered as a constant. Mach number of secondary flow at exit section:

$$M_{s,exit} = \frac{v_t}{\sqrt{\gamma R_s^* T_{s,exit}}} \quad (4.28)$$

$T_{s,exit}$  is not known, but we may refer to secondary flow inlet temperature and suppose an isentropic process, using  $\eta_s$  as isentropic efficiency:

$$T_{s,exit} = \frac{T_{0,s}}{1 + \frac{\gamma-1}{2}\eta_s M_{s,exit}^2} = \frac{T_s}{1 + \frac{\gamma-1}{2}\eta_s M_{s,exit}^2} \quad (4.29)$$

Where  $\eta_s$  is the suction efficiency accounting for friction loss. CFD study will provide information about the relationship of  $\eta_p$  with operating conditions and with flow fields. Through a variable  $\eta_p$  function, this novel thermodynamic model will be able to link global operation of the suction chamber with local flow behavior.

Substituting (4.14) in (4.13) and proceeding with calculations we obtain:

$$M_{s,exit} = v_{s,exit} \sqrt{\frac{1}{\gamma R_p^* T_s \left(1 - \frac{\gamma-1}{2} \eta_s \frac{v_{s,exit}^2}{\gamma R_s^* T_s}\right)}} \quad (4.30)$$

Hence  $T_{s,exit}$  is:

$$T_{s,exit} = \frac{T_s}{1 + \frac{\gamma-1}{2} \eta_s M_{s,exit}^2} \quad (4.31)$$

Once the equations are solved  $M_{s,exit}$ ,  $T_{s,exit}$ ,  $v_{s,exit}$  are known and from continuity equation  $(p_{s,exit} v_{s,exit} A_{s,exit}) / (R_s^* T_{s,exit}) = \dot{m}_s$ , secondary pressure at the exit of suction chamber is:

$$p_{s,exit} = \frac{R_s^* T_{s,exit}}{v_{s,exit} A_{s,exit}} \dot{m}_s \quad (4.32)$$

### 3.2.6 Mixing

In this model, mixing chamber is considered the zone that goes from nozzle and suction chamber exit to diffuser inlet (while in classical thermodynamic model is supposed that mixing zone starts at some section downstream of nozzle exit). This choice is due to the very variety of flow behavior in a subsonic ejector (Chapter 5) that make impossible to use a similar approach to the ones seen in previous thermodynamic models (section 2.2), based on Munday and Bagster's theory [29].

This novel model main feature is that mixing section is accounted using continuity, energy and momentum equations and flow behavior is introduced by a  $\eta_{mix}$  function (Chapter 5): in this way local flow behavior is linked to global parameters, without introducing additional assumptions. Balance equations are:

1. momentum balance equation:

$$\begin{aligned} \eta_{mix} (\dot{m}_p v_{p,t} + p_{p,t} A_t + \dot{m}_s v_{s,exit} + p_{s,exit} A_{s,exit}) \\ = (\dot{m}_s + \dot{m}_p) v_3 + p_3 A_3 \end{aligned} \quad (4.33)$$

2. energy balance equation with ideal gas assumption:



$$\begin{aligned} \dot{m}_p \left( c_{p,p} T_p + \frac{v_p^2}{2} \right) + \dot{m}_s \left( c_{p,s} T_s + \frac{v_s^2}{2} \right) \\ = (\dot{m}_s + \dot{m}_p) \left( c_{p,3} T_3 + \frac{v_3^2}{2} \right) \end{aligned} \quad (4.34)$$

3. continuity equation:

$$\dot{m}_3 = (\dot{m}_s + \dot{m}_p) = \frac{p_3 v_3 A_3}{R_3^* T_3} \quad (4.35)$$

Where  $\eta_{mix}$  is the efficiency that accounts friction losses during flows mixing defined, as a momentum transfer efficiency. CFD study will provide information about the relationship of  $\eta_p$  with operating conditions and flow fields.

We have a system with 3 equations and 3 variables. Here it's presented the solution; starting from:

$$\left\{ \begin{array}{l} v_3 = \frac{R_3^* T_3}{p_3 \dot{m}_3 A_3} \\ p_3 = \frac{\eta_{mix} (\dot{m}_p v_{p,t} + p_{p,t} A_t + \dot{m}_s v_{s,exit} + p_{s,exit} A_{s,exit}) - \dot{m}_3 v_3}{A_3} \\ T_3 = \frac{\dot{m}_p \left( c_{p,p} T_p + \frac{v_p^2}{2} \right) + \dot{m}_s \left( c_{p,s} T_s + \frac{v_s^2}{2} \right)}{\dot{m}_3 c_{p,3}} - \frac{v_3^2}{2 c_{p,3}} \end{array} \right. \quad (4.36)$$

Naming:

- $M_{in} = \frac{\eta_{mix} (\dot{m}_p v_{p,t} + p_{p,t} A_t + \dot{m}_s v_{s,exit} + p_{s,exit} A_{s,exit})}{A_3}$ ;
- $R_3 = \frac{\dot{m}_3}{A_3}$ ;
- $E_3 = \frac{\dot{m}_p \left( c_{p,p} T_p + \frac{v_p^2}{2} \right) + \dot{m}_s \left( c_{p,s} T_s + \frac{v_s^2}{2} \right)}{\dot{m}_3 c_{p,3}}$ ;
- $K = \frac{R_3^*}{\dot{m}_3 A_3}$

The system to be solved become:

$$\left\{ \begin{array}{l} v_3 = K \frac{T_3}{p_3} \\ p_3 = M_{in} - R_3 v_3 \\ T_3 = E_3 - \frac{v_3^2}{2 c_{p,3}} \end{array} \right. \quad (4.37)$$

Hence, substituting the second and the third equation in the first, we obtain:

$$v_3^2 \left( \frac{k}{2c_{p,3}} - R_3 \right) + v_3 M_{in} - KE_3 = 0 \quad (4.38)$$

From which we obtain the value of  $v_3$ , by accepting the only solution with physical meaning. Immediately follows that:

$$p_3 = M_{in} - R_3 v_3 \quad (4.39)$$

$$T_3 = E_3 - \frac{v_3^2}{2c_{p,3}} \quad (4.40)$$

Hence Mach number in 3-3 section is:

$$M_3 = \frac{v_3}{\sqrt{\gamma R_3 T_3}} \quad (4.41)$$

### 3.2.7 Diffuser

Supposing an isentropic process in diffuser we can calculate exit conditions:

1. exit pressure, from  $p_4/p_3 = \left[ 1 + \eta_{diff} \frac{1}{2} (\gamma - 1) M_3^2 \right]^{\frac{\gamma}{\gamma-1}}$ :

$$p_4 = p_3 \left[ 1 + \eta_{diff} \frac{1}{2} (\gamma - 1) M_3^2 \right]^{\frac{\gamma}{\gamma-1}} \quad (4.42)$$

2. exit temperature, from  $T_3/T_4 = 1 + \frac{1}{2} (\gamma - 1) M_t^2$  :

$$T_4 = \frac{T_{0,3}}{1 + \frac{1}{2} (\gamma - 1) M_4^2} \quad (4.43)$$

## 3.3 Basis of integration

In next chapter a CFD approach will be validated and will be used to provide ejector efficiency maps and efficiency functions (first and second part of Chapter 5). These efficiency functions will be used in the model presented in this chapter: due to this approach, internal efficiency LOOPS will appear in model structure (third part of Chapter 5, Figure 5-35).

## Chapter 4 CFD model

---

In this chapter the CFD modeling approach of the ejector is presented. The CFD model will be integrated with the thermodynamic model presented in the Chapter 3.

### 4.1 $Q^3$ Approach

#### 4.1.1 Introduction

As remarked in section 2.4.2, in order to insure quality in CFD, rules and procedure have to be followed: Colombo et al. [118] proposed a methodological approach to qualify CFD, named  $Q^3$  approach, which is based on three dimensions:

1. software reliability;
2. user knowledge;
3. process control.

The first dimension is mainly a specific responsibility of the software house (in this case, ANSYS FLUENT), the second dimension is ensured by university background, while the third dimension is related to the use of protocol as a process control tool. In this thesis the standard protocol for CFD analysis proposed in [118] will be used.

#### 4.2.2 Protocol structure

In Figure 4-1 the protocol structure upon which is based the CDF analysis is presented. This is structured in four main phases:

1. *CFD cycle phase 1 – Problem analysis.* Here the engineering problem and its general features need to be identified and presented;
2. *CFD cycle phase 2 – Conceptual model setting: results and approach.* Here specific goals of the CFD project are defined in order to manage the project;
3. *CFD cycle phase 3 – Model building and solving: deployment.* Here the details of the numerical model used for the analysis are reported;
4. *CFD cycle phase 4 – Problem evaluation: assessment and review.* In this section the calculation verification is performed over the temporal and spatial scale, then results of the analyses are presented by using both qualitative trends and images, and quantitative values, such as integral or mean global quantities.

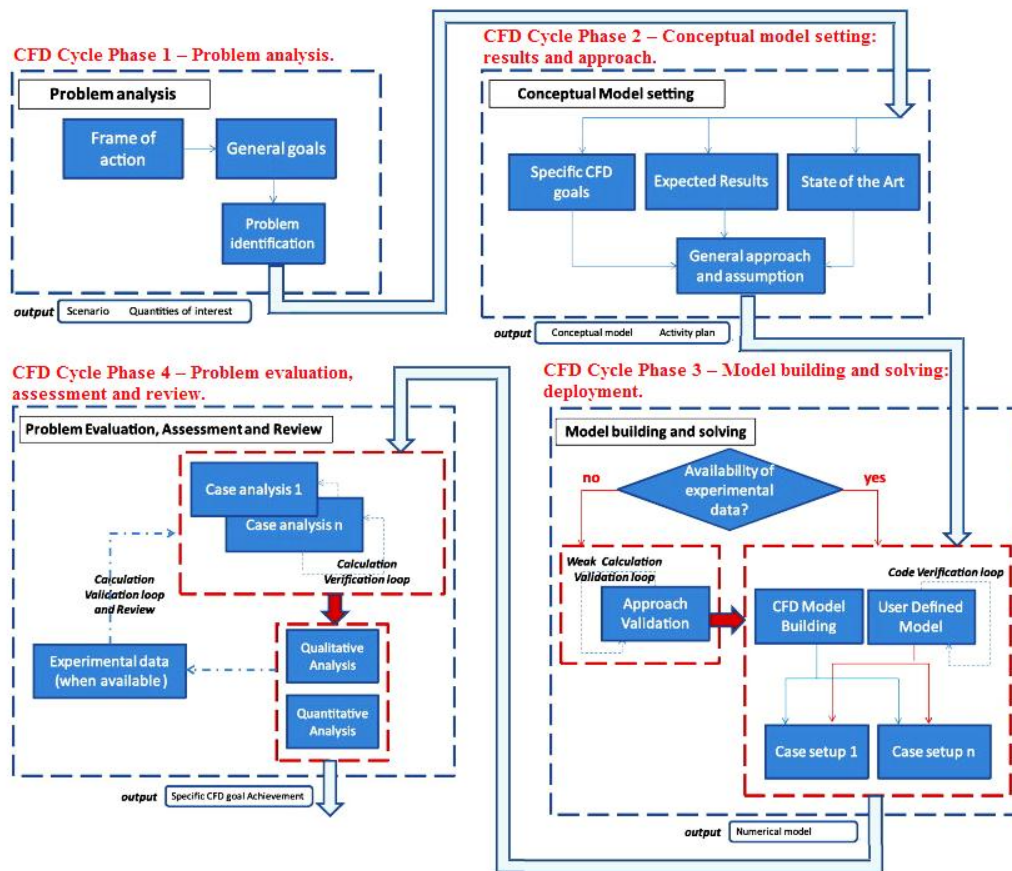


Figure 4-1 Protocol structure; modified from [118]

## 4.2 CFD cycle phase 1 - Problem analysis

### 4.2.1 Frame of action and general purposes

CFD analysis is used as a supporting tool for the development of an integrated ejector 1D-3D model. In Chapter 3 a thermodynamic 1D approach has been proposed, in the present chapter a 3D CFD model is presented, and in Chapter 5 the integrated model will be analyzed.

### 4.2.2 Problem identification

As in the Chapter 3 the thermodynamic model was applied to the case of a subsonic ejector, in this chapter the CFD approach will be applied to the same device.

## **4.3 CFD cycle phase 2 - conceptual model setting: results and approach**

### **4.3.1 Specific goals of the CFD analysis**

In literature (section 2.4) there is no article about model validation for subsonic ejector, as consequences main goals are to:

1. give an approach for studying ejectors using CFD;
2. provide guidelines on CFD simulations of single phase subsonic ejector;
3. propose the first study/analysis about performance comparison of RANS turbulence models in CFD simulations of subsonic ejectors.

The validated model will be used in Chapter 5 for

1. studying flow behavior;
2. evaluating ejector efficiencies for different operating conditions;
3. understanding how local flow structures impact over performance parameters.

### **4.3.2 State-of-the-art of CFD in the field**

CFD state-of-the-art in ejector modeling has been presented in section 2.4.

### **4.3.3 Expected results and benchmark used**

The focus of this investigation was the turbulent flow through a two-dimensional ejector nozzle: this flow features the turbulent mixing between the primary jet and entrained secondary air as well as the interaction with the wall boundary layers.

The benchmark used for model validation consists in the work of Gilbert and Hill [137]: two rectangular section ejectors (with different mixing section throats size each) were tested under different operating conditions (Table 4-1):

Run No.	Nozzle Pressure psia	Nozzle Temp. °R	Nozzle Throat Area in <sup>2</sup>	Nozzle Throat Co-efficient	Barometric Pressure psia	Atmospheric Temp °R	Measure Nozzle Flow Rate		Mixing Section Flow lb/sec in	Secondary Flow Rate lb/sec.in.	Flow Ratio	Mixing Section Throat Size	Mass-Momentum Stagnation Pressure at x = 10.5" psia
							lb/sec	lb/sec. in					
Symbol	P <sub>N</sub>	T <sub>N</sub>	A <sub>N</sub>	C <sub>N</sub>	P <sub>b</sub>	T <sub>a</sub>	-	W <sub>N</sub>	W <sub>m</sub>	W <sub>s</sub>	W <sub>s</sub> /W <sub>N</sub>		
1	31.69	641	0.9688	0.9674	14.69	538	0.6240	0.0780	0.408	.330	4.23	1.25"	16.15
2	31.60	637		0.9645	14.60	543	0.6263	0.0782	0.341	.2627	3.36		16.19
3	31.61	706		0.978	14.61	553	0.5997	0.0750	0.357	.2820	3.76		15.91
4	35.61	659		0.978	14.61	553	0.6993	0.0874	0.396	.3086	3.53		-----
5	31.71	648		0.980	14.71	544	0.6293	0.0787	0.384	.3053	3.88		15.86
6	35.80	649		0.974	14.80	547	0.7056	0.0882	0.434	.3458	3.92	1.875"	16.23
7	35.80	647		0.974	14.80	543	0.7069	0.0884	0.458	.3696	4.18		16.20
8	31.80	642		0.968	14.80	543	0.6266	0.0782	0.424	.3458	4.42		-----
9	55.73	644		0.975	14.73	550	0.7072	0.0884	0.501	.4126	4.67		16.06
10	35.70	660		0.976	14.70	547	0.6993	0.0874	0.525	.4376	5.006		15.96
11	35.68	652		0.973	14.68	548	0.7006	0.0876	0.506	.4184	4.777		16.05

Table 4-1 Operating conditions of tests performed by Gilbert and Hill [137]

We will focus on the ejector with 1.875" mixing section throat size and the experimental data to be used for comparison purposes consists of velocity and temperature measurements at axial locations on run 6, run 7, run 9 and run 10.

This benchmark [137] was used for validations performed by NASA:

1. **1994.** *Georgiadis et al.* "Modification of the two-equation turbulence model in NPARC to a chien-low Reynolds number k-ε formulation" [138];
2. **1994.** *Georgiadis et al.* "use of Navier-Stokes methods for the calculation of high-speed nozzle flow fields" [139];
3. **1994.** *Yoder.* "NPARC alliance validation archive: ejector nozzle" [119].

Moreover [137] was used for validating a CFD model in:

4. **2010.** *Thrumurthy.* "design and analysis of noise suppression exhaust nozzle systems" [140].

All of the works above used as input for the numerical computations those of run 9 in the report by Gilbert and Hill [137]

#### 4.3.4 General approach: main assumption and working hypothesis

Working fluid is treated as an ideal gas with a constant specific heat. As will be explained in next sections, geometry is represented as 2D (accordingly to previous works dealing with same benchmark).

#### 4.3.5 Activities and plan

In Figure 4-2 are represented the fluxes of information among different phases of model building; it was an iterative process where results lead to critically review the model, as can be seen.

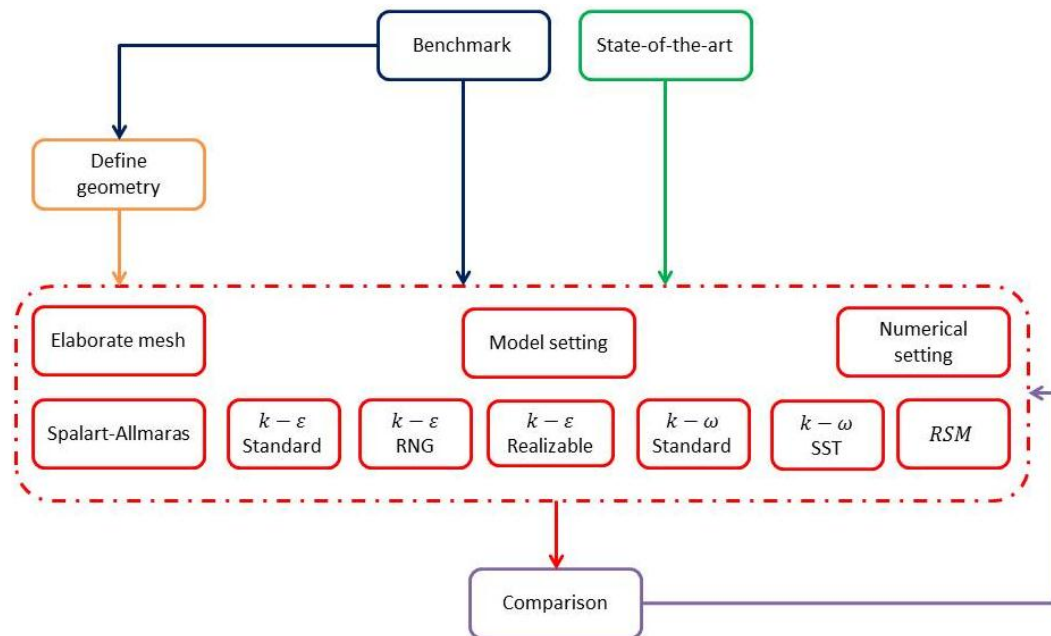


Figure 4-2 Activities and plan

## 4.4 CFD cycle phase 3 – model building and solving: deployment

### 4.4.1 Pre-processing

In this session the general preprocessing phase is identified and it aims to define the CFD domain used and how this domain has been meshed (mesh importance has already been pointed out in section 2.4.2);

#### 4.4.1.1 Domain identification and Geometry setting

Ejector studied by [137] is shown schematically in Figure 4-3.

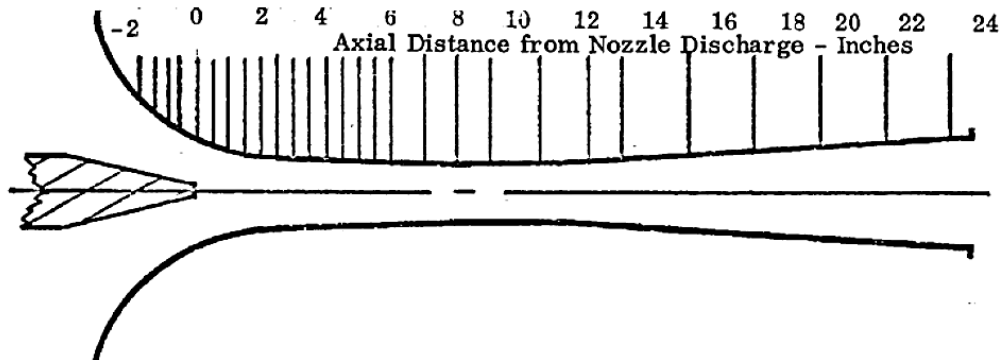


Figure 4-3 Ejector geometry; taken from [137]

The rectangular mixing section is formed by the symmetrically contoured upper and lower walls and the two flat sidewalls. The widths of both the primary nozzle discharge slot and the mixing section were 8.00 inches. Other dimensions are shown in Figure 4-4.

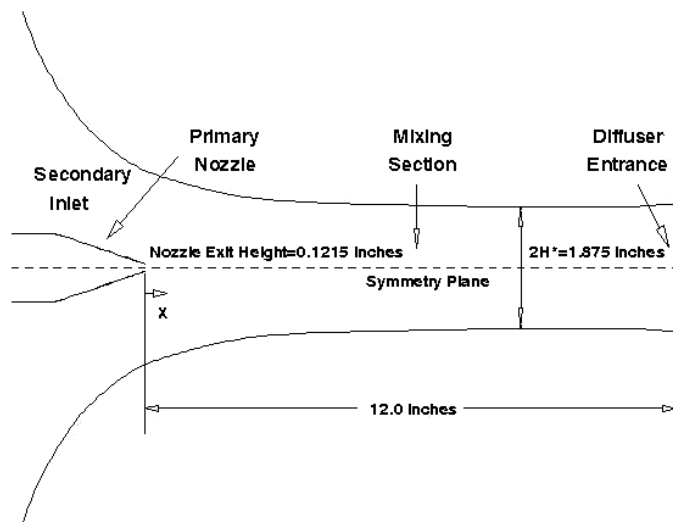


Figure 4-4 Benchmark ejector; taken from [119].

In future development a Cartesian frame of reference will be used where  $x$  axis is symmetry axis ( $x = 0$  is nozzle exit).

#### 4.4.1.2 Mesh strategy and generation

**Mesh used in previous works.** Due to the symmetric nature of the ejector nozzle and mixing section, only half of the ejector was modeled numerically in all of the previous works [119], [138], [139], [140], by a 2D block structured mesh represented in Figure 4-5.



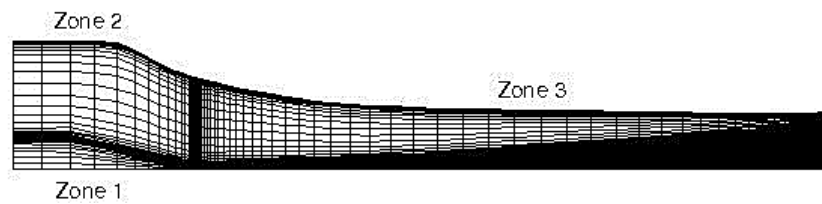


Figure 4-5 2D Mesh used in previous work; taken from [119]

That mesh is composed of 15300 cells (1200 in zone 1 “primary flow inlet”, 2100 in zone 2 “secondary flow inlet” and 12000 in zone 3 “mixing zone”), 30990 faces and 15693 nodes. Comparison between this mesh and geometry is provided in Figure 4-6:

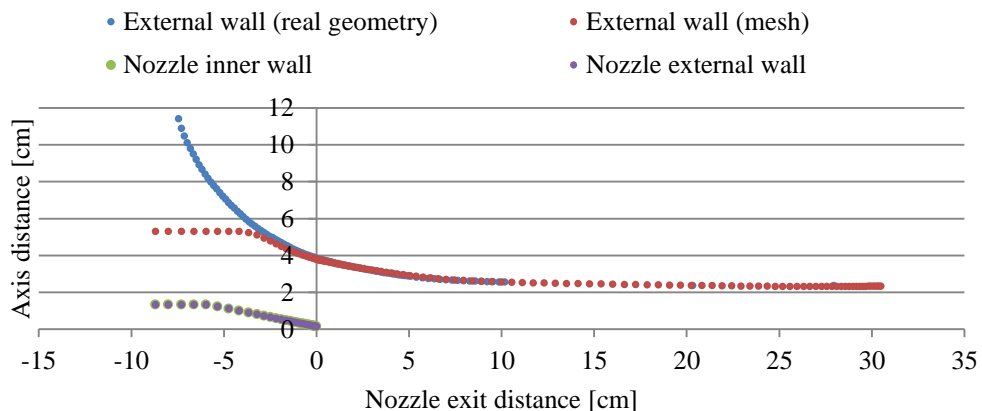


Figure 4-6 Comparison between mesh (Figure 4-5) used and geometry in [137]

**Mesh generation.** Particular care was taken into account for mesh generation, in fact a poor quality grid will cause inaccurate solutions and/or slow convergence. Moreover is important to underline that numerical diffusion is minimized when the flow is aligned with the mesh: this point is the most relevant to the choice of the grid. It is clear that using a triangular/tetrahedral mesh the flow can never be aligned with the grid and, for ejector flow behavior we can rely on a quadrilateral/hexahedral mesh to minimize numerical diffusion. Mesh developed is the result of an interactive process, as represented in Figure 4-2.

Starting from above considerations the result of mesh generation process is a structured, two-dimensional mesh, with 15246 quadrilateral cells, 30812 faces and 15567 nodes, similar to the one used all of the previous works, was created using the GAMBIT 2.4.6. In Figure 4-7 is shown the structured computational mesh in which the upstream contoured secondary flow region was neglected to avoid highly skewed cells and to be consistent with previous simulations with this geometry, accordingly with previous works.

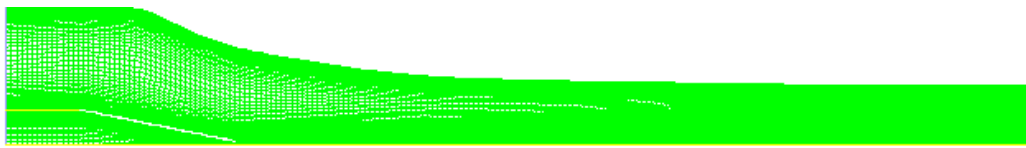


Figure 4-7 Mesh developed with GAMBIT

Figure 4-8 presents some details:

1. mesh refinement on ejector external wall in order to have a  $y_{wall}^+$  suitable for the chosen wall treatment (section 4.4.2.2);
2. mesh refinement on ejector nozzle internal and external wall in order to have a  $y_{wall}^+$  suitable for the chosen wall treatment (section 4.4.2.2);
3. mesh refinement on mixing layer.

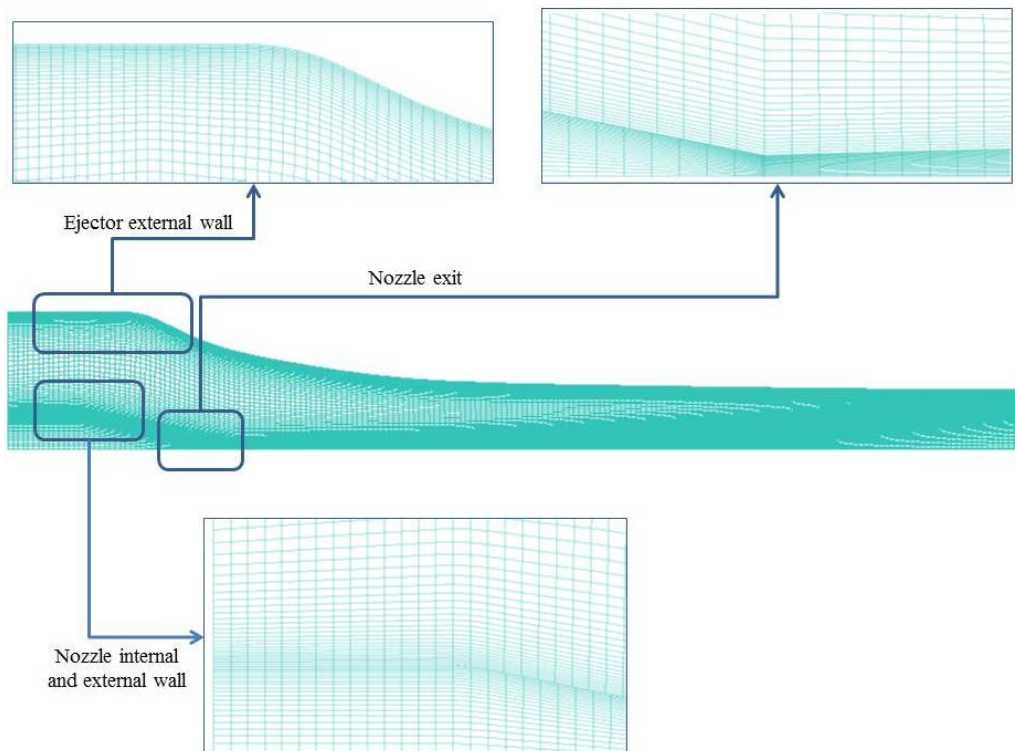


Figure 4-8 Mesh developed with GAMBIT with details

Particular attention has been given to mesh quality, because of the reasons reported above. In particular here are reported considerations on three quality parameters with comparison between previous mesh and mesh developed in this thesis.

- *Aspect ratio*. For quadrilateral and hexahedral elements is defined as:  $Asp = \frac{\max(e_1, e_2, \dots, e_n)}{\min(e_1, e_2, \dots, e_n)}$  where  $e_i$  is the average length of the edges in a coordinate

direction (i) local to the element and n is the total number of coordinate directions associated with the element. For quadrilateral elements, n=2; for hexahedral elements, n=3.  $Asp = 1$  describes an equilateral element.

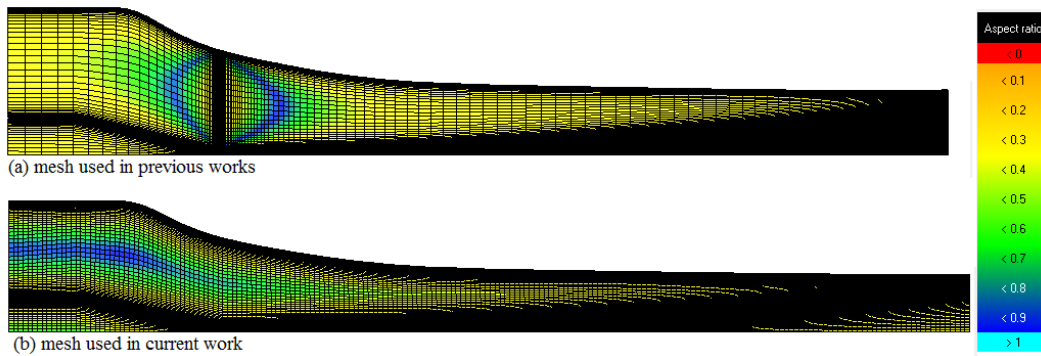


Figure 4-9 Aspect ratio comparison

- *Cell surface*. This is an interesting parameter because it helps evaluating local mesh refinement and cells area gradient.

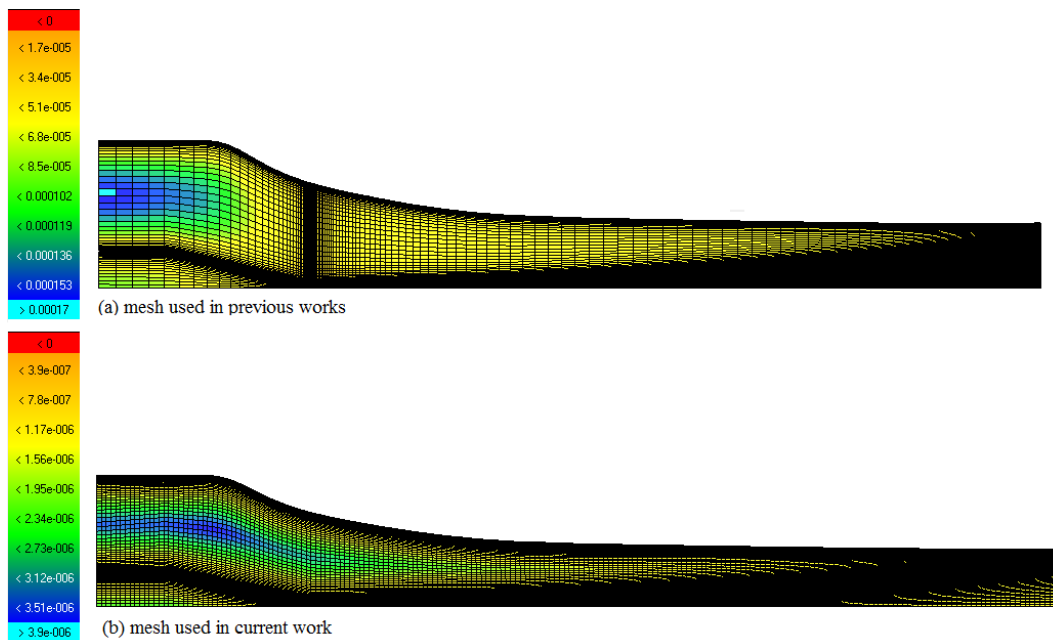


Figure 4-10 Cell surface comparison

- *Element skewness*. For quad elements it is obtained considering minimum angle  $\alpha_{min}$  and maximum angle  $\alpha_{max}$ :  $skew = \max \left[ \frac{\alpha_{max}-90}{90}; \frac{\alpha_{min}-90}{90} \right]$ .

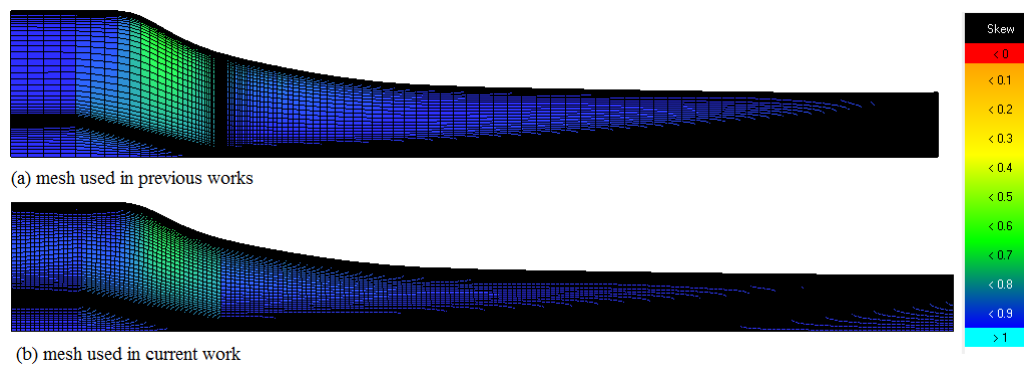


Figure 4-11 Element skewness comparison

It can be seen how current mesh has higher quality than mesh used in previous studies.

## 4.4.2 Model setting

Here the general setting of the model is explained.

### 4.4.2.1 Solver

The commercial software FLUENT 13 is used to run simulations; this software employed the finite volume method to convert all governing equations (mass, momentum and energy) to algebraic form to be solved numerically [60].

Solver	Space	Formulation	Time	Velocity formulation	Gradient Option
Density-based	2D	Implicit	Steady	Absolute	Least Squares Cell Based

Table 4-2 Solver settings

The density-based coupled solver is chosen because of the strong coupling, between density, energy and momentum. (due to the presence of high speed compressible flow).

### 4.4.2.2 Turbulence approach

RANS turbulence models are used. Previous works dealing with this type of ejector ([119], [138], [139], [140]) used:

- algebraic model: Thomas model [139], [138];
- one equation model: Spalart-Allmaras: [140];
- two equation models: NPARC  $k - \varepsilon$ : [119], Chien  $k - \varepsilon$ : [138], WIND Menter Shear Stress Transport: [119], Menter Shear Stress Transport (SST): [140];

In section 1.3 were provided considerations on turbulence models used in ejector modeling: the  $k - \varepsilon$  RNG and  $k - \omega$  SST have been extensively used in the field of the supersonic flow field, but up to now there are no guidelines on turbulence models to be used in the case of a subsonic ejector: this thesis proposes to overcome this deficiency by evaluating the performance of the following turbulence approaches:

1. *turbulence modeling*. RANS Models that will be evaluated are:
  - *Spalart – Allmaras*;
  - $k - \varepsilon$ ;
  - $k - \varepsilon$  RNG;
  - $k - \varepsilon$  Realizable;
  - $k - \omega$ ;
  - $k - \omega$  SST;
  - *RSM*;
2. *near wall treatment*. Standard Wall Function, was used in this work for  $k - \varepsilon$ ,  $k - \varepsilon$  RNG ,  $k - \varepsilon$  Realizable and *RSM* models, whereas the *Spalart – Allmaras*,  $k - \omega$  and  $k - \omega$  SST models do not need a near wall treatment because of their mathematical structure already emphasized on the flow close to the wall.

#### 4.4.2.3 Physical properties

Working fluid is air with the following properties:

$\rho$ $\left[\frac{\text{kg}}{\text{m}^3}\right]$	$c_p$ $\left[\frac{\text{J}}{\text{kg K}}\right]$	$k$ $\left[\frac{\text{W}}{\text{m K}}\right]$	$\mu$ $\left[\frac{\text{kg}}{\text{m s}}\right]$	MM $\left[\frac{\text{kg}}{\text{kg mol}}\right]$
Ideal gas law	1006.43	0.0242	1.7894e – 05	28.966

Table 4-3 Working fluid properties

#### 4.4.2.4 Operating conditions

Operating conditions for each runs are obtained from Gilbert and Hill’s report [137];

	Run 6	Run 7	Run 9	Run 10
$p_{\text{atm}}$ [Pa]	102042	102042	101560	101353

Table 4-4 Operating conditions taken from [137]

#### 4.4.2.5 Boundary conditions

Boundary conditions used in simulations are:

- primary fluid inlet: mass flow rate;
- secondary fluid inlet: mass flow rate;
- mixed flow outlet: imposed static pressure;

- external wall: no slip conditions;
- internal nozzle wall: no slip conditions;
- external nozzle wall: no slip conditions.

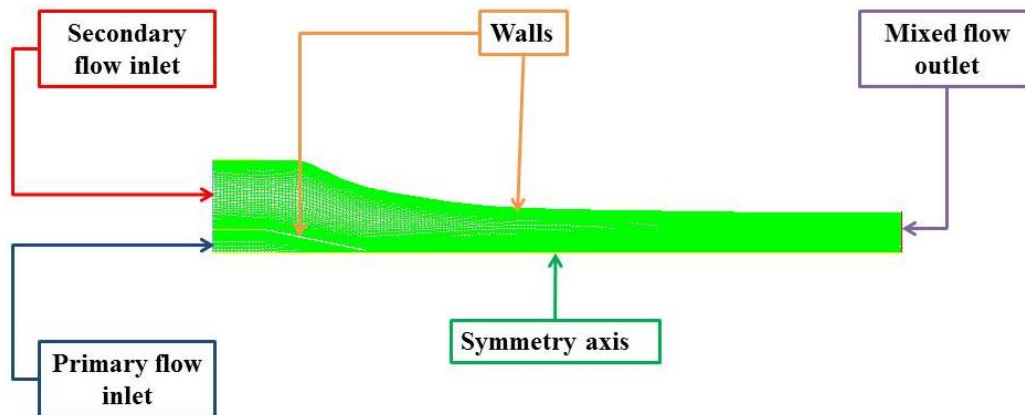


Figure 4-12 Boundary conditions used

**Pressure, temperature and mass flow rate.** For each run those boundary conditions are obtained from Gilbert and Hill report [137], through Table 4-1 (section 4.3.3). Note that outlet temperature is a backflow condition.

	Primary flow	Secondary flow	Outlet
Run 6			
Temperature [K]	360.56	303.89	303.89
Mass flow rate [kg/s]	1.575	6.174	/
Pressure [Pa]	/	/	99678
Run 7			
Temperature [K]	359.44	301.67	301.67
Mass flow rate [kg/s]	1.578	6.596	/
Pressure [Pa]	/	/	98062
Run 9			
Temperature [K]	357.77	305.6	305.6
Mass flow rate [kg/s]	1.579	7.372	/
Pressure [Pa]	/	/	92735
Run 10			
Temperature [K]	366.67	303.89	303.89
Mass flow rate [kg/s]	1.561	7.814	/
Pressure [Pa]	/	/	92735

Table 4-5 Boundary condition for temperature, mass flow rate and pressure

**Turbulence.** In [138] simulations were performed varying the inflow boundary condition to determine the effects of specifying the turbulent quantities on the mixing

downstream: in addition to the extrapolation case (typical approach used in NPARC solver [138]), two other inflows were examined:

1. primary flow:  $I_{turbulence\ intensity} = 5\%$ ;  $k_t = 500k_{molecular}$ ;  
secondary flow:  $I_{turbulence\ intensity} = 2\%$ ;  $k_t = 100k_{molecular}$ ;
2. primary flow:  $I_{turbulence\ intensity} = 5\%$ ;  $l_h = 5\%h_{nozzle,exit}$ ;  
secondary flow:  $I_{turbulence\ intensity} = 2\%$ ;  $l_h = 5\%h_{secondary,exit}$ ;

These two additional inflows were arbitrarily specified, since no turbulence measurements were available from [137]: it was found out that the calculation with former option closely matches the data than the latter. It's important to point out that the specified turbulence intensities and viscosities cannot be justified based on these results because these quantities were not taken from the experiment. In next simulations turbulence boundary conditions that will be used are:

	Primary flow	Secondary flow	Outlet
Turbulence intensity	5 %	2 %	5 %
$\frac{\mu_t}{\mu}$	500	100	500

Table 4-6 Boundary conditions for turbulence

**Wall.** No slip and adiabatic conditions are used for wall boundary conditions.

#### 4.4.3 Numerical setting

In this section numerical setting are reported and discussed.

##### 4.4.3.1 Numerical strategy

**Initialization.** Due to the presence of two inlets hybrid initialization is chosen.

**Discretization schemes.** In order to avoid an excessive numerical diffusion high order numerical scheme have to be used [59], but low order schemes are able to reach convergence more quickly: as consequence simulation is started with first-order discretization scheme and, when the simulation is defined, discretization schemes are switched to second-order (Table 4-7).

	Parameter	Numerical method
Preliminary flow field	Flow	First Order Upwind
	Turbulent Kinetic Energy	First Order Upwind
	Specific Dissipation Rate	First Order Upwind
Final results	Flow	Second Order Upwind
	Turbulent Kinetic Energy	Second Order Upwind
	Specific Dissipation Rate	Second Order Upwind

Table 4-7 Numerical setting used

**Courant number.** In order to run a stable simulation behavior calculation is started with a low Courant–Friedrichs–Lewy condotion (CFL=1), which is gradually increased till the value of 5.

**Under-relaxation factors.** In order to aid convergence first calculation steps are performed at low under-relaxation factors values. Once flow behavior is stabilized these parameters are increased (Table 4-8).

	Parameter	Value
Preliminary flow field	Turbulent Kinetic Energy	0.6
	Specific Dissipation Rate	0.6
	Turbulent Viscosity	0.8
	Solid	1
Final results	Turbulent Kinetic Energy	0.9
	Specific Dissipation Rate	0.9
	Turbulent Viscosity	0.9
	Solid	1

Table 4-8 Control parameter used

#### 4.4.3.2 Convergence control

These is no univocal way to define the achievement of convergence: in our case solution is considered as converged when the following converging criteria are satisfied:

- *residuals.* Up to Fluent® [60], a decrease in residuals by three orders of magnitude indicates at least qualitative convergence and the major flow features should be established, but it does not mean that physical convergence is reached; in fact if the case is initialized very close or very distant to the solution, the residuals criteria fails;
- *local Quantities monitoring.* Area-weighted-averaged inlet pressure of primary and secondary flow are checked;
- *global quantities monitoring.* Mass fluxes across each faces are checked (In this study, the difference of mass flow rates at the inlet and at the outlet passing through the modeled ejector are supposed to be less than  $10^{-7}$  kg/s).

## 4.5 CFD cycle phase 4 – Problem evaluation, assessment and review



In this section the results of the analyses are presented both using some qualitative trend and images that help the visualization of the thermal and fluid-dynamics behavior as well as quantitative values such as integral or mean global quantities. It's important to remark that validation is performed using local measurement and not only global parameters (guideline given in section 2.4.2).

#### 4.5.1 Calculation verification

In following sections the comparison between numerical and experimental results is presented:

1. run 6:
  - velocity profiles at:
    - i.  $x = 2.54cm$ ;
    - ii.  $x = 7.62cm$ ;
    - iii.  $x = 17.78cm$ ;
    - iv.  $x = 26.67cm$ .
2. run 7:
  - velocity profiles at:
    - i.  $x = 2.54cm$ ;
    - ii.  $x = 7.62cm$ ;
    - iii.  $x = 17.78cm$ ;
    - iv.  $x = 26.67cm$ .
3. run 9:
  - total temperature profiles at:
    - i.  $x = 7.62cm$
    - ii.  $x = 26.67cm$ ;
  - velocity profiles at:
    - i.  $x = 2.54cm$
    - ii.  $x = 5.08cm$
    - iii.  $x = 7.62cm$
    - iv.  $x = 12.70cm$
    - v.  $x = 17.78cm$
    - vi.  $x = 26.67cm$ ;
4. run 10:
  - velocity profiles at:
    - i.  $x = 2.54cm$
    - ii.  $x = 7.62cm$
    - iii.  $x = 17.78cm$
    - iv.  $x = 26.67cm$ .

**Considerations on experimental apparatus and results.** In [137] stagnation pressure and temperature profiles were measured at up 9 axial locations using a temperature probe, a pressure transducer and a direct digital readout (no information on their uncertainties were provided in [137]).

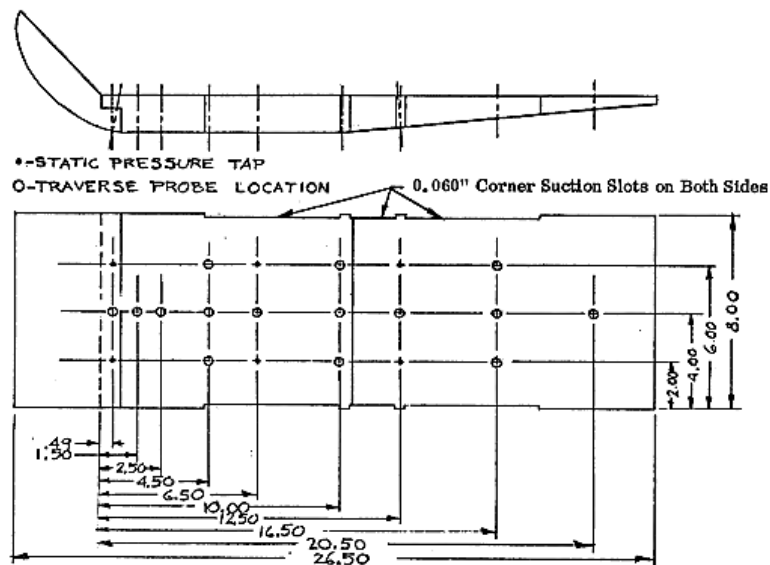


Figure 4-13 Mixing sections traverse locations; taken from [137]

Velocity profiles and mass flow rates (used in CFD model as boundary conditions), were obtained through a data reduction procedure:

- *velocity profiles.* they were calculated from the compressible relationship between Mach number and the ratio of stagnation pressure to static pressure (local velocity is calculated from the Mach number and the local speed of sound which is dependent on the local static temperature, which is calculated from the measured stagnation temperature profiles and the compressible flow relation between temperature ratio and Mach number); no information on their uncertainties were provided in [137];
- *primary nozzle mass flow rate.* They were obtained using orifice equations and ASME orifice coefficients; an uncertainty of  $\pm 0.8\%$  was obtained [137];
- *mixing section mass flow rates.* They were obtained by Gilbert and Hill [137] using a computer program to integrate the product of local velocity and local density.

It's important to underline that mass flow rate calculated by integrating the results of the stagnation pressure and temperature is influenced by many items: Gilbert and Hill [137] concluded that the average integrated mass flow rate may have a fixed error of  $+1\% \div +2\%$  and an uncertainty of about  $\pm 3\% \div \pm 4\%$

#### 4.5.1.1 Run 6: velocity

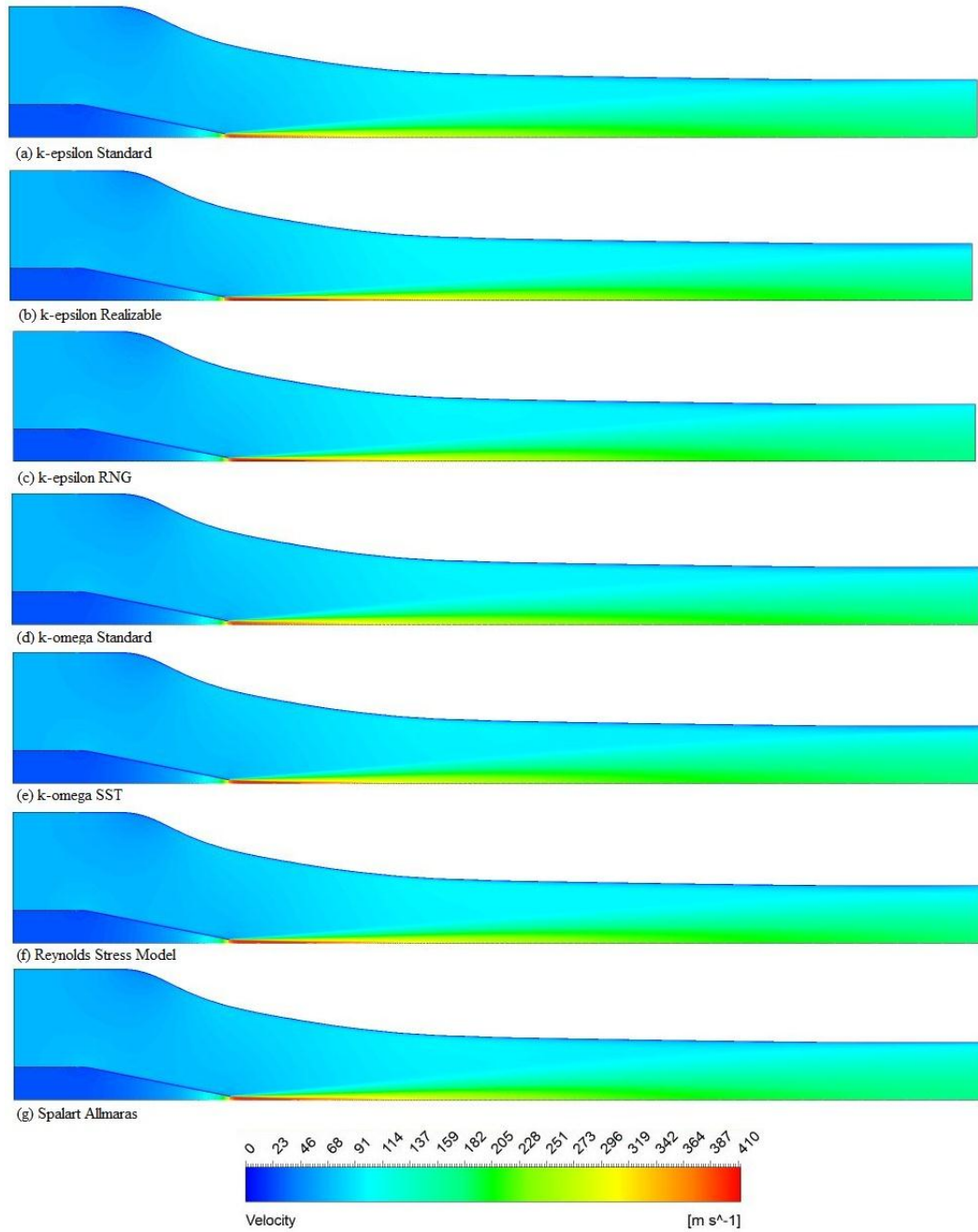


Figure 4-14 Velocity contours (run 6)

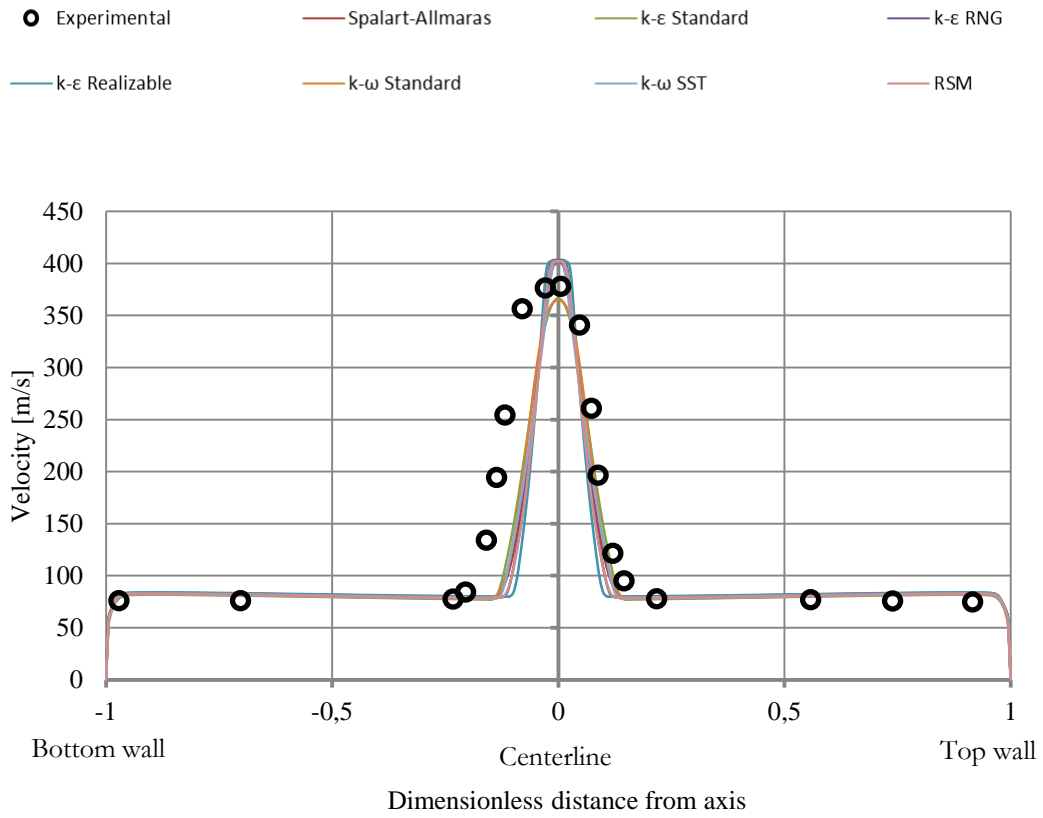


Figure 4-15 Velocity profiles at  $x = 2.54\text{cm}$  (run 6)

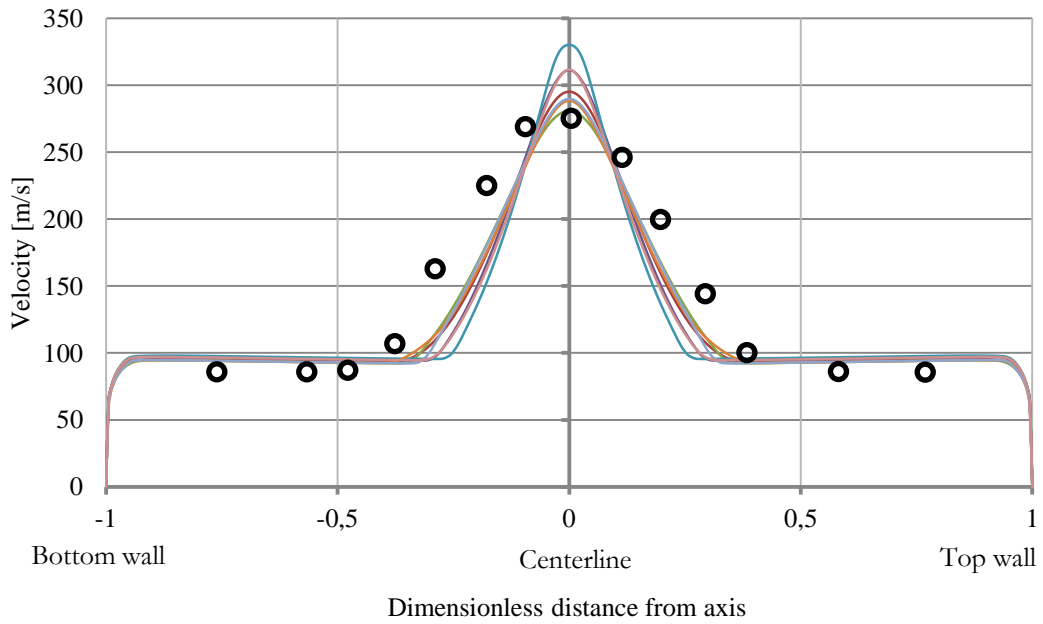


Figure 4-16 Velocity profiles at  $x = 7.62\text{cm}$  (run 6)

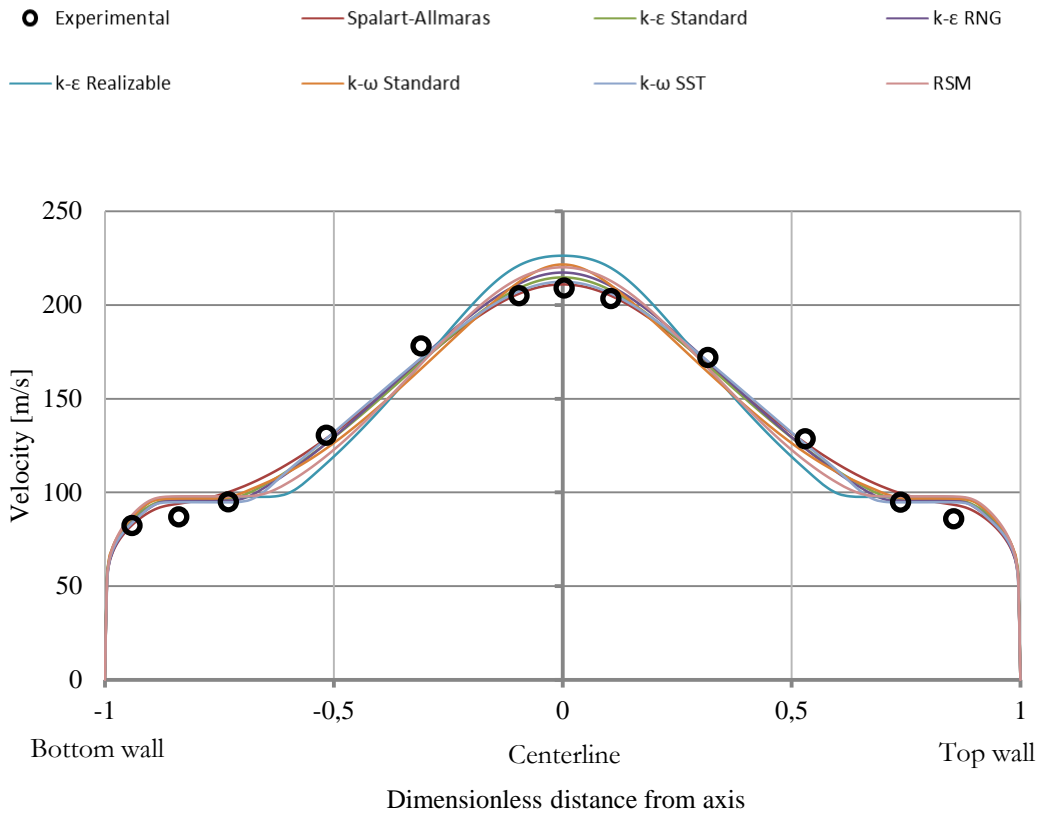


Figure 4-17 Velocity profiles at  $x = 17.78cm$  (run 6)

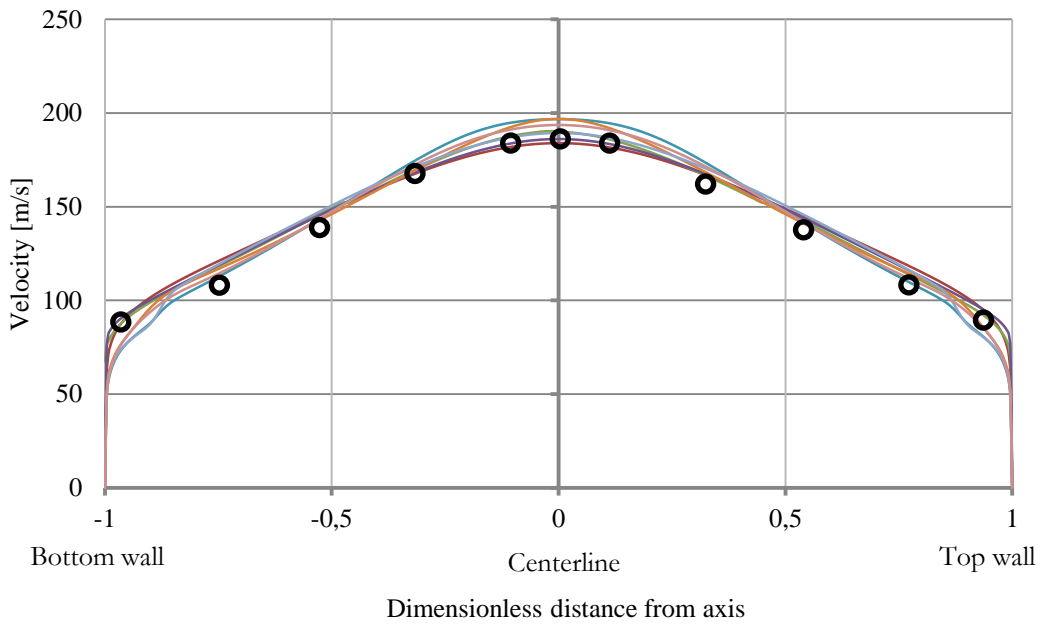


Figure 4-18 Velocity profiles at  $x = 26.67cm$  (run 6)

**Results considerations.** Considering the zone nearest to nozzle exit (Figure 4-15) is clear that the simulation of jet behavior at nozzle exit is critical: here every model almost fails in fitting correct centerline experimental data and there is poor agreement between simulation results and experimental data on lower-centerline zone ( $y^* \approx -0.15 \div -0.10$ ), due to a non-symmetrical experimental velocity profile (Figure 4-19). Main difference between different RANS turbulence models (Table 4-9) is centerline velocity profile (Figure 4-19):  $k - \varepsilon$  *Standard* and  $k - \omega$  *Standard* underestimate experimental data while other models overestimate. No remarkable difference is found comparing lateral velocity profiles, resulting from different turbulence models.

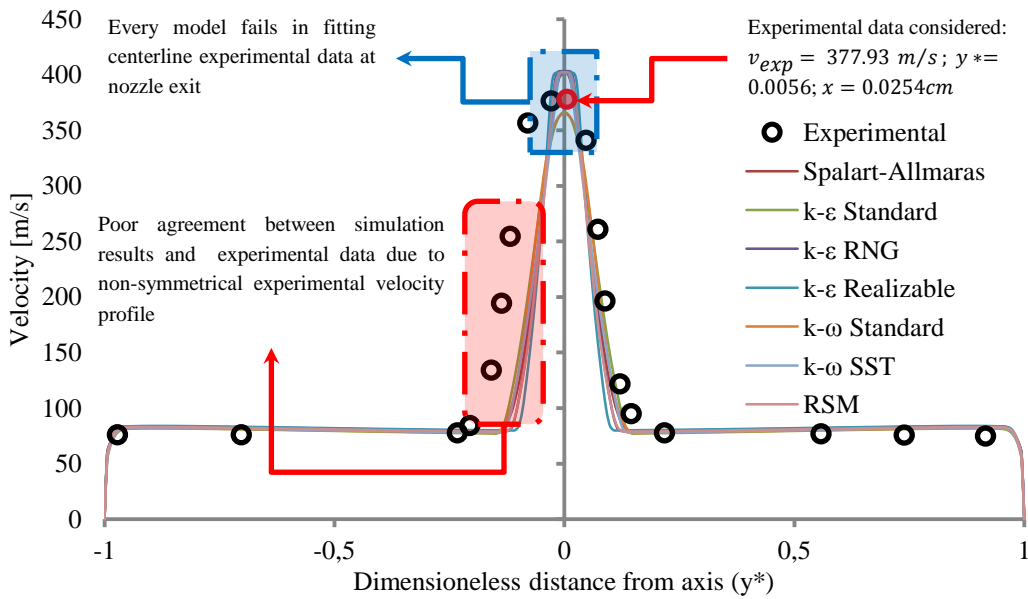


Figure 4-19 Considerations about velocity profiles at  $x = 2.54\text{cm}$  (run 6)

	<i>Spalart Allmaras</i>	$k - \varepsilon$ <i>Standard</i>	$k - \varepsilon$ <i>RNG</i>	$k - \varepsilon$ <i>Realizable</i>	$k - \omega$ <i>Standard</i>	$k - \omega$ <i>SST</i>	<i>RSM</i>
$v_{CFD}$ [m/s]	401.18	365.14	403.23	402.00	364.23	401.96	402.19
Error [%]	6.15	-3.39	6.69	6.37	-3.63	6.36	6.42

Table 4-9 Comparison between experimental data and simulation results for data point  $y^* = 0.0056$ ,  $x = 2.54\text{cm}$  and  $v_{exp} = 377.93\text{ m/s}$

Near downstream nozzle exit (Figure 4-16), there are remarkable differences between experimental data and simulation results; moreover, here, the choice of turbulence model is very important: (i)  $k - \varepsilon$  *Realizable* (the worst),  $k - \varepsilon$  *RNG* and *RSM* overestimate centerline values and are unable to predict lateral values; (ii)  $k - \omega$  *Standard*,  $k - \omega$  *SST* and *Spalart - Allmaras* have overall good performance for both centerline and lateral data; (iii)  $k - \varepsilon$  *Standard* is best turbulence model for this section. Figure 4-20 and Table 4-10 provide information focusing on centerline data.

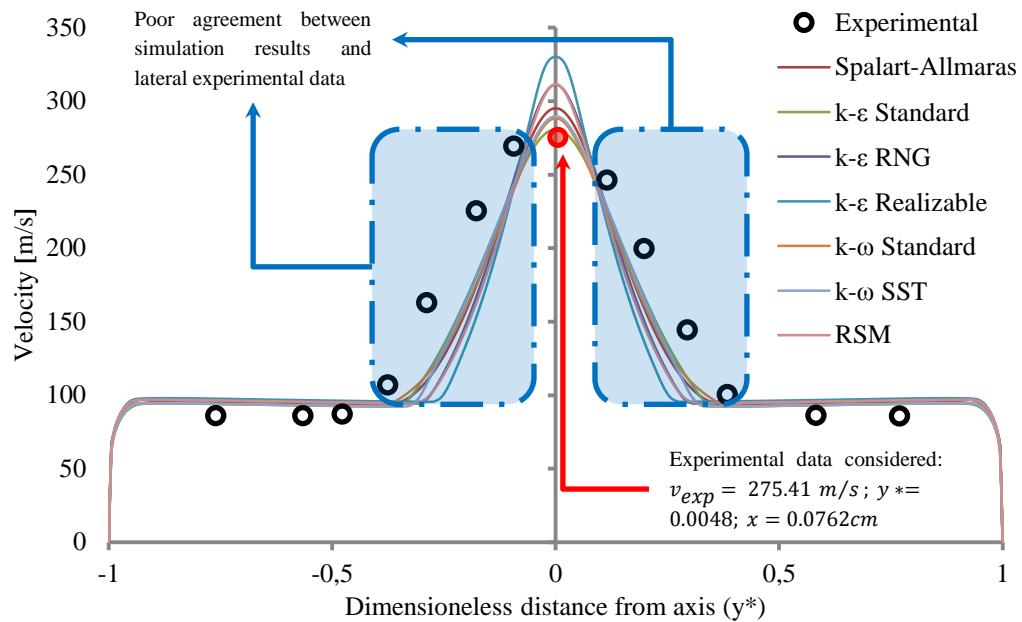


Figure 4-20 Considerations about velocity profiles at  $x = 7.62\text{cm}$  (run 6)

	<i>Spalart Allmaras</i>	<i>k - ε Standard</i>	<i>k - ε RNG</i>	<i>k - ε Realizable</i>	<i>k-ω Standard</i>	<i>k - ω SST</i>	<i>RSM</i>
$v_{CFD}$ [m/s]	294.95	280.77	311.22	330.19	288.28	289.68	311.53
Error [%]	7.10	1.95	13.00	19.89	4.67	5.18	13.12

Table 4-10 Comparison between experimental data and simulation results for data point,  $x = 7.62\text{cm}$ ,  $y^* = 0.0048$  and  $v_{exp} = 275.41\text{ m/s}$

Further downstream (Figure 4-17 and Figure 4-18), simulations are able to trace overall experimental data trend with good accuracy, with following remarks: (i) *k - ε Realizable* (the worst), *k - ω Standard* and *RSM* overestimate centerline values and underestimate lateral values; (ii) *k - ω Standard* and *k - ε RNG* have overall good performance for both centerline and lateral data; (iii), *Spalart - Allmaras* and *k - ω SST* are best turbulence model downstream sections (Table 4-14).

	<i>Spalart Allmaras</i>	<i>k - ε Standard</i>	<i>k - ε RNG</i>	<i>k - ε Realizable</i>	<i>k-ω Standard</i>	<i>k - ω SST</i>	<i>RSM</i>
<b>Experimental data: <math>x = 17.78\text{cm}</math>, <math>y^* = 0.0031</math>, <math>v_{exp} = 208.97\text{ m/s}</math></b>							
$v_{CFD}$ [m/s]	210.96	214.69	217.29	226.29	221.57	212.40	220.11
Error [%]	0.95	2.73	3.98	8.29	6.03	1.64	5.33
<b>Experimental data: <math>x = 26.67\text{cm}</math>, <math>y^* = 0.0037</math>, <math>v_{exp} = 185.96\text{ m/s}</math></b>							
$v_{CFD}$ [m/s]	183.90	190.06	186.08	196.70	196.80	189.29	193.59
Error [%]	-1.11	2.21	0.06	5.77	5.83	1.79	4.10

Table 4-11 Comparison between experimental data and simulation results

### 4.5.1.2 Run 7: velocity

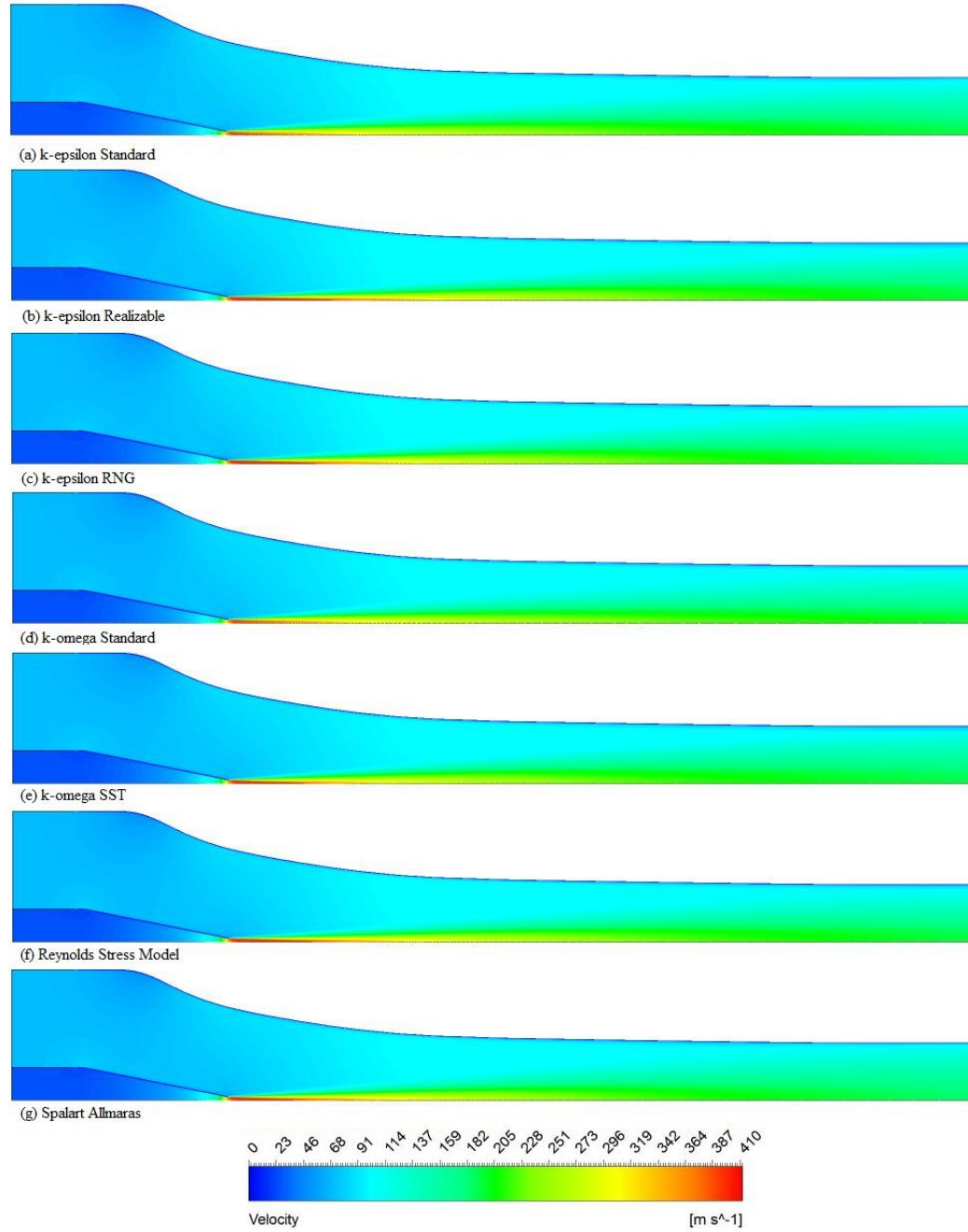
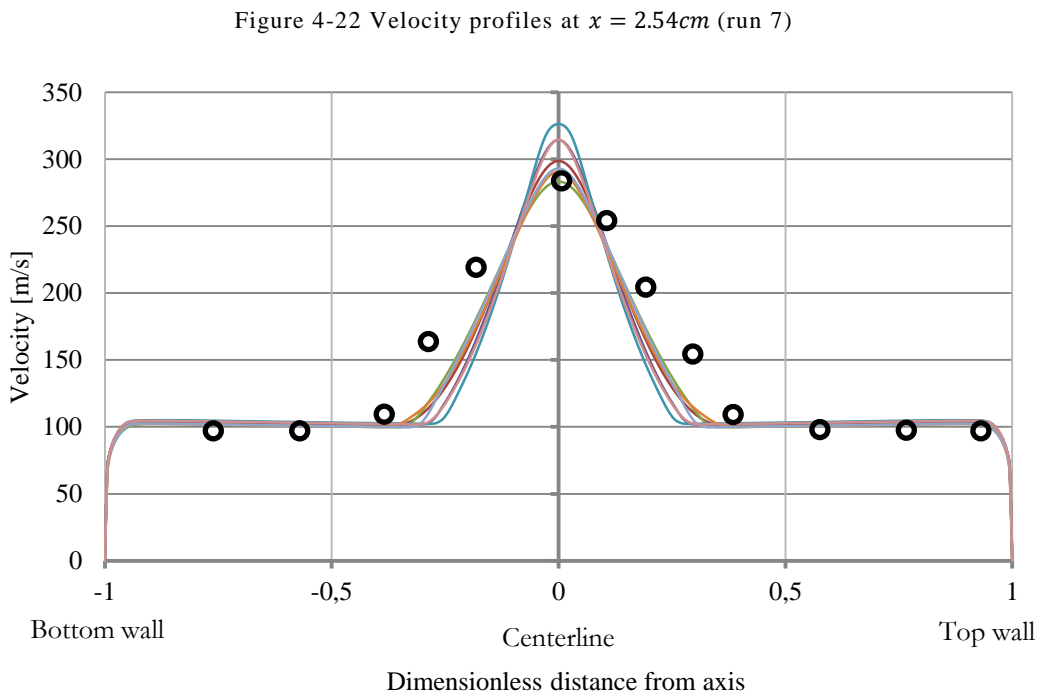
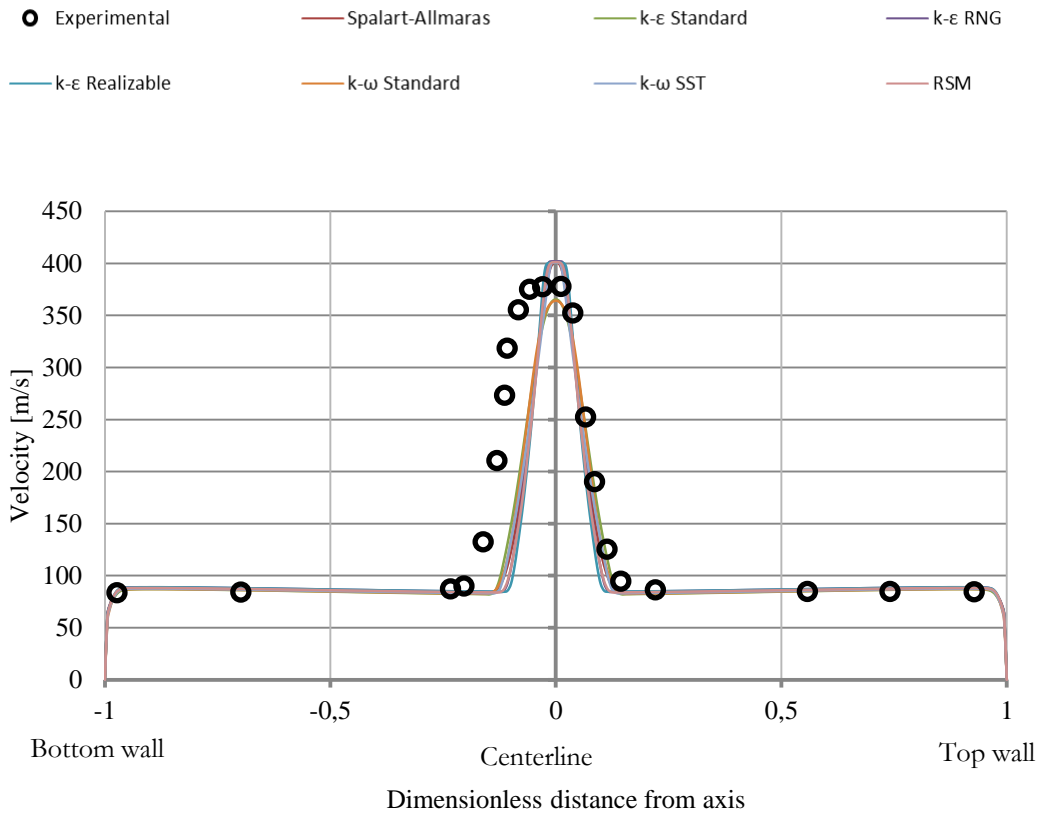


Figure 4-21 Velocity contours (run 7)





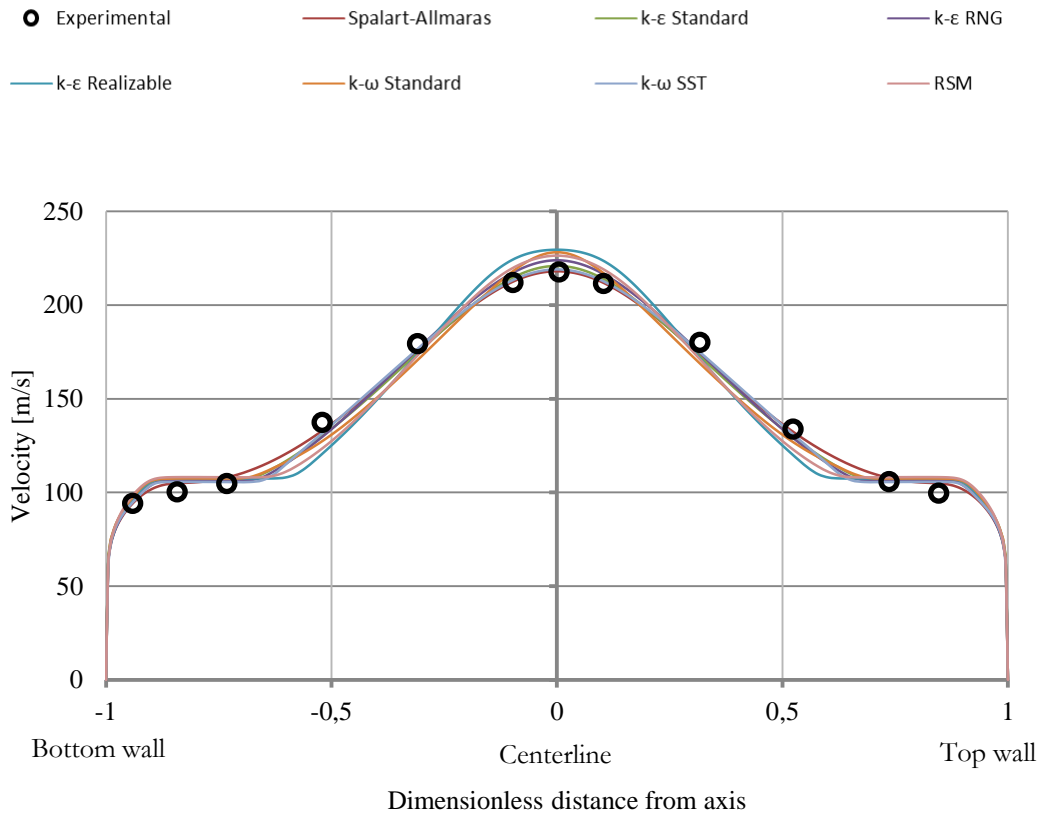


Figure 4-24 Velocity profiles at  $x = 17.78\text{cm}$  (run 7)

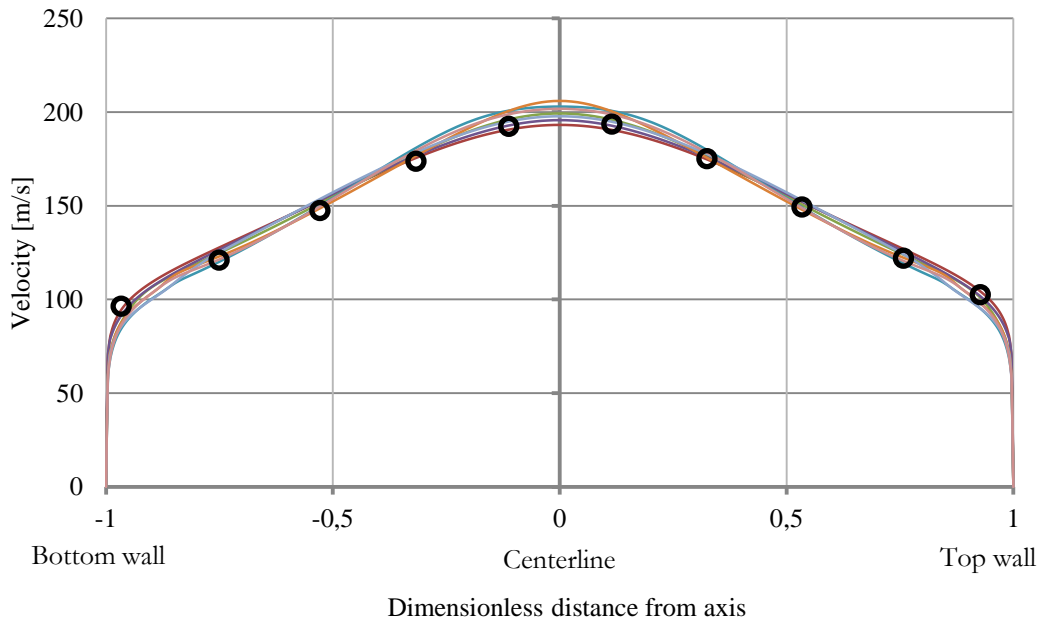


Figure 4-25 Velocity profiles at  $x = 26.67\text{cm}$  (run 7)

**Results considerations.** As stated before, the simulation of jet behavior at nozzle exit is difficult (Figure 4-22) and run 7 simulations led to comments similar to the ones stated in previous paragraph for run 6 (see Figure 4-26 for further details).

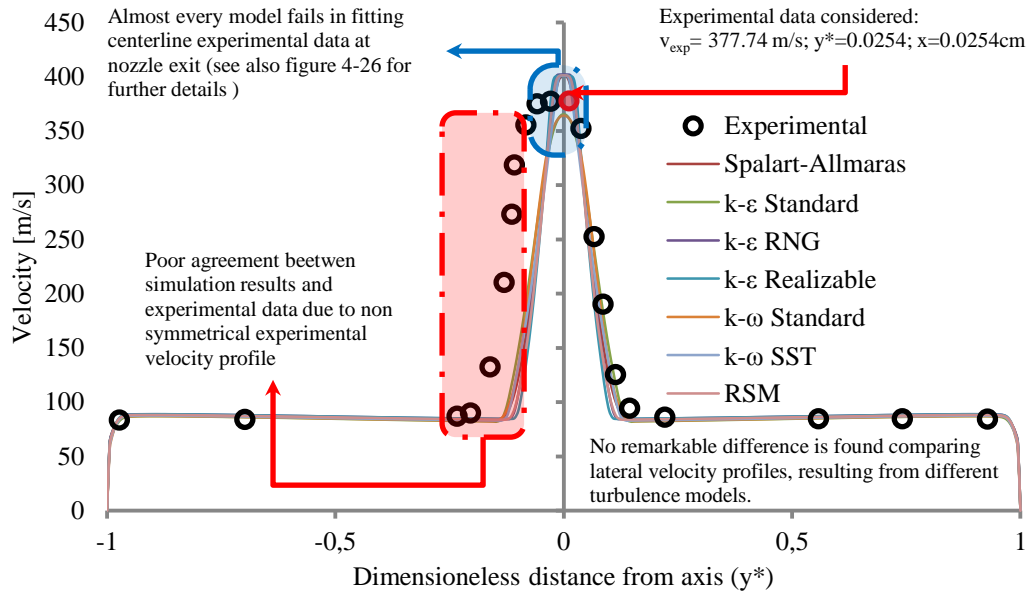


Figure 4-26 Considerations about velocity profiles at  $x = 2.54\text{cm}$  (run 6)

Due to the failure of every turbulence model in fitting centerline data point, Figure 4-27 compares velocity contours at nozzle exit for  $k - \epsilon$  Standard and  $k - \epsilon$  Realizable: the former underestimate experimental data and the latter overestimate (Table 4-12).

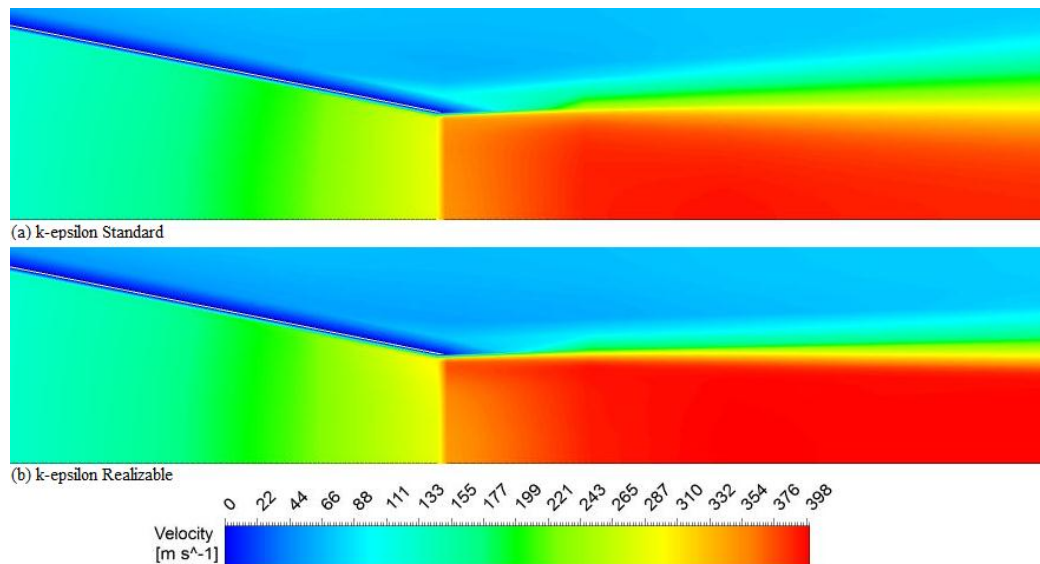


Figure 4-27 Run 7 nozzle exit velocity contours for (a)  $k - \varepsilon$  Standard and (b)  $k - \varepsilon$  Realizable

	<i>Spalart Allmaras</i>	$k - \varepsilon$ Standard	$k - \varepsilon$ RNG	$k - \varepsilon$ Realizable	$k - \omega$ Standard	$k - \omega$ SST	RSM
$v_{CFD}$ [m/s]	395.88	361.50	401.76	400.58	361.45	397.55	400.07
Error [%]	4.80	-4.30	6.36	6.05	-4.31	5.24	5.91

Table 4-12 Comparison between experimental data and simulation results for data point  $x = 2.54cm$ ,  $y^* = 0.0115$  and  $v_{exp} = 377.74$  m/s

Near downstream nozzle exit (Figure 4-23), there are remarkable differences between experimental data and simulation results (Table 4-13); moreover, in this sections, the choice of turbulence model is very important. Results obtained leads to similar consideration as the ones stated for run 6: (i)  $k - \varepsilon$  Realizable (the worst)  $k - \varepsilon$  RNG and RSM: overestimate centerline values and they are completely unable to predict lateral values; (ii)  $k - \omega$  Standard,  $k - \omega$  SST and *Spalart – Allmaras*: they all have overall good performance for both centerline and lateral data; (iii)  $k - \varepsilon$  Standard: is the turbulence model that is able to provide accurate results for this section.

	<i>Spalart Allmaras</i>	$k - \varepsilon$ Standard	$k - \varepsilon$ RNG	$k - \varepsilon$ Realizable	$k - \omega$ Standard	$k - \omega$ SST	RSM
$v_{CFD}$ [m/s]	298.30	283.04	313.90	325.87	290.32	292.63	313.90
Error [%]	5.16	-0.22	10.66	14.88	2.35	3.16	10.66

Table 4-13 Comparison between experimental data and simulation results for data point  $y^* = 0.00679$ ,  $x = 7.62cm$  and  $v_{exp} = 283.66$  m/s

Further downstream (Figure 4-24, Figure 4-25, and Table 4-14), simulations are able to fit experimental data trend with good accuracy Results obtained leads to the same consideration as the ones stated for run 6: (i)  $k - \varepsilon$  Realizable (the worst),  $k - \omega$  Standard and RSM: they all overestimate centerline values and underestimate lateral values; (ii)  $k - \omega$  Standard and  $k - \varepsilon$  RNG: they all have overall good performance for both centerline and lateral data; (iii) *Spalart – Allmaras* and  $k - \omega$  SST: they are the turbulence models that are able to provide accurate results for this section.

	<i>Spalart Allmaras</i>	$k - \varepsilon$ Standard	$k - \varepsilon$ RNG	$k - \varepsilon$ Realizable	$k - \omega$ Standard	$k - \omega$ SST	RSM
<b>Experimental data: <math>x = 17.78cm</math>, <math>y^* = 0.0762</math>, <math>v_{exp} = 217.57</math> m/s</b>							
$v_{CFD}$ [m/s]	217.98	220.82	223.82	229.49	228.08	218.97	226.31
Error [%]	0.19	1.49	2.87	5.48	4.83	0.64	4.01
<b>Experimental data: <math>x = 26.67cm</math>, <math>y^* = 0.0762</math>, <math>v_{exp} = 193.52</math> m/s</b>							
$v_{CFD}$ [m/s]	190.44	195.82	192.63	200.56	200.27	194.75	198.60
Error [%]	-1.59	1.19	-0.46	3.63	.3.49	0.64	2.63

Table 4-14 Comparison between experimental data and simulation results

### 4.5.1.3 Run 9: Velocity

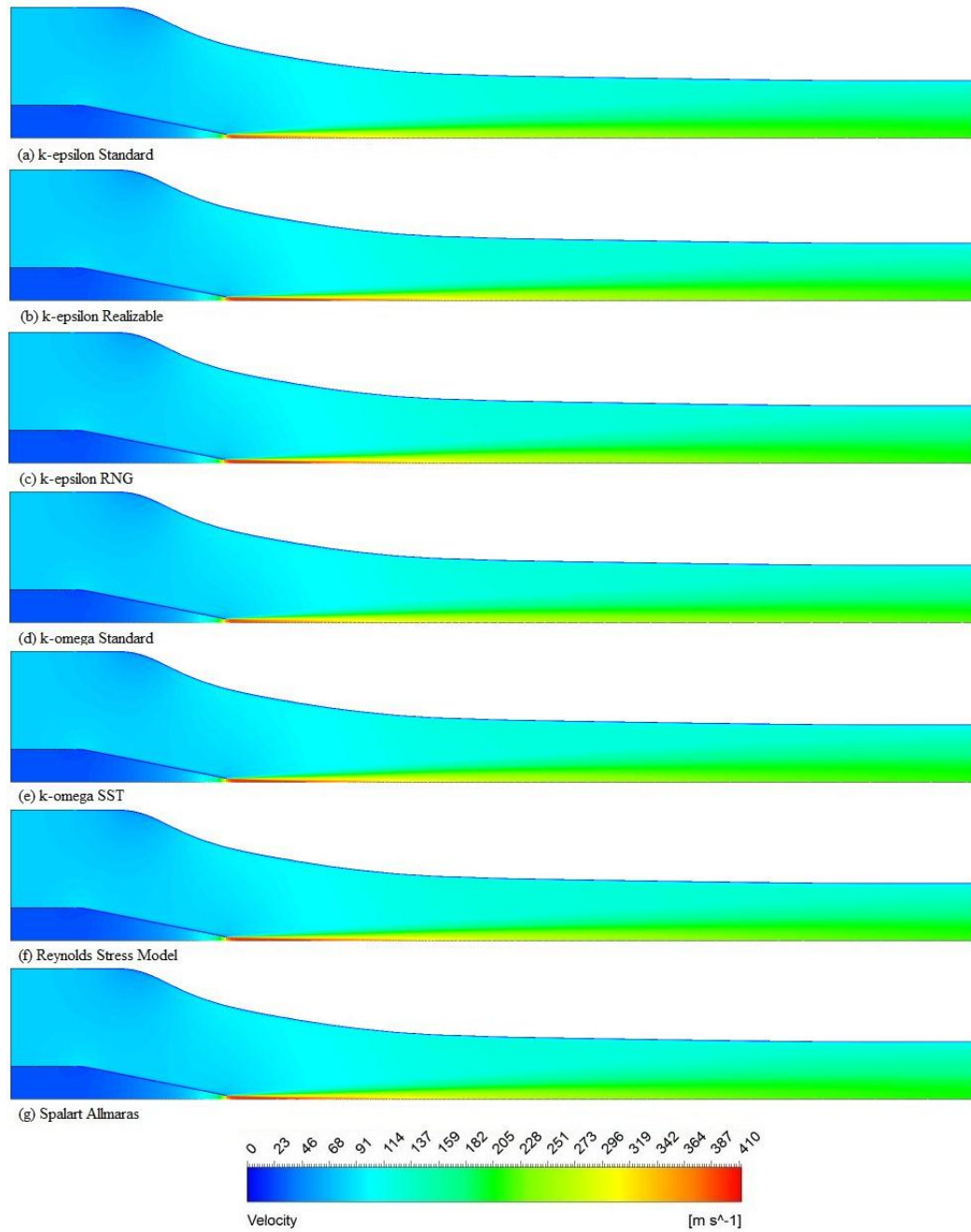


Figure 4-28 Velocity contours (run 9)

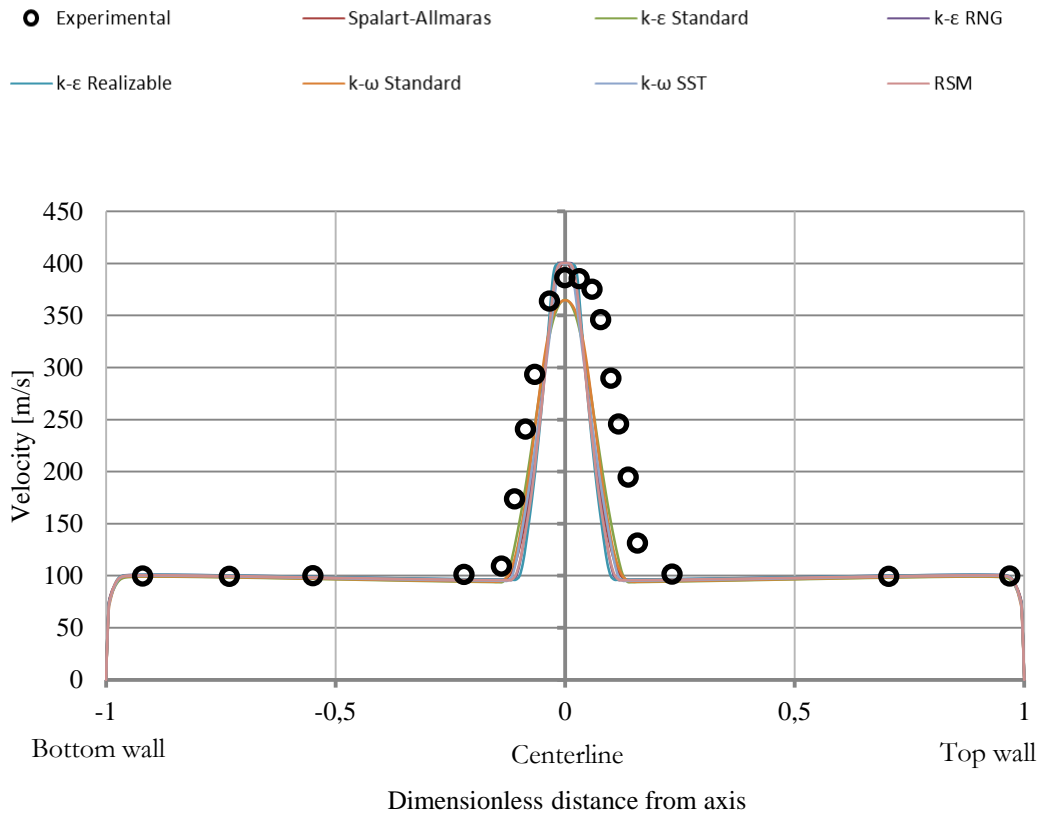


Figure 4-29 Velocity profiles at  $x = 2.54\text{cm}$  (run 9)

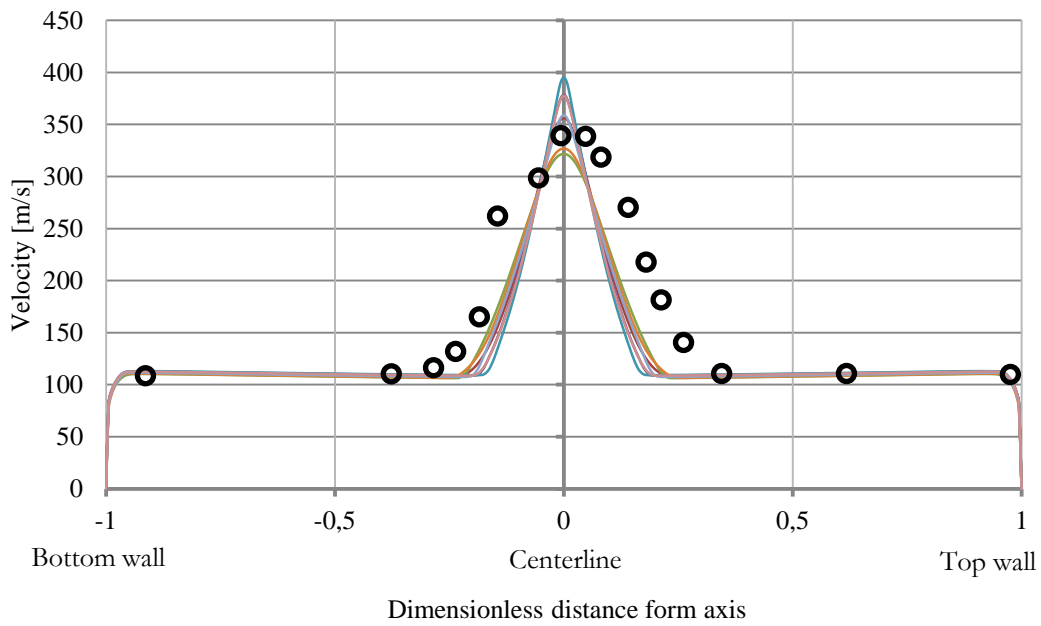
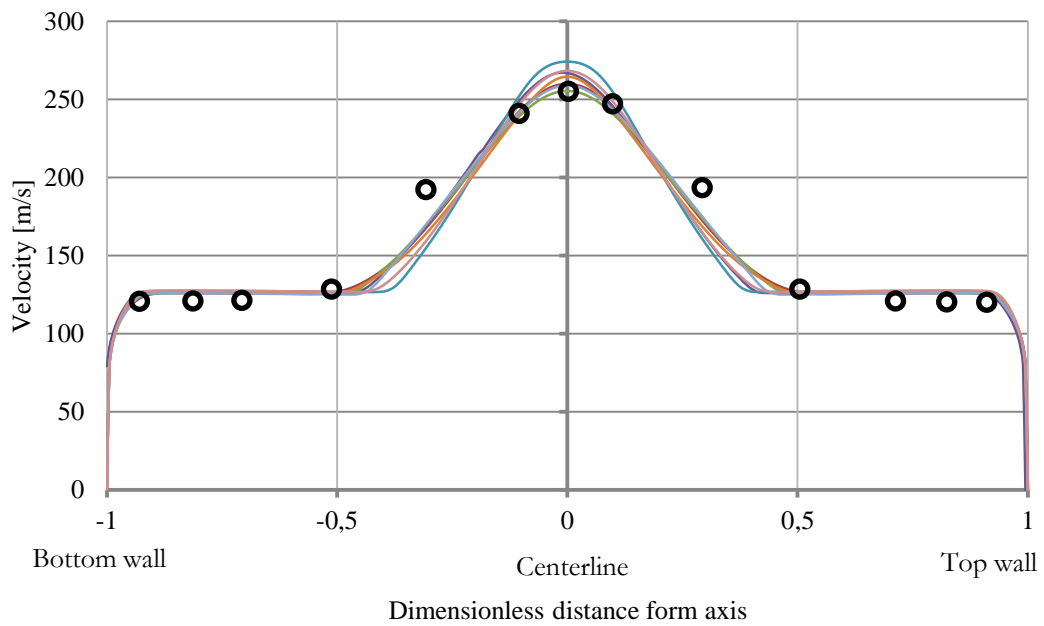
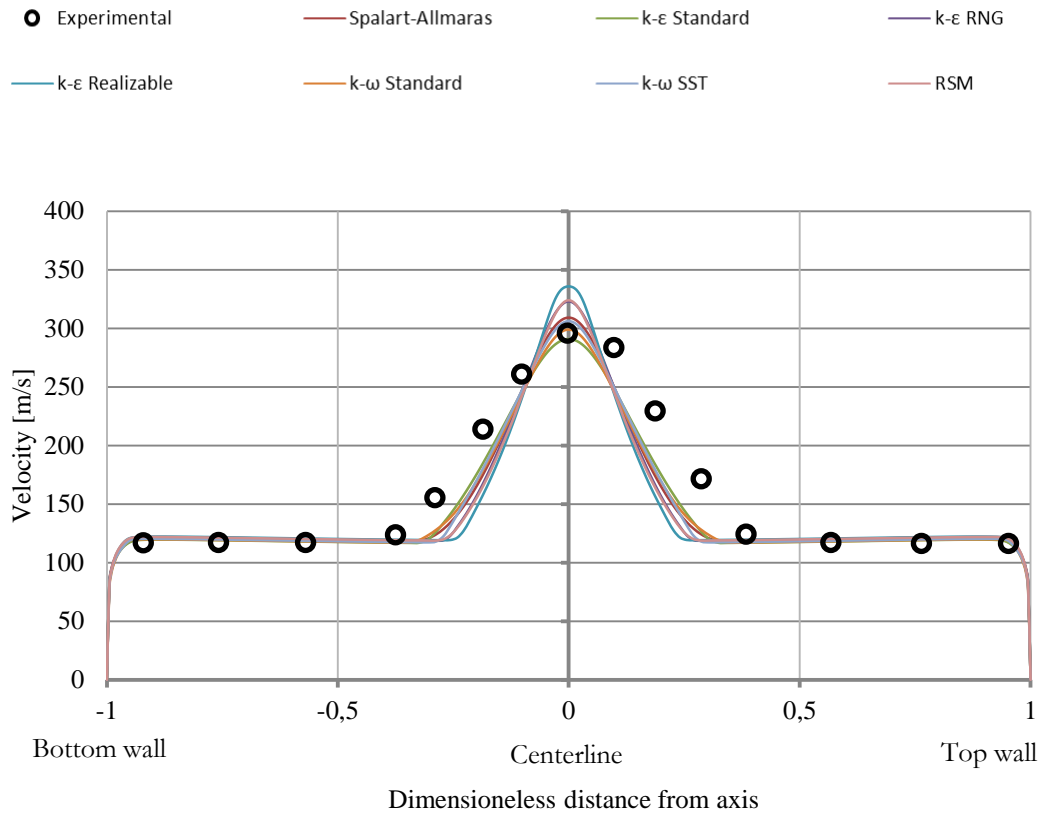


Figure 4-30 Velocity profiles at  $x = 5.08\text{cm}$  (run 9)



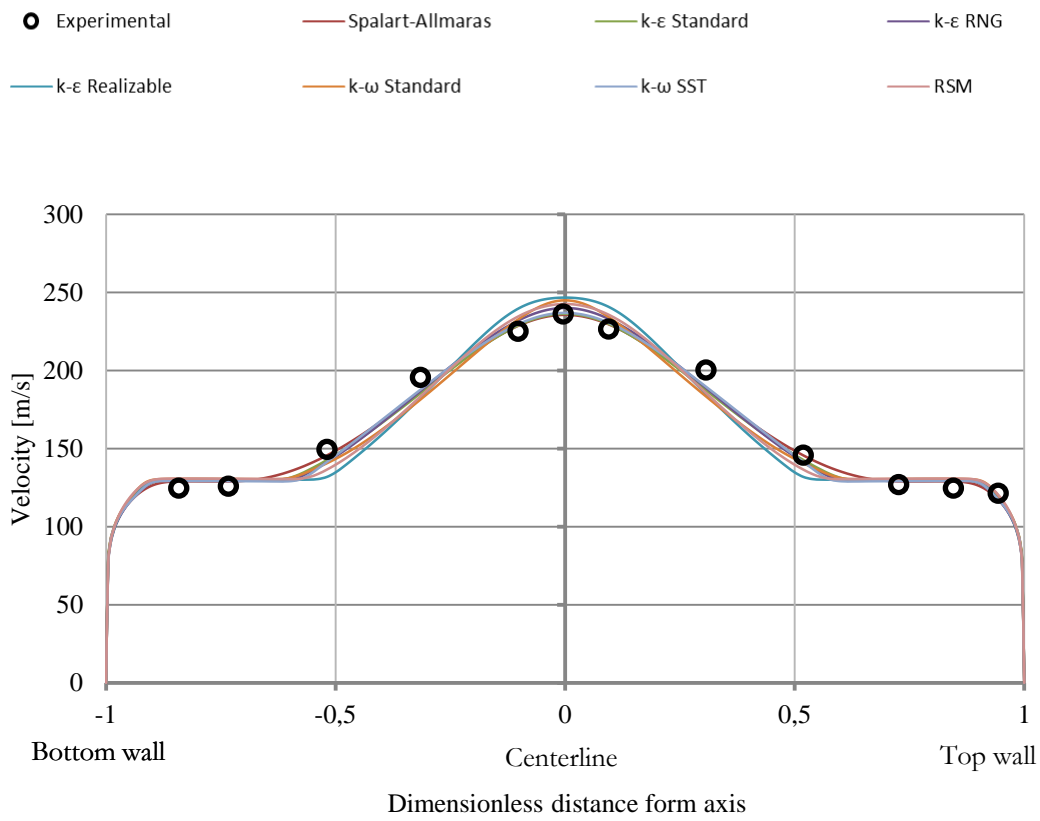


Figure 4-33 Velocity profiles at  $x = 17.78\text{cm}$  (run 9)

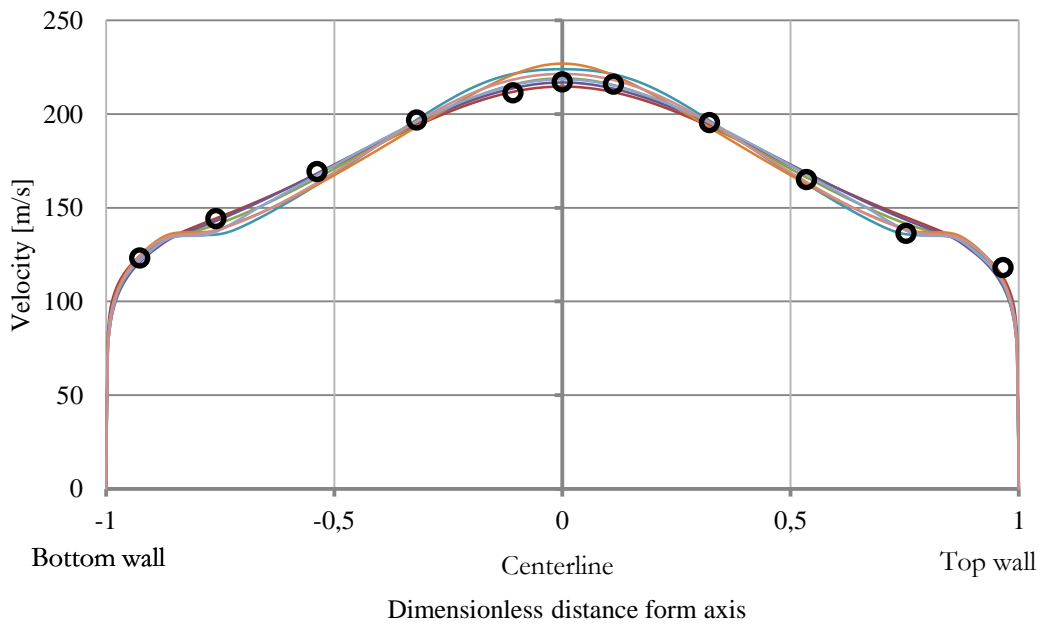


Figure 4-34 Velocity profiles at  $x = 26.67\text{cm}$  (run 9)



**Results considerations.** Benchmark used [137] provides more velocity profiles for run 9 than for run 6,7 and 10. This gives the opportunity of compare simulations results over a larger range of analysis.

As stated for run 6 and run 7, the simulation of jet behavior at nozzle exit is critical (Figure 4-22): also in this case every turbulence model fails in fitting centerline data point and there is poor agreement between simulation results and experimental data on lower-centerline zone (due to a non-symmetrical experimental velocity profile). Main difference between different RANS turbulence models (Table 4-9) is centerline velocity profile (Figure 4-26): as remarked in previous paragraph  $k - \varepsilon$  Standard and  $k - \omega$  Standard underestimate experimental data while other models overestimate. No remarkable difference is found comparing lateral velocity profiles

	<i>Spalart Allmaras</i>	$k - \varepsilon$ Standard	$k - \varepsilon$ RNG	$k - \varepsilon$ Realizable	$k - \omega$ Standard	$k - \omega$ SST	RSM
$v_{CFD}$ [m/s]	399.96	364.95	400.47	399.49	364.65	399.87	400.34
Error [%]	3.58	-5.48	3.71	3.46	-5.56	3.56	3.68

Table 4-15 Comparison between experimental data and simulation results for data point  $x = 2.54cm$ ,  $y^* = 0$  and  $v_{exp} = 386.13$  m/s

Near downstream nozzle exit (Figure 4-30 and Figure 4-31), there are remarkable differences between lateral experimental data and simulation results (Table 4-16);

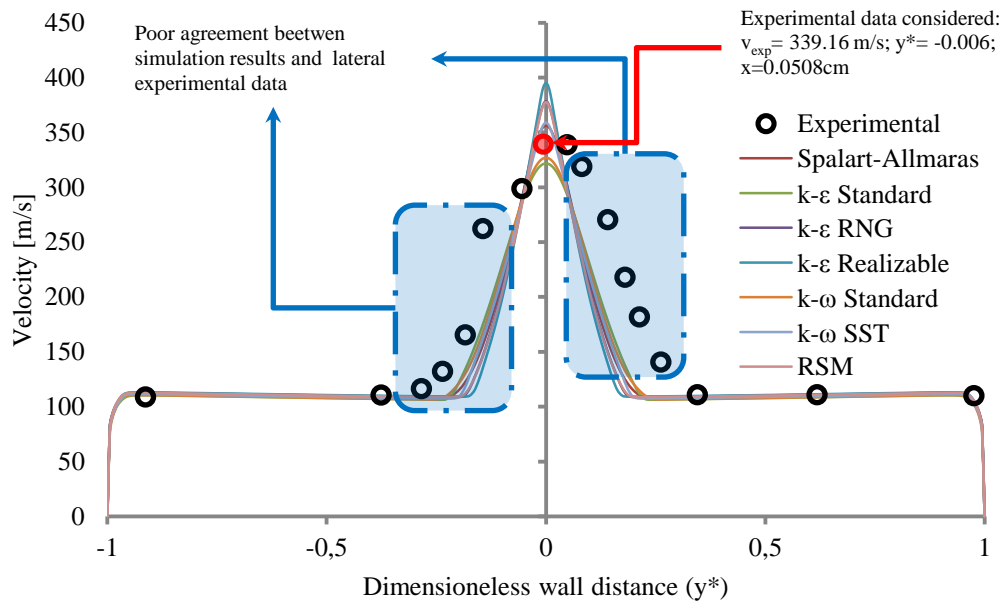


Figure 4-35 Considerations about velocity profiles at  $x = 5.08cm$  (run 9)

	<i>Spalart Allmaras</i>	$k - \varepsilon$ Standard	$k - \varepsilon$ RNG	$k - \varepsilon$ Realizable	$k - \omega$ Standard	$k - \omega$ SST	RSM
--	-------------------------	----------------------------	-----------------------	------------------------------	-----------------------	------------------	-----

<b>Experimental data: <math>x = 5.08\text{cm}, y^* = -0.006, v_{\text{exp}} = 339.16\text{ m/s}</math></b>							
$v_{CFD}$ [m/s]	354.84	321.15	375.45	391.03	326.29	356.64	374.57
Error [%]	4.62	-5.31	10.70	15.30	-3.79	5.15	10.44
<b>Experimental data: <math>x = 7.62\text{cm}, y^* = -0.003, v_{\text{exp}} = 295.85\text{ m/s}</math></b>							
$v_{CFD}$ [m/s]	309.05	290.83	322.79	335.69	298.88	305.97	323.72
Error [%]	4.46	-1.70	9.11	13.47	1.02	3.42	9.42

Table 4-16 Comparison between experimental data and simulation results

In this sections, the choice of turbulence model is very important (Figure 4-35 and Table 4-16); comparison between simulation results and experimental data, the considerations stated in previous paragraphs are confirmed:

- $k - \varepsilon$  Realizable (the worst)  $k - \varepsilon$  RNG and RSM: largely overestimate centerline values and are unable to predict lateral values;
- $k - \omega$  Standard,  $k - \omega$  SST and Spalart – Allmaras: they all have overall good performance for both centerline and lateral data;
- $k - \varepsilon$  Standard : is the turbulence model that is able to provide accurate results for this section.

Further downstream (Figure 4-32, Figure 4-33, Figure 4-34, and Table 4-17), simulations are able to trace overall experimental data trend with good accuracy:

- $k - \varepsilon$  Realizable (the worst),  $k - \omega$  Standard and RSM : they all overestimate centerline values and underestimate lateral values;
- $k - \omega$  Standard and  $k - \varepsilon$  RNG: they all have overall good performance for both centerline and lateral data;
- Spalart – Allmaras and  $k - \omega$  SST: they are the turbulence models that are able to provide very accurate results for this section.

	Spalart Allmaras	$k - \varepsilon$ Standard	$k - \varepsilon$ RNG	$k - \varepsilon$ Realizable	$k - \omega$ Standard	$k - \omega$ SST	RSM
<b>Experimental data: <math>x = 12.7\text{cm}, y^* = 00.02, v_{\text{exp}} = 295.85\text{ m/s}</math></b>							
$v_{CFD}$ [m/s]	260.27	255.64	267.51	274.40	264.94	259.18	268.64
Error [%]	2.08	0.26	4.91	7.62	3.91	1.65	5.36
<b>Experimental data: <math>x = 17.78\text{cm}, y^* = -0.004, v_{\text{exp}} = 295.85\text{ m/s}</math></b>							
$v_{CFD}$ [m/s]	235.59	236.26	240.01	246.65	244.84	236.84	242.56
Error [%]	-0.20	0.08	1.67	4.48	3.72	0.33	2.75
<b>Experimental data: <math>x = 26.67\text{cm}, y^* = 0, v_{\text{exp}} = 295.85\text{ m/s}</math></b>							
$v_{CFD}$ [m/s]	214.68	219.05	216.84	223.95	226.91	218.54	221.43
Error [%]	-1.14	0.87	-0.15	3.13	4.49	0.64	1.97

Table 4-17 Comparison between experimental data and simulation results

#### 4.5.1.4 Run 9: Total Temperature

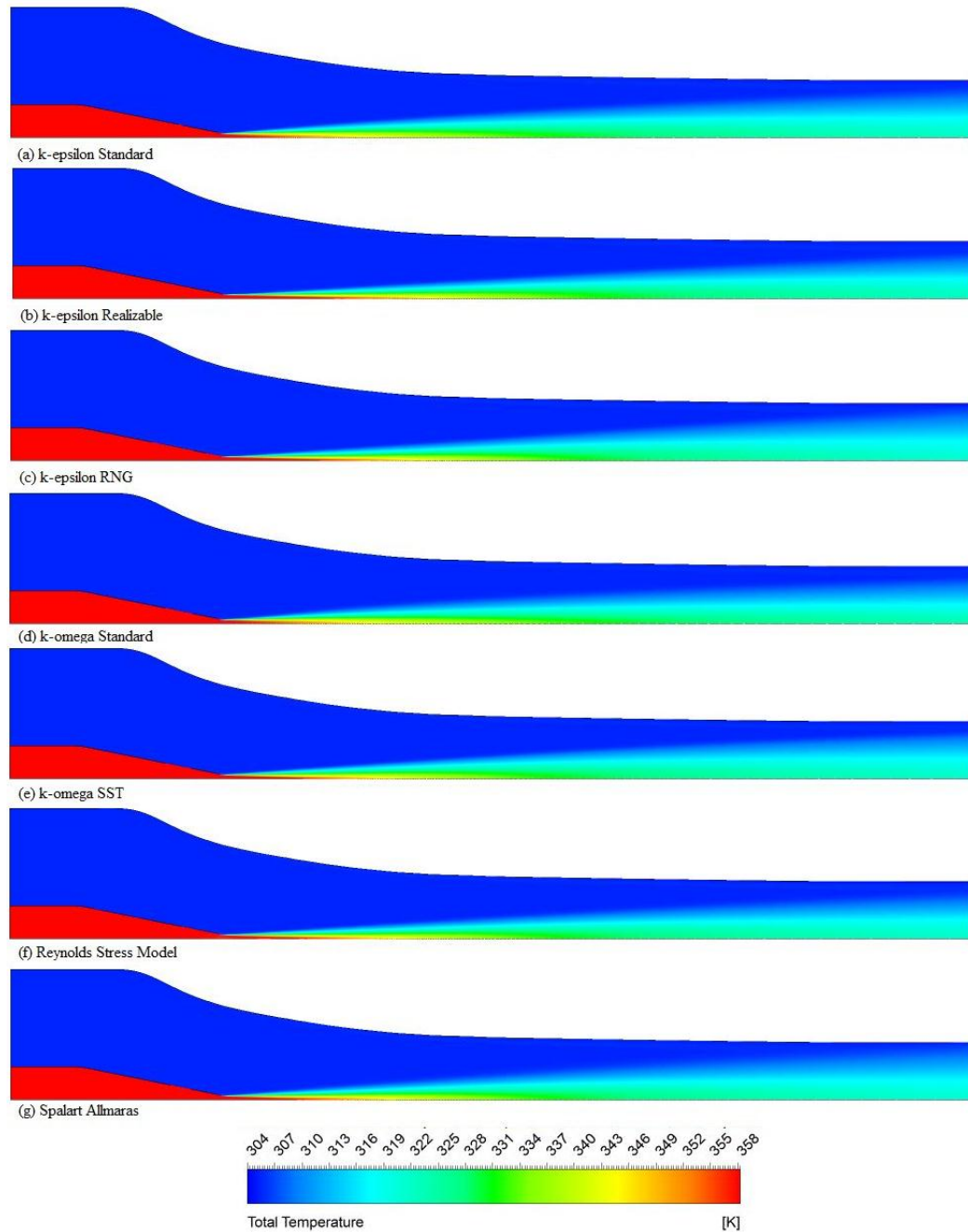


Figure 4-36 Total temperature contours (run 9)

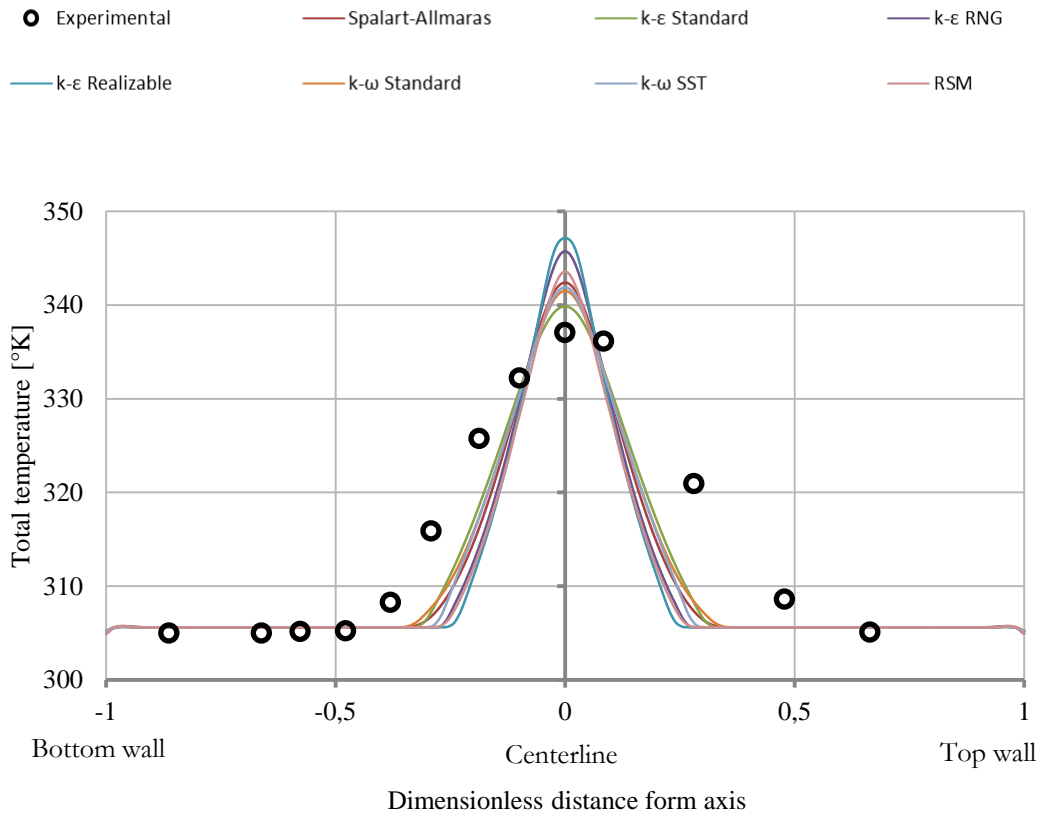


Figure 4-37 Total temperature profiles at  $x = 7.62\text{cm}$  (run 9)

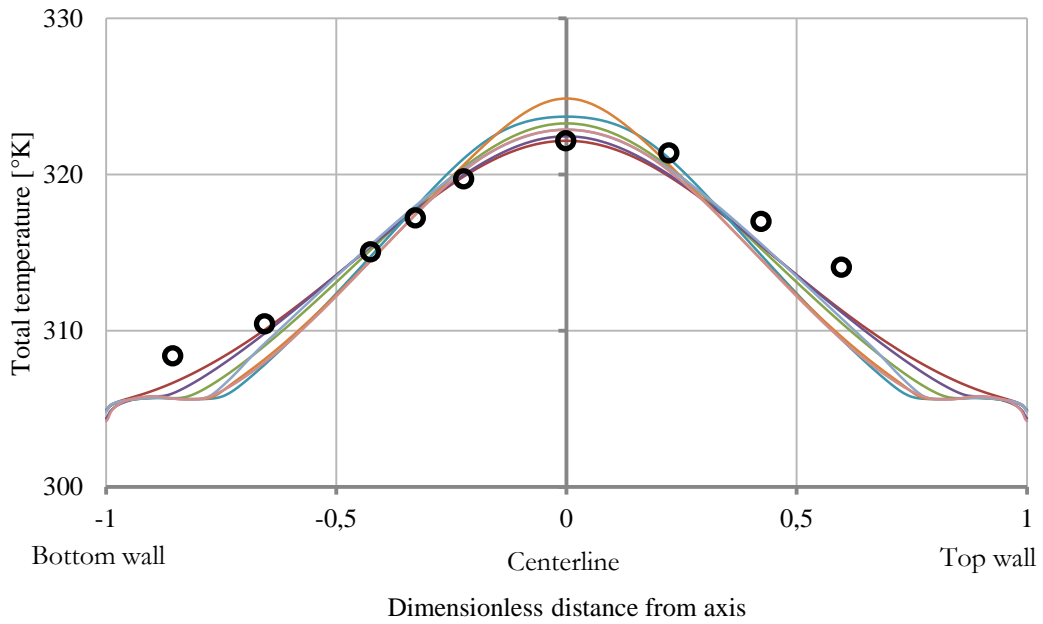


Figure 4-38 Total temperature profiles at  $x = 26.67\text{cm}$  (run 9)

**Results considerations.** Benchmark used [137] provides two total temperature profiles that are very useful to validate CFD approach using consideration about thermal field too. Jet behavior at nozzle exit is very difficult to be simulated: here every model fails in fitting correct experimental data (Figure 4-37)

	<i>Spalart Allmaras</i>	<i>k - ε Standard</i>	<i>k - ε RNG</i>	<i>k - ε Realizable</i>	<i>k-ω Standard</i>	<i>k - ω SST</i>	<i>RSM</i>
$T_{0,CFD}$ [m/s]	342.39	339.86	345.73	347.15	341.50	341.90	343.56
Error [%]	1.58	0.83	2.57	2.99	1.32	1.44	1.93

Table 4-18 Comparison between experimental data and simulation results for data point  $x = 7.62\text{cm}$ ,  $y^* = 0$  and  $T_{0,\text{exp}} = 337.06\text{ K}$

Due to the failure of every turbulence model in fitting centerline data point, Figure 4-39 compares velocity contours at nozzle exit for *k - ε Standard* and *k - ε Realizable*.

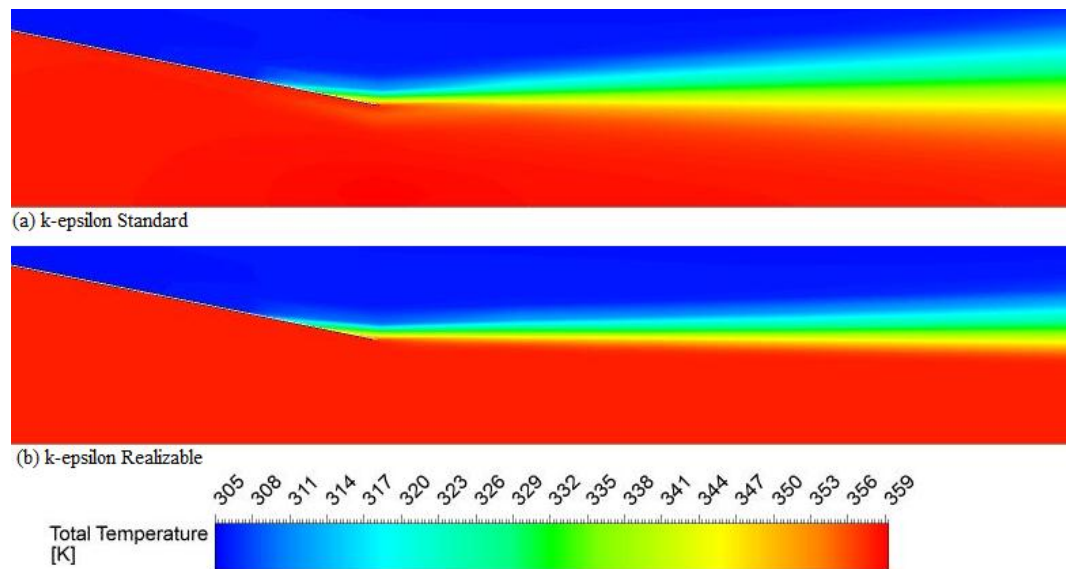


Figure 4-39 Run 9 nozzle exit total temperature contours for (a) *k - ε Standard* and (b) *k - ε Realizable*

Downstream temperature profile are better outlined by every model (except *k - ω Standard*): best model to predict temperature flow field is *Spalart-Allmaras*.

	<i>Spalart Allmaras</i>	<i>k - ε Standard</i>	<i>k - ε RNG</i>	<i>k - ε Realizable</i>	<i>k-ω Standard</i>	<i>k - ω SST</i>	<i>RSM</i>
$T_{0,CFD}$ [m/s]	322.16	323.27	322.44	323.70	324.86	322.87	322.87
Error [%]	-0.003	0.34	0.09	0.48	0.84	0.22	0.22

Table 4-19 Comparison between experimental data and simulation results for data point  $x = 26.67\text{cm}$ ,  $y^* = -0.01$  and  $T_{0,\text{exp}} = 322.17\text{ K}$

### 4.5.1.5 Run 10: velocity

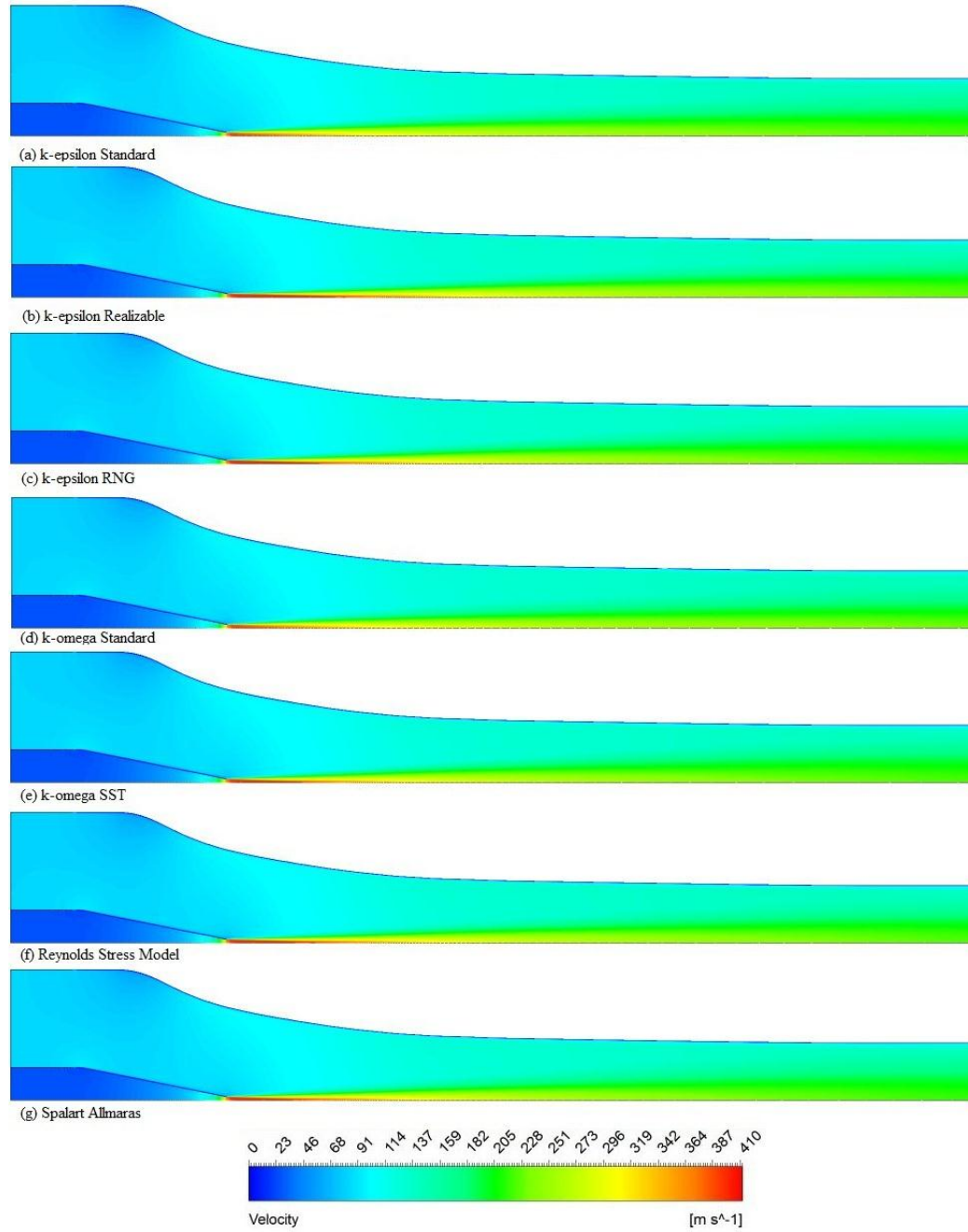
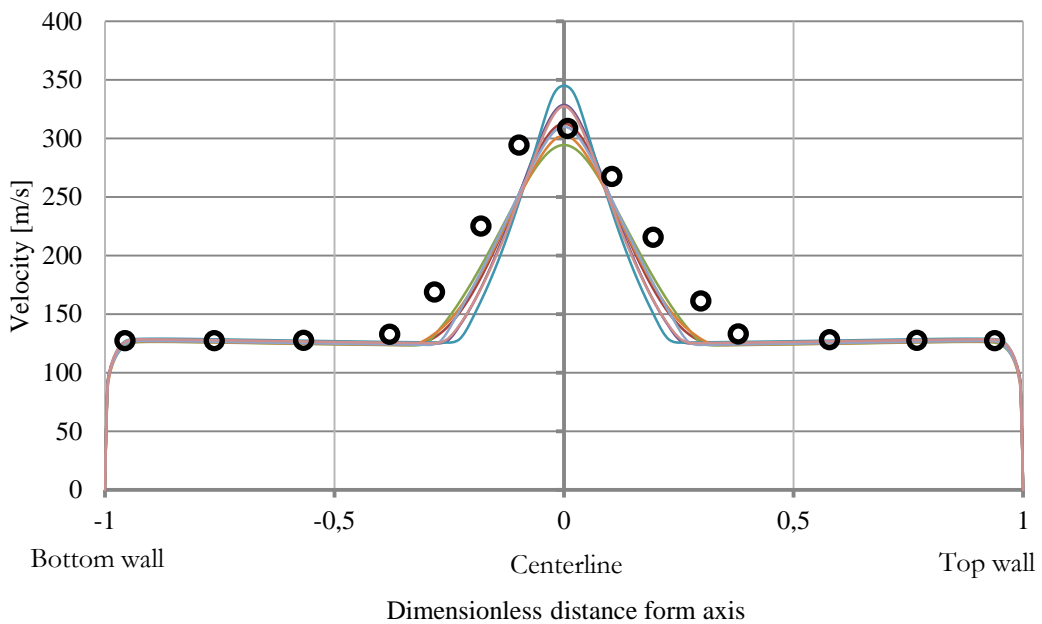
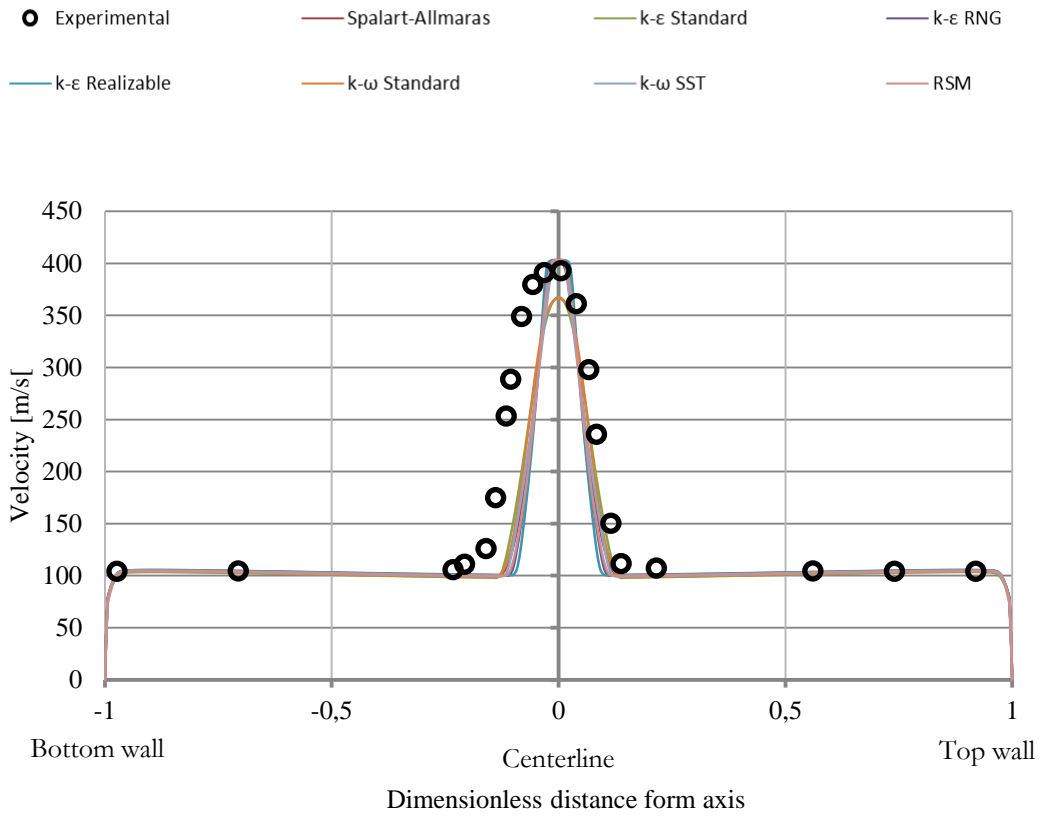


Figure 4-40 Velocity contours (run 10)



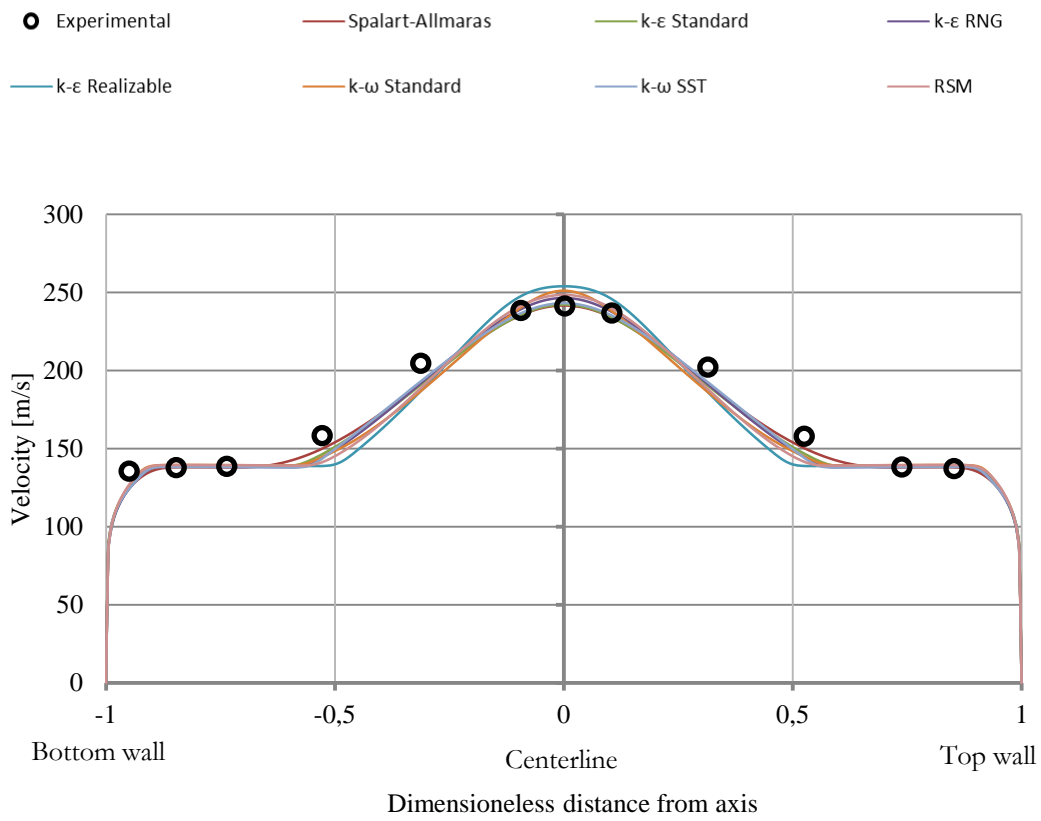


Figure 4-43 Velocity profiles at  $x = 17.78cm$  (run 10)

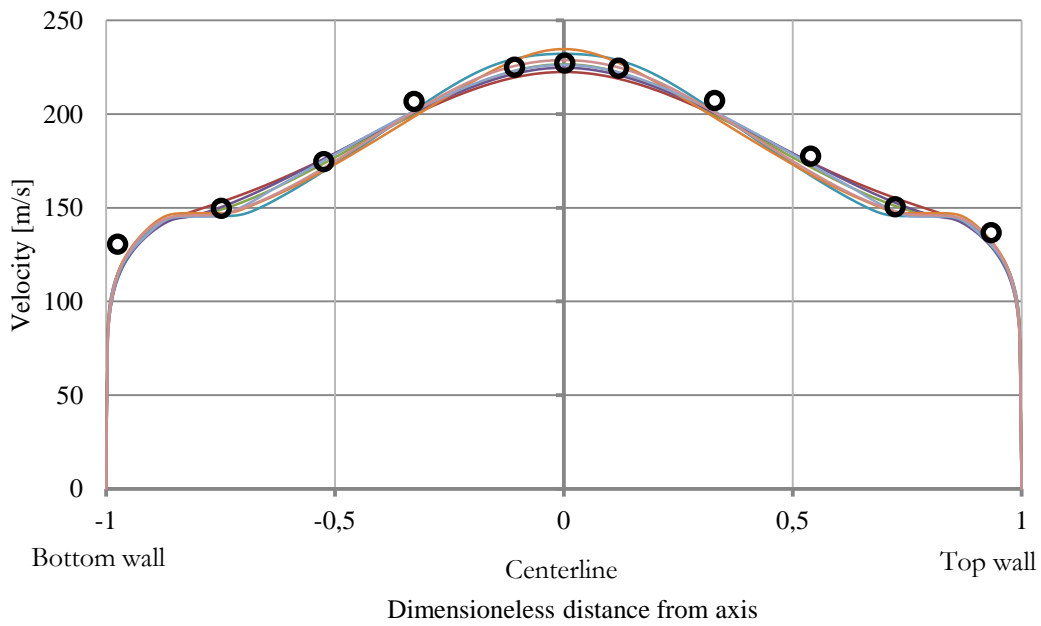


Figure 4-44 Velocity profiles at  $x = 26.67cm$  (run 10)



**Results considerations.** Run 10 simulation results confirm considerations stated before for run 6, run 7 and run 9. Here are remarked main considerations, using also quantitative results reported in Table 4-20, which is focused on centerline data.

	<i>Spalart Allmaras</i>	<i>k – ε Standard</i>	<i>k – ε RNG</i>	<i>k – ε Realizable</i>	<i>k – ω Standard</i>	<i>k – ω SST</i>	<i>RSM</i>
<b>Experimental data: <math>x = 2.54\text{cm}</math>, <math>y^* = 0.0056</math>, <math>v_{\text{exp}} = 392.57\text{ m/s}</math></b>							
$v_{\text{CFD}}$ [m/s]	402.04	366.52	403.23	402.57	365.79	402.88	403.27
Error [%]	2.41	-6.64	2.72	2.55	-6.82	2.63	2.73
<b>Experimental data: <math>x = 7.62\text{cm}</math>, <math>y^* = 0.00796</math>, <math>v_{\text{exp}} = 308.21\text{ m/s}</math></b>							
$v_{\text{CFD}}$ [m/s]	312.02	293.96	327.65	344.15	301.73	309.31	326.27
Error [%]	1.24	-4.62	6.31	11.66	-2.10	0.36	5.86
<b>Experimental data: <math>x = 17.78\text{cm}</math>, <math>y^* = 0.0025</math>, <math>v_{\text{exp}} = 241.28\text{ m/s}</math></b>							
$v_{\text{CFD}}$ [m/s]	241.60	242.18	246.44	253.92	251.02	243.08	248.41
Error [%]	0.13	0.37	2.14	5.24	4.04	0.75	2.96
<b>Experimental data: <math>x = 26.67\text{cm}</math>, <math>y^* = 0.0029</math>, <math>v_{\text{exp}} = 227.22\text{ m/s}</math></b>							
$v_{\text{CFD}}$ [m/s]	222.41	226.52	224.69	232.12	234.62	226.18	228.75
Error [%]	-2.12	-0.31	-1.11	2.16	3.26	-0.46	0.68

Table 4-20 Comparison between experimental data and simulation results

At nozzle exit, at  $x = 2.54\text{cm}$  (Figure 4-41), the simulation of jet behavior is very difficult and every turbulence model fails in fitting centerline data point. Main difference between different RANS turbulence models is centerline velocity profile (Figure 4-26): also in this case  $k - \varepsilon$  Standard and  $k - \omega$  Standard underestimate experimental data while other models overestimate. No remarkable difference is found comparing lateral velocity profiles

Near downstream nozzle exit, at  $x = 7.62\text{cm}$  (Figure 4-42), the choice of turbulence model is very important: (i)  $k - \varepsilon$  Realizable (the worst),  $k - \varepsilon$  RNG and RSM largely overestimate centerline values and are completely unable to predict lateral values; (ii)  $k - \omega$  Standard,  $k - \omega$  SST and Spalart – Allmaras have overall good performance for both centerline and lateral data; (iii)  $k - \varepsilon$  Standard is best turbulence model for this section.

Further downstream (Figure 4-43 and Figure 4-44), simulations are able to trace overall experimental data trend with good accuracy, with following remarks: (i)  $k - \varepsilon$  Realizable (the worst),  $k - \omega$  Standard and RSM overestimate centerline values and underestimate lateral values; (ii)  $k - \omega$  Standard and  $k - \varepsilon$  RNG have overall good performance for both centerline and lateral data; (iii), Spalart – Allmaras and  $k - \omega$  SST are best turbulence model for downstream sections.

### 4.5.2 Calculation validation and critical review of the model

Ultimate model is the result of a cyclic process:

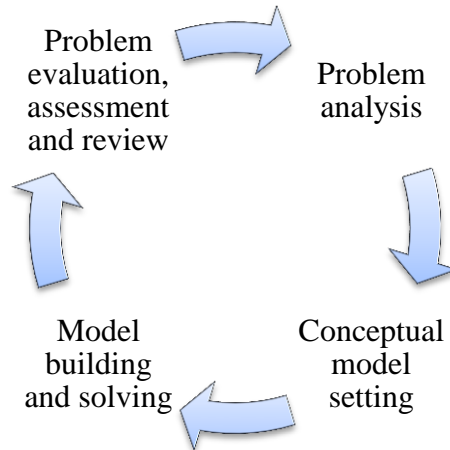


Figure 4-45 CFD cyclic process

Cyclic process allowed developing a high quality mesh (that lets stable simulations) and established a model that provide results in very good agreement with benchmark data; it's important to point out that:

- mesh has been modified not only for quality purpose but also for stable simulation running and in order to have a  $y_{wall}^+$  suitable for the chosen wall treatment;
- the influence of different numerical method settings on results have been analyzed: in previous section best combination of methods have been presented.

### 4.5.3 Strategy improvement

In this study was not performed calibration of turbulence model constants: an improvement can be reached by investigating the role of closure coefficients for ejector flow mixing.

## 4.6 Important remarks

This chapter provided an approach to CFD ejector modeling which have been applied to the case of a subsonic ejector. In this section major remarks are presented.

### 4.6.1 Turbulence models performance comparison

Validation reported in previous sections provided a turbulence models comparison for the case of a subsonic ejector: this is important because up today in literature information on turbulence models performance can only be found for supersonic ejectors. RANS turbulence models performance will be evaluated basing on: (i) convergence behavior, (ii) flow field and (iii) thermal field.

#### 4.6.1.1 Convergence behavior

Convergence is supposed to be achieved when criteria exposed in section 4.4.3.2 are reached: (i) residuals, (ii) local quantities and (iii) global quantities:

- $k - \varepsilon$ : there is no convergence problem and convergence is fast;
- $k - \varepsilon RNG$ : there are convergence problems and simulations are very sensible to boundary conditions;
- $k - \varepsilon Realizable$ : simulation are quite sensible to boundary conditions, which carry to slight convergence problems;
- $k - \omega$ : convergence is reached very slowly (more that the double of other models iterations are needed);
- $k - \omega SST$ : there is no convergence problem and convergence is reached fast (it's important to point out that just after flow behavior is stabilized courant number can be increased without stability problems and with minimal variation on simulation results);
- *Spalart - Allmaras*: its behavior is very similar to the one of  $k - \omega SST$ , but convergence is reached more quickly due to the fact that this is a one equation model and not a two equation one;
- *RSM*: there are convergence problems and simulations are very sensible to boundary conditions.

#### 4.6.1.3 Flow field (comparison with velocity data)

This performance comparison has been performed using data and simulation results of run 6, 7, 9, 10 reported in section 4.5.1:

- $k - \varepsilon$ : at nozzle exit this model large underestimate experimental data while downstream there is good agreement between simulation results and experimental data;
- $k - \varepsilon RNG$ : at nozzle exit this model large overestimate experimental data while downstream there is good agreement between simulation results and experimental data;
- $k - \varepsilon Realizable$ : this turbulence model provides results that by far overestimate experimental data form nozzle exit to diffuser inlet;
- $k - \omega$ : at nozzle exit this model large underestimates experimental data and at diffuser inlet it overestimate by far them (more than  $k - \varepsilon Realizable$  model);

- $k - \omega$  SST: at nozzle exit it slightly overestimates experimental data, but just near downstream it's able to correctly represent experimental data;
- Spalart – Allmaras: it has a similar behavior to the one of  $k - \omega$  SST, with a slightly better performance for bottom and top wall data;
- RSM: at nozzle exit this model large underestimate experimental data while downstream there is a slightly data overestimation.

Previous works [119], [138], [139], [140] reported discrepancies between simulation results and experimental data near to ejector nozzle, while downstream good agreement is achieved: model proposed above had better performance than previous one in representing flow field.

#### 4.6.1.2 Thermal field (comparison with temperature data)

This performance comparison has been performed using data and simulation results of run 9 in two section, which are reported here for the sake of clearness.

In the section near ejector nozzle almost every model had difficulties in fitting experimental data and overestimated centerline values.

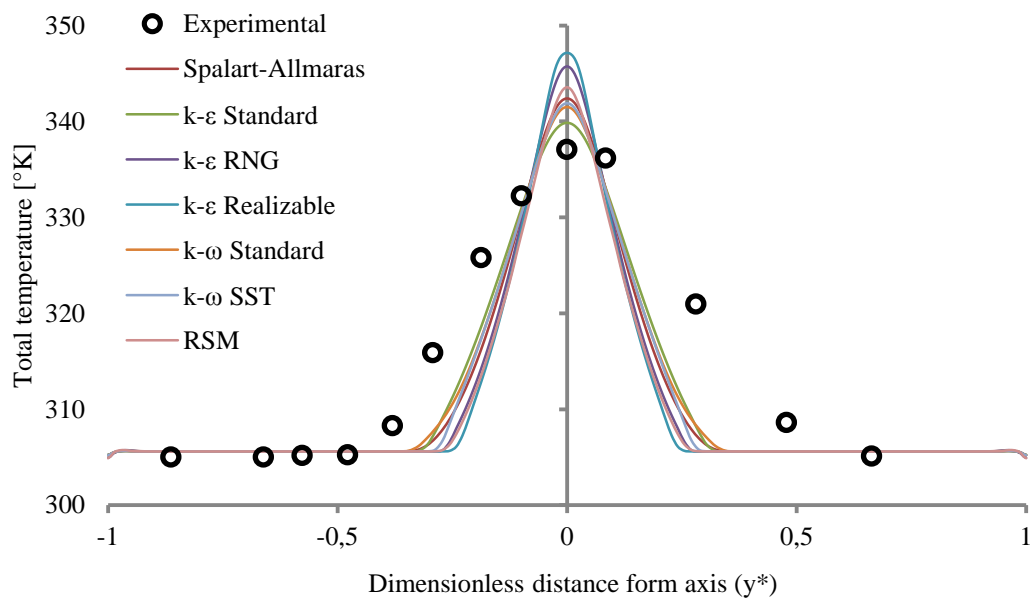


Figure 4-46 Total temperature profiles at  $x = 7.62\text{cm}$  (run 9)

Downstream temperature profile are better outlined by every model (except  $k - \omega$ ), but the best models to predict temperature flow field are Spalart-Allmaras while  $k - \omega$  SST under predict later values.

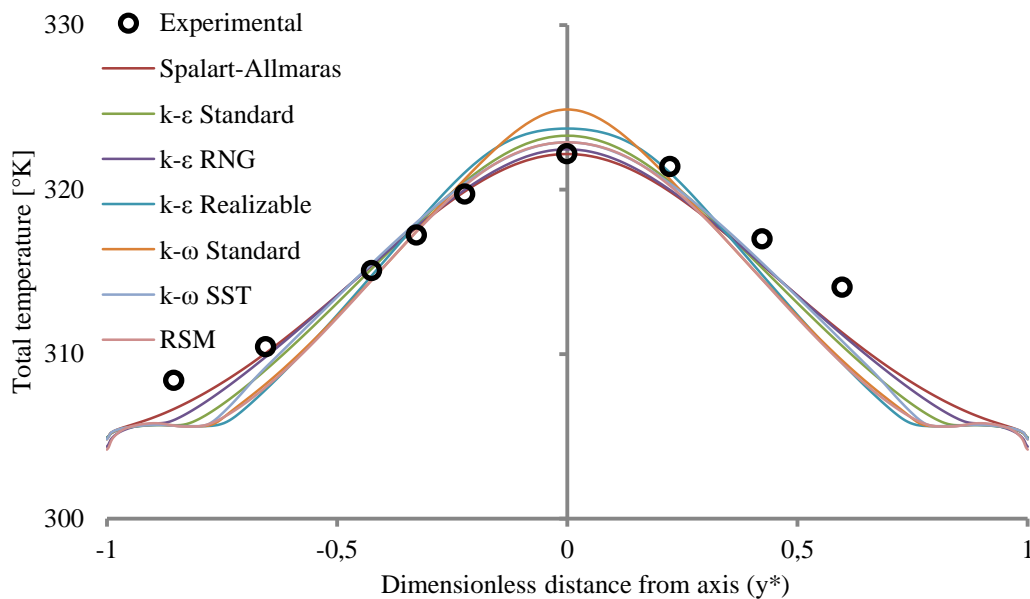


Figure 4-47 Total temperature profiles at  $x = 26.67\text{cm}$  (run 9)

Those results are coherent with previous works performed on the benchmark chosen: difficulties were encountered in representing temperature flow fields, but our numerical results are by far in better agreement with experimental data than previous works were.

#### 4.6.1.4 Results

Due to previous consideration, we conclude that the CFD approach presented here is an improvement compared to past studies [119], [138], [139], [140].

As results we propose Spalart-Allmaras and  $k - \omega SST$  as the turbulence models recommended for subsonic ejector simulation; taking into account that previous works [24] proposed  $k - \varepsilon RNG$  and  $k - \omega SST$  as turbulence models advised for supersonic ejector simulations,  $k - \omega SST$  is marked as the turbulence model to be used in ejector simulation, regardless of nozzle geometry (for both subsonic and supersonic ejector).

#### 4.6.2 Approach and guidelines for CFD ejector modeling.

Beyond general guidelines in CFD ejector modeling provided in section 2.4.2 (that came out from bibliographical review), this chapter provides step by step indications to build up a CFD approach for ejector, in the frame of the  $Q^3$  approach.

Moreover the approach presented was applied to the case of a subsonic ejector, providing an application of the guidelines proposed.

### **4.6.3 Applications**

The subsonic ejector CFD approach presented here will be applied in next chapter and, along with thermodynamic model (Chapter 3) is one of the basis of the integrated thermodynamic/CFD approach to ejector modeling.

# Chapter 5      Integration

---

“Everything should be made as simple as possible, but no simpler” (A. Einstein)

---

As remarked before, to improve ejectors performance it is very important to understand the internal fluid behavior in detail and CFD tools have been proved to be valuable tools for understanding and analyzing complex fluid flow problems, on the other side classic thermodynamic models cannot predict local phenomena: in this chapter an integrated model will be presented, which has the potentiality of overcoming thermodynamic model limitations.

In the first part of this chapter we will use the validated approach (Chapter 4) in order to investigate ejector flow fields and obtain ejector efficiencies.

In the second part the relations among ejector efficiencies and flow behaviors will be investigated: these results are the basis of the integrated thermodynamic/CFD approach.

In the third part will be explained how thermodynamic model and CFD approach integrate using results obtained in the first part: CFD analysis is used to implement in a 1D thermodynamic model the effects of the flow field over ejector efficiency through efficiency functions. It's clear how this method has potentiality of putting together the advantages of both thermodynamic models (less computational time and cost than experimental method for predicting ejector performance) and computational models (deep understanding of local interactions).

## **5.1 Part 1: application of the CFD approach**

The validated approach will be used to investigate ejector flow fields; here will be presented the range of analysis of Computational Fluid-Dynamics, resulting flow fields and efficiencies obtained.

### **5.1.1 Range of analysis**

#### **5.1.1.1 Primary range of analysis: primary mass flow rate variation**

Starting from benchmark case, named run 9, primary mass flow rate is changed. In Table 5-1 is reported this range of analysis.

	CASE number	$\dot{m}_p \left[ \frac{kg}{s \cdot m} \right]$	$\dot{m}_s \left[ \frac{kg}{s \cdot m} \right]$	$\omega$	$\Delta \dot{m}_p$ [%]
<b>Case base</b>	<b>Run 9</b>	<b>1.579</b>	<b>7.372</b>	<b>4.67</b>	<b>Case base</b>
Increasing primary mass flow rate	CASE1	0.197	7.372	37.36	-50.0
	CASE2	0.395	7.372	18.68	-75.0
	CASE3	0.789	7.372	9.34	-87.5
	CASE4	1.973	7.372	3.74	25.0
	CASE5	2.368	7.372	3.11	50.0
	CASE6	2.763	7.372	2.67	75.0
	CASE7	3.157	7.372	2.34	100.0
	CASE8	3.947	7.372	1.87	150.0
	CASE9	4.736	7.372	1.56	200.0
	CASE10	5.525	7.372	1.33	250.0
	CASE11	6.315	7.372	1.17	300.0
	CASE12	7.893	7.372	0.93	400.0
	CASE13	9.472	7.372	0.78	500.0
	CASE14	12.629	7.372	0.58	700.0

Table 5-1 Primary range of analysis

### 5.1.1.2 Secondary range of analysis: secondary mass flow rate variation.

Starting from primary range of analysis, secondary mass flow rate is changed. In Table 5-2 is reported this range of analysis: in column one case reference (from Table 5-1) is indicated, while in columns two information on  $\dot{m}_s$  variation are reported.

CASE reference	Secondary mass flow rate variation	CASE number	$\dot{m}_p \left[ \frac{kg}{s \cdot m} \right]$	$\dot{m}_s \left[ \frac{kg}{s \cdot m} \right]$	$\omega$	$\Delta \dot{m}_s$ [%]
CASE BASE	↑ Increasing	BASE1	1.579	3.686	2.34	-50
		BASE2	1.579	1.843	1.17	-75
	↓ Decreasing	BASE3	1.579	11.058	7.01	50



		BASE4	1.579	14.745	9.34	100
CASE1	↓ Decreasing	CASE1a	0.197	1.843	9.34	-75
	↑ Increasing	CASE1b	0.197	14.745	74.72	100
CASE2	↓ Decreasing	CASE2a	0.395	1.843	4.67	-75
	↑ Increasing	CASE2b	0.395	14.745	37.36	100
CASE3	↓ Decreasing	CASE3a	0.789	1.843	2.34	-75
	↑ Increasing	CASE3b	0.789	14.745	18.68	100
CASE4	↓ Decreasing	CASE4a	1.973	1.843	0.93	-75
	↑ Increasing	CASE4b	1.973	14.745	7.47	100
CASE5	↓ Decreasing	CASE5a	2.368	1.843	0.78	-75
	↑ Increasing	CASE5b	2.368	14.745	6.23	100
CASE6	↓ Decreasing	CASE6a	2.763	1.843	0.67	-75
	↑ Increasing	CASE6b	2.763	14.745	5.34	100
CASE7	↓ Decreasing	CASE7a	3.157	1.843	0.58	-75
	↑ Increasing	CASE7b	3.157	14.745	4.67	100
CASE8	↓ Decreasing	CASE8	3.947	1.843	0.47	-75
	↑ Increasing	CASE8b	3.947	14.745	3.74	100
CASE9	↓ Decreasing	CASE9a	4.736	1.843	0.39	-75
	↑ Increasing	CASE9b	4.736	14.745	3.11	100
CASE10	↓ Decreasing	CASE10a	5.525	1.843	0.33	-75
	↑ Increasing	CASE10b	5.525	14.745	2.67	100
CASE11	↓ Decreasing	CASE11a	6.315	1.843	0.29	-75
	↑ Increasing	CASE11b	6.315	14.745	2.34	100
CASE14	↑ Increasing	CASE14b	12.629	14.745	1.17	100

Table 5-2 Secondary range of analysis

## 5.2.2 Results

### 5.2.2.1 Efficiencies

In this work, the efficiencies were estimated according to the following definitions. Nozzles efficiencies were determined by comparing simulated enthalpies to an isentropic process:

1. primary nozzle:

$$\eta_p = \frac{h_{p,in} - h_{p,nozzle,exit}}{h_{p,in} - h_{p,nozzle,exit,is}} \quad (6.1)$$

2. suction:


$$\eta_s = \frac{h_{s,in} - h_{s,nozzle,exit}}{h_{s,in} - h_{s,nozzle,exit,is}} \quad (6.2)$$

Mixing efficiency is defined as a momentum transfer efficiency, taking into account both velocity and pressure contribution (in literature pressure contribution was always neglected); it's important to point out as mixing efficiency is evaluated from nozzle and suction exit to diffuser inlet (while in classical model it is supposed that mixing zone starts at some section downstream of nozzle exit): this choice is due to the very variety of flow behavior in a subsonic ejector (see next section) that make impossible to use a similar approach to the ones based on Munday and Bagster's theory [29] (section 2.2),

3. mixing:

$$\eta_{mix} = \frac{(\dot{m}_s + \dot{m}_p)v_{mix,out} + p_{mix,out}A_{mix,out}}{(\dot{m}_p v_{p,in,mix} + p_p A_{p,in,mix}) + (\dot{m}_s v_{s,in,mix} + p_s A_{s,in,mix})} \quad (6.3)$$

Input data were calculated as mass average quantities except for pressure, in which case area averaging was applied. Thermodynamic properties were evaluated using FluidProp [141] with air as working fluid and TPSI as thermodynamic library.

		CASE number	$\eta_p$	$\eta_s$	$\eta_{mix}$
		Case base	0.749	0.511	0.715
<b>Primary mass flow rate variation</b>  <b>Increasing primary mass flow rate</b> 		CASE1	0.519	0.528	0.677
		CASE2	0.537	0.530	0.680
		CASE3	0.599	0.529	0.688
		CASE4	0.795	0.504	0.728
		CASE5	0.831	0.493	0.743
		CASE6	0.856	0.477	0.758
		CASE7	0.878	0.475	0.774
		CASE8	0.903	0.455	0.799
		CASE9	0.921	0.442	0.820
		CASE10	0.934	0.434	0.838
		CASE11	0.945	0.434	0.854
		CASE12	0.946	0.459	0.875
		CASE13	0.947	0.463	0.890
		CASE14	0.950	0.494	0.907
Secondary mass flow rate variation starting from run9	↑ Increasing	BASE1	0.748	0.409	0.690
		BASE2	0.744	0.368	0.681
	↓ Decreasing	BASE3	0.746	0.595	0.734
		BASE4	0.754	0.654	0.742
Secondary mass flow rate variation starting from CASE 1	↓ Decreasing	CASE1a	0.477	0.441	0.620
	↑ Increasing	CASE1b	0.613	0.640	0.732
Secondary mass flow rate variation starting from CASE 2	↓ Decreasing	CASE2a	0.499	0.438	0.624
	↑ Increasing	CASE2b	0.629	0.644	0.733

Secondary mass flow rate variation starting from CASE 3	↓ Decreasing	CASE3a	0.578	0.421	0.637
	↑ Increasing	CASE3b	0.667	0.650	0.734
Secondary mass flow rate variation starting from CASE 4	↓ Decreasing	CASE4a	0.795	0.349	0.704
	↑ Increasing	CASE4b	0.795	0.653	0.746
Secondary mass flow rate variation starting from CASE 5	↓ Decreasing	CASE5a	0.831	0.312	0.729
	↑ Increasing	CASE5b	0.831	0.652	0.751
Secondary mass flow rate variation starting from CASE 6	↓ Decreasing	CASE6a	0.857	0.284	0.756
	↑ Increasing	CASE6b	0.857	0.655	0.757
Secondary mass flow rate variation starting from CASE 7	↓ Decreasing	CASE7a	0.876	0.246	0.790
	↑ Increasing	CASE7b	0.883	0.653	0.763
Secondary mass flow rate variation starting from CASE 8	↓ Decreasing	CASE8	0.903	0.197	0.837
	↑ Increasing	CASE8b	0.903	0.652	0.773
Secondary mass flow rate variation starting from CASE 9	↓ Decreasing	CASE9a	0.922	0.145	0.880
	↑ Increasing	CASE9b	0.928	0.647	0.782
Secondary mass flow rate variation starting from CASE 10	↓ Decreasing	CASE10a	0.934	0.112	0.911
	↑ Increasing	CASE10b	0.941	0.647	0.790
Secondary mass flow rate variation starting from CASE 11	↓ Decreasing	CASE11a	0.945	0.091	0.933
	↑ Increasing	CASE11b	0.945	0.648	0.798
Secondary mass flow rate variation starting from CASE 14	↑ Increasing	CASE14b	0.950	0.643	0.841

Table 5-3 Efficiency results

### 5.2.2.2 Flow behavior

**Effects of primary mass flow rate.** Here is presented the influence of primary mass flow rate on resulting flow fields; preliminary considerations are given by Figure 5-1 (with references to Figure 5-2), where the relationship between primary mass flow rate variation, primary inlet pressure and primary inlet velocity are illustrated.

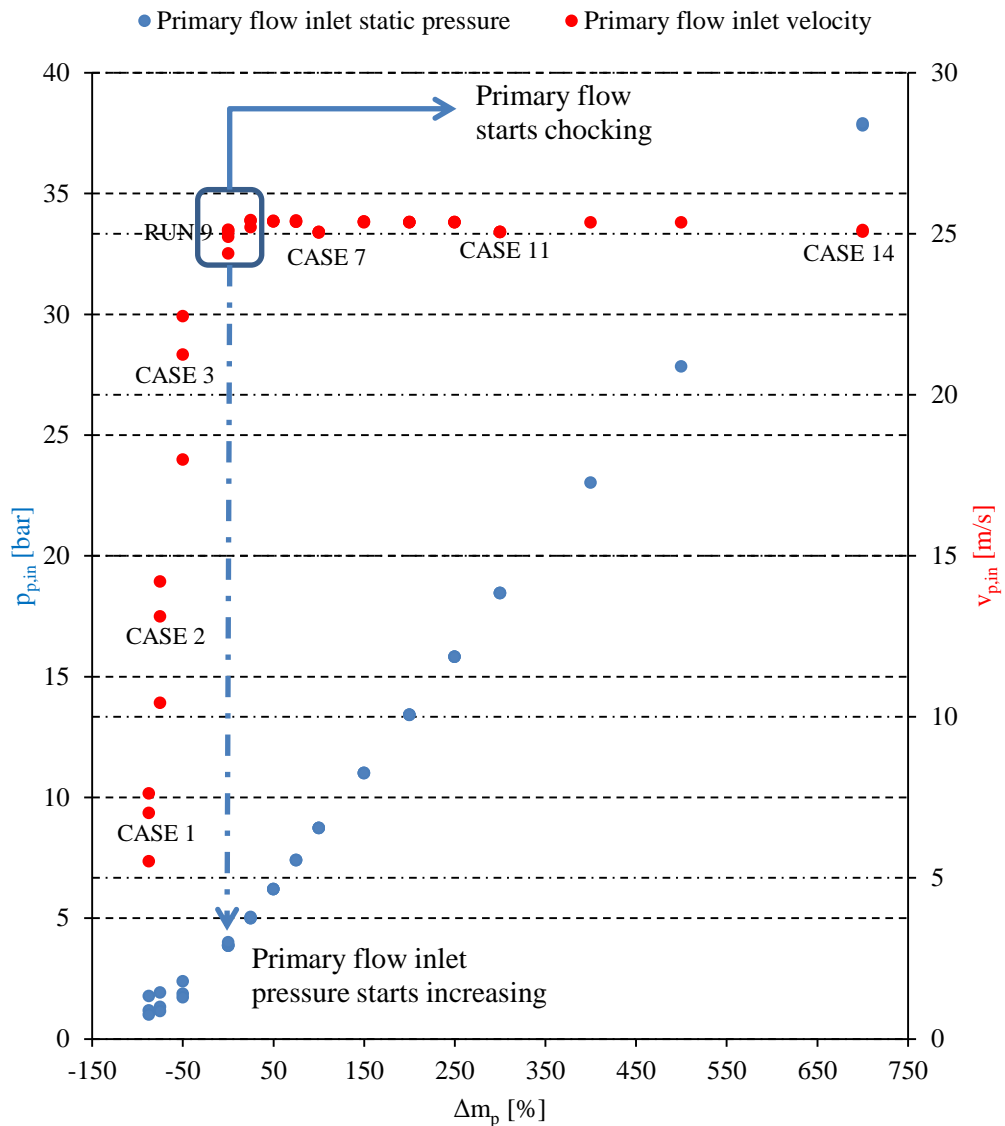


Figure 5-1 Relations between primary mass flow rate variations, primary inlet pressure and primary inlet velocity

As geometry is fixed, till  $\dot{m}_p$  is below a critical value  $\dot{m}_p < \dot{m}_p^{choking}$ , primary flow is entirely subsonic (Figure 5-2 case 1,2,3) so an improvement of  $\dot{m}_p$  results on an increase of  $v_{p,in}$  and  $p_{p,in}$  is near constant. When  $\dot{m}_p \geq \dot{m}_p^{choking}$  (Figure 5-2 run 9), flow is choked:  $v_{p,in}$  is almost constant (as result of choking) and the improvement of  $\dot{m}_p$  results on  $p_{p,in}$  increasing (Figure 5-2 case 7,11,14). It's important to remark the formation of shock cells, which are more and more important at high  $\dot{m}_p$ .

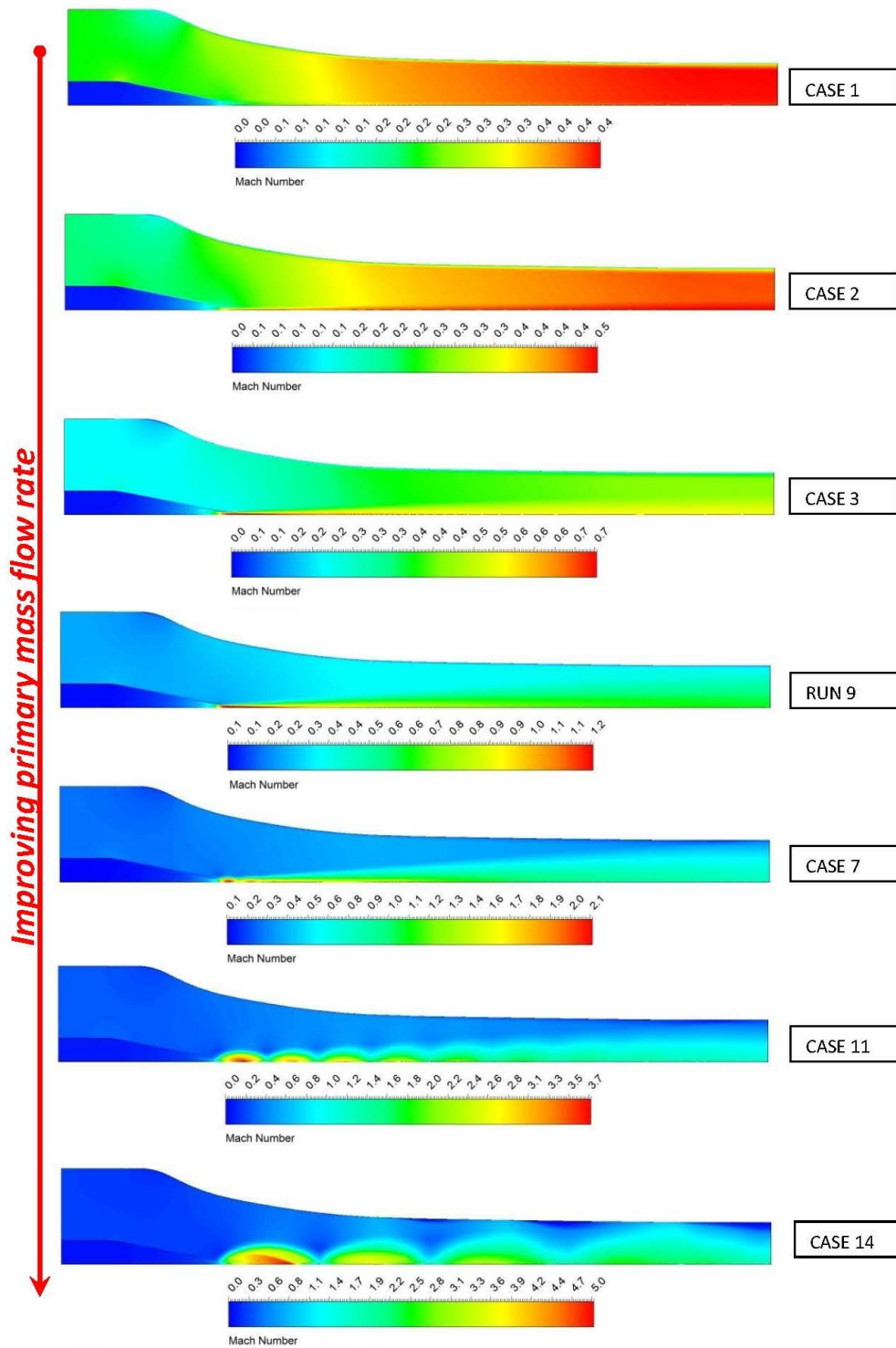


Figure 5-2 Simulation results: Mach contours.

**Qualitative confirmation of results.** In this section flow visualization in a subsonic ejector will be presented: those images can give qualitative confirmation of results presented above (Figure 5-2): the importance of having flow field visualization was a guidelines for CFD ejector simulations (section 2.4.2).

For understanding simulation results (Figure 5-1 and Figure 5-2) and visualization images (from Figure 5-6 to Figure 5-11) is required a clear idea of flow behavior inside a subsonic ejector, which can be related to the under-expanded jet behavior [142]: a flow which comprises both shock-wave containing compressibility effects and turbulent mixing. The profile of the jet, during its initial expansion phase, is primarily dependent on the Nozzle Pressure Ratio ( $NPR = p_{0,p}/p_{amb}$ ), as described by Donaldson and Snedeker [143].

A jet may be categorized into one of three types:

1. *Subsonic jet (Figure 5-3).* when  $1 < NPR < 1.89$ . The pressure everywhere in the jet, including at its throat pressure  $p_t$ , are equal to  $p_{amb}$ . The jet is characterized by a core, surrounded by a mixing region. The radius of this core decreases to zero with increasing downstream distance. Beyond this point, the jet goes through a transitional phase as it continues to expand (as the velocity decays, in order to conserve axial momentum).

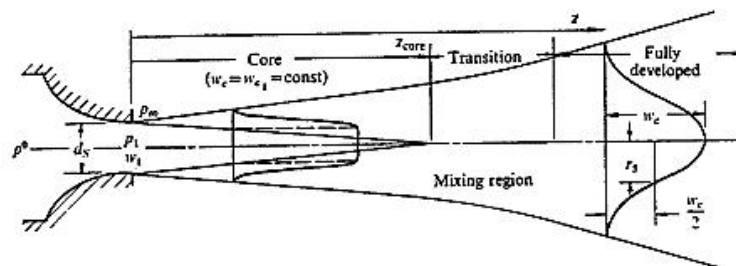


Figure 5-3 Subsonic jet flow from a sonic nozzle; taken from [143]

2. *Moderately under-expanded jet (Figure 5-4).* when  $2.08 < NPR < 3.85$ . If the pressure of the jet is higher than the critical (sonic) pressure, shocks begin to be formed at the nozzle exit, and the nozzle pressure,  $p_t$ , will be higher than  $p_{amb}$ , in the range  $1.1 < p_t/p_a < 2$ . The jet expands to  $p_{amb}$  through a series of oblique shock waves (shock diamonds). The boundaries of what was the core in subsonic case are now characterized by the outer boundary of the shock cells, outside of which, the pressure is in equilibrium with ambient and mixing can take place. Downstream, beyond the range of this core, the jet becomes entirely subsonic, and can be assumed to expand as would a free jet.

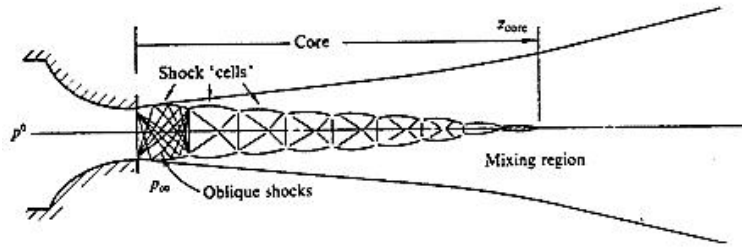


Figure 5-4 Moderately under-expanded jet flow from a sonic nozzle; taken from [143]

3. *Highly under-expanded jet (Figure 5-5).* when  $NPR > 3.85$ . The rapid expansion along the jets centerline produces a very low axial pressure, and the recompression towards the end of the first cell exceeds the limiting case for the oblique shocks: a normal shock wave is therefore formed (a Mach disk) at short distance downstream nozzle exit. Upstream of the Mach disk, the flow is supersonic, downstream it is subsonic. The nozzle pressure will now be higher,  $p_t / p_a > 2$ . This profile will remain if  $p_{0,p}$  is increased further, and may result in additional axial shock disks, as the subsonic flow downstream of the first shock is rapidly accelerated (a second axial shock disk may be evident when  $p_t / p_a > 4$ ).

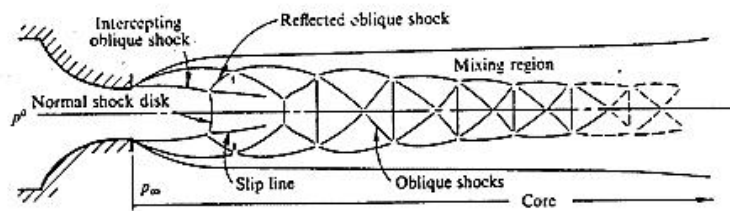


Figure 5-5 Highly under-expanded jet flow from a sonic nozzle; taken from [143]

After this brief introduction, here are presented shadowgraph images of flow fields in a subsonic ejector, taken from [136], for different value of Nozzle Pressure Ratio ( $NPR = p_{0,p} / p_{amb}$ ), which is with related to primary mass flow rate (Figure 5-1).

When NPR exceeds a critical value ( $NPR=1.893$ ) the primary flow is choked and under expanded. In such a flow field an expansion wave is generated at the nozzle lip and is reflected as a compression wave when it reaches jet boundary; such wave reflection repeats itself and as a result the cellular structure of the jet is formed.

$NPR = 1.893$  to  $2.0$ : the impingement of the secondary flow on the jet boundary of the first cell makes the jet boundary narrow.



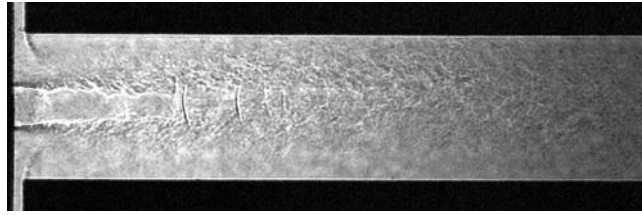


Figure 5-6 NPR=1.893; taken from [136]

$NPR = 2.25$  to  $2.50$ : the strength of the expansion and compression waves in the primary jet increases and the jet boundary of the first cell expands; secondary flow rate increases because of the increase of shearing action.

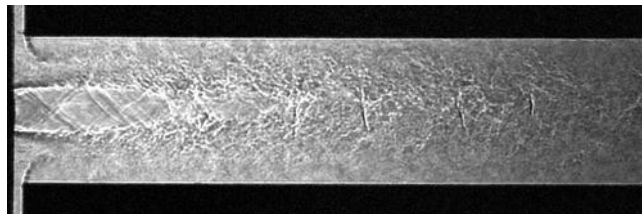


Figure 5-7 NPR=2.50; taken from [136]

$NPR = 2.75$  to  $2.80$ : the compression wave in the primary jet becomes stronger and the oblique shock forms and are reflected in the jet boundary, forming the second cell.

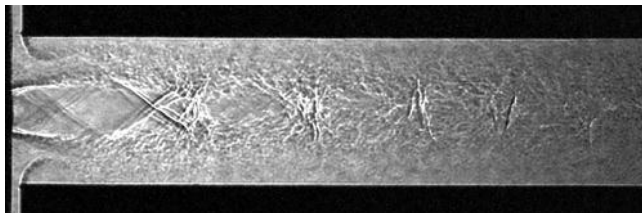


Figure 5-8 NPR=2.75; taken from [136]

$NPR = 2.90$  to  $3.00$ : the secondary flow is separated at the corner of the port and then reattached on the ejector wall. When this reattachment occurs, is generated a compression wave, which interferes with the oblique shock in the primary jet, strengthening it.

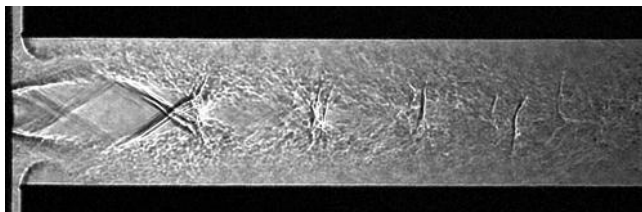


Figure 5-9 NPR=3.00; taken from [136]

$NPR = 3.10$  : the oblique shock wave in the first cell is stronger and further downstream at the end of the first cell another oblique shock wave appears.

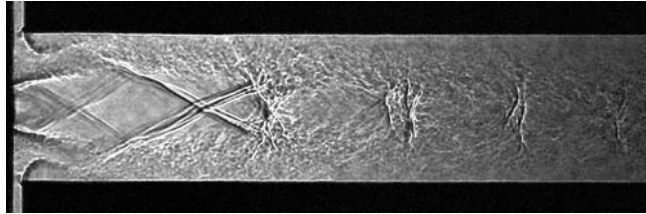


Figure 5-10 NPR=3.10; taken from [136]

$NPR = 3.20$  to  $4.20$ : the oblique shock in the primary jet becomes strong and reaches the turbulent boundary layer on the wall from which it is reflected: pressure increases downstream and velocity decreases as the air passes through each oblique shock wave. Pressure rise propagates upstream through the boundary layer: the pressure at the exit of the secondary fluid increase, resulting in the reduction of the secondary flow rate.

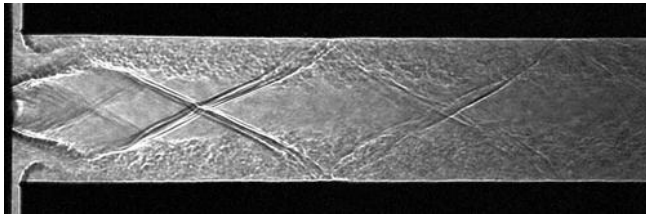


Figure 5-11 NPR=4.00; taken from [136]

It's important to point out that those images (from Figure 5-6 to Figure 5-11) are able to qualitatively confirm simulation results presented before (Figure 5-2).

**Effects of secondary mass flow rate.** Here is presented the influence of secondary mass flow rate on resulting flow fields; preliminary considerations are given in Figure 5-12 where reported the relationship between  $\dot{m}_p$  and  $v_{s,in}$  and  $p_{s,in}$  at different  $\dot{m}_s$ .

Secondary flow inlet static pressure in case of secondary mass flow: ▲ -75% ● RUN9 ◆ 100%

Secondary flow inlet velocity in case of secondary mass flow: ▲ -75% ● RUN9 ◆ 100%

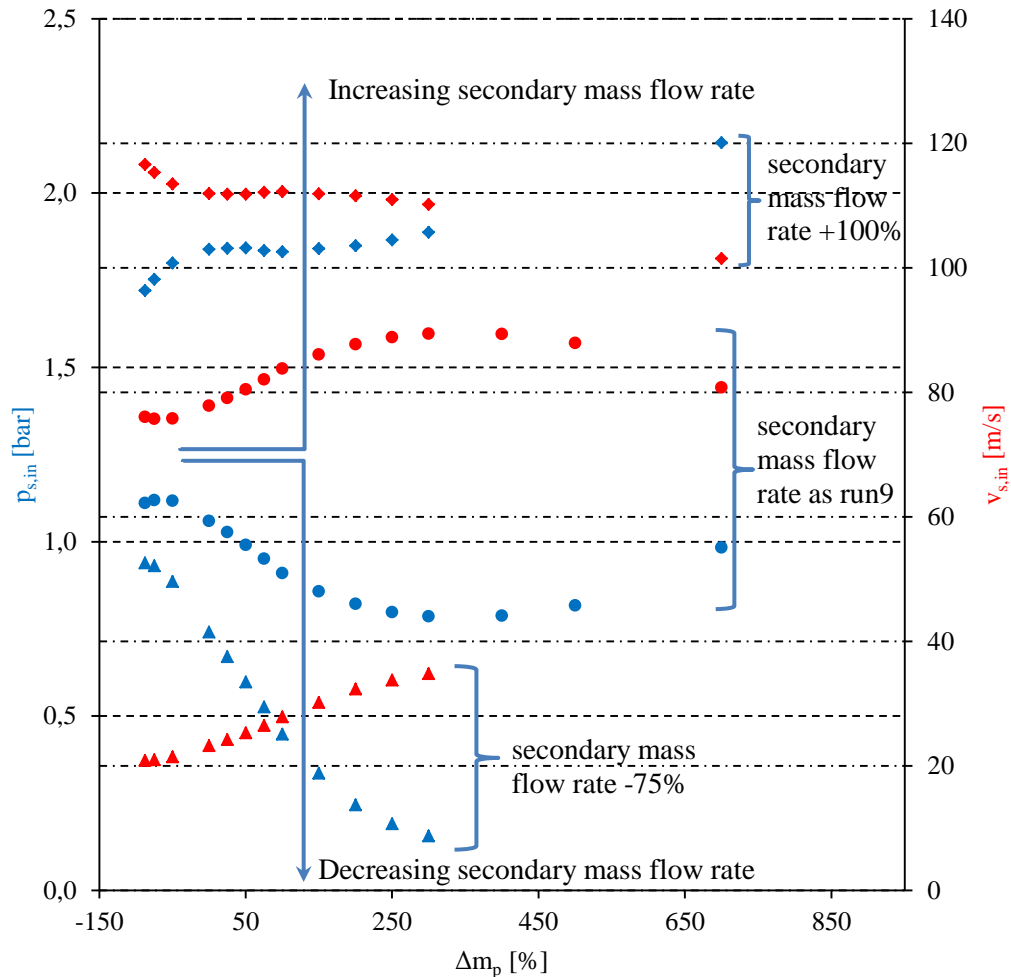


Figure 5-12 Relations between primary mass flow rate variations, secondary inlet pressure, secondary inlet velocity

An increase of primary mass flow rate initially causes an increase of the entertainment ratio : as consequences  $v_{s,in}$  increases and  $p_{s,in}$  decreases with an increase of primary mass flow rate. At very high  $\dot{m}_p$ , shock cells are very important and led to a minor entertainment effects, causing an inversion:  $v_{s,in}$  decreases and  $p_{s,in}$  increase with an increase of  $\dot{m}_p$ .

Above considerations can be easily understood by looking at flow behavior at different secondary mass flow rate; here are some considerations using as reference CASE 11 (Figure 5-13):

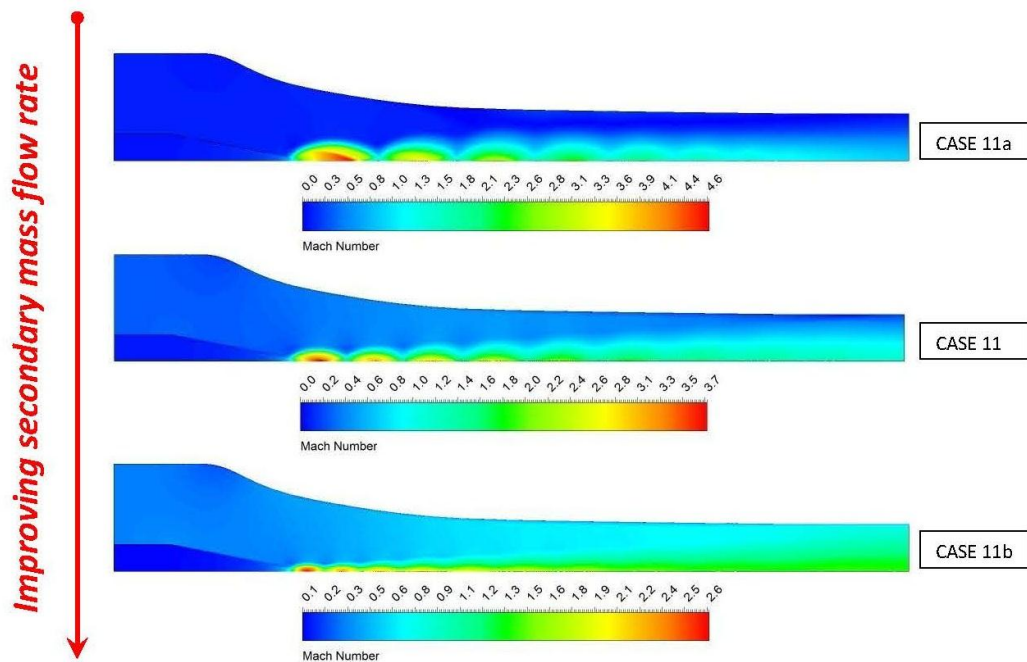


Figure 5-13 Simulation results: Effects of improving  $\dot{m}_s$  (CASE11) - Mach contours

When the secondary mass flow rate increases, shearing action between the primary and secondary fluids becomes more active:

- the boundary of the primary jet is narrowed because the mass flow of the secondary fluid is large;
- the boundaries of the cells are narrowed more and the cellular structures are generated further downstream.

When the secondary flow decreases the under-expanded jet of the primary fluid in the vacuum ejector can be said generally to expand more than the free jet because of the presence of low pressure region near the nozzle exit.

It's important to remark that above considerations are qualitatively confirmed in [136] by using optical measurement techniques.

Similar consideration can be expanded to other cases; in following figures are reported Mach contours for run9 (Figure 5-14) and CASE 2 (Figure 5-15) at different secondary mass flow rate.

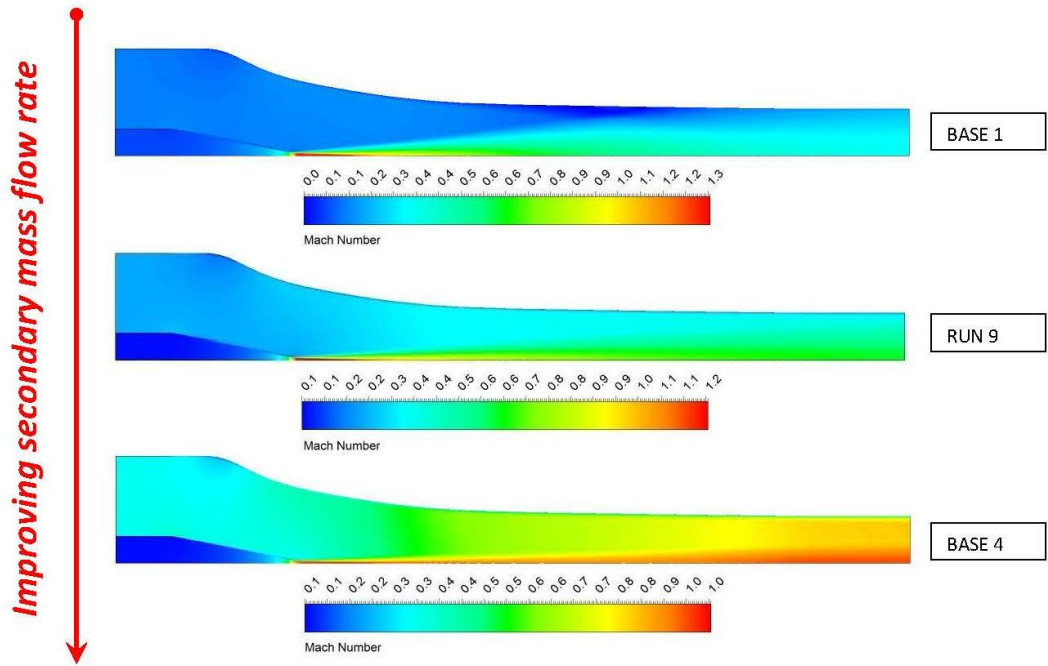


Figure 5-14 Simulation results: Effects of improving  $\dot{m}_s$  (run9) - Mach contours

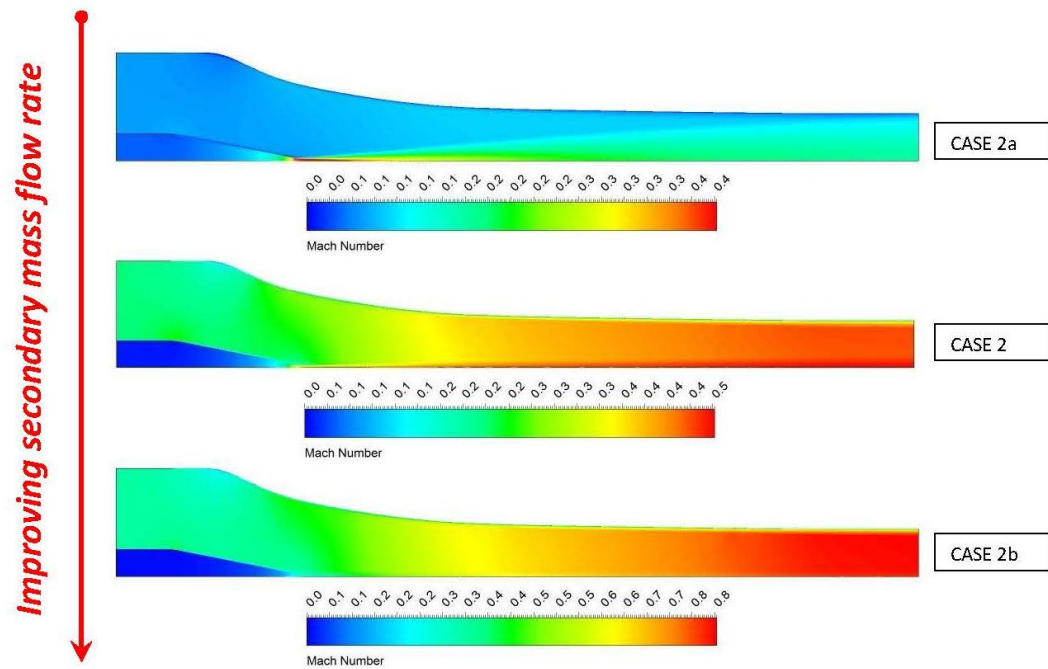


Figure 5-15 Simulation results: Effects of improving  $\dot{m}_s$  (CASE2) - Mach contours

## 5.2 Part 2: the relationship between internal flow and efficiencies.

In part 1 efficiencies and flow fields resulting from CFD simulation were presented. In this part are reported comments on the relationship between local flow behavior and global parameters for nozzle, suction and mixing chamber. Efficiencies function will also be proposed at the end of each paragraph, taking into account that a preliminary analysis proved that nozzle, suction and mixing efficiencies are related to the following fluid-dynamics parameters:

- $\varphi_p = (p_{0,p,in}/p_{out})$
- $\varphi_s = (p_{0,s,in}/p_{out})$

### 5.2.1 Nozzle

Figure 5-16 presented nozzle efficiency values as function of both  $\varphi_p$  and  $\varphi_s$ :

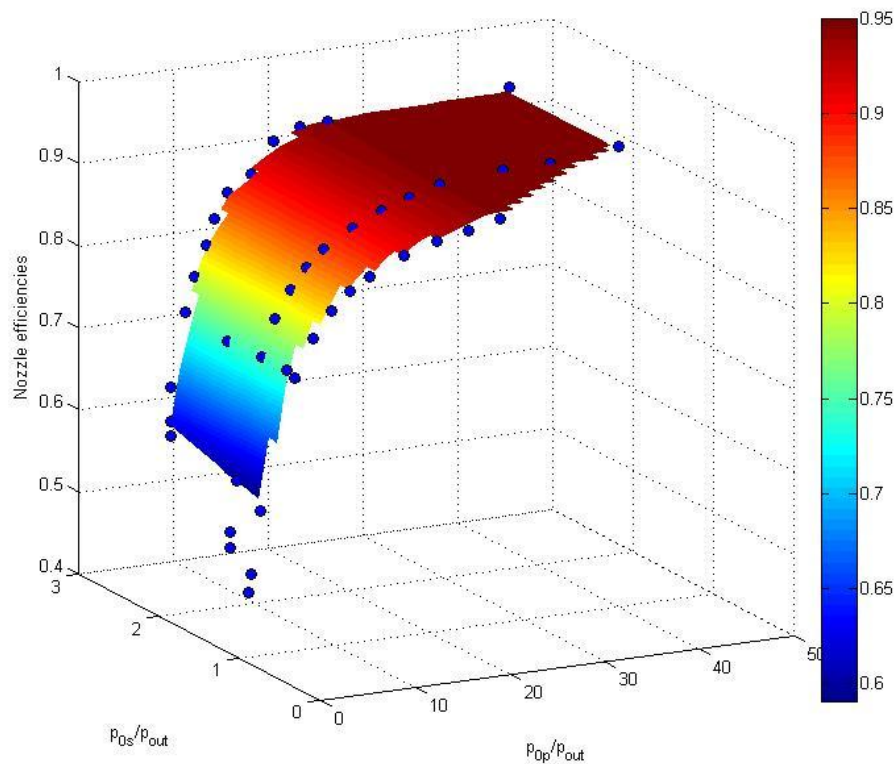


Figure 5-16 Nozzle efficiencies 3D plot

It's clear how  $\varphi_s$  does not affect  $\eta_p$  (see also Figure 5-17), so:

$$\eta_p = f(\varphi_p) \quad (6.4)$$

Before presenting interpolating function for  $\eta_p$ , it's interesting analyzing the relationship between  $\eta_p$  and flow behavior:  $\eta_p$  ranges from very low values to an asymptotic value ( $\eta_p = 0,95$ ). Low  $\eta_p$  values are related to a fully subsonic flow field, while the asymptotic value is related to the presence highly under-expanded jet (Figure 5-17).

**Qualitative confirmation of result.** This  $\eta_p$  trend, resulting from CFD simulations, is similar to  $\eta_s$  trend resulting from experimental data in the work of Liu et al. [73] (in [73] suction chamber is a convergent nozzle). Moreover, the presence of a constant value is in accordance with Varga's et al. [63] results for supersonic ejectors (which is correct, in fact shock cells is the typical flow behavior for supersonic ejectors).

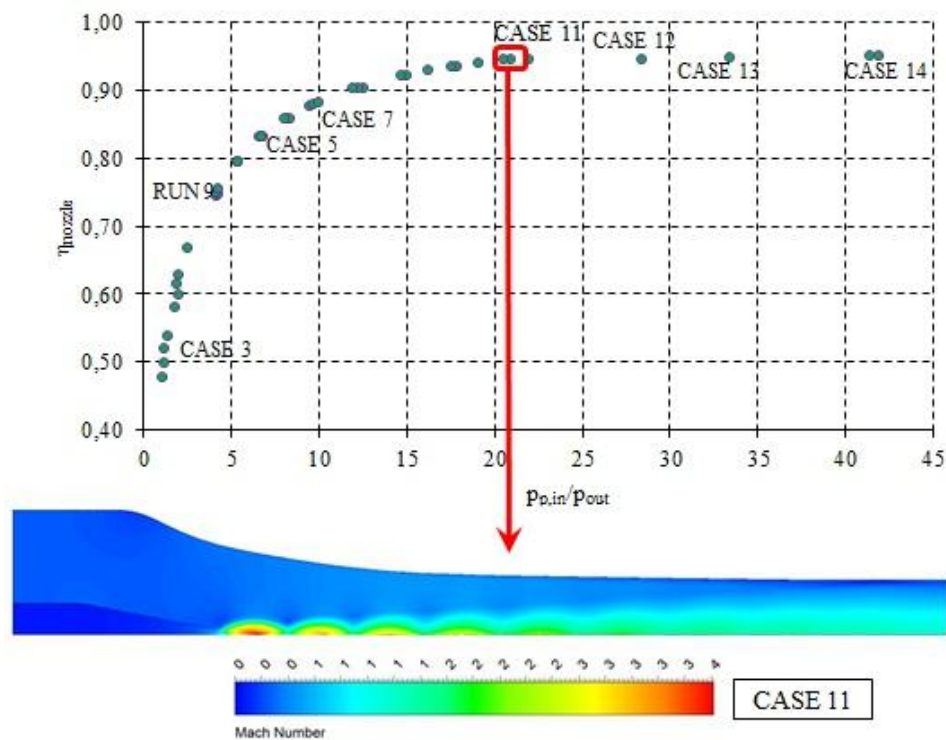


Figure 5-17 Nozzle efficiencies 2D plot

For the sake of clearness here are presented two figures that report the relationship between  $\eta_p$  and flow behavior: it's clear how a fully subsonic flow field implies very low  $\eta_p$ . An high-efficiency nozzle should be operated with very high  $\dot{m}_p$  (or  $p_{0p,in}$ ).

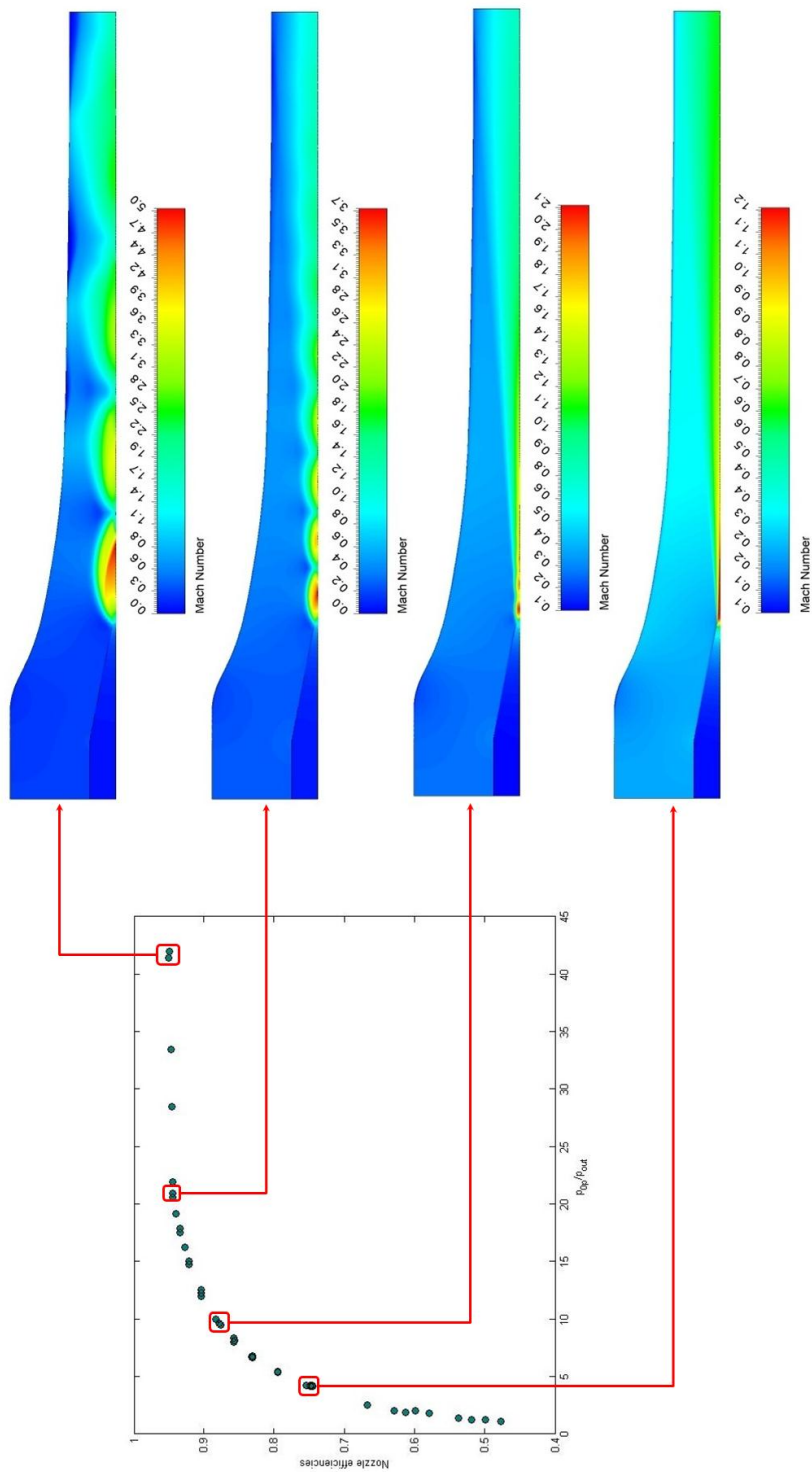


Figure 5-18 Nozzle efficiencies relationship with flow fields (part a)



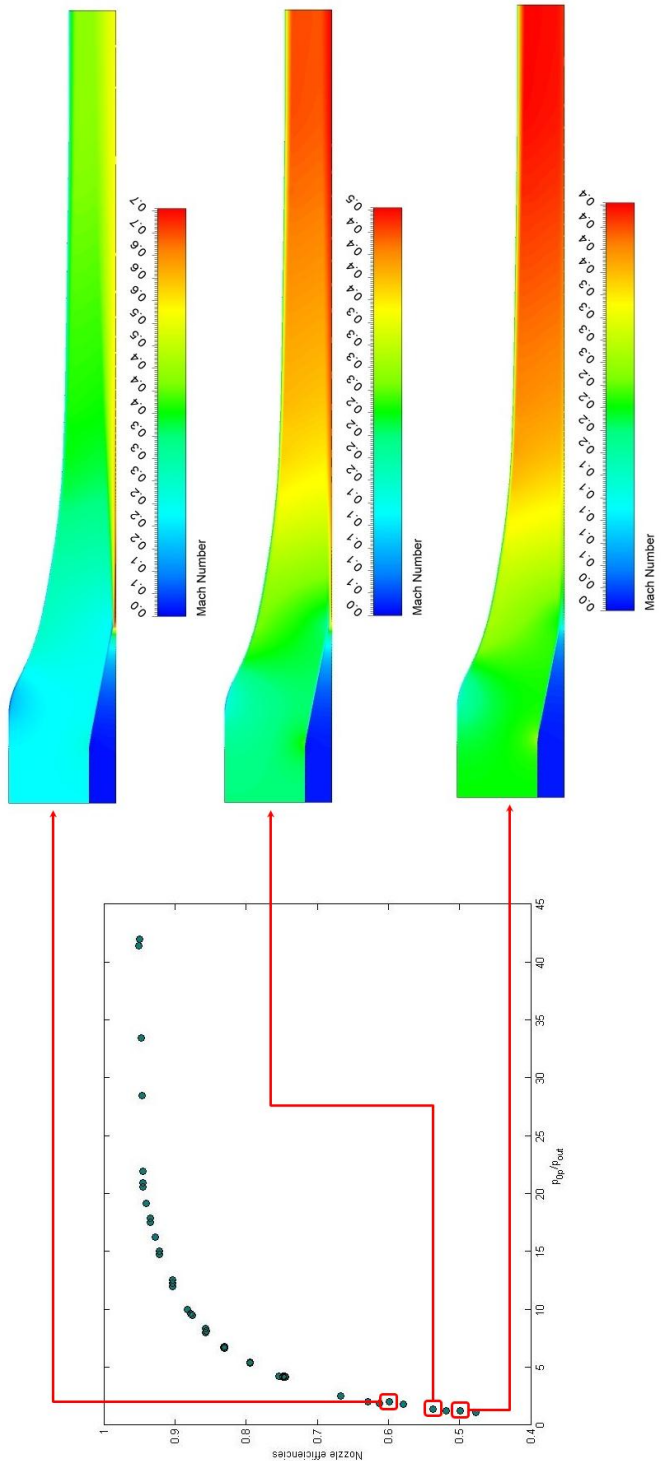


Figure 5-19 Nozzle efficiencies relationship with flow fields (part b)

As remarked before  $\eta_p = f(\varphi_p)$ ; best interpolating function is found to be composed of the sum of two exponential one:

$$\eta(x) = ae^{b\varphi_p} + ce^{d\varphi_p} \tag{6.5}$$

Coefficients	Value
a	0.9391
b	0.000308
c	-0.5029
d	-0.2176

Table 5-4 Coefficients of nozzle efficiency interpolating function

Above function gives a very good approximation of numerical efficiencies data ( $R^2 = 0.9968$ ):

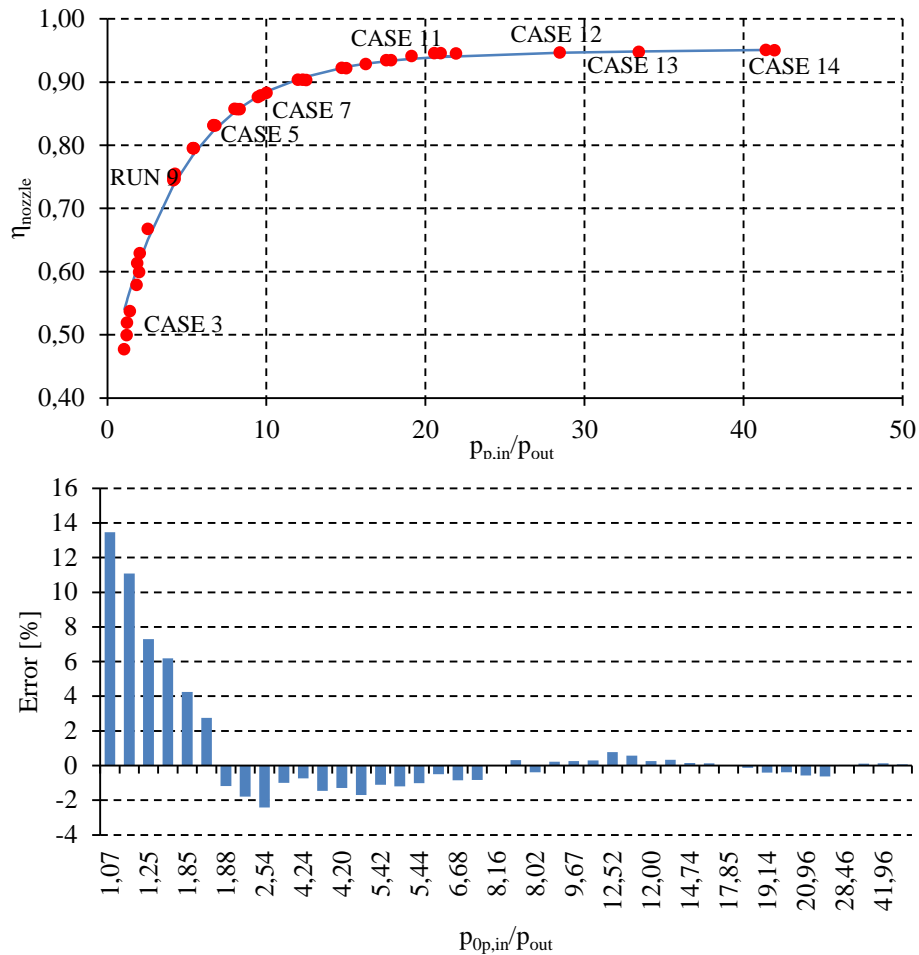


Figure 5-20 Error between CFD nozzle efficiencies and interpolating function proposed

### 5.2.2 Suction

Suction chamber is a non-optimized geometry, in fact it is not a converging duct, but it is affected by a brief diverging part, causing a low pressure zone: for this reason low  $\eta_p$  are supposed to be found; Figure 5-21 presented nozzle efficiency values as function of both  $\varphi_p$  and  $\varphi_s$

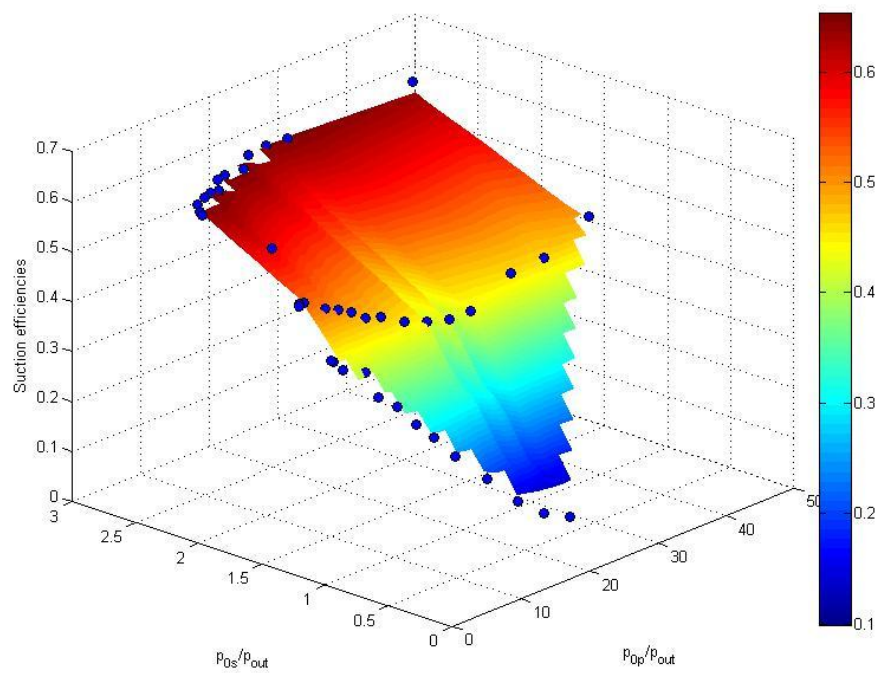


Figure 5-21 Suction efficiencies 3D plot

It's clear how  $\varphi_p$  does not affect  $\eta_s$  (see also Figure 5-22), so:

$$\eta_s = f(\varphi_s) \quad (6.6)$$

As put forward suction efficiencies are poor:  $\eta_p$  starts from a very low values ( $\eta_p \approx 0.10$ ), reaches a maximum value ( $\eta_p \approx 0.65$ ) and then it decreases to a slightly lower value ( $\eta_p \approx 0.64$ ). Due to this non optimized geometry, efficiency are bound to flow fields and, in particular, to  $\dot{m}_s$  (Figure 5-22), with is related to  $\varphi_s$ :

- $\eta_s$  low values are related to the cases where  $\dot{m}_s$  was reduced;
- $\eta_s$  middle values are related to the cases where  $\dot{m}_s$  was maintained the same of run 9;

- $\eta_s$  high values are related to the cases where  $\dot{m}_s$  was increased

This is due to the fact that, having a fixed geometry, low mass flow rate streams are also a low velocity streams and those are more affected by the non-optimized geometry.

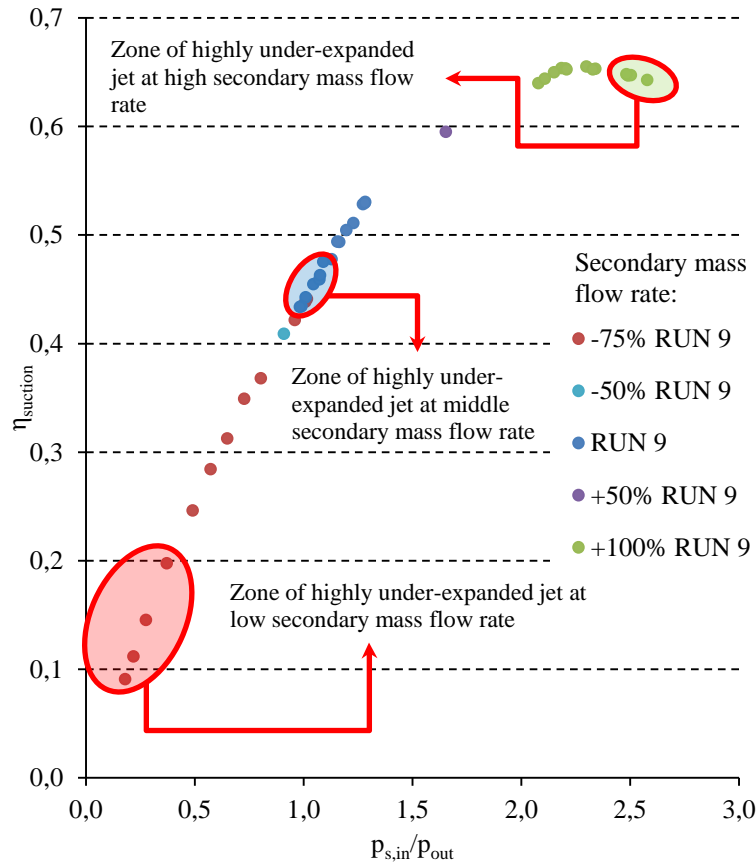


Figure 5-22 Suction efficiencies 2D plot with considerations

It's interesting pointing out that presence of an highly under-expanded jet (Figure 5-22) further reduce suction efficiencies, in fact the presence of this particular flow behavior is related to the low efficiency zone of (i) low  $\dot{m}_s$  (brown spots), (ii) benchmark  $\dot{m}_s$  (blue spots) and (iii) high  $\dot{m}_s$  (green spots): for a better understanding, Figure 5-23 reports the relationship between  $\eta_p$  and flow behavior.

It could be interesting to perform optimization of suction chamber geometry and study the relationship between the geometry and  $\eta_p$ , remarking how trend reported in Figure 5-22 modifies.

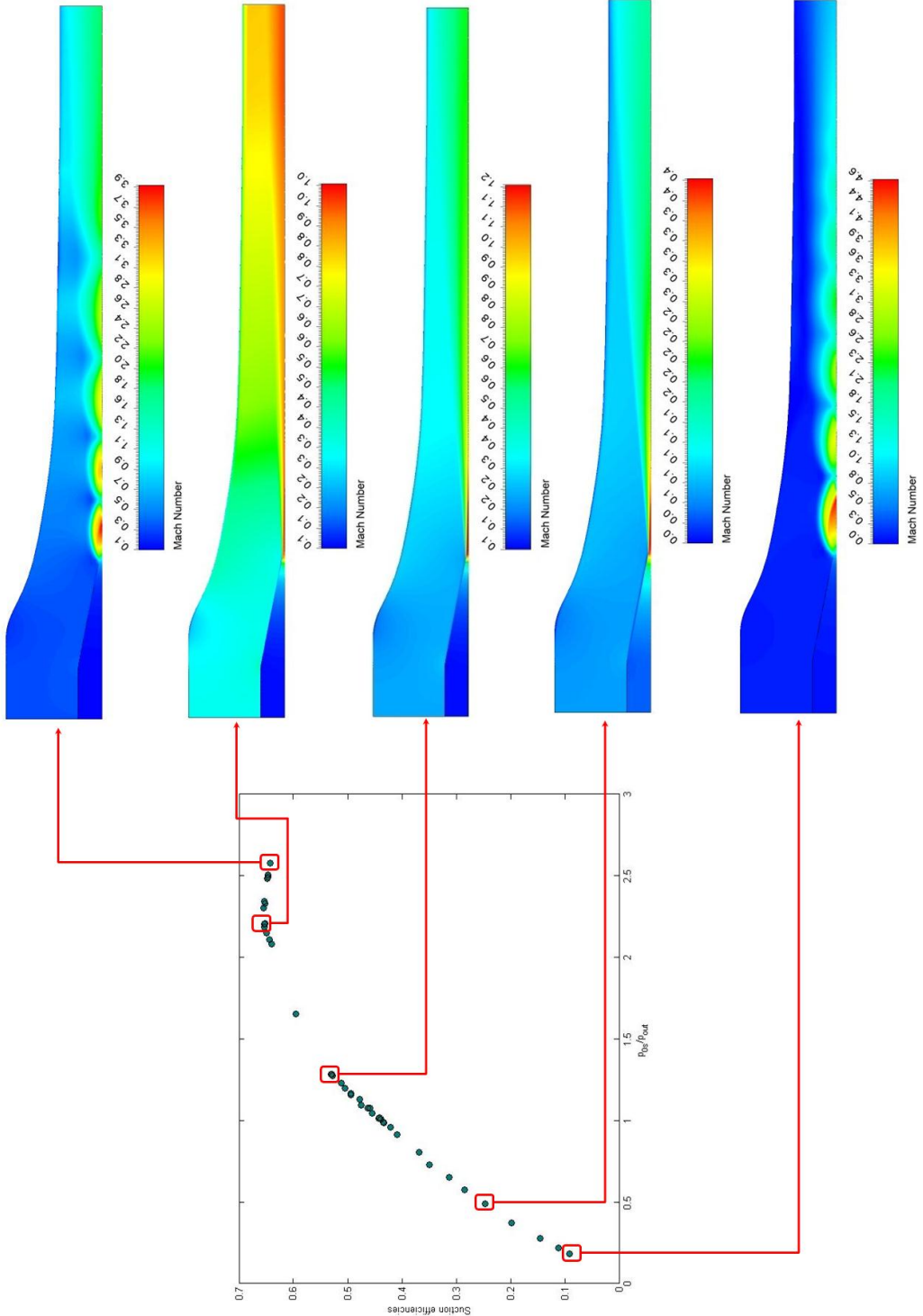


Figure 5-23 Suction efficiencies relationship with flow fields

As remarked before  $\eta_s = f(\varphi_s)$ ; best interpolating function is found to be a parabola:

$$\eta_s(\varphi_s) = a\varphi_s^2 + b\varphi_s - c \quad (6.7)$$

Coefficients	Value
a	-0.1234
b	0.5699
c	0.0053

Table 5-5 Coefficients of suction efficiency interpolating function

Above function gives a very good approximation of numerical efficiencies data ( $R^2 = 0.9993$ ):

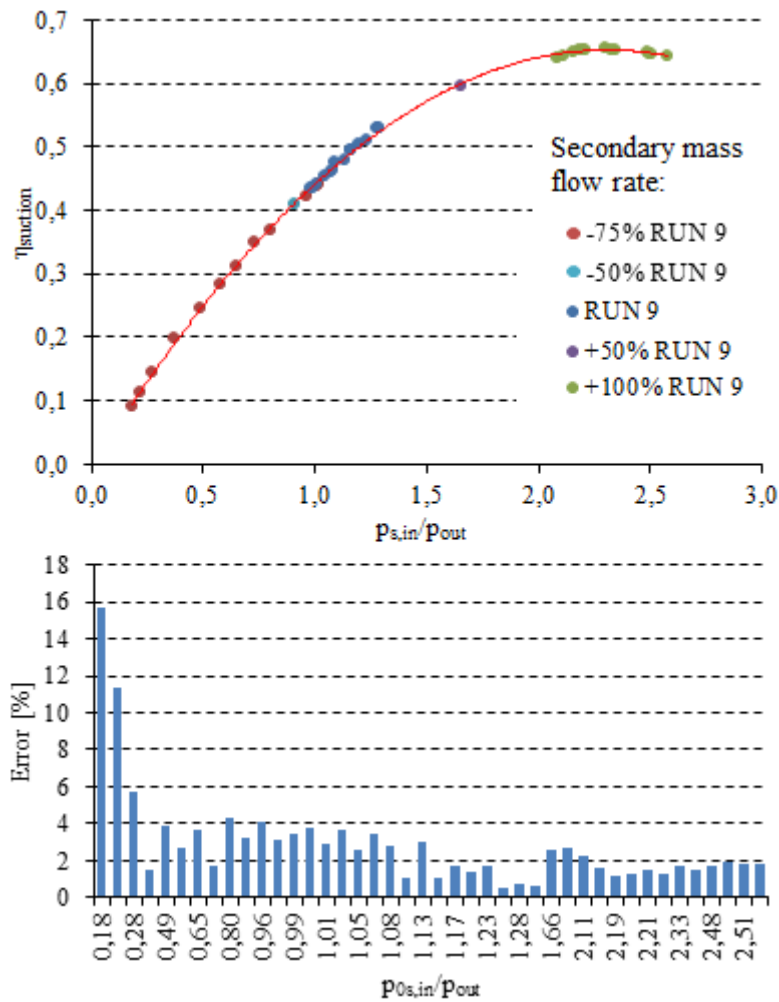


Figure 5-24 Error between CFD suction efficiencies and interpolating function proposed

### 5.2.3 Mixing

Mixing efficiency is the most important parameter in the thermodynamic model presented in Chapter 4 because in this  $\eta_{mix}$ , are gathered all of the information of the flow behavior otherwise impossible to take in account in a simple thermodynamic model; in fact, due to the very variety of flow behavior in a subsonic ejector was impossible to use an approach similar to the ones based on Munday and Bagster's theory [29] (section 2.2).

Figure 5-25 presented mixing efficiency values as function of both  $\varphi_p$  and  $\varphi_s$

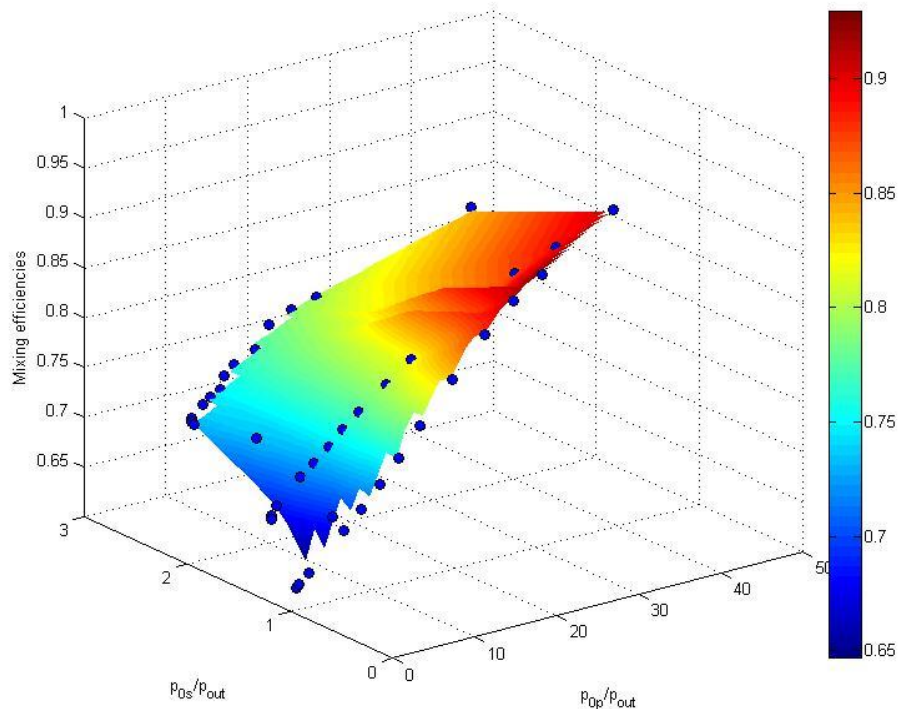


Figure 5-25 Mixing efficiencies

It's clear both  $\varphi_p$  and  $\varphi_s$  affect  $\eta_{mix}$ , so:

$$\eta_{mix} = f(\varphi_p, \varphi_s) \quad (6.8)$$

Even if  $\eta_{mix}$  depends on both  $\varphi_p$  (related to  $\dot{m}_p$ ) and  $\varphi_s$  (related to  $\dot{m}_s$ ), it's important and interesting to plot  $\eta_{mix}$  as function of  $\varphi_p$  (Figure 5-26): this representation makes clear how  $\dot{m}_s$  (and, hence,  $p_s$ ) affect mixing performance:

- at low  $\varphi_p$  an increase of  $\dot{m}_s$  leads to an increase  $\eta_{mix}$ , whereas a lowering of  $\dot{m}_s$  leads to a reduction of  $\eta_{mix}$ ;
- at middle values  $\varphi_p$ , both an increase or a decrease of  $\dot{m}_s$  do not affect  $\eta_{mix}$ ;
- at high  $\varphi_p$  an increase of  $\dot{m}_s$  leads to a decrease  $\eta_{mix}$ , whereas a lowering of  $\dot{m}_s$  leads to an improvement of  $\eta_{mix}$ .

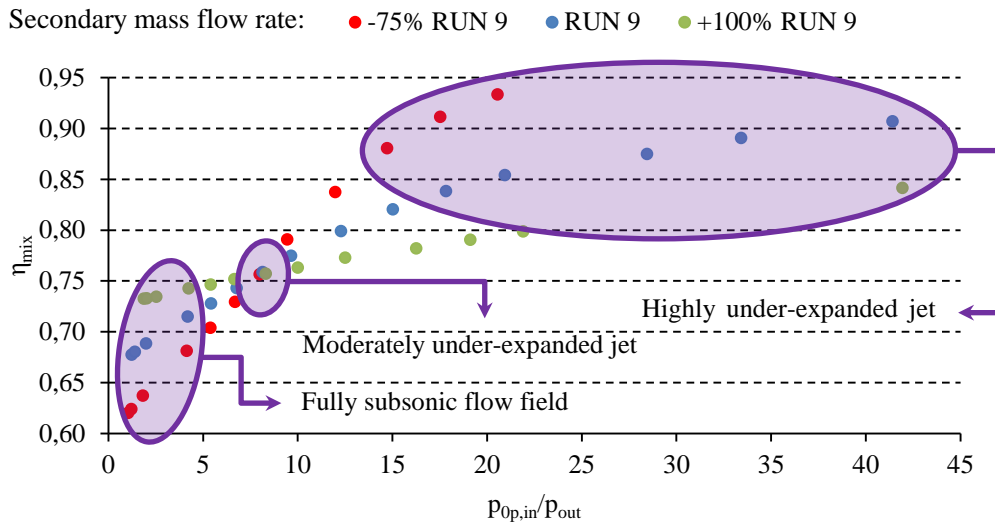


Figure 5-26 Mixing efficiencies 2D plot with considerations

This trend inversion can be explained analyzing the relationship between  $\eta_p$  and flow behavior and remarking that at low  $\varphi_p$  flow fields is fully subsonic, at middle  $\varphi_p$  there is a moderately under-expanded jet and at high  $\varphi_p$  there is a highly under-expanded jet (Figure 5-26 and Figure 5-27). Starting from this consideration, in order to understand  $\eta_{mix}$  behavior, it's important to point out how a variation of  $\dot{m}_s$  affect flow field.:

- in a flow with a highly under-expanded jet (Figure 5-28) an improvement of  $\dot{m}_s$  reduce shock cells (whose presence improves mixing efficiency);
- in a flow with moderately under-expanded jet (Figure 5-29),  $\dot{m}_s$  ha a minor effect on flow field behavior;
- in a fully subsonic flow fields (Figure 5-30 and Figure 5-31) an improvement of  $\dot{m}_s$  results on the suppression of jet structure at nozzle exit.

From above consideration it's clear that  $\eta_{mix}$  depends on primary flow behavior on exit nozzle and high mixing efficiencies ( $\eta_{mix} \approx 0,85 \div 0,95$ ) are related to the presences of highly under-expanded jet, medium mixing efficiencies ( $\eta_{mix} \approx 0,75 \div 0,80$ ) are connected to the presence of a moderately under-expanded jet at exit nozzle and low mixing efficiencies ( $\eta_{mix} \approx 0,60 \div 0,70$ ) are correlated with a fully subsonic flow field.



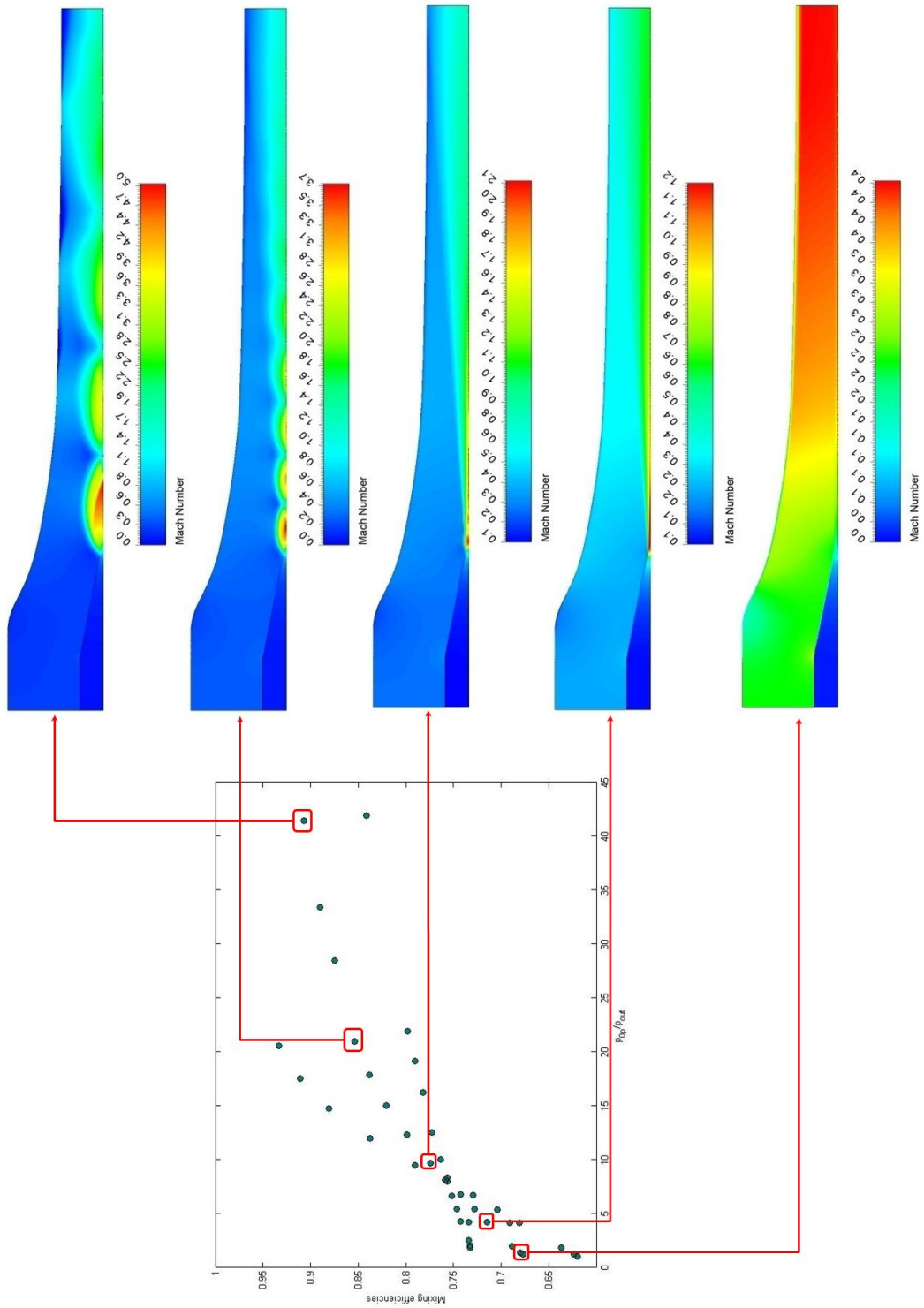


Figure 5-27 Mixing efficiencies relationship with flow fields (part a)

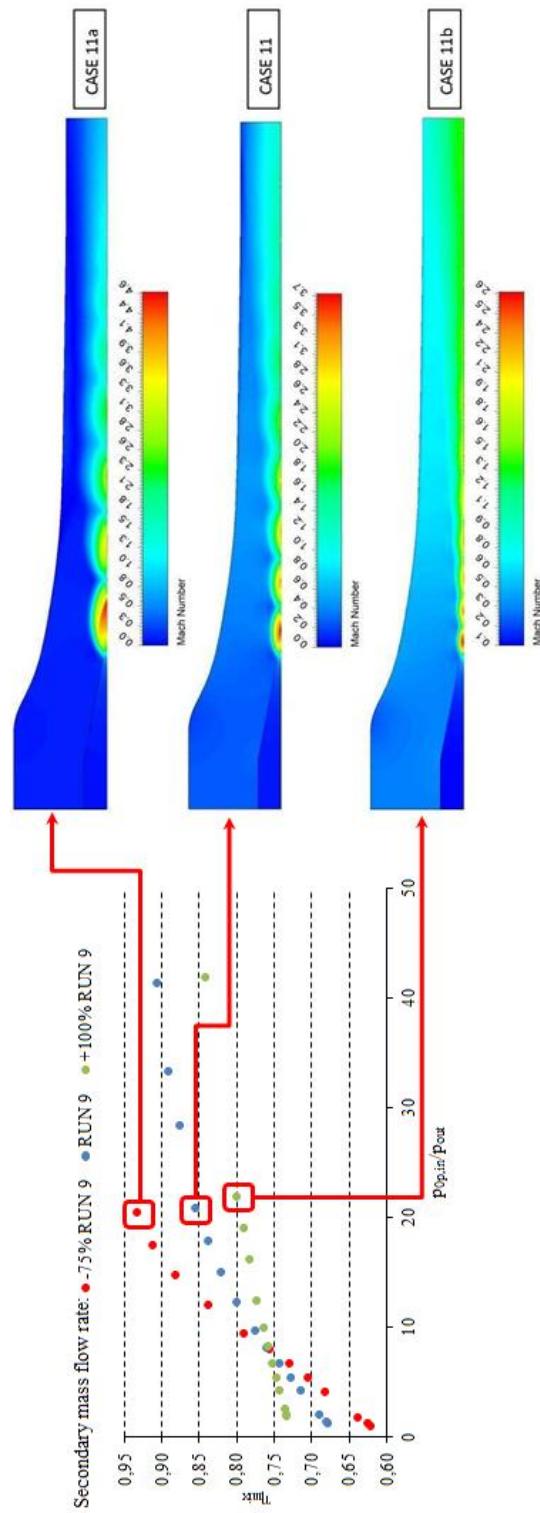


Figure 5-28 Mixing efficiencies relationship with flow fields (part b)

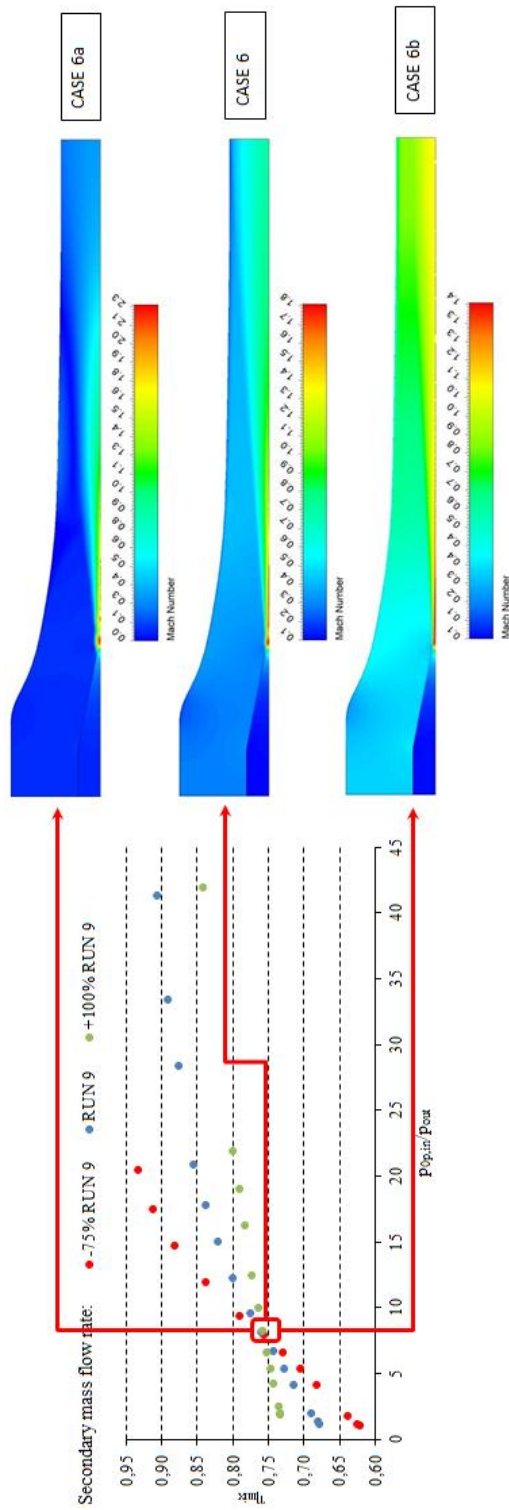


Figure 5-29 Mixing efficiencies relationship with flow fields (part c)

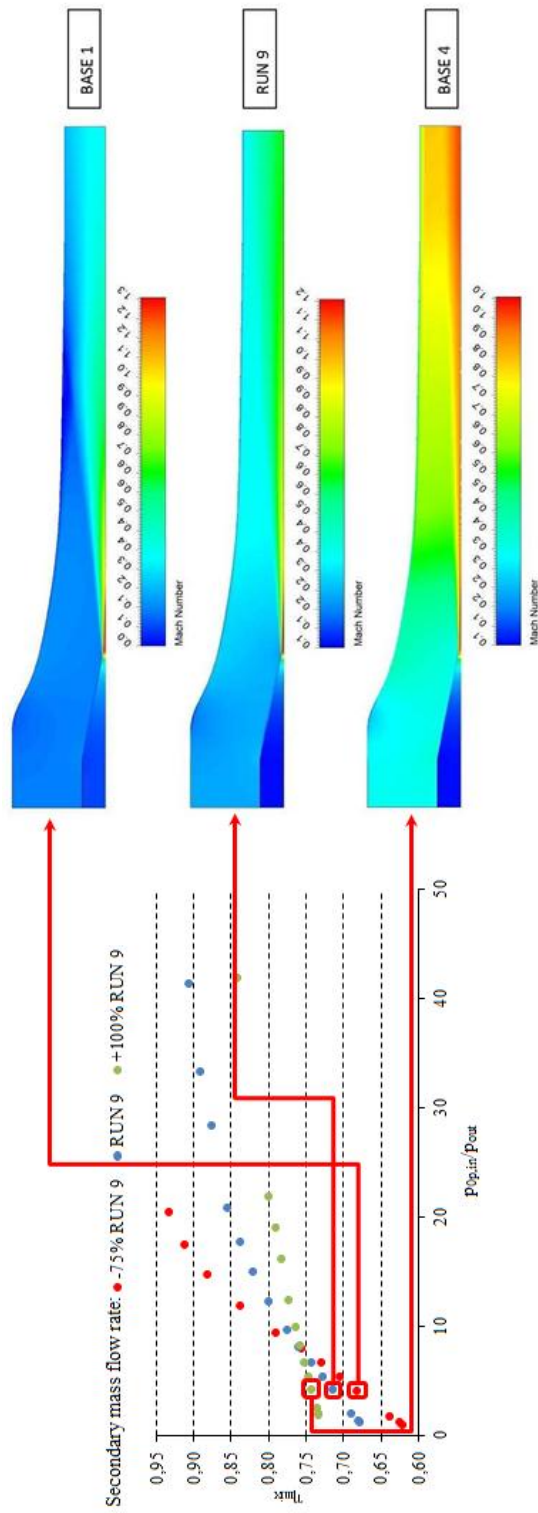


Figure 5-30 Mixing efficiencies relationship with flow fields (part d)

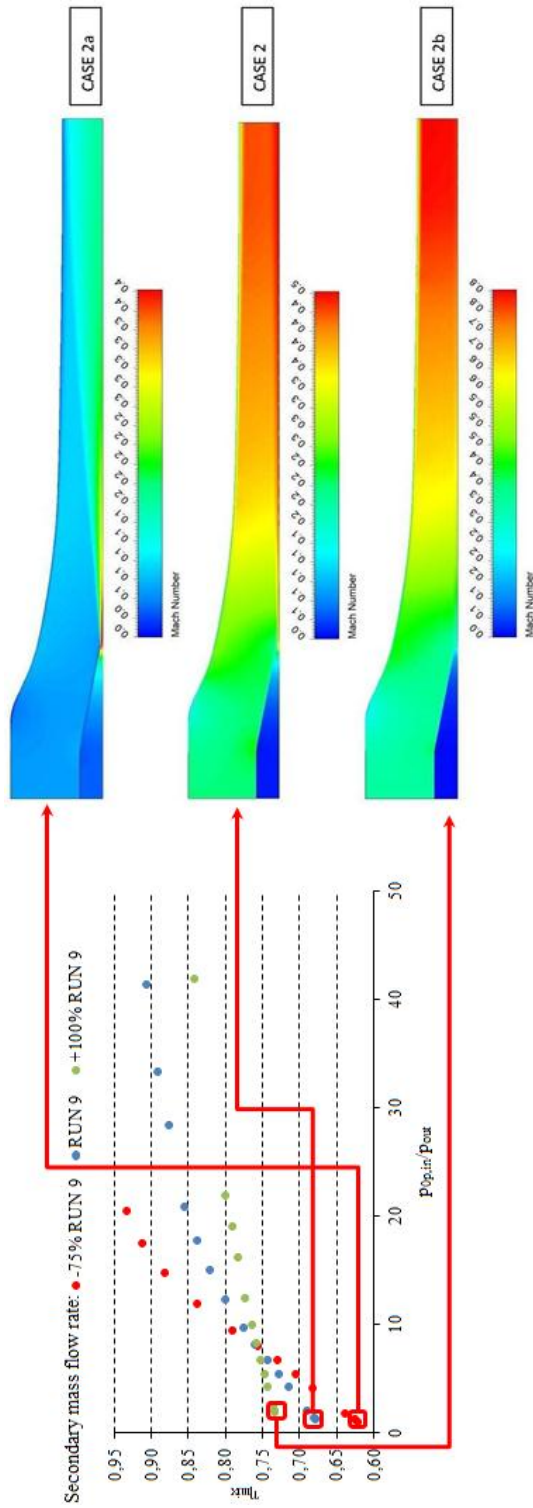


Figure 5-31 Mixing efficiencies relationship with flow fields (part e)

As remarked before  $\eta_{mix} = f(\varphi_p, \varphi_s)$ ; best interpolating surface is found to be:

$$\begin{aligned} \eta_{mix}(\varphi_p, \varphi_s) = & p_{00} + p_{10}\varphi_p + p_{01}\varphi_s + p_{20}\varphi_p^2 \\ & + p_{11}\varphi_p\varphi_s + p_{02}\varphi_s^2 + p_{30}\varphi_p^3 + p_{21}\varphi_p^2\varphi_s \\ & + p_{12}\varphi_p\varphi_s^2 + p_{03}\varphi_s^3 \end{aligned} \quad (6.9)$$

Coefficients	Value
$p_{00}$	0.6417
$p_{10}$	0.02571
$p_{01}$	-0.0569
$p_{20}$	-0.0005567
$p_{11}$	-0.007734
$p_{02}$	0.06695
$p_{30}$	0.000003393
$p_{21}$	0.0001373
$p_{12}$	-0.00002624
$p_{03}$	-0.01243

Table 5-6 Coefficients of mixing efficiency interpolating function

From which follows this surface:

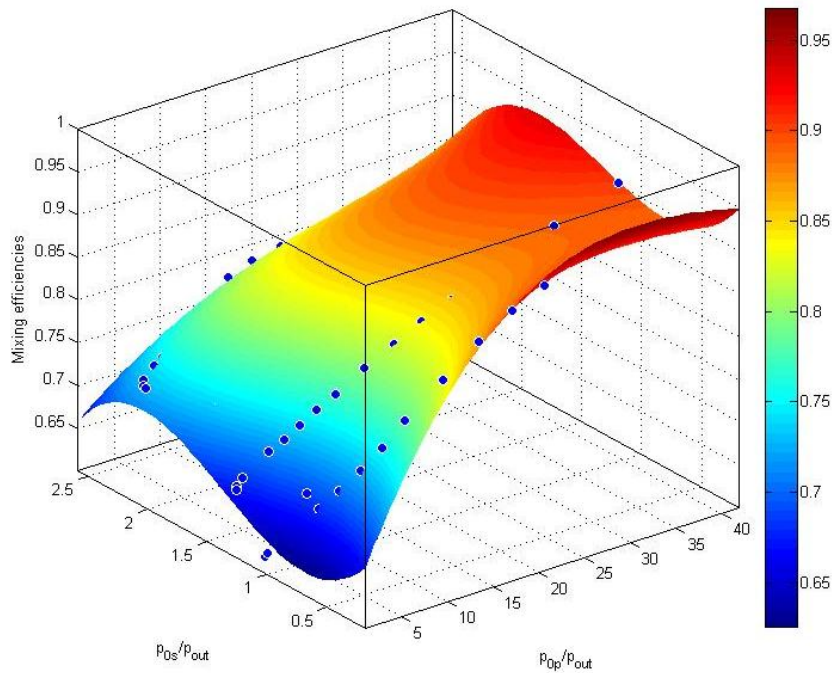


Figure 5-32 Interpolating surface

Upper view of this surface (Figure 5-33) is able to summarize previous considerations:

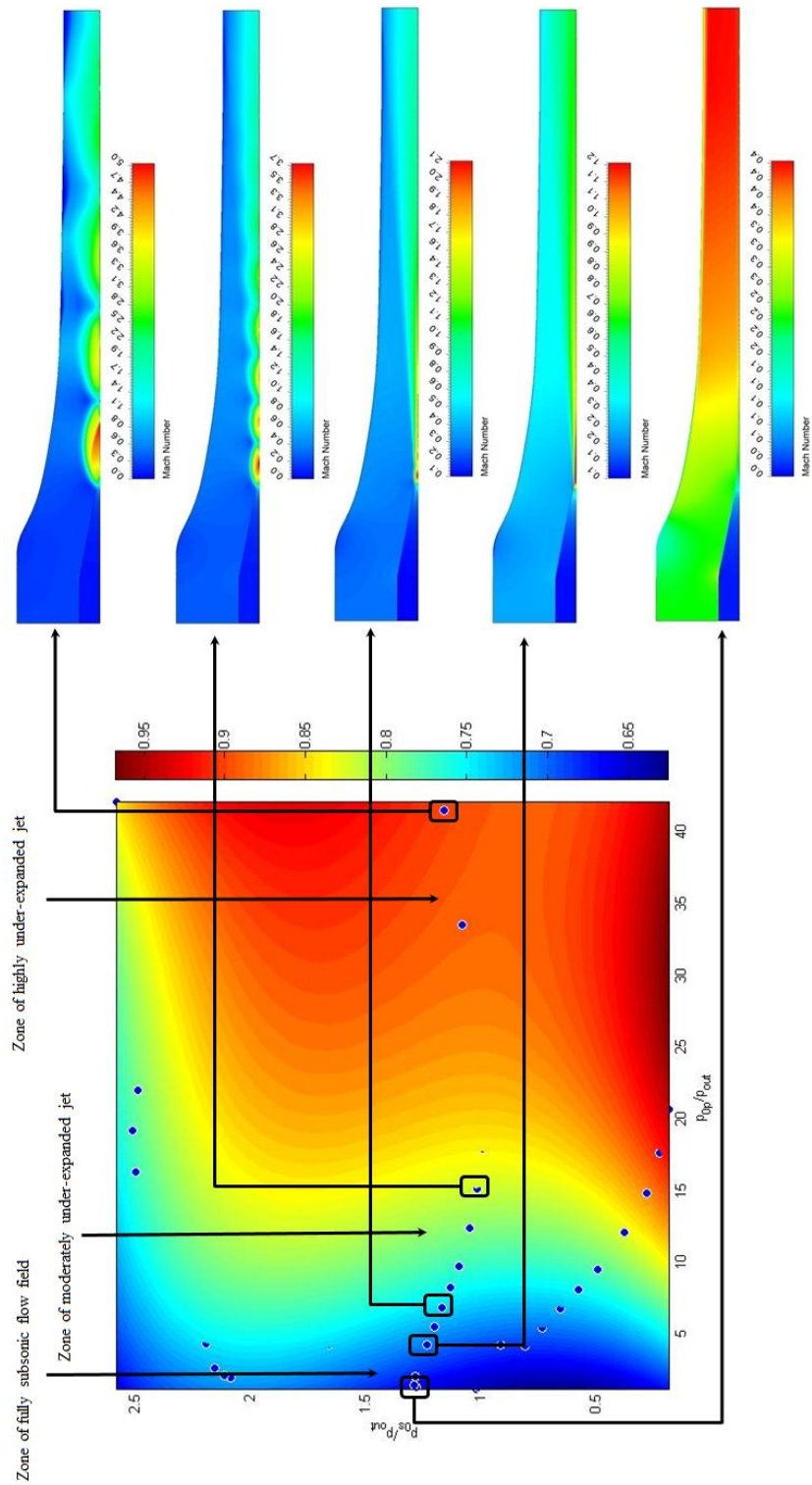


Figure 5-33 Mixing efficiencies relationship with flow fields (with interpolating surface)

Above function gives a very good approximation of numerical efficiencies data ( $R^2 = 0.9884$ ):

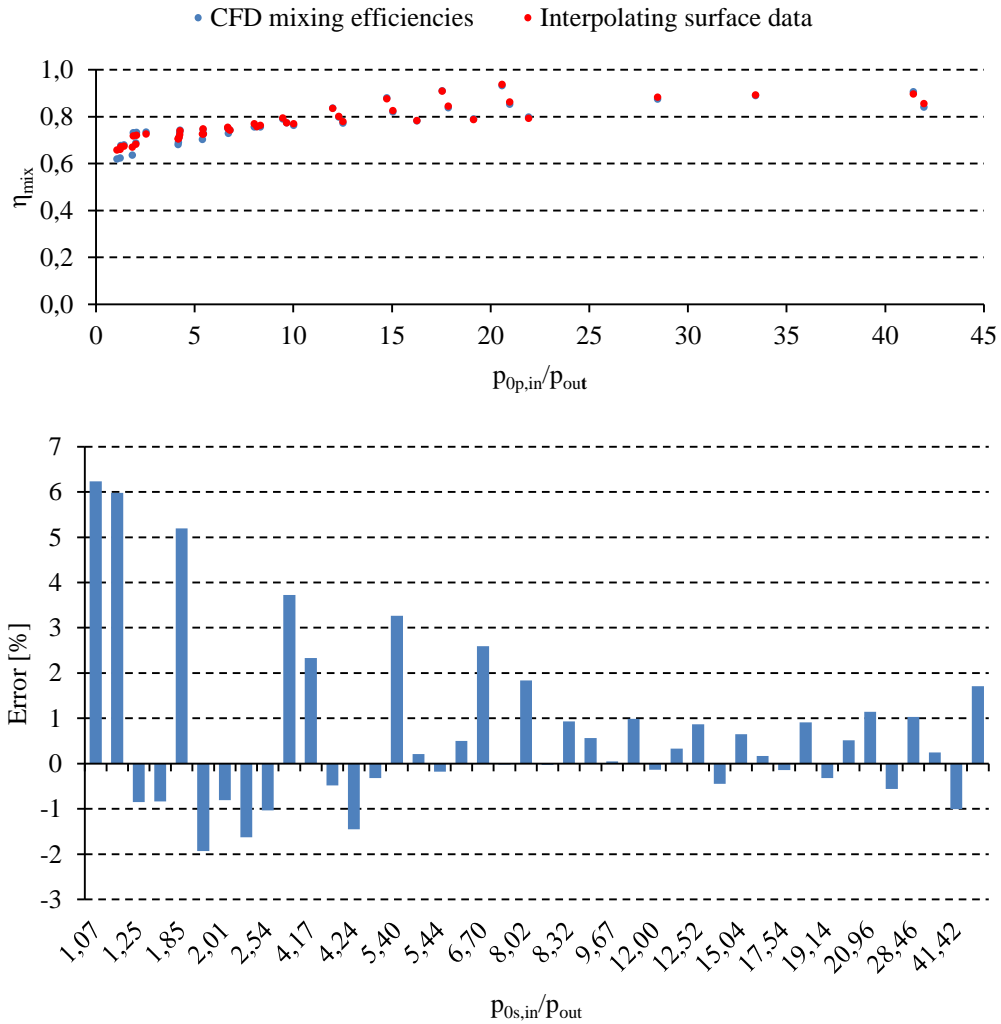


Figure 5-34 Error between CFD mixing efficiencies and interpolating function proposed



### **5.3 Part 3: the integrated thermodynamic/CFD model for single phase subsonic ejector**

A lot of studies remarked that ejectors performance can be improved by understanding the internal fluid behavior and CFD tools have been proved to be valuable tools for analyzing complex fluid flow problems, on the other side classic thermodynamic models cannot predict local phenomena. The integration of thermodynamic and CFD modeling has the great potentiality of putting together the advantages of both thermodynamic models (less computational time and cost than experimental method) and CFD models (understanding of local interactions), creating a new model that is able to provide global parameters by considering local flow behavior, which is accounted using efficiency functions.

This novel integrated model is composed by 3 interconnected sections (Figure 5-35):

1. initialization;
2. thermodynamic model core;
3. CFD LOOP iterations;

Due to the interconnection between efficiency function obtained through CFD analysis and flow behavior, an iterative approach has to be used.

#### **5.3.1 Initialization**

An initialization is required because of the presence of LOOPS. This part is composed by equations 3.1 to 3.41 and required first attempt ejector efficiencies, beyond other inputs stated in sections 3.2.2.

#### **5.3.2 Thermodynamic model code**

Main core of the novel integrated model has the structure explained in Chapter 3 and is composed by equations 3.16 to 3.43.

#### **5.3.3 CFD efficiency LOOPS**

CFD model provided efficiencies maps used to obtain efficiency function that are now connected with thermodynamic core; this approach required iterative calculations caused by the fact that efficiencies are related with thermodynamics properties of flow field inside ejector (which are evaluated using isentropic efficiencies themselves).

#### **5.3.4 Model structure**

In Figure 5-35 is reported model structure with fluxes information.

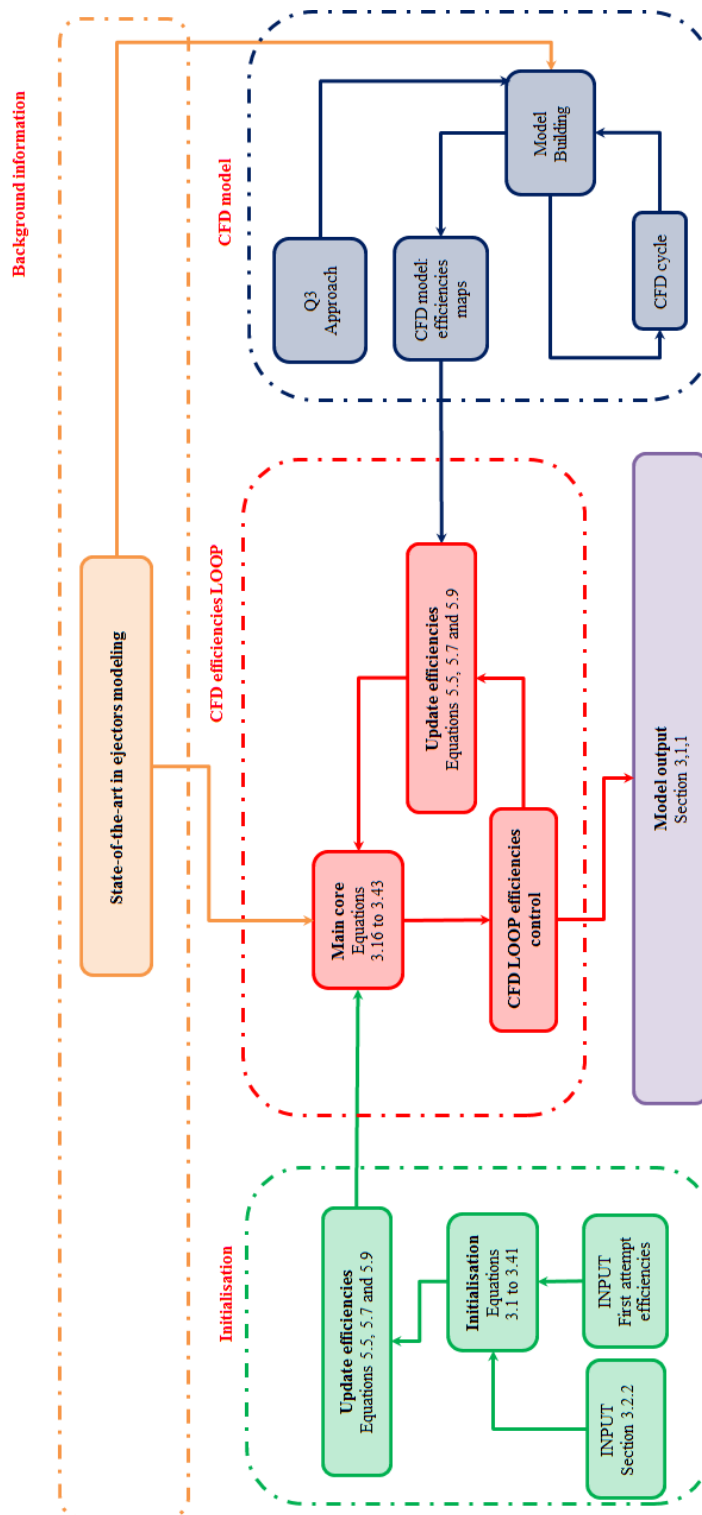


Figure 5-35 The integrated thermodynamic/CFD model

# Conclusions

---

This thesis provided an integrated thermodynamic/CFD approach to ejector modeling and this approach has been applied to the case of a single phase ejector, developing a novel model with following new features, compared with current state-of-the-art in ejector modeling:

1. thermodynamic model uses variable isentropic coefficients (those efficiencies were provided by CFD simulations);
2. the model presented is ready to be integrated in energy power plant simulation codes.

In order to reach those achievements state-of-the-art in ejector thermodynamic and CFD modeling was outlined (Chapter 2). Starting from this review, were presented both the structure of a novel thermodynamic model (Chapter 3) and step to step indications to build up CFD models for ejector in the frame of the  $Q^3$  approach (Chapter 4), taking into account general guidelines in CFD ejector modeling given at the end of Chapter 3.

This thermodynamic model and this CFD approach have been applied to the case of a single phase subsonic ejector.

The application of CFD approach to above case produced results in very good agreement with experimental data and provided the first evaluation of different RANS turbulence models for the case of a convergent nozzle-ejector: as conclusion of this comparison we propose Spalart-Allmaras and  $k - \omega SST$  as the turbulence models recommended for subsonic ejector simulations. Taking into account that previous works [24] proposed  $k - \varepsilon RNG$  and  $k - \omega SST$  as turbulence models advised for supersonic ejector simulations,  $k - \omega SST$  is marked as the turbulence model to be used in ejector simulation, regardless of nozzle geometry (for both subsonic and supersonic ejector).

Integration of thermodynamic and CFD modeling strategies was presented in Chapter 5 where the validated CFD approach was used to supply efficiency maps and efficiency functions to be included in thermodynamic model; moreover, the relationship between efficiencies and flow behavior was investigated.

The new thermodynamic/CFD integrated model (Figure 5-35) has the potentiality to be an advanced tool able to produce global information taking into consideration local flow behavior.

This thesis produced a clear progression in ejector modeling, not only overcoming problems and limitations pointed out by the recent review of He et al. [23], but also providing a better understanding of ejector working conditions and flow phenomena.

Future developments may concern both single phase subsonic ejectors (extending present work), and single phase supersonic ones:

- (i) *single phase subsonic ejector*. Present work pointed out the possibility:
  1. of studying the influence of working fluid on ejector efficiencies: this is very interesting because molecular weight of working fluid have a direct correlation with sonic velocity and ejector efficiencies are strongly affected by the presence of subsonic/sonic/supersonic flow fields (moreover this investigation could be very interesting because subsonic ejector find their application in PEMFC system with Hydrogen as working fluid);
  2. of performing geometry optimization and studying the influence of ejector geometry (e.g. Suction chamber) on ejector efficiencies;
  3. of including diffuser in ejector CFD model in order to obtain diffuser efficiency maps too;
- (ii) *single phase supersonic ejectors*. Present work can be extended to supersonic ejectors by:
  1. applying the proposed approach to the case of a supersonic ejector and retracing above work for that case, building and integrated thermodynamic/CFD model for single phase supersonic ejectors;
  2. comparing subsonic ejector efficiency maps with supersonic ejector ones in order to remark how flow behavior affects performances.

It would be very interesting to modify current approach to the case of two phase flow ejector (importance of two phase flow in ejector has already been recognized by Bartosiewicz et al. in [24], where presence of condensation affected results).

Moreover, the integrated thermodynamic/CFD model for a single phase subsonic ejector proposed in this thesis can be further developed to be integrated in a specific code for energy power plant simulation: GS code. This is a simulation software developed at the Department of Energy at Politecnico di Milano, that is used to predict the performance of a wide variety of chemical processes and systems for electricity production: it was originally designed to calculate gas-steam cycles [144], [145], [146] and has been progressively extended and developed to calculate complex systems including gasification processes, chemical reactors, fuel cells and essentially any kind of plant for power generation from fossil fuels [147], [148], [149].

## References

- [1] H. Bravo, R. Rodríguez, J. Gutiérrez, R. Best y Brown, R. Aguila and H. Peña, "State of art of simple and hybrid jet compression refrigeration systems and the working fluid influence," *International Journal of Refrigeration*, vol. 35, no. 2, p. 386–396, March 2012.
- [2] K. Chunnanond and S. Aphornratana, "Ejectors: applications in refrigeration technology," *Renewable and Sustainable Energy Reviews*, vol. 8, no. 2, p. 129–155, 2004.
- [3] J. Larminie and D. James, *Fuel Cell Systems Explained (Second Edition)*, Wiley, 2003.
- [4] G. Angelino and C. Invernizzi, "Ejector-assisted liquid metal topping cycles," *Proceedings of the Institution of Mechanical Engineers - Part A - Journal of Power and Energy*, vol. 218, pp. 111-121, 2004.
- [5] N. Lior, "Advanced energy conversion to power," *Energy Conversion and Management*, vol. 38, no. 10–13, p. 941–955, July–September 1997.
- [6] G. Angelino, "The potential role of jet compression in high temperature energy conversion," *Energy Conversion*, vol. 12, no. 2, pp. 69-75, June 1972.
- [7] S. Aphornratana, "A small capacity steam-ejector refrigerator: experimental investigation of a system using ejector with movable primary nozzle," *International Journal of Refrigeration*, vol. 20, no. 5, p. 352–358, August 1997.
- [8] K. Chunnanond and S. Aphornratana, "An experimental investigation of a steam ejector refrigerator: the analysis of the pressure profile along the ejector," *Applied Thermal Engineering*, vol. 24, no. 2-3, p. 311–322, February 2004.
- [9] I. Eames, A. Ablwaifa and V. Petrenkoc, "Results of an experimental study of an advanced jet-pump refrigerator operating with R245fa," *Applied Thermal Engineering*, vol. 27, no. 17–18, p. 2833–2840, December 2007.
- [10] R. Yapici, H. Ersoy, A. Aktoprakoğlu, H. Halkaci and O. Yiğit, "Experimental determination of the optimum performance of ejector refrigeration system depending on ejector area ratio," *International Journal of Refrigeration*, vol. 31, no. 7, p. 1183–1189, November 2008.

- [11] B. Huang and J. Chang, "Empirical correlation for ejector design," *International Journal of Refrigeration*, vol. 22, no. 5, p. 379–388, August 1999.
- [12] T. Sankarlal and A. Mani, "Experimental investigations on ejector refrigeration system with ammonia," *Renewable Energy*, vol. 32, no. 8, p. 1403–1413, July 2007.
- [13] Y.-J. Chang and Y.-M. Chen, "Enhancement of a steam-jet refrigerator using a novel application of the petal nozzle," *Experimental Thermal and Fluid Science*, vol. 22, no. 3-4, p. 203–211, September 2000.
- [14] I. Eames, "A new prescription for the design of supersonic jet pumps: the constant rate of momentum change method," *Applied Thermal Engineering*, vol. 22, no. 2, p. 121–131, February 2002.
- [15] K. Cizungu, A. Mani and M. Groll, "Performance comparison of vapour jet refrigeration system with environment friendly working fluids," *Applied Thermal Engineering*, vol. 21, no. 5, p. 585–598, 2001.
- [16] J. Godefroy, R. Boukhanouf and S. Riffat, "Design, testing and mathematical modelling of a small-scale CHP and cooling system (small CHP-ejector trigeneration)," *Applied Thermal Engineering*, vol. 27, no. 1, p. 68–77, 2007.
- [17] D.-W. Sun, "Comparative study of the performance of an ejector refrigeration cycle operating with various refrigerants," *Energy Conversion and Management*, vol. 40, no. 8, p. 873–884, 1999.
- [18] J. Hernandez, R. Dorantes, R. Best and C. Estrada, "The behaviour of a hybrid compressor and ejector refrigeration system with refrigerants 134a and 142b," *Applied Thermal Engineering*, vol. 24, no. 13, p. 1765–1783, September 2004.
- [19] R. Yapıcı and C. Yetişen, "Experimental study on ejector refrigeration system powered by low grade heat," *Energy Conversion and Management*, vol. 48, no. 5, pp. 1560-1568, 2007.
- [20] D. Scott, Z. Zidoun and M. Ouzanne, "An experimental investigation of an ejector for validating numerical simulation," *International Journal of Refrigeration*, vol. 34, pp. 1717-1723, 2011.
- [21] A. Bouhanguel, P. Desevaux and E. Gavignet, "Flow visualization in supersonic ejectors using laser tomography techniques," *International Journal of Refrigeration*, vol. 34, no. 7, p. 1633–1640, November 2011.

- [22] A. Little and S. Garimella, "A review of ejector technology for refrigeration applications," *International Journal of Air-Conditioning and Refrigeration*, vol. 19, no. 1, pp. 1-15, March 2011.
- [23] S. He, Y. Li and R. Wang, "Progress of mathematical modeling on ejectors," *Renewable and Sustainable Energy Reviews*, vol. 13, no. 8, p. 1760–1780, 2009.
- [24] Y. Bartosiewicz, Z. Aidoun, P. Desevaux and Y. Mercadier, "CFD - Experiments Integration in the Evaluation of Six Turbulence Models for Supersonic Ejectors Modeling," in *Proceedings of Integrating CFD and Experiments*, Glasgow, 2003.
- [25] Y. Zhu and Y. Li, "New teoretical model for convergent nozzle ejector in the proton exchange membrane fuell cell system," *Journal of Power Sources*, no. 191, pp. 510-519, 2009.
- [26] E. Groll, "Ejector technology (editorial)," *International Journal of Refrigeration*, vol. 34, no. 7, p. 1543–1544, November 2011.
- [27] B. Huang, J. Chang, C. Wang and V. Petrenko, "A 1-D analysis of ejector performance," *International Journal of Refrigeration*, vol. 22, no. 5, p. 354–364, 1999.
- [28] H. Keenan, E. Neumann and F. Lustwerk, "An investigation of ejector design by analysis and experiment.," *Journal of Applied Mechanical.*, no. 72, p. 299–309, 1950.
- [29] J. Munday and D. F. Bagster, "Industrial & Engineering Chemistry Process Design and Development," vol. 16, p. 442–449, 1977.
- [30] B. Huang and J. Chang, "Empirical correlation for ejector design," *International Journal of Refrigeration*, vol. 22, no. 5, pp. 379-388, 1999.
- [31] S. Elbel, "Historical and presentdevelopments of ejector refrigeration systems with emphasis on transcritical carbon dioxide air-conditioning applications," *International Journal of Refrigeration*, vol. 34, no. 7, p. 1545–1561, November 2011.
- [32] B. Zheng and Y. Weng, "A combined power and ejector refrigeration cycle for low temperature heat sources," *Solar Energy*, vol. 84, no. 5, pp. 784-791, 2010.
- [33] J. Abdulateef, K. Sopian, M. Alghoul and M. Sulaiman, "Review on solar-driven ejector refrigeration technologies," *Renewable and Sustainable Energy Reviews*, vol. 13, no. 6–7, p. 1338–1349, 2009.
- [34] A. Khaliq, B. Agrawala and R. Kumarb, "First and second law investigation of waste heat

- based combined power and ejector-absorption refrigeration cycle," *International Journal of Refrigeration*, vol. 35, no. 1, p. 88–97, 2012.
- [35] A. Khaliq, B. Agrawala and R. Kumarb, "Thermodynamic performance assessment of a novel waste heat based triple effect refrigeration cycle," *International Journal of Refrigeration*, vol. 35, no. 6, p. 1647–1656, 2012.
- [36] A. Meyer, T. Harms and R. Dobson, "Steam jet ejector cooling powered by waste or solar heat," *Renewable Energy*, vol. 34, no. 1, p. 297–306, 2009.
- [37] M. Ameri, A. Behbahaninia and T. A.A., "Thermodynamic analysis of a tri-generation system based on micro-gas turbine with a steam ejector refrigeration system," *Energy*, vol. 35, no. 5, pp. 2203-2209, 2010.
- [38] C. M. Invernizzi and P. Iora, "Heat recovery from a gas microturbine by vapour jet refrigeration," *Applied Thermal Engineering*, vol. 25, pp. 1233-1246, 2005.
- [39] X. Li, C. Zhao and H. K., "First and second law investigation of waste heat based combined power and ejector-absorption refrigeration cycle," *Energy*, vol. 42, no. 1, p. 342–349, 2012.
- [40] V. Petrenkoa and O. Volovyk, "Theoretical study and design of a low-grade heat-driven pilot ejector refrigeration machine operating with butane and isobutane and intended for cooling of gas transported in a gas-main pipeline," *International Journal of Refrigeration*, vol. 34, no. 7, p. 1699–1706, November 2011.
- [41] K. Pianthong, W. Seehanam, M. Behnia, M. Sriveerakul and S. Aphornratana, "Investigation and improvement of ejector refrigeration system using computational fluid dynamics technique," *Energy Conversion and Management*, vol. 48, pp. 2556-2564, 2007.
- [42] J. Sarkar, "Ejector enhanced vapor compression refrigeration and heat pump systems - A review," *Renewable and Sustainable Energy Reviews*, vol. 16, no. 9, p. 6647–6659, December 2012.
- [43] K. Sumeru, H. Nasution and F. Ani, "A review on two-phase ejector as an expansion device in vapor compression refrigeration cycle," *Renewable and Sustainable Energy Reviews*, vol. 16, no. 7, p. 4927–4937, September 2012.
- [44] F. Marsano, L. Magistri and A. Massardo, "Ejector performance influence on a solid oxide fuel cell anodic recirculation system," *Journal of Power Sources*, vol. 129, no. 2, p. 216–228, April 2004.



- 
- [45] D. Bernardi, F. Marsano, M. Bozzolo, O. Tarnowsky and G. Agnew, "Ejectors Design in the Rolls-Royce 1MW Hybrid System," in *ASME Turbo Expo 2005*, Reno, Nevada, USA, 2005.
- [46] F. Trasino, M. Bozzolo, L. Magistri and A. Massardo, "Modeling and Performance Analysis of the Rolls-Royce Fuel Cell Systems Limited: 1 MW Plant," *Journal of Engineering for Gas Turbines and Power*, vol. 133, no. 2, February 2011.
- [47] B. Kim, D. Kim, J. Lee, S. Kang and H. Lim, "The operation results of a 125 kW molten carbonate fuel cell system," *Renewable Energy*, vol. 42, p. 145–151, June 2012.
- [48] B. Kim, D. Kim, J. Lee, S. Kang and H. Lim, "The Ejector Performance of a 75 kW Molten Carbonate Fuel Cell System," *Journal of Fuel Cell Science and Technology*, vol. 8, no. 1, February 2011.
- [49] R. Peters, E. Riensche and P. Cremer, "Pre-reforming of natural gas in solid oxide fuel-cell systems," *Journal of Power Sources*, vol. 86, no. 1–2, p. 432–441, March 2000.
- [50] Y. Zhu, W. Cai, C. Wen and Y. Li, "Fuel ejector design and simulation model for anodic recirculation SOFC system," *Journal of Power Sources*, vol. 173, no. 1, pp. 437-449, 2007.
- [51] EG&G Technical Services, Inc., *Fuel Cell Handbook (Seventh Edition)*, Department of Energy's (DOE) , 2004.
- [52] C. Bao, M. Ouyang and B. Yi, "Modeling and control of air stream and hydrogen flow with recirculation in a PEM fuel cell system - I. Control-oriented modeling," *International Journal of Hydrogen Energy*, vol. 31, no. 13, pp. 1879-1896, October 2006.
- [53] A. Y. Karnik, J. Sun and J. H. Buckland, "Control analysis of an ejector based fuel cell Anode recirculation system," in *Processing of the 2006 American Control Conference ( June 14-16 )*, Minneapolis, Minnesota ( USA ), 2006.
- [54] J. He, S.-Y. Choe and C.-O. Hong, "Analysis and control of a hybrid fuel delivery system for a polymer electrolyte membrane fuel cell," *Journal of Power Sources*, no. 185, pp. 973-984, 2008.
- [55] J. He, J. Ahn and S. Choe, "Analysis and control of a fuel delivery system considering a two-phase anode model of the polymer electrolyte membrane fuel cell stack," *Journal of Power Sources*, vol. 196, no. 10, p. 4655–4670, May 2011.
- [56] S. Penati, « Applicazione di Processi “Chemical Looping Combustion” in Impianti IGCC

- con Cattura della CO<sub>2</sub>,» in *Tesi di laurea, Politecnico di Milano.*, 2011.
- [57] A. Prosperetti and G. Tryggvason, *Computational Methods For Multiphase Flow*, Cambridge University Press, 2007.
- [58] M. H. T. Ishii, *Thermo-Fluid Dynamics of Two-Phase Flow*, Springer, 2010.
- [59] H. Versteeg and W. Malalasekera, *An Introduction to Computational Fluid Dynamics: The Finite Volume Method (2nd Edition)*, Pearson Education, 2007.
- [60] Ansys FLUENT, *Ansys FLUENT 13 - Theory guide*, Ansys FLUENT, 2010.
- [61] I. Eames, S. Aphornratana and H. Haider, "A theoretical and experimental study of a small-scale steam jet refrigerator. *International Journal of Refrigeration*," *International Journal of Refrigeration*, vol. 18, no. 6, p. 378–386, 1995.
- [62] N. H. Aly, A. Karameldina and M. Shamloul, "Modelling and simulation of steam jet ejectors," *Desalination*, vol. 123, no. 1, p. 1–8, 1999.
- [63] S. Varga, A. C. Oliveira and B. Diaconu, "Numerical assessment of steam ejector efficiencies using CFD," *International Journal of Refrigeration*, vol. 32, no. 6, p. 1203–1211, 2009.
- [64] J. Yu and Y. Li, "A Theoretical Study of a Novel Regenerative Ejector Refrigeration Cycle," *International Journal of Refrigeration*, vol. 30, no. 3, p. 464–470, May 2007.
- [65] J. Yu, H. Chen, Y. Ren and Y. Li, "A new ejector refrigeration system with an additional jet pump," *Applied Thermal Engineering*, vol. 26, no. 2-3, pp. 312-319, 2006.
- [66] H. Keenan and E. Neumann, "A simple air ejector," *Journal of Applied Mechanics*, vol. 69, pp. 75-84, 1947.
- [67] E. Rogdakis and G. Alexis, "Design and parametric investigation of an ejector in an air-conditioning system," *Applied Thermal Engineering*, vol. 20, no. 2, pp. 213-223, 2000.
- [68] A. Selvaraju and A. Mani, "Analysis of an ejector with environment friendly refrigerants," *Applied Thermal Engineering*, vol. 24, no. 5-6, pp. 827-838, 2004.
- [69] R. Yapic and H. Ersoy, "Performance characteristics of the ejector refrigeration system based on the constant area ejector flow model," *Energy Conversion and Management*, vol. 46, no. 18-19, pp. 3117-3135, 2005.

- [70] J. Yu, Y. Ren, H. Chen and Y. Li, "Applying mechanical subcooling to ejector refrigeration cycle for improving the coefficient of performance," *Energy Conversion and Management*, vol. 48, p. 1193–1199, 2007.
- [71] J. Cardemil and S. Colle, "A general model for evaluation of vapour ejector performance for application in refrigeration," *Energy Conversion and Management*, vol. 64, pp. 79-86, 2012.
- [72] F. Liu, E. Groll and D. Li, "Modeling study of an ejector expansion residential CO<sub>2</sub> air conditioning system," *Energy and Buildings*, vol. 53, p. 127–136, October 2012.
- [73] F. Liu and A. Groll, "Analysis of a two phase flow ejector for the transcritical CO<sub>2</sub> cycle," in *International Refrigeration and Air Conditioning Conference at Purdue*, Purdue, 2008.
- [74] M. Ouzzane and Z. Aidoun, "Model development and numerical procedure for detailed ejector analysis and design," *Applied Thermal Engineering*, vol. 23, no. 18, pp. 2337-2351, 2003.
- [75] Y. Zhu, W. Cai, C. Wen and Y. Li, "Shock circle model for ejector performance evaluation," *Energy Conversion and Management*, vol. 48, no. 9, p. 2533–2541, 2007.
- [76] Y. Zhu, W. Cai, Y. Li and C. Wen, "Anode gas recirculation behavior of a fuel ejector in hybrid solid oxide fuel cell systems: Performance evaluation in three operational modes," *Journal of Power Sources*, vol. 185, no. 2, p. 1122–1130, 2008.
- [77] Y. Zhu and Y. Li, "Novel ejector model for performance evaluation on both dry and wet vapors ejectors," *International Journal of Refrigeration*, vol. 32, no. 1, p. 21–31, 2009.
- [78] Y. Zhu, W. Cai, C. Wen and Y. Li, "Simplified ejector model for control and optimization," *Energy Conversion and Management*, vol. 49, no. 6, p. 1424–1432, June 2008.
- [79] J. Fabri and R. Siestrunk, "Supersonic Air Ejectors," *Advances in Applied Mechanics*, vol. 5, p. 1–34, 1958.
- [80] J. C. Dutton, C. D. Mikkelsen and A. L. Addy, "Theoretical and experimental investigation of the constant area, supersonic-supersonic ejector," *AIAA Journal*, vol. 20, no. 10, pp. 1392-1400., 1982.
- [81] J. C. Dutton and B. F. Carroll, "Optimal Supersonic Ejector Designs," *Journal of Fluids Engineering*, vol. 108, no. 4, pp. 414-421, Decembre 1986.

- [82] M. Sokolov and D. Hershal, "Enhanced ejector refrigeration cycles powered by low grade heat. Part 2. Design procedures," *International Journal of Refrigeration*, vol. 13, pp. 357-363, 1990.
- [83] J. Guo and H. Shen, "Modeling solar-driven ejector refrigeration system offering air conditioning for office buildings," *Energy and Buildings*, vol. 41, pp. 175-181, 2009.
- [84] J. W. Mitchel and A. L. London, "Design Parameters for Subsonic Air-Air Ejectors," Stanford University, Department of Mechanical Engineering, 1958.
- [85] S. Varga, A. Oliveira and B. Diaconu, "Influence of geometrical factors on steam ejector performance – A numerical assessment," *International Journal of Refrigeration*, vol. 32, no. 7, p. 1694–1701, 2009.
- [86] K. Tyagi and K. Murty, "Ejector-compression systems for cooling: Utilising low grade waste heat," *Journal of Heat Recovery Systems*, vol. 5, no. 6, p. 545–550, 1985.
- [87] C. Korres, A. Papaioannou, V. Lygerou and N. Koumoutsos, "Solar cooling by thermal compression: the dependence of the jet thermal compressor efficiency on the compression ratio," *Energy*, vol. 27, no. 8, p. 795–805, August 2002.
- [88] P. Domanski, "Minimizing Throttling Losses in the Refrigeration Cycle," in *Proceedings of 19th Congress of Refrigeration*, 1995.
- [89] P. Menegay and A. Kornhauser, "Ejector expansion refrigeration cycle with underexpanded motive nozzle," *Am. Inst. Aeronaut. Astronaut*, vol. 2, p. 915–920, 1994.
- [90] D.-W. Sun, "Variable geometry ejectors and their applications in ejector," *Energy*, vol. 21, no. 10, p. 919–929, 1996.
- [91] G. Grazzini and A. Mariani, "A simple program to design a multi-stage jet-pump for refrigeration cycles," *Energy Conversion and Management*, vol. 39, no. 16-18, p. 1827–1834, 1998.
- [92] H. El-Dessouky, H. Ettouney, I. Alatiqi and G. Al-Nuwaibit, "Evaluation of steam jet ejectors," *Chemical Engineering Processing*, vol. 41, no. 6, p. 551–561, 2002.
- [93] G. Alexis and E. Rogdakis, "A verification study of steam-ejector refrigeration model," *Applied Thermal Engineering*, vol. 23, no. 1, p. 29–36, January 2003.
- [94] S. Elbel and P. Hrnjak, "Effects of Internal Heat Exchanger on Performance of Transcritical CO<sub>2</sub> Systems with ejectors," in *Proceedings of 10th International*

- Refrigeration and Air Conditioning Conference at Purdue*, Purdue, 2004.
- [95] D. Li and A. Groll, "Transcritical CO<sub>2</sub> refrigeration cycle with ejector-expansion device," *International Journal of Refrigeration*, vol. 28, no. 5, p. 766–773, August 2005.
- [96] E. Ksayer and D. Clodic, "Enhancement of CO<sub>2</sub> Refrigeration Cycle Using an Ejector: 1D Analysis," in *Proceeding of International Refrigeration and Air Conditioning Conference at Purdue*, Purdue, 2006.
- [97] J. Deng, P. Jiang, T. Lu and W. Lu, "Particular Characteristics of Transcritical CO<sub>2</sub> Refrigeration Cycle with an ejector," *Applied Thermal Engineering*, vol. 27, no. 2-3, p. 381–388, February 2007.
- [98] J. Yu, H. Zhao and Y. Li, "Application of an ejector in autocascade refrigeration cycle for the performance improvement," *International Journal of Refrigeration*, vol. 31, no. 2, p. 279–286, 2008.
- [99] Y. Bartosiewicz, Z. Aidoun, P. Desevaux and Y. Mercadier, "Numerical and experimental investigations on supersonic ejectors," *International Journal of Heat and Fluid Flow*, vol. 26, no. 1, pp. 56-70, February 2005.
- [100] S. Riffat, G. Gan and S. Smith, "Computational fluid dynamics applied to ejector heat pumps," *Applied Thermal Engineering*, vol. 19, no. 4, p. 291–297, April 1996.
- [101] F. Chen, C. Liu and J. Yang, "Supersonic flow in the second-throat ejector–diffuser system," *Journal of Spacecraft and Rockets*, vol. 31, no. 1, pp. 123-129, January 1994.
- [102] J. Wang and F. Chen, "On the start condition of a second-throat ejector–diffuser," *Aeronautical Journal*, p. 321–326, October 1996.
- [103] S. B. Riffat and A. Omer, "CFD modelling and experimental investigation of an ejector refrigeration system using methanol as the working fluid.," *International Journal of Energy Research*, vol. 25, no. 2, pp. 115-128, February 2001.
- [104] S. Riffat and P. Everitt, "Experimental and CFD modelling of an ejector system for vehicle air conditioning," *Journal of the Institute of Energy*, vol. 72, p. 41–47, 1999.
- [105] S. Varga, A. Oliveira, X. Ma, S. Omer, W. Zhang and S. Riffat, "Experimental and numerical analysis of a variable area ratio steam ejector," *International Journal of Refrigeration*, vol. 34, no. 7, p. 1668–1675, November 2011.
- [106] Y. Bartosiewicz, Y. Z. Aidoun and Mercadier, "Numerical assessment of ejector operation

- for refrigeration applications based on CFD," *Applied Thermal Engineering*, vol. 26, pp. 604-612, 2006.
- [107] A. Hemidi, F. Henry, S. Leclaire, J. Seynhaeve and Y. Bartosiewicz, "CFD analysis of a supersonic air ejector. Part 1: Experimental validation of single-phase and two phase operation," *Applied Thermal Engineering*, vol. 29, pp. 1523-1531, 2009.
- [108] E. Rusly, L. Aye, W. Charters and A. Ooi, "CFD analysis of ejector in a combined ejector cooling system," *International Journal of Refrigeration*, vol. 28, no. 7, p. 1092-1101, November 2005.
- [109] A. Hemidi, F. Henry, S. Leclaire, J. Seynhaeve and Y. Bartosiewicz, "CFD analysis of a supersonic air ejector. Part 2: Relation between global operation and local flow features," *Applied Thermal Engineering*, vol. 29, pp. 2990-2998, 2009.
- [110] T. Sriveerakul, S. Aphornratana and K. Chunnanond, "Performance prediction of steam ejector using computational fluid dynamics - Part 2: Flow structure of a steamejector influenced by operating pressures and geometries," *International Journal of Thermal Sciences*, vol. 46, no. 8, p. 823-833, August 2007.
- [111] Y. Zhu, W. Cai, C. Wen and Y. Li, "Numerical investigation of geometry parameters for design of high performance ejectors," vol. 29, no. 5-6, p. 898-905, April 2009.
- [112] M. Ji, T. Utomo, J. Woo, Y. Lee, H. Jeong and H. Chung, "CFD investigation on the flow structure inside thermo vapor compressor," *Energy*, vol. 35, no. 6, p. 2694-2702, June 2010.
- [113] M. Opgenortha, D. Sederstroma, W. McDermottb and C. Lengsfelda, "Maximizing pressure recovery using lobed nozzles in a supersonic ejector," *Applied Thermal Engineering*, vol. 37, p. 396-402, May 2012.
- [114] X. Yang, X. Log and X. Yao, "Numerical investigation on the mixing process in a steam ejector with different structures," *International Journal of Thermal Sciences*, vol. 56, pp. 95-106, 2012.
- [115] N. Ruangtrakoon, T. Thongtip, S. Aphornratana and T. Sriveerakul, "CFD simulation on the effect of primary nozzle geometries for a steam ejector in refrigeration cycle," *International Journal of Thermal Sciences*, vol. Article in press, pp. 1-13, 2012.
- [116] S. Varga, M. Lebre and A. Oliveira, "CFD Study of a variable area ratio ejector using R600a and R152a refrigerants," *International Journal of Refrigeration*, pp. In Press, Accepted Manuscript, October 2012.

- [117] T. Sriveerakul, S. Aphornratana and K. Chunnanond, "Performance prediction of steam ejector using computational fluid dynamics - Part 1: Validation of the CFD results," *International Journal of Thermal Sciences*, vol. 46, no. 8, p. 812–822, August 2007.
- [118] E. Colombo, F. Inzoli and R. Mereu, "A methodology for qualifying industrial CFD: The Q3 approach and the role of a protocol," *Computers & Fluids*, vol. 54, p. 56–66, January 2012.
- [119] D. Yoder, "NPARC Alliance Validation Archive: Ejector Nozzle," NASA, 6 January 2011. [Online]. Available: <http://www.grc.nasa.gov/WWW/wind/valid/eject/eject.html>. [Accessed March 2012].
- [120] P. Desevaux and O. and Aeschbacher, "Numerical and Experimental Flow Visualization of the Mixing Process Inside an Induced Air Ejector," *International Journal of Turbo and Jet Engines*, vol. 19, pp. 71-78, 2002.
- [121] P. Desevaux, F. Lanzetta and Y. Bailly, "CFD Modelling of Shock Train inside a Supersonic Ejector: Validation against Flow Visualization and Pressure Measurements in the case of Zero-Secondary Flow," in *10th Int. Symp. on Flow Visualization*, Kyoto, Japan, 2002.
- [122] R. Porcar and J. Prenel, "Visualization of shock waves in a supersonic ejector – utilization of the polarization of diffuse light," *Optics Communications*, vol. 17, p. 346–349, 1976.
- [123] N. M. M. Clemens, "A planar Mie scattering technique for visualizing supersonic mixing flows," *Experiments in Fluids*, vol. 11, no. 2-3, pp. 175-185, 1991.
- [124] M. Chandrasekhara, A. Krothapalli and D. Baganoff, "Performance characteristics of an underexpanded multiple jet ejector," *Journal of Propulsion and Power*, vol. 7, p. 462–464, 1991.
- [125] P. Desevaux, J. Prenel and G. Hostache, "An optical analysis of an induced flow ejector using light polarization properties," *Experiments in Fluids*, vol. 16, p. 165–170, 1994.
- [126] P. Desevaux, J. Prenel and G. Hostache, "Flow visualization methods for investigating an induced flow ejector," *Journal of Flow Visualization and Image Processing*, vol. 2, p. 61–74, 1995.
- [127] S. Kim, H. Kim and S. Kwon, "Transitional behavior of a supersonic flow in a two-dimensional diffuser," *KSME International Journal*, vol. 15, p. 1816–1821, 2001.
- [128] P. Desevaux, "A method for visualizing the mixing zone between two co-axial flows in an

- ejector," *Optics and Lasers in Engineering*, vol. 35 , p. 317–323, 2001.
- [129] P. Desevaux, "Formation of water nanodroplets in an induced ejector – flow visualization," *Canadian Journal of Chemical Engineering*, vol. 79 , p. 273–278, 2001.
- [130] V. Dvorak and P. Safarik, "Supersonic Flow Structure in the Entrance Part of a Mixing Chamber of 2D Model Ejector.," *Journal of Thermal Science* , vol. 12, no. 4, pp. 344-349, 2003.
- [131] P. Desevaux, A. Mellal and Y. Alves De Sousa, "Visualization of secondary flow choking phenomena in a supersonic air ejector," *Journal of Visualization* , vol. 7, no. 3, pp. 249-256, 2004.
- [132] V. Dvorak and P. Safarik, "Transonic instability in entrance part of mixing chamber of high-speed ejector," *Journal of Thermal Science* , vol. 14, no. 3, p. 258–264, 2005.
- [133] H. Sugiyama, Y. Tsujiguchi and T. Honma, "Structure and oscillation phenomena of pseudo-shock waves in a straight square duct at Mach 2 and 4," in *15th AIAA International Space Planes and Hypersonic Systems and Technologies Conference*, Dayton, Ohio, 2008.
- [134] P. Desevaux, T. Marynowski and Y. Mercadier, "CFD simulation of a condensing flow in a supersonic ejector: validation against flow visualization," in *ISFV13, International Symposium on Flow Visualization*, Nice, France, 2008.
- [135] T. Marynowski, P. Desevaux and Y. Mercadier, "Experimental and numerical visualizations of condensation process in a supersonic ejector," *International Journal of Turbo and Jet Engines*, vol. 26 , no. 1, pp. 61-78, 2009.
- [136] T. Koita and J. Iwamoto, "A study on flow behavior inside a simple model of ejector," in *10<sup>th</sup> International Conference on Fluid Control, Measurement and Visualisation*, Moscow, Russia, 2009.
- [137] G. Gilbert and P. Hill, "Analysis and Testing of Two-Dimensional Slot Nozzle Ejectors With Variable Area Mixing Sections," NASA, 1973.
- [138] N. Georgiadis, T. Chitsomboon and J. Zhu, "Modification of the Two-Equation Turbulence Model in NPARC to a Chien Low Reynolds Number k-epsilon Formulation," NASA, 1994.
- [139] N. J. Georgiadis and D. A. Yoder, "Use of Navier-Stokes Methods for the Calculation of High-Speed Nozzle Flow Fields," NASA, 1994.



- 
- [140] D. Thrumurthy, "Design and analysis of noise suppression exhaust nozzle systems," Purdue University, 2010.
- [141] P. Colonna and T. van der Stelt, "FluidProp: a program for the estimation of thermo physical properties of fluids," Energy Technology Section, Delft University of Technology, The Netherlands, 2004. [Online]. Available: [www.fluidprop.com](http://www.fluidprop.com).
- [142] C. Lea, "Underexpanded jet," Ercoftac, [Online]. Available: [http://qnet-ercoftac.cfms.org.uk/w/index.php/Abstr:Underexpanded\\_jet](http://qnet-ercoftac.cfms.org.uk/w/index.php/Abstr:Underexpanded_jet). [Accessed September 2012].
- [143] C. Donaldson and R. Snedeker, "A study of free jet impingement - Part 1: mean properties of free and impinging jets," *Journal of Fluid Mechanics*, vol. 45, no. 2, pp. 281-319, 1971.
- [144] G. Lozza, "Bottoming Steam Cycles for Combined Gas-steam Power Plants: A Theoretical Estimation of Steam Turbine Performance and Cycle Analysis.," New Orleans, USA, 1990 .
- [145] S. Consonni, G. Lozza, E. Macchi, P. Chiesa and P. Bombarda, "Gas turbine-based cycles for power generation. Part A. Calculation model," in *International Gas Turbine Congress*, Yokohama, Japan, 1991.
- [146] Consonni, "Performance prediction of Gas/Steam cycles for power generation ( Ph.D. thesis )," Princeton Univ., Princeton, NJ, USA., 1992.
- [147] P. Chiesa, S. Consonni, T. Kreutz and R. Williams, "Co-production of hydrogen, electricity and CO<sub>2</sub> from coal with commercially ready technology. Part A. Performance and emissions," *International Journal of Hydrogen Energy*, vol. 30, p. 747-767, 2005.
- [148] P. Chiesa, G. Lozza, A. Malandrino, M. Romano and V. Piccolo, "Three reactors chemical looping process for hydrogen production," *International Journal of Hydrogen Energy*, vol. 33 , p. 2233-2245, 2008.
- [149] M. Romano and G. Lozza, "Long-term coal gasification-based power plants with near-zero emissions. Part A. Zecomix cycle," *International Journal of Greenhouse Gas Control*, vol. 4, p. 459-468, 2009.